



# THE UNIVERSITY *of* EDINBURGH

This thesis has been submitted in fulfilment of the requirements for a postgraduate degree (e.g. PhD, MPhil, DClinPsychol) at the University of Edinburgh. Please note the following terms and conditions of use:

- This work is protected by copyright and other intellectual property rights, which are retained by the thesis author, unless otherwise stated.
- A copy can be downloaded for personal non-commercial research or study, without prior permission or charge.
- This thesis cannot be reproduced or quoted extensively from without first obtaining permission in writing from the author.
- The content must not be changed in any way or sold commercially in any format or medium without the formal permission of the author.
- When referring to this work, full bibliographic details including the author, title, awarding institution and date of the thesis must be given.

---

# Superconducting Generators for Large Offshore Wind Turbines

---

*Ozan Keysan*



*Doctor of Philosophy*

THE UNIVERSITY OF EDINBURGH

2014





*To Asuman,*

*Without whom  
nothing is worth finishing...*



---

# Abstract

---

This thesis describes four novel superconducting machine concepts, in the pursuit of finding a suitable design for large offshore wind turbines. The designs should be reliable, modular and light-weight. The main novelty of the topologies reside in using a single loop shaped stationary superconducting field winding, which eliminates the rotating transfer couplers and electric brushes or brushless exciters. Furthermore, the electromagnetic forces in the superconducting wire are also eliminated, which simplifies the design and manufacturing of the cryostat and the support structure.

Among the four topologies presented, the claw pole type machine is the most promising one. The rotor of the machine composes of claw-poles made from laminated electrical sheets, the superconducting field winding and the armature winding are stationary. The machine is analysed using 3D FEA simulations and a small linear machine prototype is manufactured to verify the simulations.

For large scale applications, a double-sided claw pole machine is proposed, which has balanced magnetic attraction forces in the rotor. The machine has a modular cryostat structure, which increases the availability of the machine. Thus, even if a fault occurs in the cryocoolers or in the armature coils, the rest of the machine can operate at partial load until the maintenance is performed. Moreover, it is much easier to replace the faulty parts, as full disassemble of the machine is not required, and a small on-site crane can be used. As a result, it offers operational advantages over the existing superconducting topologies.

A 10 MW, 10 rpm generator design is presented, which has a diameter of 6.6 m and an axial length of 1.4 m. The total active mass of the generator is 58 tonnes, and the structural mass is 126 tonnes, which gives a total mass of 184 tonnes. There are four independent cryostats and two independent armature windings in the machine to improve modularity. The biggest advantage of the design is the significantly less superconducting wire usage compared to any other designs; 10 MW machine just needs 15 km of  $\text{MgB}_2$  wire at 30 K. Thus, it is believed that the proposed topology is a very cost effective and suitable candidate for a successful entry to the wind turbine market.



---

# Acknowledgements

---

I would like to thank my principal supervisor, Markus Mueller. He gave me the idea, opportunity, support and freedom to carry out my research. Without him this work would not be possible. I also would like to express my warmest gratitude to my second supervisor Ewen Macpherson, who provided timely advice during the writing of this thesis.

I thank the support received from Hopewell Holding and the scholarship from the Institute for Energy Systems and University of Edinburgh.

Although, this dissertation has just my name on it, many friends and colleagues are contributed to the completion of this dissertation, both directly, by helping me throughout my studies, as well as indirectly, by making my life complete and enjoyable during the last four years.

Here's a game to find your names, probably it is much more fun than reading the following pages.

A P P E H J I K A Z B G H R G W  
I L M Z K U N Q F W E F V Y O Z  
Y N A H T A N O J U G Y U D K C  
B W R S C N O N Z N S D N D S N  
B E I H D P G E M A E W I E E A  
U C O S M A T A L B S T Z B L Z  
C P S J T B I G O S I U R I C I  
S B N A R L U R U W A K M U I K  
G I I R L O A K R A M A Z A N E  
M Y S I D H R D D T C Y E P N Y  
A K A S W A R D E N I Z Y I R D  
Y R R A M A R I S C A U N P L G  
U T F A H E E M E L M T E Z W W  
Y O I C F W N C E U F O P S S L  
N M I K E A O J T W C A L X W P  
F R A N S I S C A M P H S B P N



---

# Declaration

---

I declare that this thesis was composed by myself, that the work contained herein is my own except where explicitly stated otherwise in the text, and that this work has not been submitted for any other degree or professional qualification except as specified.

Significant parts of the work outlined in this thesis have been published:

- Chapter 2 and 3 is based on: “Application of high temperature superconducting machines to direct drive renewable energy systems”, O. Keysan, Chapter in *Electrical Drives for Direct Drive Renewable Energy Systems*, Woodhead Publication, 2013.
- Chapter 4 and 5 is based on: “A Homopolar HTSG Topology for Large Direct-Drive Wind Turbines”, O. Keysan and M. Mueller, *IEEE Transactions on Applied Superconductivity*, vol.21(5), October 2011.
- While not explicitly part of this thesis, the work in Chapter 4 and 5 provided the basis and led directly to: “A linear superconducting generator for wave energy converters”, O. Keysan and M. Mueller, *IET International Conference on Power Electronics, Machines and Drives*, 2012 and “Superconducting generators for renewable energy applications”, O. Keysan, M. Mueller, *IET Conference on Renewable Power Generation*, 2011.
- Chapter 6 is based on: “A Modular Superconducting Generator for Offshore Wind Turbines”, O. Keysan, D. Olczak, M. Mueller, *Journal of Superconductivity and Novel Magnetism*, 2012. and “A Transverse Flux High-Temperature Superconducting Generator Topology for Large Direct Drive Wind Turbines”, O. Keysan, M. Mueller, *Superconductivity Centennial Conference*, 2011.
- Chapter 7 is based on: “Magnetic and Structural Analysis of a Transverse Flux Claw Pole Linear Machine”, O. Keysan, J. Burchell, M. Mueller, *IEEE International Conference on Industrial Technology*, 2013.

The full list of publications is presented in Appendix J.

---

**Ozan Keysan**





---

# Contents

---

<b>Abstract</b>	<b>v</b>
<b>Acknowledgements</b>	<b>vii</b>
<b>Declaration</b>	<b>ix</b>
<b>1 Motivation</b>	<b>1</b>
1.1 Current status of wind energy . . . . .	1
1.2 Tower Head Mass Problem . . . . .	3
1.2.1 Power Take-Off Alternatives . . . . .	4
1.2.2 Superconducting Generators . . . . .	6
1.2.3 Mass Comparison of Direct Drive Generators . . . . .	7
1.3 Reliability . . . . .	9
1.4 Availability . . . . .	10
1.5 Summary & Aim of Thesis . . . . .	10
1.6 Layout of Thesis . . . . .	11
<b>2 A Brief Introduction to Superconductivity</b>	<b>13</b>
2.1 Properties of Superconductors . . . . .	14
2.1.1 Zero Resistivity . . . . .	14
2.1.2 Perfect Diamagnetism . . . . .	18
2.1.3 Quench . . . . .	21
2.2 Common Superconducting Wire Materials . . . . .	22
2.2.1 BSCCO . . . . .	22
2.2.2 YBCO . . . . .	26
2.2.3 Magnesium Diboride( $\text{MgB}_2$ ) Wire . . . . .	28
2.3 Conclusion . . . . .	29
<b>3 Applications of Superconductors in Electric Power</b>	<b>31</b>
3.1 Superconducting Transmission Lines . . . . .	31
3.2 Superconducting Fault Current Limiters . . . . .	32
3.3 Superconducting Transformers . . . . .	34
3.4 Superconducting Magnetic Energy Storage . . . . .	35
3.5 Superconducting Electrical Machines . . . . .	36
3.5.1 Advantages . . . . .	36
3.5.2 Technical Challenges . . . . .	38

3.6	Superconducting Machine Topologies . . . . .	42
3.6.1	Conventional Stator - Superconducting Rotor . . . . .	43
3.6.2	Homopolar Superconducting Machine . . . . .	45
3.6.3	Axial-Flux Superconducting Machines . . . . .	48
3.6.4	All Superconducting Machines . . . . .	48
3.7	Major Superconducting Machine Projects . . . . .	49
3.7.1	American Superconductor . . . . .	49
3.7.2	General Electric . . . . .	51
3.7.3	Super-GM Japan . . . . .	52
3.7.4	Siemens . . . . .	53
3.7.5	University of Southampton . . . . .	53
3.8	Superconducting Wind Turbine Generators . . . . .	55
3.8.1	AMSC-SeaTitan . . . . .	55
3.8.2	Advanced Magnet Lab . . . . .	56
3.8.3	GE - Ecomagination . . . . .	57
3.8.4	Other Projects . . . . .	59
3.8.5	Economics and Market Readiness . . . . .	61
3.9	Discussion . . . . .	62
<b>4</b>	<b>Design I: Axial Homopolar Superconducting Machine</b>	<b>63</b>
4.1	Introduction . . . . .	63
4.2	Machine Topology . . . . .	63
4.2.1	Stator . . . . .	63
4.2.2	Rotor . . . . .	65
4.3	Electromagnetic Analysis of the Machine . . . . .	65
4.3.1	Analytical Magnetic Model . . . . .	65
4.3.2	Finite Element Analysis . . . . .	72
4.4	Simulation of the Axial Homopolar Machine . . . . .	73
4.5	Discussion of Results . . . . .	75
4.5.1	Chapter Summary . . . . .	76
<b>5</b>	<b>Design II: Axial Bipolar Superconducting Machine</b>	<b>77</b>
5.1	Introduction . . . . .	77
5.2	Reluctance Network Model . . . . .	79
5.3	FEA Results . . . . .	80
5.3.1	Magnetic Core Optimisation . . . . .	80
5.3.2	Discussion of Results . . . . .	87
5.4	Chapter Summary . . . . .	90
<b>6</b>	<b>Design III: Claw Pole Transverse Flux Superconducting Machine</b>	<b>91</b>

6.1	Claw Pole Machines . . . . .	91
6.1.1	Transverse Flux Machines . . . . .	92
6.2	Proposed Claw Pole Topology . . . . .	94
6.2.1	Superconducting Field Winding . . . . .	94
6.2.2	Inner Stator . . . . .	96
6.2.3	Rotor . . . . .	97
6.2.4	Outer Stator . . . . .	97
6.3	Analytical Model . . . . .	97
6.3.1	Parameter Definition . . . . .	99
6.4	FEA Simulations . . . . .	99
6.4.1	Modelling the Inner Stator . . . . .	102
6.4.2	Modelling the Claw Pole . . . . .	103
6.4.3	Modelling the Outer Stator . . . . .	104
6.5	Design of a Rotary Prototype . . . . .	105
6.5.1	Varying Pole Number . . . . .	107
6.5.2	Flux Density in the Inner Core . . . . .	111
6.5.3	Varying Core-to-Pole Pitch Ratio . . . . .	112
6.5.4	Varying Superconducting Coil MMF . . . . .	115
6.5.5	Cogging Torque . . . . .	117
6.5.6	Varying Stator Slot Number . . . . .	121
6.6	Modelling of the Superconducting Coil . . . . .	125
6.6.1	Flux Penetrating into Superconducting Coil . . . . .	126
6.6.2	Cooling System . . . . .	129
6.7	Structural Modelling . . . . .	131
6.8	Conclusion . . . . .	137
<b>7</b>	<b>Development of a</b>	
	<b>Linear Claw Pole Prototype</b>	<b>139</b>
7.1	Design of Linear Claw Pole Machine . . . . .	139
7.1.1	Electromagnetic Modelling . . . . .	140
7.2	Assembly of the Machine . . . . .	146
7.3	Experiment Results . . . . .	152
7.3.1	Deflections in the Air-gap Clearance . . . . .	152
7.3.2	Flux Linkage Tests . . . . .	153
7.3.3	Flux Density Comparison . . . . .	154
7.3.4	Induced Voltage Tests . . . . .	156
7.4	Conclusion . . . . .	159
<b>8</b>	<b>Up-scaling for Large Power:</b>	
	<b>Double-Claw Pole Design</b>	<b>161</b>

8.1	Double Sided Claw Pole Machine . . . . .	161
8.1.1	Analytical Model . . . . .	162
8.2	FEA Simulations . . . . .	164
8.2.1	Material Selection: VacoFlux50 . . . . .	164
8.3	Electromagnetic Modelling . . . . .	165
8.4	Sectioned Field Coil . . . . .	169
8.5	Optimisation . . . . .	169
8.5.1	Genetic Algorithm Optimisation . . . . .	170
8.5.2	Objective Function & Penalty Factors . . . . .	171
8.5.3	Flowchart . . . . .	172
8.5.4	Computation Time . . . . .	173
8.6	Design of a 10 MW Generator . . . . .	174
8.6.1	Optimisation Outputs . . . . .	174
8.6.2	Optimum Design . . . . .	176
8.6.3	Superconducting Coil & Cooling System . . . . .	179
8.6.4	Structural Mass . . . . .	186
8.7	Design of a 36.5 MW Ship Propulsion Motor . . . . .	188
8.8	Mass Comparison . . . . .	191
8.9	Conclusions . . . . .	192
<b>9</b>	<b>Concluding Remarks</b>	<b>195</b>
9.1	The Approach to the Problem . . . . .	195
9.2	Contribution to Knowledge . . . . .	197
9.3	Further Work . . . . .	199
<b>Appendices</b>		
<b>A</b>	<b>Accessing Data and Models</b>	<b>201</b>
<b>B</b>	<b>Data Sheets for Some Superconducting Wires</b>	<b>203</b>
B.1	Bi-2223 . . . . .	203
B.2	YBCO . . . . .	205
B.3	MgB <sub>2</sub> . . . . .	206
<b>C</b>	<b>Reluctance Network Parameters</b>	<b>207</b>
C.1	Homopolar Superconducting Machine . . . . .	207
C.1.1	Basic Magnetic Circuit . . . . .	207
C.1.2	Extended Magnetic Circuit . . . . .	209
C.1.3	Dimensions & Parameters . . . . .	210
C.2	Bipolar Superconducting Machine . . . . .	210
C.3	Claw Pole Superconducting Machine . . . . .	211

---

C.4	Double-Claw Pole Superconducting Machine . . . . .	213
<b>D</b>	<b>Software</b>	<b>215</b>
D.1	SolidWorks . . . . .	215
D.2	Opera - Vector Fields . . . . .	215
D.2.1	Pre-Processor and Modeller: . . . . .	216
D.2.2	Solver: . . . . .	217
D.2.3	Post-processor: . . . . .	218
D.3	R/RStudio . . . . .	218
<b>E</b>	<b>Linear Versions of Homopolar and Bipolar Machine</b>	<b>219</b>
E.1	Linear Homopolar Machine . . . . .	219
E.2	Linear Bipolar Machine . . . . .	220
<b>F</b>	<b>Specific Magnetic and Electric Loading</b>	<b>221</b>
<b>G</b>	<b>Cryocooler Comparison</b>	<b>225</b>
G.1	Cooling Power vs.Temperature . . . . .	225
<b>H</b>	<b>Technical Drawings</b>	<b>227</b>
H.1	10 MW, 10 rpm Generator . . . . .	227
<b>I</b>	<b>Linear Prototype Technical Drawings</b>	<b>229</b>
<b>J</b>	<b>List of Publications</b>	<b>233</b>
	<b>Bibliography</b>	<b>235</b>



# Motivation

---

### 1.1 Current status of wind energy

Increasing oil and gas prices and the threat of global warming makes renewable energy a favourable option to supply the world's energy demand. Wind energy is one of the most well developed options among renewable energy technologies. There has been a remarkable increase in the installed wind energy capacity around the world over the last two decades and this trend is expected to continue for many years [162]. According to a report by the Global Wind Energy Council, the total wind turbine capacity of the world has reached 282 GW at the end of 2012, which corresponds to 4 % of the world's total installed capacity [7]. The numbers in this report, which are presented in figure 1.1, show that the installed wind capacity has doubled almost every three years for the last 15 years.

The biggest challenge that the wind energy sector faces is to reduce the cost of energy. The current cost of wind turbines is about €1.6m/MW for onshore and €3m/MW for offshore wind turbines with a typical rating of 2.5 MW for onshore and 3.6 MW for offshore [97]. There is a trend toward higher power-rated turbines, which help to reduce the installation and maintenance costs per kilo-watt-hour [28]. This trend can be observed over the last 25 years as given in figure 1.2. The power rating of the turbines increased by 100 times since 1985 and this trend seems to continue. The onshore wind energy market is considered to be quite mature and the power rating is not expected

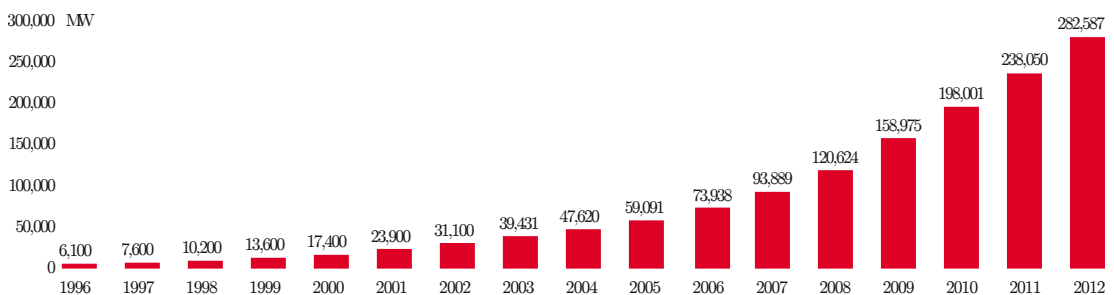


**Figure 1.1:** Cumulative installed wind capacity around the world 1996–2012 [7]



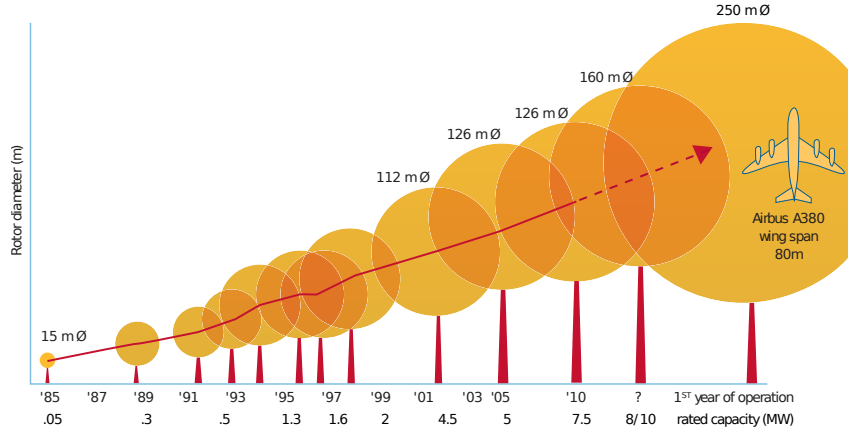


**Figure 1.2:** Increase in the wind turbines power rating and size in the last 25 years [13].

to go beyond the present 3–3.6 MW size due to transportation limitations. However, large offshore wind turbines can be assembled in port and transported in one piece.



**Figure 1.3:** Commercial offshore wind farms turbine size for UK and Europe. Bubble size is proportional to the wind farm rated output [36].

Another variable that can reduce the cost of energy for a wind turbine is the capacity factor. Offshore wind turbines benefit from higher wind speeds and regular wind regimes. Thus, offshore wind turbines draw interest of manufacturers for this untapped energy resource. According to market projections of [8], until 2020 annual world production of offshore wind turbines will increase from 2.7 GW to 6.2 GW. In figure 1.3, the turbine power ratings for commercial offshore wind farms across the UK and the rest of Europe are presented. The power rating of the offshore wind turbines increased from 2 MW to 5 MW in the last decade. In [8], it is predicted that the size of the offshore wind turbines will continue to increase beyond 5 MW as presented in figure 1.4. This figure shows that in 2020 85 % of the wind turbine installations are expected to be larger than 5 MW. In [17], it is stated that 10 MW offshore wind

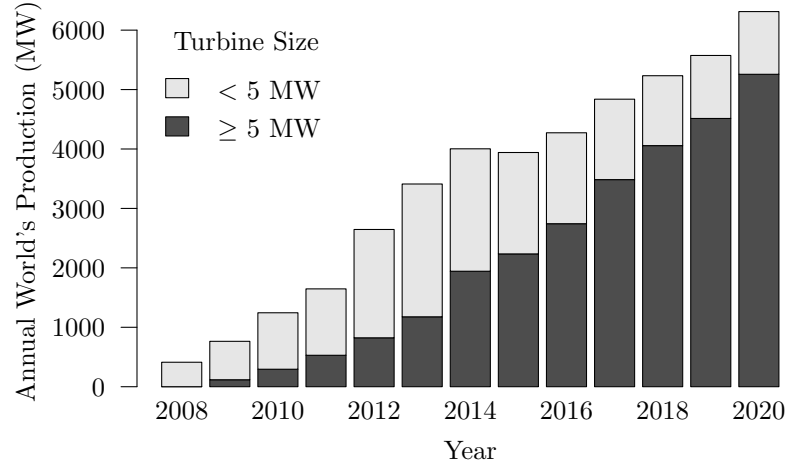


**Figure 1.4:** Emerging market projection for offshore wind energy converters (Produced with data from [8]).

turbines are desirable in 2020, which will reduce tower and installation cost per installed power. In [97], it is proposed that the aim of the offshore wind turbine industry is to manufacture 10 MW turbines which cost €2.2m/MW or less.

## 1.2 Tower Head Mass Problem

There are many studies that aim to solve challenges of a large wind turbine. In a recently completed EU project (Up-Wind), the feasibility of 10 MW and 20 MW wind turbines has been investigated. Up-Wind concluded that the excessive top-head mass as one of the most critical issues for very large wind turbines [13]. The mass estimations for the main components of 5, 10, and 20 MW turbines are presented in table 1.1. The top-head mass for a 20 MW turbine is estimated to be 880 tonnes. The tower mass for this turbine is estimated as 2,780 tonnes. If the tower-head mass is reduced, significant savings can be made in the structural, foundation and installation costs. A smaller, lighter generator also enables the nacelle to be transported and lifted to the tower in one piece, which reduces the installation time. Furthermore, when the capacity of current offshore installation vessels is considered, which is around 300 tonnes [99], the demand for a lighter, high power density power take-off system is clear.

	5 MW	10 MW	20 MW
Turbine Diameter	126 m	178 m	252 m
Rotational Speed	12 rpm	9 rpm	6 rpm
Torque Rating	4.0 MNm	10.6 MNm	31.8 MNm
Rotor Mass	122 t	305 t	770 t
Tower Head Mass	320 t	760 t	880 t
Tower Mass	347 t	983 t	2,780 t

**Table 1.1:** Mass estimations for 5, 10 and 20 MW wind turbines [13].

### 1.2.1 Power Take-Off Alternatives

#### Direct Drive Permanent-Magnet Generators

Direct-drive permanent magnet generators simplify the drive-train by minimizing moving parts and exhibit higher part-load efficiency [100]. However, as the power rating of the turbine increases they become enormously heavy. The structural mass of the generator has a large share in the overall mass [113]. For example, for a 5 MW turbine, structural mass has 65 % share in the total mass. In [153] different mechanical structures are compared. Air-cored permanent magnet machines are proposed to eliminate the magnetic attraction force between rotor and stator [112, 118, 92]. Thus, the structural mass of the generator can be reduced.

Transverse flux permanent-magnet machines(TFPM) have a higher torque density than radial flux PM machines, which can help to reduce the generator size and mass. The winding space in a TFPM can be utilized better without decreasing the available space for the main flux [27]. Thus, the machine can have a short pole pitch which helps to increase the frequency and magnitude of the induced voltage at low rotational speeds. In [27], it is stated that a 5 MW TFPM machine is 25 % lighter than an iron-cored radial flux PM generator. In general, TFPM machines have simple concentrated windings and higher torque densities. However, the flux path is more complex making the mechanical design and manufacturing more complicated [28, 29].

One big drawback of permanent magnet generators is the high cost of rare-earth magnets, which has increased more than tenfold between 2009 and 2011 due to export regulations introduced by China [53]. In figure 1.5 the price variation of Neodymium Oxide is presented. Although, it is now much cheaper than the peak in 2011, the prices are still volatile and it is still four times more expensive compared to four years ago. It is stated in [117] that the future DDPMGs are in risk due to high demand of rare-earth metals and supply chain problems due to political risk.

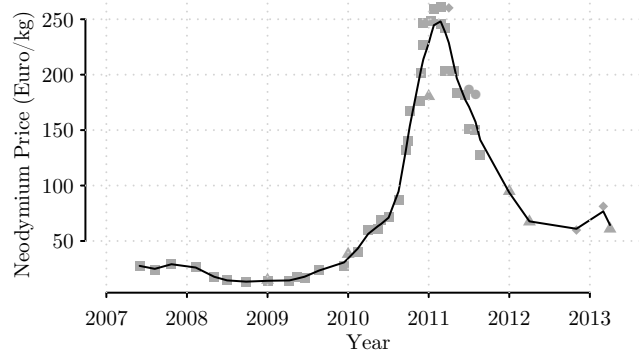


**Figure 1.5:** Neodymium Oxide price variation between 2007 and 2013 (data points obtained from Peak Resources Ltd and Lynas Corp.).

### Medium Speed Generators

In order to reduce the cost of a direct-drive generator, medium speed power take-off systems are introduced that use single stage or double stage gearboxes. In this way, the high speed stage of the gearbox, which is considered to be the least reliable part, is eliminated [130]. The generator, which can be a PM generator or an induction generator, rotates at around 150–600 rpm. The gearbox and generator can be combined into a single unit to reduce the structural mass and reduce the number of bearings, as in Areva Multibrid 5 MW turbine. Another design is GE Drive-train’s 3.5 MW IntegraDrive coupled generator-gearbox concept. Although, this concept is economically very favourable for 5–6 MW offshore wind turbines, the scalability of this concept beyond 10 MW has not been proved yet.

### Hydraulic Systems

There are some hydraulic power take-off designs which use variable speed hydraulic transmission such as WinDrive [48] and Artemis Intelligent Power [138]. A hydraulic motor runs the electrical generator at constant synchronous speed, which eliminates the power electronics. Artemis plans to build a 7 MW hydraulic gearbox coupled to twin synchronous generators. The weak point of a hydraulic system is the fault ride through capabilities. Since there are no intermediate stages between generator and grid, in case of a grid-fault the control loop of the hydraulic system needs to be fast enough to respond within grid requirements.

Another novel idea is generation at sea level. A hydraulic pump is placed in the nacelle, but the hydraulic motor and generator is placed at the sea level. A 5 MW concept has been developed by ChapDrive. In the We-at-Sea project, a common generator unit that connects several wind turbines is proposed [45]. However, the overall efficiency of the system is expected to be lower than direct-drive systems.

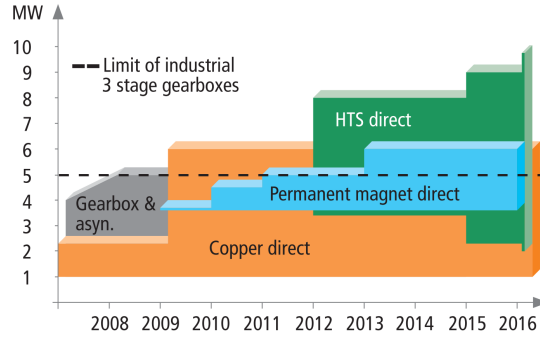


**Figure 1.6:** Comparison of the different generator types for wind turbines from 2008 to 2016 [97].

### 1.2.2 Superconducting Generators

One promising candidate to reduce the generator mass and volume for a large off-shore wind turbine (10 MW and beyond) power take-off system is the superconducting generator [97, 99, 79]. Superconducting wires can conduct much larger currents than copper wires and they can create magnetic fields much larger than rare-earth permanent magnets. It is stated in [36] that the introduction of direct-drive superconducting drive trains has the largest technical potential impact of any drive train innovation.

Although, superconducting machines use expensive materials and require additional cooling equipment, the extra cost of the generator can be compensated by reduced installation costs and increased energy generation. It is estimated that superconducting generators can increase the annual energy production (AEP) by two percent, and decrease the capital expenditure by two percent [36]. It is stated in [99] that a 6 MW HTS direct drive generator can have 50 % of the mass of a direct drive PM generator and the lower generator mass may make it possible to transport and install the turbine in one piece.

As the power ratings increase and rotational speeds of the turbines decrease gearboxes become infeasible due to size limitations. Although, a 6.5 MW gearbox is manufactured by Winergy, it is stated in [97] that the economical limit for 3-stage gearboxes is 5 MW. In [97], it is proposed that for generators larger than 6 MW, HTS generators are the only feasible solution. Although it has not happened yet, Lesser suggested that we will see superconducting wind turbines starting from 2012 (see figure 1.6). A more conservative study suggests, in 2020 superconducting generators will have 10 % market share for wind turbines around 8 MW rating [36].

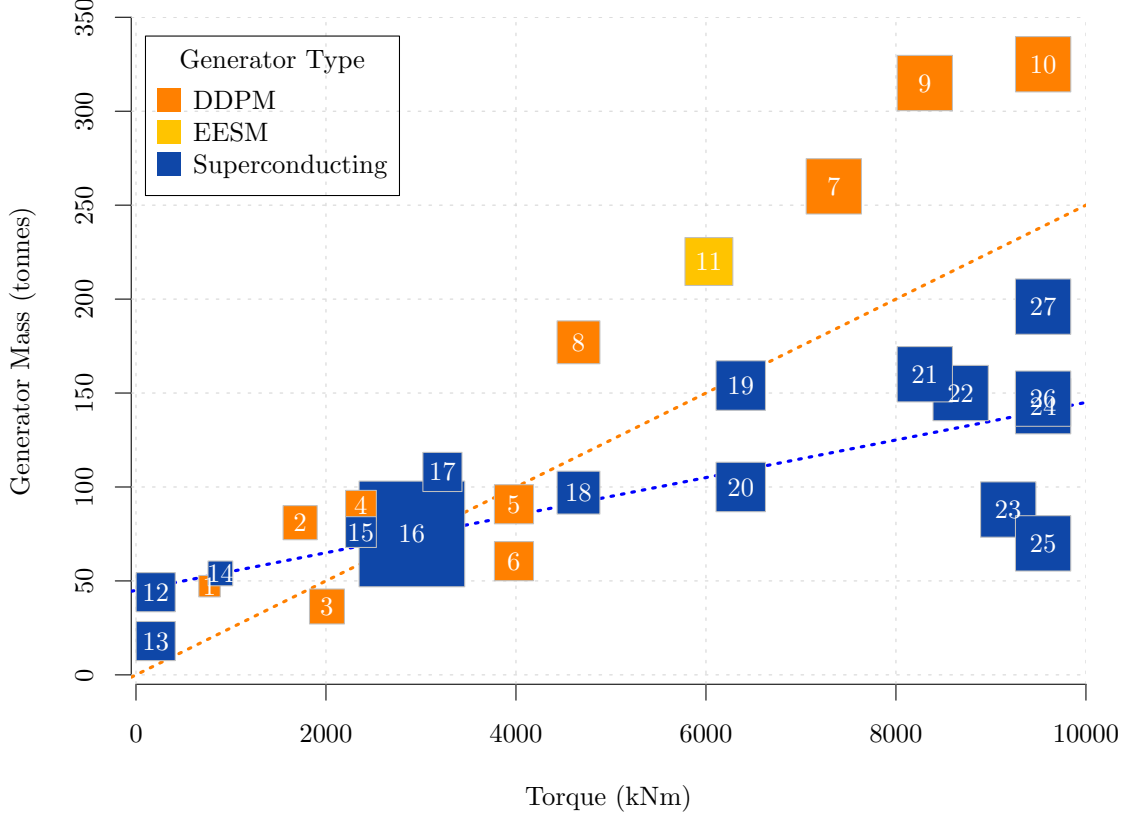


**Figure 1.7:** Mass of different large direct-drive machines as a function of the torque, area of the square represents the power rating. DDPM: Direct drive permanent magnet generator, EESM: Electrically excited synchronous machine, Superconducting: High-temperature superconducting generator. Orange line represents generator mass to torque ratio ( $m/T$ ) of 25 kg/kNm for permanent-magnet machines as given in [28]. Blue line is the linear trend line for the superconducting machines.

### 1.2.3 Mass Comparison of Direct Drive Generators

Data from different direct-drive systems has been collected to compare the mass to torque ratio of HTS machines with other types of direct-drive generators. The result is presented in figure 1.7 and tabulated in table 1.2. It should be noted that some of the machines are final designs or commercial products (e.g., Enercon, Harakosan), whereas some designs are provisional or it is not clear how the structural mass is estimated. Final designs tend to be heavier than initial designs, but it is believed that the graph will provide a good understanding of torque density capability of HTS machines. The orange line represents the ratio of generator mass to torque for permanent-magnet machines which is estimated as 25 kg/kNm by Bang *et al.* in [28]. The Enercon-E126, which has a high  $m/T$  ratio (36.4 kg/kNm) is the only copper field synchronous generator in the graph. The blue line represents the linear trend line estimated using the HTS machines in the graph. The equation of the trend line is given in (1.1).

**Table 1.2:** Torque density comparison conventional and superconducting generators.

	Manufacturer	Power (MW)	Speed (rpm)	Mass (t)	Torque (kNm)	Mass/T (kg/kNm)	Type
1	Harakosan [47]	1.5	18	47.2	796	59.3	PMG
2	The Switch [47]	3.8	21	81	1728	46.9	PMG
3	NewGen [50]	4	19	36.4	2010	18.1	PMG
4	NREL-AMSC [106]	3.1	12.5	90	2368	38.0	PMG <sup>a</sup>
5	Bang et. al. [29]	5	12	90.8	3979	22.8	TFPM
6		5	12	60.5	3979	15.2	TFPM <sup>b</sup>
7	NTNU Reference [150]	10	13	260	7346	35.4	PMG
8	NREL-AMSC [106]	6	12.3	177	4658	38.0	PMG <sup>c</sup>
9		10	11.5	315	8304	37.9	PMG <sup>d</sup>
10	Bang et. al. [28]	10	10	325	9549	34.0	PMG <sup>e</sup>
11	Enercon-E126	7.5	12	220	6031	36.4	EESM
12	Lee et. al. [96]	5	230	44	208	212.0	HTSG <sup>f</sup>
13		5	230	18	208	86.7	HTSG <sup>g</sup>
14	Maki [105]	2	21.5	54	888	60.8	HTSG
15	NREL-AMSC [106]	3.1	12.5	76	2368	32.1	HTSG
16	AMSC [80]	36.5	120	75	2905	25.8	HTSG
17	Maki [105]	5	14.8	108	3226	33.5	HTSG
18	NREL-AMSC [106]	6	12.3	97	4658	20.8	HTSG
19	Maki [105]	8	12	154	6366	24.2	HTSG
20	Converteam [99]	8	12	100	6366	15.7	HTSG
21	NREL-AMSC [106]	10	11.5	160	8303	19.3	HTSG
22	AMSC [151]	10	11	150	8681	17.3	HTSG
23	Abrahamsen et. al. [17]	10	10.4	88	9182	9.6	HTSG <sup>h</sup>
24	General Electric [51]	10	10	143	9549	15.0	HTSG <sup>i</sup>
25	AML [110]	10	10	70	9549	7.3	HTSG <sup>j</sup>
26	Sung et. al. [156]	10	10	147	9549	15.4	HTSG <sup>k</sup>
27		10	10	196	9549	20.5	HTSG <sup>l</sup>

<sup>a</sup>The machine is not optimised for minimum mass.<sup>b</sup>Ring-shaped TFPM.<sup>c</sup>The machine is not optimised for minimum mass.<sup>d</sup>The diameter is limited to 4.3 m.<sup>e</sup>Estimated mass.<sup>f</sup>Homopolar superconducting machine.<sup>g</sup>Air-cored superconducting synchronous machine.<sup>h</sup>The machine is found to be economically infeasible.<sup>i</sup>The generator actually uses NbTi low temperature superconductor wire.<sup>j</sup>Fully superconducting generator with MgB<sub>2</sub> wires.<sup>k</sup>With YBCO wire.<sup>l</sup>With Bi-2223 wire.

It can be seen from the graph that HTS machines are generally lighter than PM generators for applications with torque requirements larger than 3000 kNm. There are two PMG topologies below the HTS machine trend line; a transversal flux permanent magnet machine [29] and the NewGen topology which reduces the structural mass significantly [50]. It should be noted that implementation of similar techniques to HTS machines can further decrease their mass.

$$Mass(t) = 0.011 \times Torque(kNm) + 45 \quad (1.1)$$

### 1.3 Reliability

Offshore wind turbines operate in a harsher environment compared to onshore wind turbines. Furthermore, access to offshore wind turbines is much more difficult and any repair is subject to the weather and the sea conditions. Especially, in winter it may take weeks to find a suitable window for maintenance. If a crane is required for a major replacement, it is also subject to the availability of appropriate vessels. All these factors add weeks or even months of lost energy income on top of the repair cost. Thus, reliability of an offshore wind turbine is very important.

The reliability of superconducting generators is not proven in normal operating conditions, yet alone in such a harsh environment. A recent Danish project (Superwind) aims to find out the challenges of a superconducting wind turbine, and de-risk the design before large scale use. It is stated in [17] that, for a successful market entry the main challenge is to prove that a direct drive superconducting generator is as reliable as alternative drive trains.

In a superconducting machine, the cryogenic system is the most critical component. Cryocoolers of offshore superconducting wind turbines will be subject to temperature variations, humidity, saline environment and vibrations. The reliability of the cryocoolers under this harsh environment is still questionable. Unfortunately, the cryocoolers cannot be eliminated until a room-temperature superconductor, if ever, is discovered. However, the cooling system can be simplified and moving parts can be minimized by using a stationary superconducting coil design, which has many advantages [58]:

- No rotating transfer coupler, more robust and cheaper cooling system.
- No electrical brushes or complex excitation systems.
- No centrifugal forces and transient torques that can damage the superconducting material.
- Simpler winding support.



## 1.4 Availability

The availability of the generator has a direct effect on the electricity generation income. The interval of maintenance should be scheduled starting from the design stage. The present generation of cryocoolers do require periodic maintenance. If a maintenance event requires turning off the cryocooler, then cooling time becomes a very important issue. For instance, a cold magnetic core is used in [171] for a 100 kW generator, with a cooling power of 120 W. The generator can be cooled down to operating temperature from ambient temperature in 18 hours. Another example is Siemens' 4 MW machine, which has a total cooling power of 135 W. The cooling time for this machine is approximately 75 hours [90].

Therefore, in order to increase availability:

- The cold mass should be minimized, a warm-iron core is preferable.
- The cryocooler system should have some redundancy to enable maintenance while keeping the superconducting coil at cryogenic temperatures.

It is also important to have modularity in the design to improve fault tolerance. Thus, in case of a fault, the generator can operate at part-load the maintenance. This results in increased energy income. More importantly, in a modular machine the faulty sections can be replaced using a small on-site crane without dismantling the whole generator.

## 1.5 Summary & Aim of Thesis

The number of offshore wind turbine installations and power rating of these turbines is expected to increase in the next decade. 10 MW wind turbines are desirable to reduce the installation and operational costs. However, high tower head mass and reliability are the biggest challenges.

In this chapter it has been shown that, the superconducting machines become lighter than direct-drive permanent-magnet generators for applications that demand more torque than 3000 kNm (e.g. a 5 MW, 13 rpm wind turbine). However, reliability of superconducting machines is still a critical issue for wind turbine applications. It should be proved that superconducting generators are at least as reliable as conventional generators and they are more cost effective in the long run with reduced installation costs and increased efficiency. Only then, the wind industry market can adopt to superconducting generators.

The main aim of this thesis is to propose a suitable superconducting generator topology for large offshore wind turbines. It is aimed to understand shortcomings of common superconducting machines and propose a novel topology that can outperform existing topologies in terms of reliability and modularity.

## 1.6 Layout of Thesis

The next chapter of this thesis introduces the phenomenon of superconductivity. The fundamental properties of superconducting materials and some common superconducting wire materials are reviewed.

In Chapter 3, the power applications of superconductors are presented. Different types of superconducting machine topologies and major superconducting machine designs are presented, with an emphasis on the superconducting wind turbine designs.

Chapter 4, presents a homopolar superconducting machine topology suitable for large diameter applications. The machine uses a single stationary superconducting field winding and a variable reluctance rotor structure.

In Chapter 5, the topology proposed in Chapter 4 is improved by using two independent superconducting field windings. The machine is superior to the homopolar topology in terms of the electromagnetic design, but has some mechanical difficulties.

Chapter 6 proposes a novel topology, which uses a stationary superconducting field winding and a modified claw-pole rotor. Finite element analysis is used to predict the flux distribution in the machine and to analyse different aspects such as flux penetrating into superconducting coils and magnetic attraction forces.

In Chapter 7, a small linear claw pole prototype is presented. The prototype is used to highlight the challenges in manufacturing and to verify the finite element simulations.

Chapter 8 proposes a modified version of the claw pole machine which is suitable for large-scale applications. This machine is built in a modular way and expected to have high reliability and availability. A 10 MW, 10 rpm design is presented, including mass, superconducting wire and cooling power requirements.

In Chapter 9, the proposed topologies are reviewed in terms of their strengths and shortcomings. Finally, suggestions for future research are provided.



---

## Chapter 2

# A Brief Introduction to Superconductivity

---

It is usually assumed that superconductivity is a cutting-edge technology. On the contrary, the superconductivity phenomenon was first discovered over a century ago in 1911, by a scientist named H. Kamerlingh Onnes. Onnes was doing experiments on the physical properties of mercury at very low temperatures when he observed an abrupt decrease in resistivity. A photo of Onnes and his colleagues in their low-temperature laboratory is presented in figure 2.1.

Electrical resistances of conventional materials decrease as the material is cooled-down. The resistivities of these materials converges to a non-zero value as the temperature is reduced down to absolute zero ( $-273^{\circ}\text{C}$ ). Superconductors differ from normal conductors as their electrical resistivities plunge from a finite value to zero at a specific temperature which is called the critical temperature ( $T_c$ ). The resistivity variation of a normal conductor and a superconductor with temperature is given in figure 2.2.

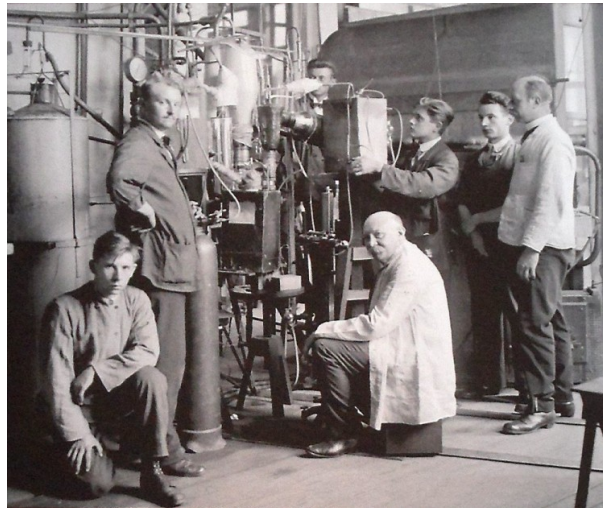


**Figure 2.1:** H. Kamerlingh Onnes (in the middle, sitting) and colleagues trying to liquefy helium.

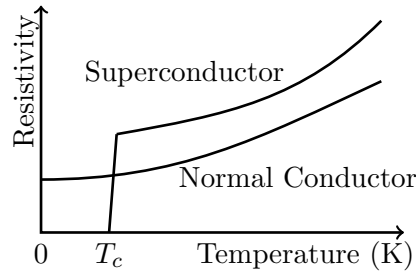


**Figure 2.2:** Temperature vs. electrical resistivity for normal conductors and superconductors.  $T_c$  is the critical temperature of the superconductor.

The first superconductor discovered was mercury which has a critical temperature of 4.2 K. In the following years, many other superconductors have been discovered such as lead and niobium. Superconductors are not exotic and rare materials. In fact, there are many superconducting elements and many more superconducting compounds. Some elements only become superconducting under high pressure. The superconducting elements and the elements that take part in superconducting compounds are illustrated in a periodic table in figure 2.3.

The most important feature of a superconductor is its critical temperature point. There are many superconductors without any practical application due to very low critical temperature. A high critical temperature ( $T_c$ ) is desirable, but it is not the only attribute of a superconductor. Superconductivity is also limited by current density and magnetic field applied to the material. The critical temperature ( $T_c$ ), the critical current density ( $J_c$ ), and the critical magnetic field strength ( $H_c$ ) defines the boundaries of the superconductivity state as illustrated in figure 2.4. The superconducting materials lose superconductivity outside this region.

## 2.1 Properties of Superconductors

### 2.1.1 Zero Resistivity

The most distinctive property of superconductors is the zero-resistivity (or infinite-conductivity). The resistivity of a material can be simply expressed as:

$$R = \rho \frac{L}{A} \quad (2.1)$$

where  $\rho$  is the resistivity,  $L$  is the length and  $A$  is the cross sectional area of the material. It is experimentally difficult to prove the superconductors exactly have zero resistivity ( $\rho = 0$ ) just by measuring the resistance due to the contact resistance and measurement

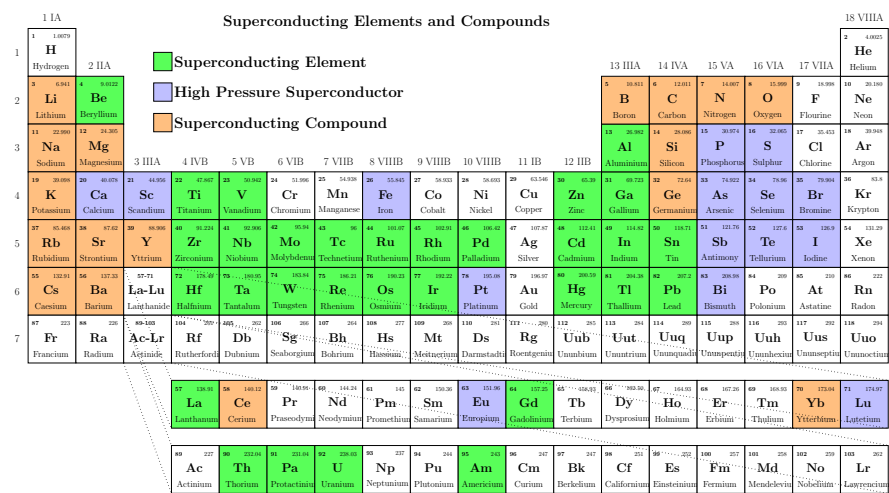


**Figure 2.3:** Known superconducting elements and elements that constitute superconducting compounds.

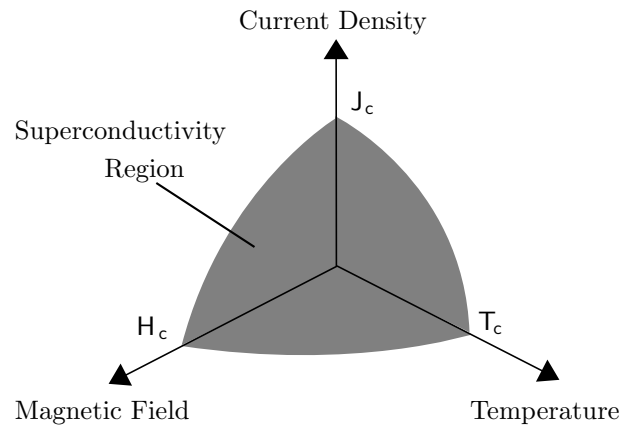


**Figure 2.4:** Superconductivity boundaries(current density, temperature, and magnetic field).



**Figure 2.5:** An extension cord plugged into itself to obtain persistent(!) currents (Photo: Göksel Keysan).

accuracy. However, it is not the resistance measurement that proves the zero resistance state of a superconductor, but it is the existence of persistent currents [25]. When a current is applied to a superconducting wire loop, the current flows through the loop indefinitely with no external power source. This is like plugging an extension cord into itself and observing non-decaying currents as shown in figure 2.5. It is this phenomenon that proves the zero resistivity state of a superconductor material.

The definition of the resistivity is the ratio of the electrical field to current density:

$$\rho = \frac{E}{J} \quad (2.2)$$

where  $J$  is the electrical current density,  $E$  is the external electric field. The resistivity of a superconductor is zero ( $\rho = 0$ ). Thus, the electric field ( $E$ ) has to be zero in order to have a finite current density ( $J$ ), which implies a current flow without electric field [25].

$$E = 0 \quad (2.3)$$

The electric field potential through a closed loop can be expressed as:

$$\oint E dl = - \int_S \nabla \times E dA = - \int_S \frac{\partial B}{\partial t} dA = - \frac{d\Phi}{dt} \quad (2.4)$$

Thus the magnetic field change in the superconductor is zero, which implies persistent magnetic field and electric current. Unfortunately, this statement is only valid when a direct current (DC) is conducted. Superconductors dissipate power when alternating current is applied. This is due to the fact that superconductors have two different types of electrons: super-electrons and normal-electrons [75]. As the temperature is reduced below the critical temperature ( $T_c$ ), super-electrons begin to develop which are capable of conducting current without any resistance at all. The remaining electrons are called

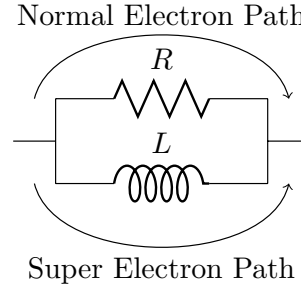


**Figure 2.6:** Electrical representation of a superconductor.

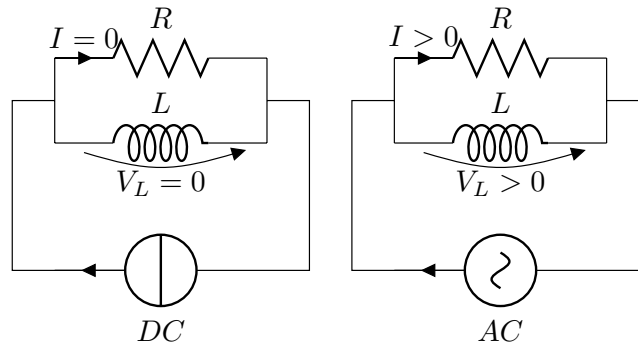


**Figure 2.7:** Electric current path in a superconductor under direct and alternating current.

normal-electrons and they suffer collisions and dissipate power as the current flows. The fraction of super-electrons increases as the temperature is further decreased and at 0 K all the conduction electrons become super-electrons [75].

In a superconductor, current can be conducted by both normal and super electrons. The super-electron path short-circuits the normal-electron path when a direct current is applied. As a result, no current is conducted through the normal electron path. However, under alternating current conditions the electric field must exist to accelerate (and to decelerate) the electrons. The inertia of an electron is very small, but still there will be a lag between current and electric field. This means the super-electrons introduce an inductive impedance. In other words, superconductors can be modelled by an ideal inductance in parallel with a resistance [75] as given in figure 2.6. The inductive component creates a voltage potential under AC conditions and some of the current conducts through the resistive path as shown in figure 2.7. As a consequence, the lossless transmission of superconductors is disrupted for alternating currents. The fraction of the current carried by super-conductors and normal-conductors is dependent on the material properties and operating temperature. For most cases, only a very small portion of the current is conducted by normal-electrons, but even this spoils the absolute zero-resistivity of the superconductor at alternating currents.



### 2.1.2 Perfect Diamagnetism

A lesser known property of superconductors is perfect diamagnetism. When a magnetic field is applied to a superconductor, non-decaying screening currents are induced on the surface of the superconducting material which expels the magnetic field. It should be noted that this is a different phenomenon than zero-resistivity. If it were because of zero resistivity, as equation 2.3 implies, the change in the magnetic field would be zero. Thus, if an external field was applied before cooling the material below its critical temperature, it should have kept the flux density at the initial value. On the contrary, superconductors expel magnetic field irrespective of applying the magnetic field before or after the cooling. This behaviour is called the "Meissner-Ochsenfeld effect" which was discovered in 1933 by Walter Meissner and Robert Oschenfeld. The relation between magnetic field and magnetic flux density can be expressed as:

$$B = \mu_0(H + M) \quad (2.5)$$

where  $B$  is the magnetic flux density,  $\mu_0$  is the permeability of free space,  $H$  is the magnetic field,  $M$  is the magnetization. The magnetic field density inside a superconductor is zero which implies:

$$B = \mu_0(H + M) = 0 \quad \Rightarrow \quad H = -M \quad (2.6)$$

The magnetic susceptibility is the ratio of the magnetization to the applied magnetic field. The magnetic susceptibility for a superconductor is therefore equal to:

$$\chi = \frac{M}{H} = -1 \quad (2.7)$$

The magnetic susceptibility of a material can also be expressed using relative permeability ( $\mu_r$ ) as:

$$\chi = \frac{\mu}{\mu_0} - 1 = \mu_r - 1 \quad \Rightarrow \quad \mu_r = 0 \quad (2.8)$$

Relative permeability and susceptibility values of some materials are presented in table 2.1. Ferromagnetic materials have very large relative permeabilities. The relative permeability of paramagnetic materials are greater, but very close to one. The relative permeability of common diamagnetic materials is smaller, but very close to one. Superconductors have a relative permeability of zero, which implies perfect diamagnetism ( $M/H = -1$ ) [75].

Material	Type	Relative Permeability ( $\mu_r$ )	Susceptibility ( $\chi$ )
Vacuum	NA	1	0
Electrical Steel	Ferromagnetic	4,000	3,999
Aluminium	Paramagnetic	1.000022	$2.2 \times 10^{-5}$
Bismuth	Diamagnetic	0.999834	$-1.66 \times 10^{-4}$
Superconductor	Perfect Diamagnetic	0	-1

**Table 2.1:** Relative permeability and susceptibility values of some materials.

Material	Critical Temp. ( $T_c$ )
Titanium	0.4 K
Aluminium	1.2 K
Mercury	4.2 K
Lead	7.2 K

**Table 2.2:** Critical temperatures for some type-I superconductors.

However, there is a special type of superconductor (so called type-II superconductors) that allows some flux to penetrate through. The superconductors can be classified according to their behaviour under external magnetic fields as follows:

### Type-I Superconductors

Type-I superconductors expel the magnetic field up to a critical value ( $H_c$ ) and exhibit perfect diamagnetism inside that region. If a larger magnetic field is applied, superconductivity breaks down and material returns to normal conducting state. Most type-I superconductors are metallic elements. The critical temperatures of some type-I superconductors are presented in table 2.2.

### Type-II Superconductors

Type-II superconductors have two critical magnetic field limits:  $H_{c1}$ ,  $H_{c2}$ . If the magnetic field is smaller than  $H_{c1}$ , the superconductor is in perfect diamagnetic state and behaves similar to type-I superconductors. However, if a magnetic field larger than  $H_{c1}$  is applied, the perfect diamagnetic state is lost and the magnetic field starts to penetrate into the material. This phenomenon is called flux-pinning. In this stage, the material is still a superconductor with zero-resistivity but has a mixed state (also known as the vortex state). If the magnetic field is further increased, a full-penetration point is achieved and at that point the material loses its superconductivity. This point is called the upper critical value of the magnetic field ( $H_{c2}$ ). Figure 2.8 shows these two different states for the type-I and type-II superconductors. The magnetization as a function of applied magnetic field is presented in figure 2.10.

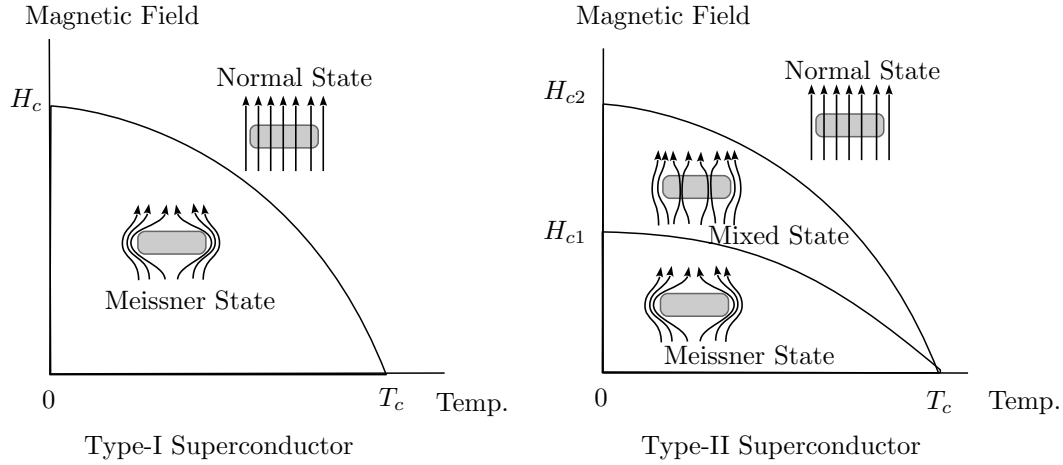


**Figure 2.8:** Superconducting states and critical magnetic field values for the type-I and type-II superconductors



**Figure 2.9:** A superconductor levitating above permanent magnets (Photo: Kim Chan-Joong).

The mixed state of a type-II superconductor gives mechanical stability during magnetic levitation. In other words, it is the Meissner effect that creates the levitation force and it is the flux-pinning that gives stiffness and balance to the levitation. In figure 2.9 a superconductor levitating above permanent magnets is shown.

Type-II superconductors are mostly alloys and compounds. They usually have higher critical temperatures than type-I superconductors. The critical temperatures of these materials are presented in table 2.3. High temperature superconductors, which have a critical temperature higher than the boiling temperature of nitrogen (77 K), are all type-II superconductors.

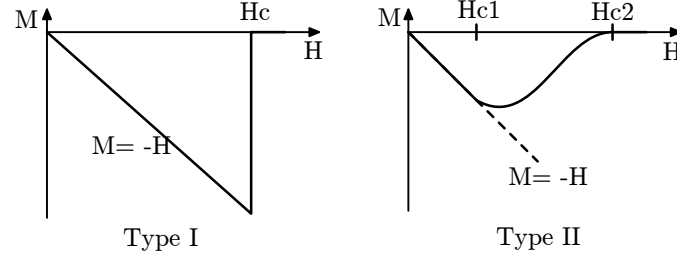


**Figure 2.10:** Magnetization as a function of applied magnetic field for type-I and type-II superconductors [25].

Material	Critical Temp. ( $T_c$ )
$Nb_3Al$	18 K
$Nb_3Si$	19 K
$MgB_2$	39 K
$YbBa_2Cu_3O_7$	89 K

**Table 2.3:** Critical temperatures for some type-II superconductors

### 2.1.3 Quench

Quench is the process of a superconductor abruptly transforming from the superconducting state to the normal state. It can be triggered by a change in temperature, current density or magnetic field. As a consequence, the superconductor goes from having no resistance to being resistive and it generates a large amount of joule heating which in return accelerates the quenching process. Furthermore, the heat capacity of superconductors is usually very low at cryogenic temperatures which make them very susceptible to temperature excursions from very small energy inputs [34]. This positive feedback mechanism is one of the most critical issues in superconducting coil applications and it is a common failure for superconducting coils. One example of such a damage is presented in figure 2.11.

Quench is usually a design challenge, but it is very useful for some applications. For example, resistive superconducting fault current limiters relies on this property to quickly limit high fault currents in a grid by instantly going from the superconducting state to the normal state.

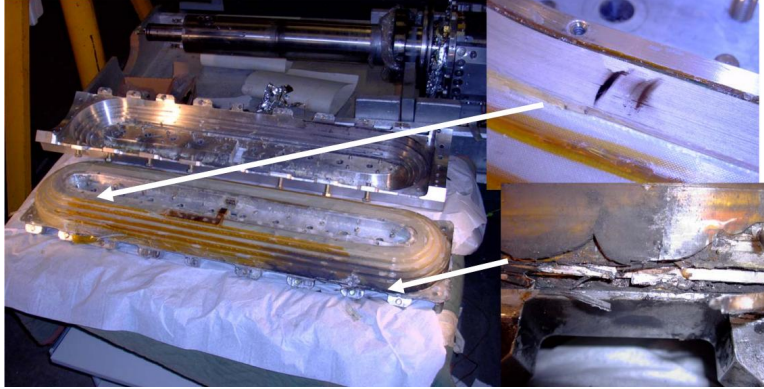


**Figure 2.11:** Destructive quench in a superconducting coil of a 1.2 MW motor [145].

## 2.2 Common Superconducting Wire Materials

There has been intense research activity to discover new superconducting materials with high critical temperatures. In the late 1980's a significant step in finding new superconductors was achieved by the discovery of superconducting properties of rare-earth metal oxides. These metal oxides have much higher critical temperatures than any of the previous superconductors as illustrated in figure 2.12. Furthermore, the critical temperature of these materials are higher than the boiling temperature of liquid nitrogen (77 K). Nitrogen is abundant and nearly 100 times cheaper compared to previously used helium. Moreover, nitrogen cryocooler technology is mature and they are widely used in various industries.

### 2.2.1 BSCCO

Bismuth Strontium Calcium Copper Oxide (BSCCO,  $\text{Bi}_2\text{Sr}_2\text{CaCu}_2\text{O}_8$ ) is a copper oxide material. Copper oxides are not very good conductors at room temperature. The critical temperature for BSCCO is 108 K. BSCCO is the first high-temperature superconductor (HTS) to be used for making superconducting wires and it is the first HTS discovered that does not contain any rare-earth elements. BSCCO wires are usually called the first-generation (1G) HTS wires. Figure 2.13 shows the size comparison of a BSCCO tape and a similar rated copper wire.

BSCCO itself has a ceramic structure and thus it is brittle and has low mechanical strength. In order to manufacture BSCCO in the form of tape, stronger materials are required. This is achieved by embedding BSCCO filaments into a silver matrix through the use of a method which is called “powder in tube method”. In this method, the superconducting powder is packed in silver tubes that are then packed in a larger silver tube and repeatedly drawn and repacked until fine superconducting filaments are created [146]. Then the round conductor is reshaped to make flat tape conductors. The

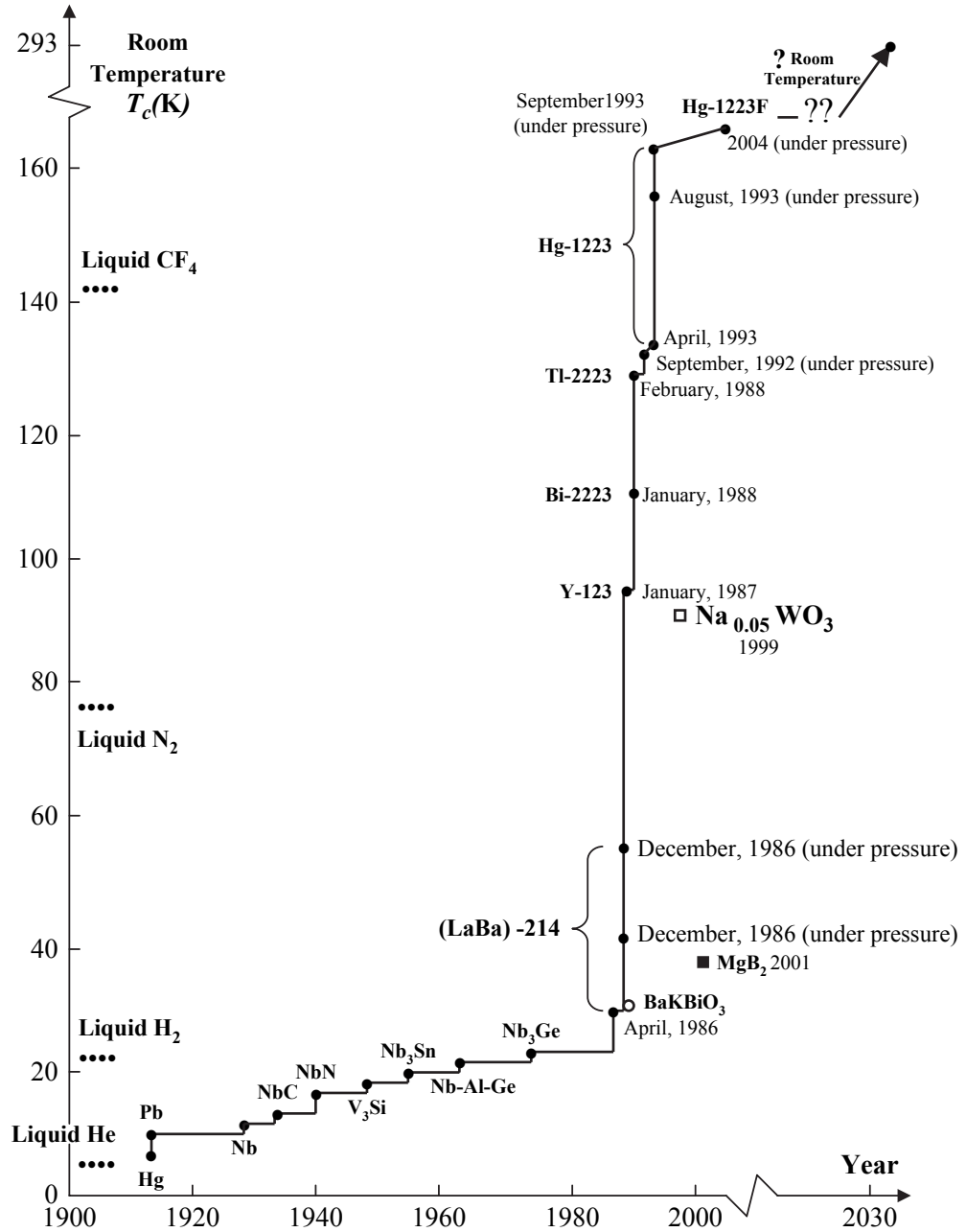


**Figure 2.12:** History of superconductors' discovery and of critical temperature increasing over years [129].

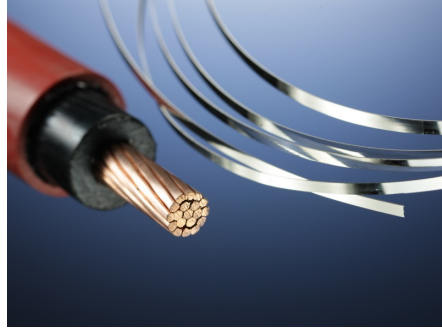


**Figure 2.13:** Size comparison of BSCCO tape with a similar rated copper wire (Courtesy of Bruker EST).



**Figure 2.14:** Cross section of a 4x0.22 mm Bi-2223 tape with 121 filaments (Courtesy of Bruker ETS).

high silver content and the complex processing method increases the cost of BSCCO wires [146]. A cross section of a 4x0.22 mm BSCCO wire with 121 superconducting filaments is presented in figure 2.14.

There are a few types of BSCCO compounds. The two most common types of BSCCO superconductors are: Bi-2212 ( $\text{Bi}_2\text{Sr}_2\text{CaCu}_2\text{O}_8$ ) and Bi-2223 ( $\text{Bi}_2\text{Sr}_2\text{Ca}_2\text{Cu}_3\text{O}_6$ ). Bi-2212 has a critical temperature of 95 K which enables the use of liquid nitrogen as the coolant gas, but most of the applications that use Bi-2212 material are operated at much lower temperatures to increase the wire performance.

Bi-2223 has the highest critical temperature (108 K) among BSCCO compounds. The cooling system for a Bi-2223 based application is less expensive due to a higher critical temperature. Moreover, the material can be manufactured as wire or tape. Thus, Bi-2223 is a common superconductor material for transformers, motors and generators. The usual tape has 4 mm width and 0.2 mm thickness. The specifications of a Bi-2223 tape are presented in table 2.4. The critical current of the wire can be significantly improved by reducing the operating temperature as presented in figure 2.15. For example, at 30 K the wire's critical current quadruples with respect to the critical current at 77 K. The external magnetic field also changes the magnitude of the critical current. Critical current variation graphs of Bi-2223 tape with external magnetic field and temperature are presented in Appendix B.1.

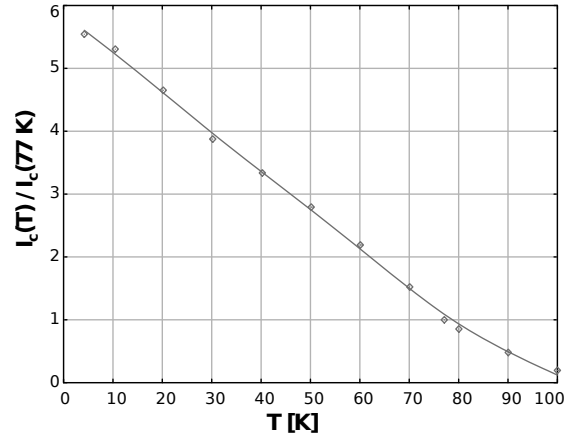


**Figure 2.15:** Critical current variation of Bi-2223 tape with temperature [46].

Dimensions	4 mm x 0.22 mm
Average Length	500 m
Filling Factor	30 %
Number of Filaments	121
$I_c$ (77 K)	>110 A
Mechanical Strength	>250 MPa (77 K)
Young's Modulus	60 GPa

**Table 2.4:** Specifications of the Bi-2223 superconducting tape with respect to the critical current at 77 K [46].

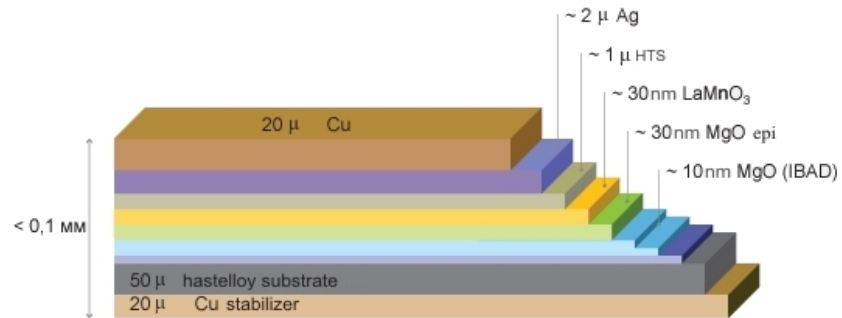


**Figure 2.16:** Layers in a YBCO coated conductor [11].





**Figure 2.17:** YBCO, BSCCO and copper wire price (€/kAm) projection [11].

### 2.2.2 YBCO

Yttrium Barium Copper Oxide (YBCO or  $\text{YBa}_2\text{Cu}_3\text{O}_7$ ), which was discovered in 1986, is also a copper oxide similar to BSCCO. YBCO has a critical temperature of 93 K and it is the first superconductor discovered with a critical temperature higher than the boiling temperature of nitrogen. This was a significant breakthrough because nitrogen is the most abundant element in the atmosphere and it is inexpensive. Moreover, liquid nitrogen based crycoolers are reliable and have been commonly used in various industries for many years. All these factors makes YBCO a promising option and the research on superconducting technology boomed after the discovery of YBCO.

Although YBCO was discovered earlier than BSCCO, it took longer to develop a manufacturing technique for YBCO wires. YBCO wires are usually referred as the second generation (2G) superconducting wires. YBCO tapes are usually made up of multiple layers as presented in figure 2.16. This can be done as a continuous reel to reel process adding many layers in a controlled environment. All the materials used in these layers are cheaper than silver used in 1G wires. The lower raw material cost and simpler manufacturing methods make 2G YBCO wires less expensive than 1G wires [146]. According to a study by [91], the cost of 2G HTS wires are expected to reduce by about one half or less as the manufacturing volume increases. This is supported by an industrial feasibility analysis by Converteam that predicts the cost of 2G HTS wires will be cheaper than current copper prices in 2020 [99]. The same results are presented in [11] (see figure 2.17).

A major advantage of YBCO wire is its ability to remain at superconducting state with current densities ( $J_c$ ) greater than  $10^3 \text{ A/mm}^2$  in fields up to several Tesla. Also some

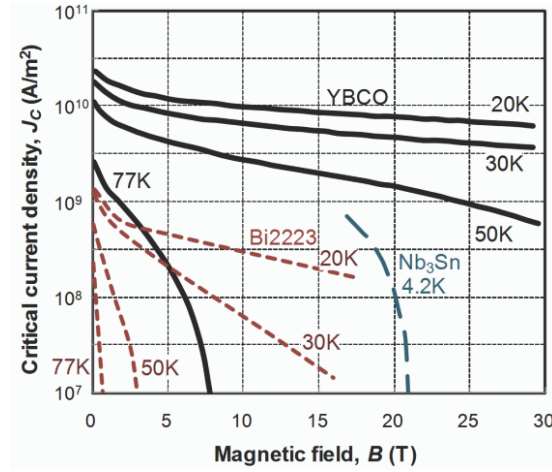


**Figure 2.18:** Performance comparison of YBCO and Bi-2223 superconducting wires at various temperature and magnetic field [123].

Type	Price (€/m)	Current Density (A/mm <sup>2</sup> )	Flux Density (T)	Temp. (K)
NbTi	0.4	1000	5	4.2
Nb <sub>3</sub> Sn	3	1000–4000	5	4.2
MgB <sub>2</sub>	4	100	3	20
Bi-2223	20	390	3	20
		10	3	50
YBCO	30	480	3	20
		190	3	50

**Table 2.5:** Performance and price comparison for some common superconductor materials (The flux density for YBCO, Bi-2223 is perpendicular to tape) [72].

manufacturing methods successfully applied on YBCO and YBCO-coated conductors have resulted in improvements in the quality [32]. The maximum available length of YBCO wire is stated as 500 m in [77].

The characteristics of YBCO and BSCCO wires are compared in figure 2.18. From the figure, it may be seen that the performances of the wires increase significantly with reducing temperature. In Appendix B.2 the critical current versus temperature and magnetic field characteristics of YBCO wire are presented.

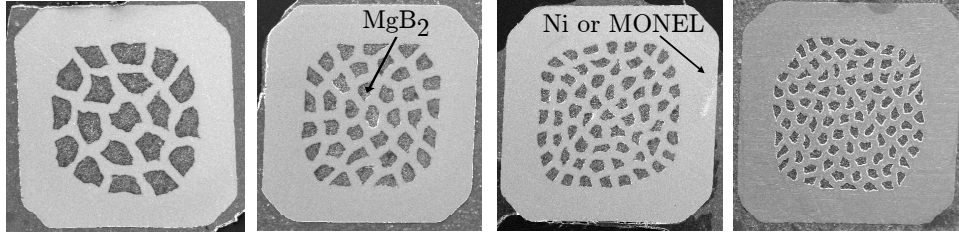


**Figure 2.19:** Cross-sections of  $\text{MgB}_2$  wires with 19, 37, 61, 91 filaments respectively (Courtesy of Columbus Superconductor) [1].

### 2.2.3 Magnesium Diboride( $\text{MgB}_2$ ) Wire

Although  $\text{MgB}_2$  is not a new compound, it was only discovered to be a superconductor in 2001. Magnesium diboride ( $\text{MgB}_2$ ) is an inexpensive superconducting material.  $\text{MgB}_2$  has a critical temperature of 39 K. Although, it is lower than the boiling temperature of nitrogen, it is much higher than the critical temperatures of other alloys. For example, Niobium-titanium( $\text{NbTi}$ ), which is commonly used in MRI devices, has a critical temperature of 9.2 K.  $\text{MgB}_2$  can be cooled without using expensive liquid helium. Instead liquid hydrogen (boiling point: 14 K) or liquid neon cryocoolers (boiling point: 27 K) can be used for cooling. The price and performance of  $\text{MgB}_2$  are compared with other superconductor materials in table 2.5.

The current carrying capacity of the  $\text{MgB}_2$  wire improves significantly as the temperature is reduced below 39 K. For example, at 20 K a wire with 15–30 %  $\text{MgB}_2$  cross-section can carry 2000 A/mm<sup>2</sup> in a magnetic field of 1 T [132]. Another example is the Columbus  $\text{MgB}_2$  wire, which has a cross section area of 1.21 mm<sup>2</sup>, can conduct 400 A at a temperature of 24 K and external magnetic field of 0.5 T [1]. The variation of the critical current of a typical  $\text{MgB}_2$  wire is presented in Appendix B.3.

The biggest advantage of  $\text{MgB}_2$  is its simple structure. It is relatively easy and inexpensive to manufacture  $\text{MgB}_2$  tapes and wires. Columbus Superconductor retails  $\text{MgB}_2$  wires less than €10/kAm [1]. It can be manufactured in lengths of a few kilometres. For example, in [139] an MRI device using 18 km of  $\text{MgB}_2$  wire is presented. Furthermore,  $\text{MgB}_2$  can be manufactured in round, square and flat with various filaments (see figure 2.19), this gives more freedom to the electric machine designer.

## 2.3 Conclusion

This chapter provides background introducing superconductivity and some common superconducting wire materials. The superconducting state of a material is not only limited by temperature, but also current density and magnetic field. Furthermore, superconductors are lossless only when conducting DC. These are the primary issues that should be considered in designing a superconducting machine.

In section 2.2, three common superconducting wire materials are summarized. BSCCO and YBCO have critical temperatures above the boiling temperature of nitrogen. Thus, the cooling burden for these materials is relatively low. However, these materials can be cooled down to low temperatures to improve their critical currents.  $\text{MgB}_2$  wires can be manufactured in great lengths and they are much cheaper than YBCO and BSCCO. However, they have to be cooled below 39 K.

It should be noted that, although just three superconducting wires are presented in this chapter, many others exist. Furthermore, new superconducting materials are still being discovered every year. For example, very recently a novel iron-based superconducting material is presented in [147]. This superconductor is more durable and cheaper than other HTS materials. This example and many others in the history reminds us that the performances of superconductors can only go up, which will increase the attractiveness of superconducting applications.



# Applications of Superconductors in Electric Power

---

Superconductors are used in many different applications. They are used in magnetic resonance imaging(MRI) devices, particle accelerators, maglev trains, high performance RF filters, and superconducting quantum interference devices. In this chapter the power applications of the superconductors will be summarized. The main application areas are fault-current limiters, transmission lines, magnetic energy storage devices, transformers and electric machines. Early superconductor applications could not leave the laboratories due to technical difficulties imposed by the very low operating temperatures. However, with the discovery of HTS materials they became economically feasible and technically less challenging to build.

## 3.1 Superconducting Transmission Lines

One of the first application of superconductivity is superconducting transmission lines. The obvious advantage of superconducting transmission lines is the absence of copper losses. The other main advantage is the reduced cross section area. A size comparison of conventional copper cable and superconducting cable is presented in figure 3.1. The superconducting power cables can conduct 3–5 times more power than conventional transmission lines. Thus, the grid capacity can be increased without laying new power lines which reduces the cost of rights-of-way [128]. Finally, the impedance of superconducting cables is much lower than conventional cables, which helps to increase grid stability. Superconductor transmission lines can be used for both DC and AC. Two different designs are presented in figure 3.2.

The biggest drawback of the superconducting transmission lines is the cooling requirements. Currently, superconducting cables can be manufactured at only a few hundred meters length. A 200 m HTS cable (BSCCO wire) with a power rating 2 kA -20 kV has been manufactured and is being tested in Russia, in 2012 [165]. In China, a 33.5 m 35 kV superconducting cable system was commissioned in 2008 and the system is further



**Figure 3.1:** Size comparison of conventional and superconducting cables (used in large hadron collider) with a rating of 12.5 kA (Source: Wikimedia Commons).

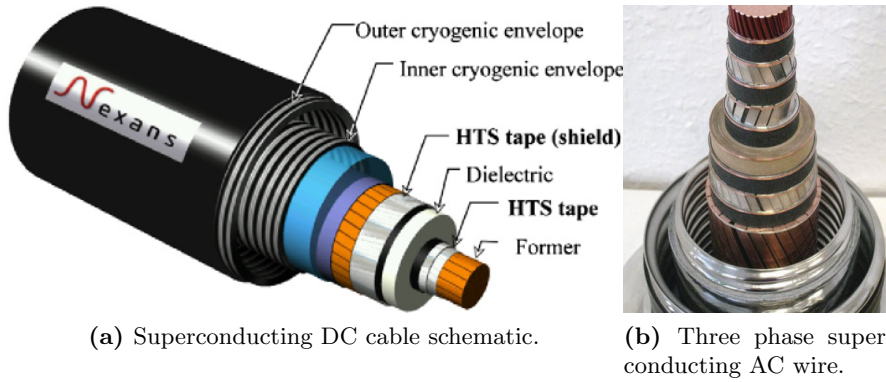


**Figure 3.2:** Superconducting transmission lines (Courtesy of Nexans).

extended with the addition of a superconducting fault current limiter [173]. A 6 km superconducting cable that will replace an existing system in Amsterdam is presented in [115]. In [61], it is proposed that superconducting transmission lines can be used to deliver liquid hydrogen as well, as an alternative supply of energy.

### 3.2 Superconducting Fault Current Limiters

Fault current controllers and circuit breakers are essential in the electric grid in order to limit the unexpected high currents, which may be caused from lightning strikes or short-circuits in power lines. Conventional high/medium voltage circuit breakers can only cut out the current through zero crossing, which may take them several milliseconds to respond and a few cycles to clear out the fault [160]. Therefore, all other equipment in the distribution system (transformers, cables) are required to withstand 20–25 times

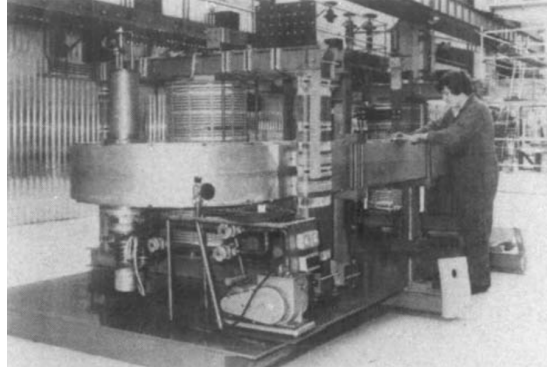


**Figure 3.3:** One of the earliest superconducting fault current limiter prototype manufactured in Edinburgh in 1982 [137].

of the rated current, which is equivalent to more than 400 times the rated joule loss during the short circuit.

An ideal fault current limiter should be invisible to grid (i.e. should have zero impedance) during normal operation and it should have a very high impedance during fault conditions. Superconductors are ideal for such an application. During normal operation, they can operate with minimum loss and impact to the grid. When a fault current occurs, the current exceeds the critical current of the superconductor and, as a result it quenches and transforms to the resistive state passively and precisely in the order of microseconds [160]. Another advantage of superconducting fault current limiters (SFCL) is that they are capable of switching to normal state as soon as the fault current is cleared and the superconductor is cooled down. Therefore, no external control or human intervention is required.

The idea of SFCLs dates back to 1960s, but the first notable SFCL prototype, which is presented in figure 3.3 was manufactured by NEI Peebles Ltd in Edinburgh [137] in 1982. At present, there are many companies that manufacture SFCLs such as: ABB, Tokyo Electric, NEC, Rolls Royce, and Siemens [121]. The first commercial SFCL, which is presented in figure 3.4, was installed in 2009 by Nexans in Germany.

There are mainly two types of SFCLs: resistive and inductive type [140]. Resistive fault-current limiters are basically short superconducting wires connected in series with the grid. The superconductor wire quenches as the current exceeds the predefined limit. The other type is the inductive type with a few different configurations. The two most common types are “shielded core” and “saturable core” designs [140]. In the shielded core design, an iron cored transformer is used with a short-circuited superconducting wire as the secondary winding. During normal operation, the flux from the copper winding and superconducting winding cancel each other. Thus, the iron-core stays unexcited and out of the circuit [140]. During a short-circuit, the superconducting coil quenches,





**Figure 3.4:** The world's first commercial SFCL installed by Nexans at a coal power plant in Boxberg, Germany in 2009 (Courtesy of Nexans).

the current in the copper winding saturates the core and the impedance of the circuit is determined by the iron core.

Saturable core SFCL is the only type that does not rely on the quenching of the superconductor. Instead, a superconductor winding is excited by DC to heavily saturate the iron-core. During normal operation, the conventional windings operate as a low-impedance air-cored reactor. However, when short-circuit occurs the iron core comes out of saturation, which increases the equivalent impedance [140]. This design has the minimum cooling power since there are no AC losses in the superconductor. Moreover, this design has the shortest recovery time because the superconducting coil does not quench during short-circuit. One drawback of the inductive type SCFLs is having an iron core, which increases the size and the mass.

One of the promising applications for SFCLs are DC transmission lines, where conventional circuit-breakers are very challenging and expensive, since there are no zero voltage crossings on a DC system. However, SCFLs can cope with DC more easily since AC losses are eliminated, which reduces the cooling requirements.

### 3.3 Superconducting Transformers

Superconducting transformers are up to 50 % lighter and smaller than conventional transformers [121]. Although, the initial cost of HTS transformers is higher, the cost of ownership will be less due to increased efficiency. Another advantage is increased operational safety. Conventional transformers have fire and environmental hazard risk whereas HTS transformers are cooled by non-hazardous liquid nitrogen [128]. Furthermore, superconducting transformers can easily compensate overloads which can

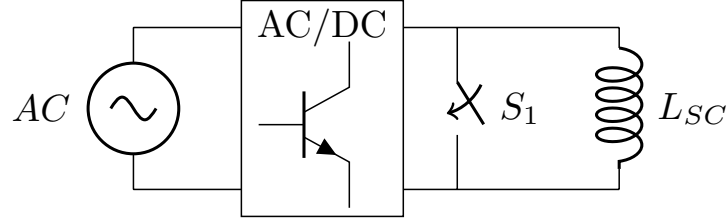


**Figure 3.5:** Basic schematic of superconducting magnetic energy storage system.

cope with grid peak demands. Moreover, there are some designs that combine fault current limiters and transformers in a single unit[94]. The main manufacturers of superconducting transformers are Waukesha Electric, Siemens, ABB, and Fuji Electric.

### 3.4 Superconducting Magnetic Energy Storage

It is essential for grid operators to smooth the energy demand as much as possible, so that the installation cost of power lines and transmission components can be reduced. Furthermore, the capacity factors for power stations can be maximized and cost of energy can be minimized. The only scalable solution at present is pumped hydro storage. A recently proposed method is compressed air storage [74]. However, efficiencies of these methods are not high enough and suitable sites are quite limited.

Non-decaying currents in a superconducting coil loop can be utilized to store energy efficiently. Consider a simple superconducting coil with an inductance of  $L$ ; the stored energy in the inductor can be expressed as;

$$W = \frac{1}{2} L I^2 \quad (3.1)$$

where  $I$  is the current in the coil. A simple schematic for a superconducting magnetic energy storage (SMES) system is presented in figure 3.5. The system can be charged or discharged by the controlled rectifier after the switch is opened. When the switch is closed the current stored in the superconducting coil flows without any loss.

At the moment, SMES systems are proposed for some industrial sites where the power quality is important, as a protection to voltage dips. In [167], it is proposed to use superconducting magnetic energy storages to smooth power output in large wind farms.

### 3.5 Superconducting Electrical Machines

Electric machines generate and use most of the electricity in an electric system. Thus, it is not surprising that many superconducting machines have been designed and manufactured since the early days of superconductivity. The primary motivation is to get a higher efficiency and to reduce size. The early prototypes were challenging due to very low operating temperatures. However, the discovery of HTS materials made them more feasible.

The main advantages and challenges of superconducting machines can be listed as follows:

#### 3.5.1 Advantages

##### High Power Density

Superconducting machines operate at higher air-gap flux densities due to the higher MMF created by superconducting wires that can conduct  $100 \text{ A/mm}^2$  compared to  $5\text{--}6 \text{ A/mm}^2$  of a copper coil. Thus, they have higher power densities than conventional electrical machines.

In figure 3.6 direct-drive permanent magnet generators are compared with superconducting generators in terms of mass and size. Also, in figure 3.7, the size of a conventional induction motor is compared with an HTS synchronous motor. There are many studies in the literature that present a comparison between superconducting machines in terms of mass and losses. Some examples are:

- Siemens 4 MVA superconducting generator has 82 % of the volume and has 63 % of the weight of a similar rated conventional generator [90].
- Half the losses of conventional motors in a package with half the volume can be achieved with superconducting machines [18].
- An HTS ship propulsion motor is one-third of the size and half of the weight of conventional one, including the cooling system [31].
- It is possible to reduce mass and volume by 40–50 % with HTS machines [90].
- HTS machine applications can reduce motor losses to half and at the same time can reduce the overall machine weight and volume to half [146].

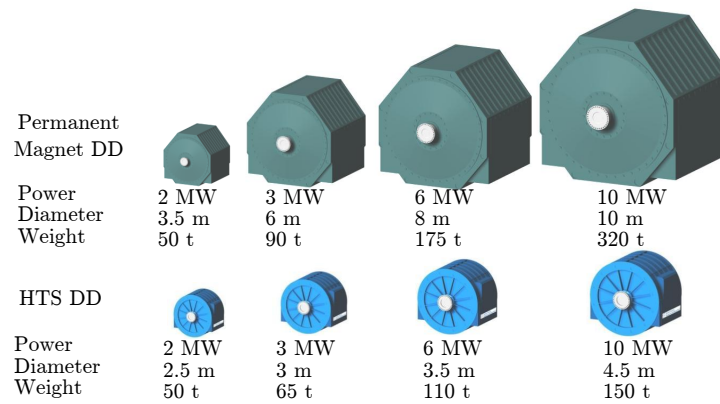


**Figure 3.6:** Size and mass comparison of direct-drive permanent magnet generator and superconducting generator for different power ratings [24].

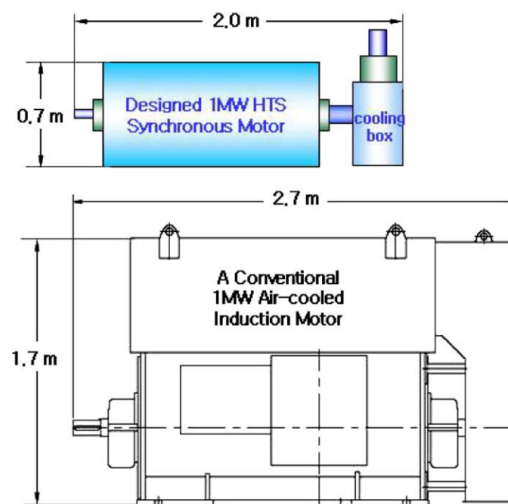


**Figure 3.7:** Size comparison of a conventional 1MW induction motor with HTS synchronous motor [26].

### Superior Grid Performance

In a slotless(air-cored) superconducting machine, the magnetic air-gap is much larger than a conventional slotted machine. A large magnetic air-gap reduces the synchronous reactance, which improves the dynamic stability of the machine during transient grid faults. Furthermore, the efficiency of the superconducting machines is almost independent of the power factor and the field excitation current. Thus, superconducting machines can be over-excited for power factor correction. This eliminates the necessity of synchronous reactors and capacitor banks and improves the reactive power performance of the machine for both over-excited and under-excited operating conditions [79, 32].

### Slow Thermal Ageing

Insulation materials of the conventional electrical machine windings experience degradation during thermal cycles of the machine, which decrease the expected lifetime of the insulation. In a superconducting machine, superconducting windings are always kept at cryogenic temperatures. The insulation in superconducting coils does not experience any thermal cycles. As a result, they have longer expected life than insulation materials used in conventional machines [32, 56].

### 3.5.2 Technical Challenges

Apart from the initial cost, the design of superconducting machines has many technical challenges. The most obvious one is having a cryocooler system to keep the superconducting windings cool enough. The design of the rotor mechanical structure is another challenge that should be addressed properly.

### Cooling System

The operating temperature is the most important parameter of a superconducting machine. Although, the performance of superconductors increases with reducing temperature, this also increases the cooling requirements.

The efficiency of the cooling system is about 1–10 % depending on the operating temperature [140]. At liquid nitrogen temperatures, removal of 1 W of heat requires 15–25 W of cooling power [103]. It is stated in [146] that the power required to cool the superconducting coils is roughly proportional to the inverse of the operating temperature in Kelvin. The relative cooling powers required for various coolant gases are presented in figure 3.8.

For a 4.5 MW superconducting machine operating at 30 K, the cooling power required is about 0.16 % of the total power [146]. However, for a low-temperature superconducting

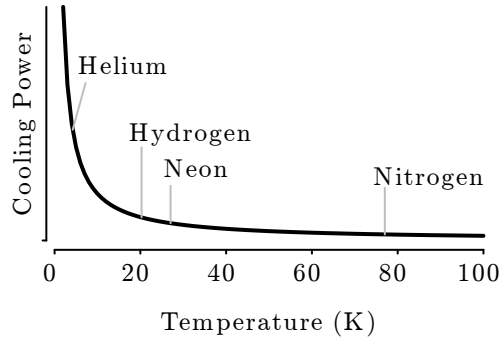


**Figure 3.8:** Comparison of cooling power required with different coolant gases (Assuming the power is inversely proportional to the operating temperature [146]).

machine operating at 4 K the cooling power increases to 1.2 % of its rated power, which has a significant effect on the overall efficiency [146]. This was the main technical and economical drawback for the early superconducting machine applications, in which helium was used as the coolant.

### Coolant Gases

Some coolants suitable for superconducting machine applications can be listed as:

*Helium:* Helium gas, with a boiling temperature point of 4.2 K, used to be the only available option for LTS machines. Helium can also be used with some HTS materials to improve the performance. However, the world's helium resources are scarce. It is stated in [122] that, the helium gas market is not sustainable with the current levels of production as the demand is constantly increasing, with the biggest demand coming from cryogenics, which is 29 % of the total market. The current price of helium is around £50/l, which increases operating cost. Furthermore, the specific heat capacity of helium is relatively low, which means a large amount of coolant has to be stored and the flow rate of coolant should be high.

*Hydrogen:* Although hydrogen is very cheap and readily available, it is rarely preferred as a coolant as it is highly flammable and volatile. However, in [59] it is suggested as a favourable option for superconducting machine applications. Hydrogen can be cooled down to 15–20 K and it is suitable for  $\text{MgB}_2$  wires.

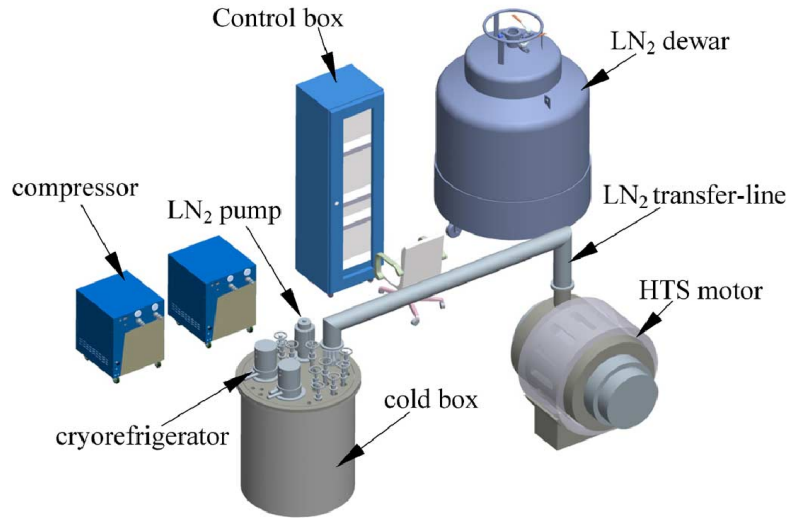


**Figure 3.9:** Layout of a typical liquid nitrogen cryocooler for HTS machines [37].

*Neon:* Neon, which has a boiling temperature of 27 K, is a noble gas and safe to operate. Neon cryocoolers are cheaper than helium cryocoolers, but the neon itself is very expensive. Furthermore, Neon's thermal conductivity is smaller than helium, thus cooling with neon is not very efficient [98]. However, in [143] it is proposed to use a helium-neon mixture to make neon cooling more feasible.

*Nitrogen:* Nitrogen is the most common gas in the atmosphere. It is easy to obtain and commonly used in industry. However, the operating temperature is limited to 63 K. Liquid nitrogen based cryocooler technology is mature, reliable, and has a maintenance cycle of 10,000 hours [146]. A typical liquid nitrogen cooling system is presented in figure 3.9.

*Liquid Air:* Liquid air has not been generally preferred for HTS applications, but it has been commercialized by BOC as a safe option for the food industry [19]. Liquid air has a freezing temperature of 57 K, which is lower than the freezing point of nitrogen. This 6 K difference can increase the critical current of a superconductor wire by 80 % [19].

Rotational Speed	Power Rating	Suggested Method
Low	Small-Large	Pipe evaporative cooling
High	Small	Thermosyphon
High	Large	Open evaporative cooling

**Table 3.1:** Suggested cooling methods for superconducting machines [38].

### Cryocooler Types:

Gifford-McMahon (GM) regenerative cycle cryocoolers are favoured for HTS applications [32]. Air conditioning systems work on the same principle, and they have a long history in MRI applications. They are quite reliable, but not very efficient and compact. The active carbon filter and reciprocating displacer are the two critical components of a cryocooler, with the filter being replaced every two years and the displacer's life is about one year [176]. GM cryocoolers are slowly being replaced by Stirling and maintenance free pulse-tube cryocoolers [31, 176].

There are three ways to circulate the coolant gas [38]:

- Thermosyphon Method.
- Open Evaporative Cooling.
- Piping Evaporative Cooling.

The thermosyphon method is fail-safe and self-driven, in which condensed coolant gas is circulated with the help of gravity. As the liquid evaporates, it removes the heat and returns to the cryocooler. Circulation pumps are not required, and so it is more reliable. The disadvantages of this method are listed in [162] as:

- Non-flexibility in the operating temperature,
- Possibility of freezing of the cold-heads,
- Non-homogeneous cooling of the rotor windings when the machine is stationary.

Cryocoolers that operate at lower temperatures use closed gas circulations (e.g. helium gas cryocoolers). In this case, an external pump is required for circulation of the coolant. Both thermosyphon cooling and open evaporative cooling are not applicable for superconducting coils with low rotational speeds, because the liquid can not homogeneously cool the superconducting coil when the centrifugal acceleration is less than  $20g$  [38]. Suggested cooling methods for different machines are presented in table 3.1.

There are some research on more reliable cooling systems. Snitchler *et al.* described a refrigeration system which has mean time between failure rate longer than nine years [151]. They also proposed using six to ten cryocoolers with N+1 redundancy with a maintenance cycle of two years for cryocoolers, fans and seals.



### Thermal Expansion

Thermal expansion differences of the materials in a superconducting machine structure should be carefully addressed. One option is to make the structure more flexible in order to prevent high mechanical stresses [60]. Many ferromagnetic materials are not suitable for superconductor applications since they are brittle at cryogenic temperatures and have a high thermal expansion coefficient. The most common magnetic materials used at cryogenic temperatures are Invar ( $\text{FeNi}_{36}$ ) and 9 % Ni-steel, which offers a higher saturation flux density and it is mostly preferred for cryogenic applications [60].

### Vacuum System

In order to reduce the heat leakage from the cold section of the machine, the superconducting coil is placed in a vacuum jacket. It is common to vacuum the air-gap to pressures as low as  $10^{-5}$  Torr [2]. In order to reduce vacuum pump requirements, bearings should be carefully sealed against any leakages. Layers of super-insulation can be used as an alternative or in addition to a vacuum jacket [60].

### Rotor Mechanical Structure

The superconducting coils are placed in the rotor for most superconducting machine topologies. The main challenge is that the rotor should be kept at cryogenic temperatures, whilst keeping thermal losses to a minimum while transferring the high torque from the shaft. Invar is a structural material used widely in superconducting applications, but in air-cored machines, the torques act directly on the superconductor material, which is mostly ceramic based and incapable of withstanding large forces. Different types of carbon fibre materials can be utilized to support superconducting windings. An important advantage of carbon fibre is its low thermal conductivity. Thus, it can also behave as an insulation between cold mass and warm mass of the machine. An example for that kind of application is developed by University of Southampton as presented in figure 3.10.

## 3.6 Superconducting Machine Topologies

Superconducting machine designs are limited by the aforementioned AC characteristic of the superconducting wires. As a result, it is common to employ superconductors only as the dc-field winding. There are also some machine designs that use magnetized bulk-superconductor materials. The main topologies can be listed as:

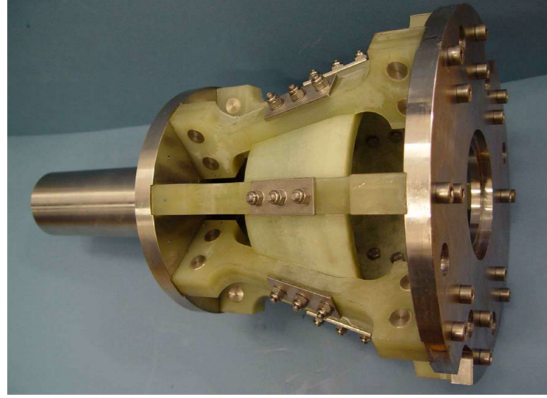


**Figure 3.10:** Rotor fibreglass (G10-CR) beams connecting cold and warm mass [60].

### 3.6.1 Conventional Stator - Superconducting Rotor

The conventional stator, superconducting rotor is by far the most common configuration applied to many commercial products [32, 79, 151]. In this configuration only the field winding in the rotor is superconducting. Conventional copper windings are used in the armature. This means only the magnetic loading (i.e. flux density in the air-gap) of the machine is improved compared to conventional machines whereas the electrical loading (i.e. the current density in the armature winding) is similar to conventional machines.

A typical schematic of a superconducting synchronous generator is given in figure 3.11. The superconductor is fitted to the rotor and isolated from the stator and ambient using insulation layers and a vacuum jacket. The superconducting winding can be excited using conventional brushes or brushless exciters.

The biggest challenge for this type of machine is the design of the superconducting rotor. The rotor requires a rotating transfer coupling that transfers coolant from the stationary cooling system to the rotating rotor. The coupling increases the cost of the system, and the long-term reliability of the coupling is also questionable.

The machines in this category can be subdivided into four groups [162].

- Slotted stator with superconducting rotor with magnetic core.
- Slotted stator with air-cored superconducting rotor.
- Slotless stator with magnetic-cored superconducting rotor.
- Slotless stator with air-cored superconducting rotor.

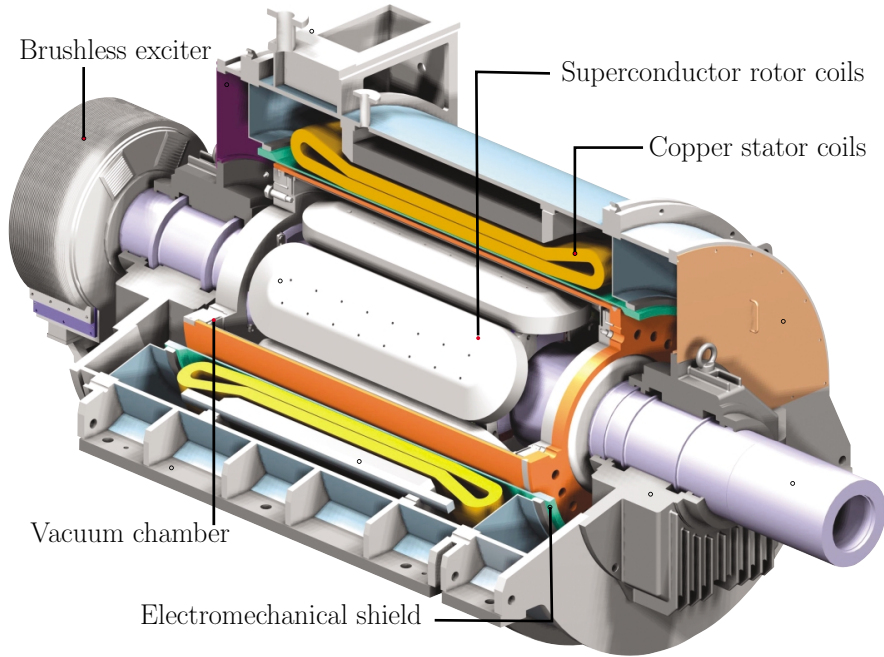


**Figure 3.11:** Cutaway view of a copper stator, superconducting rotor motor. (Image reproduced from [35].)

### Rotor: Magnetic or Air Cored

In conventional synchronous machines, the rotor has a magnetic core to minimize the reluctance of the flux path. However, the magnetic core can be eliminated in a superconducting machine and extra MMF required for an air-cored (non-magnetic) rotor can be easily supplied by the superconducting field winding.

An air-cored rotor construction helps to reduce the mass of the machine. Furthermore, the rotor will have a lower moment of inertia, which will increase the dynamic performance of the machine. However, the air-cored rotor requires more superconducting coil, which increases the cost.

It is also possible to use a magnetic cored rotor. The presence of the core greatly reduces the magnetizing current which allows the rotor to be constructed using much less superconducting tape and also allows the flux penetrating into the superconductor to be diverted [20], which helps to maximize the performance of the coil. The magnetic-cored rotor machine is the most common type because it can be easily manufactured.

In the magnetic cored configuration, there are two options for the cooling. The rotor can be cooled together with the superconducting coil, which is referred as the “cold rotor”. Alternatively, it can be thermally insulated and kept at room-temperature, which is referred as the “warm rotor”. The layouts of warm and cold iron rotor machines are presented in figure 3.12. Both configurations have similar electromagnetic characteris-

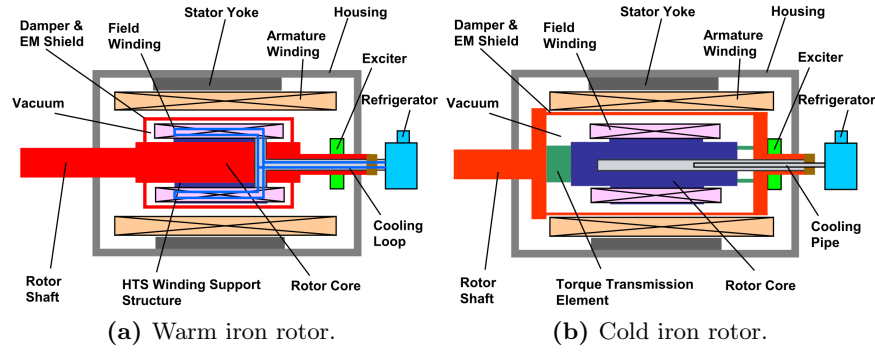


**Figure 3.12:** Magnetic rotor core arrangements according to thermal insulation method [91].

tics, but the warm iron rotor configuration has mechanical advantages such as reduced cold mass and elimination of torque transmission element (see figure 3.10) [90].

### Stator: Slotted or Slotless

For the stator design, the first option is to use a slotted stator, which is no different than a conventional electrical machine. In this case, a superconducting rotor can be retrofitted into an existing synchronous machine. However, the power density is limited by the magnetic saturation in the stator teeth. The other option is to replace the magnetic stator teeth with a non-magnetic material such as carbon fibre. Thus, a higher flux density can be obtained and the full advantage of using superconducting coils can be exploited. Moreover, the slot harmonics are eliminated and armature reaction is reduced, which increases the power quality of the machine. Litz wires can also be used in armature windings in order to minimize the eddy current losses at higher flux densities [91].

The conventional synchronous machine, air-cored superconducting machine, and magnetic-cored superconducting machine are compared in table 3.2. Air-cored superconducting machines have higher power densities, but they require excess amount of superconducting wire.

### 3.6.2 Homopolar Superconducting Machine

An alternative superconducting machine topology with reduced cost and increased robustness is the homopolar superconducting synchronous machine (HSSM). Homopolar machines differentiate from other topologies by having a stationary superconducting coil. The layout of a HSSM is given in figure 3.13. HSSMs have a variable reluctance rotor core. The biggest advantage of HSSMs is the stationary superconducting field winding, which eliminates the cryocoupler and the electrical exciter. Furthermore, the

Concept	non-HTS	Air Cored	Iron Cored
Magnetic Field Strength	Low	High	Low
Magnetic Rotor Core	Yes	No	Yes
Magnetic Stator Teeth	Yes	No	Yes
Performance			
Efficiency	Low	High	High
Reactive Power Capability	Low	High	High
System Stability	Medium	High	Medium
Design Considerations			
Size Reduction	Low	High	Medium
Superconductor Requirement	N/A	High	Low
Cryocooler Requirement	N/A	Medium	High
Simplicity of Field Winding	Medium	Low	Medium
Simplicity of Armature Winding	Medium	Low	Medium
Reliability			
Thermal Cyclic Capability	Medium	High	High
Rotor Torque Transfer	Easy	Difficult	Easy
Auxiliaries	High	Low	Medium

**Table 3.2:** Comparison between conventional, air-cored superconducting and iron-cored superconducting machines [22].

centrifugal and the electromagnetic forces on the superconducting coil are eliminated by using a stationary superconducting coil. However, HSSMs are much heavier than the other types of superconducting machines due to large mass of the rotor core. The advantages of homopolar synchronous machines can be listed as:

- The superconducting field is stationary, so the cooling and excitation system are simplified.
- Magnetic flux penetrating into the superconductor winding is minimized by the magnetic rotor core.
- The superconducting wire requirement is minimum due to small magnetic air-gap.
- There is no electromagnetic torque acting on the superconducting winding.

Homopolar machines are mechanically very robust. Therefore, they are usually preferred for superconducting ship propulsion systems. For example, in [96], a conceptual design for a 5 MW, 230 rpm ship propulsion motor is presented. In table 3.3 the homopolar machine design is compared with an air-cored superconducting synchronous machine. It can be seen from the table that, the air-cored machine requires double the superconducting wire length compare to the homopolar machine. However, the homopolar machine is twice as heavy as the air-cored superconducting generator.

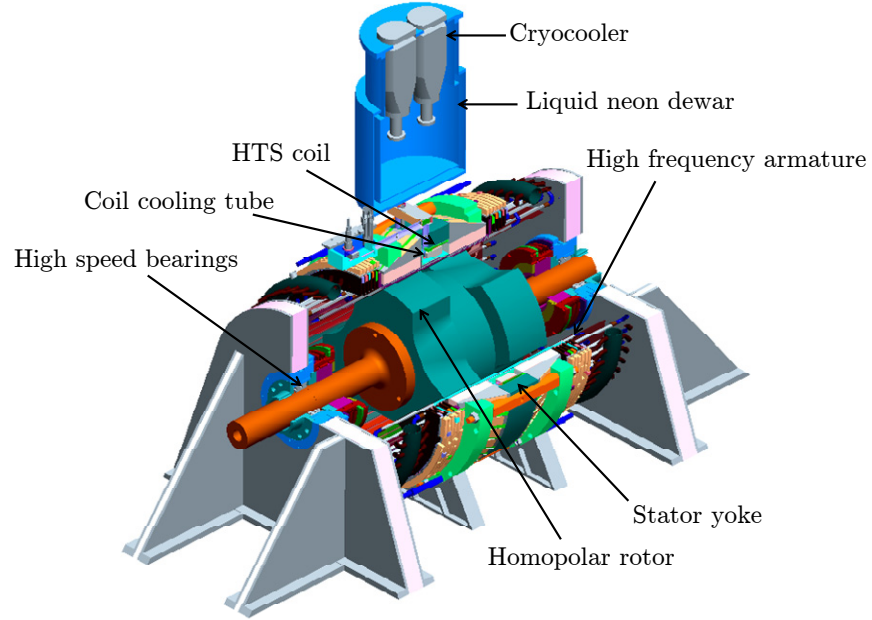


**Figure 3.13:** Layout of a homopolar superconducting motor [178].

	Air-cored HTS	Homopolar
Outer Diameter	1.75 m	2.5 m
Volume	3.15 m <sup>3</sup>	6.95 m <sup>3</sup>
Weight	18 t	44 t
SC wire length	100 km	50 km

**Table 3.3:** Comparison for air-cored superconducting machine with a homopolar synchronous machine for a 5 MW, 230 rpm design [96].

### 3.6.3 Axial-Flux Superconducting Machines

Axial flux superconducting machines are not very common and there are just a few prototypes with small power ratings. In [126, 111], an axial superconducting ship propulsion motor is presented. Also in [108], an axial flux HTS machine topology is proposed for an aircraft propulsion system. For conventional copper stator axial-flux superconducting machines, there are two options for the field winding: magnetized bulk superconducting field or a superconducting field winding.

#### Magnetized Bulk Superconducting Field

This topology is similar to the permanent magnet axial-flux synchronous machines, but rather than using rare-earth permanent magnets, magnetized bulk-superconductors are used. Superconductors can be magnetized by an external field and the field can be trapped in the superconductor by non-decaying surface currents. It is possible to trap magnetic flux densities up to 17 T [161]. One problem in the magnetization process is the cracking of the material due to high tensile stress. Thus, it is necessary to support bulk superconductor with a steel tube. However, the material can still crack because of flux jumps that results from thermal instabilities [63].

For large scale applications, superconductors can be magnetized in situ or externally. External magnetization is not a feasible method since it would be extremely difficult to handle the pre-magnetized bulk superconductors during the machine assembly. Moreover, if the cooling system fails, the superconducting magnets will de-magnetize and the machine will be required to be disassembled. Thus, in situ magnetization method is the only feasible method for superconducting machines. In [111], HTS bulk magnets are magnetized by the pulsed field magnetization method by using a pair of the armature coils (see figure 3.14). However, the maximum flux density magnitude is limited by the current density of armature coils. The average flux density is not more than 0.5 T [111]. There are some novel flux pumping methods that magnetize superconductors gradually by magnetic flux or thermal waves such as [109, 40], but these methods are not yet proven for large scale applications.

### 3.6.4 All Superconducting Machines

The aim of superconducting machine designers is to replace all copper windings with superconducting wires. By this way, a very high power dense machine with almost 100% efficiency can be achieved. However, AC power loss in the superconducting coils is a serious barrier at present. It is stated in [32, 91] that without an AC-tolerant HTS wire, the construction of a superconducting stator would not be possible or is limited to small power applications. In [95] a 7.5 kW fully-superconducting homopolar machine

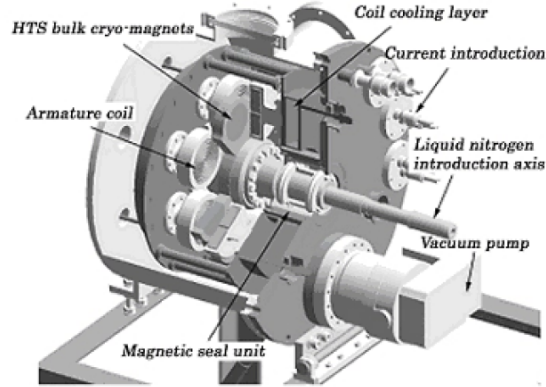


**Figure 3.14:** Schematic of bulk HTS axial flux machine [111].

is proposed. A larger rated machine with superconducting armature and permanent-magnet rotor is developed in the University of Fukui [155]. However, the remnant flux density of the permanent magnets is 1.2 T and the rated frequency is kept at 16.7 Hz, in order to reduce the AC losses on the superconducting armature. A 400 kW, 3600 rpm fully superconducting motor is presented in [71]. There are also some designs with permanent-magnet rotor and superconducting armature [101].

## 3.7 Major Superconducting Machine Projects

### 3.7.1 American Superconductor

American Superconductor (AMSC) is one of the major players in the large superconducting machine applications and developed many superconducting machines. In 2001, AMSC manufactured and tested a 3.7 MW, 1800 rpm HTS synchronous motor [76].

AMSC has been designing a superconducting ship propulsion motor for the US Navy. The first prototype they built is a 5 MW, 230 rpm synchronous motor with a superconducting rotor (see figure 3.15). A brushless exciter has been designed to increase reliability. In the second stage of the project, a 36.5 MW, 120 rpm superconducting machine was designed [79, 151]. The final tests were completed in 2011 [57]. The generator's efficiency at full-load is 97.3 %. The motor including the cooling system weights 75 tonnes, which means more than 50 % reduction compared to a conventional drive system. The size of the machine is compared with a conventional machine in figure 3.16.



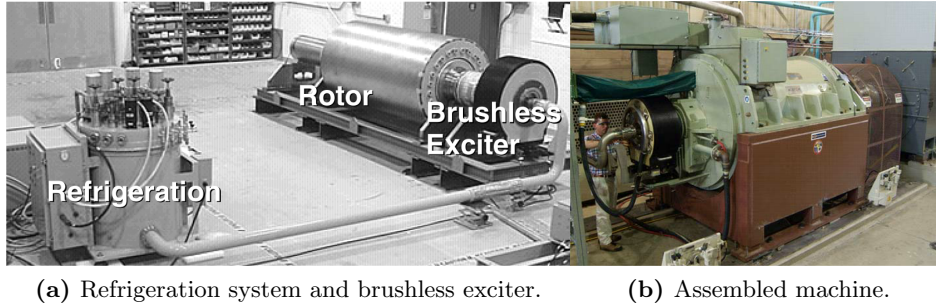


**Figure 3.15:** AMSC's 5 MW, 230 rpm HTS ship propulsion motor [80].

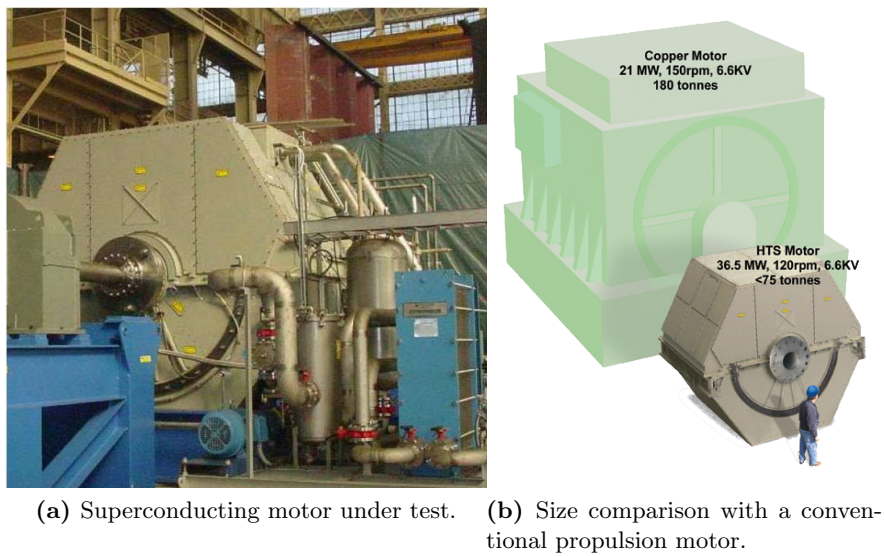


**Figure 3.16:** 36.5 MW superconducting ship propulsion motor for US Navy (Courtesy of AMSC).

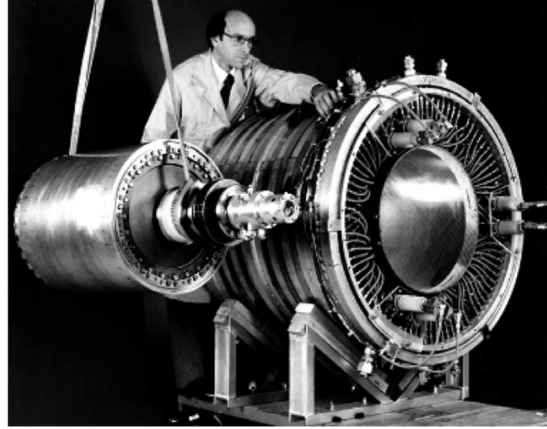


**Figure 3.17:** General Electric's 20 MW low-temperature superconducting generator with Nb-Ti wire [32].

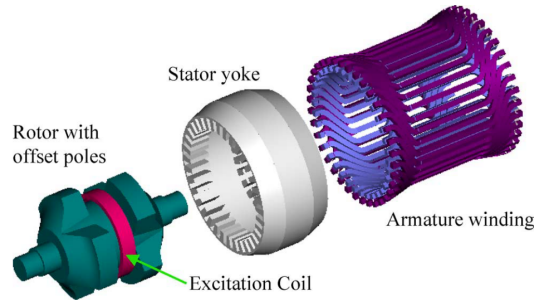


**Figure 3.18:** Schematic of GE's 1.3 MW, 10,000 rpm homopolar superconducting machine [149].

### 3.7.2 General Electric

General Electric is one of the first companies that initiated commercial research on superconducting machines. They have developed a 20 MW low-temperature superconducting generator in 1981 (see figure 3.17), they are currently designing a 1.3 MW, 10,000 rpm homopolar superconducting machine for the US Air Force [149]. A double cold head is preferred for increased reliability and serviceability. The rotor chamber is vacuumed down to a few Torr and sealed with ferro-fluid seals in order to minimize windage losses [149].

GE is also developing a 100 MVA, 3600 rpm HTS generator for power plants [56]. The machine has a warm-rotor superconducting field winding which can also be retrofitted into existing machines, and has 30 % less synchronous reactance than conventional generators, which increases stability and gives more margin for reactive power generation [56, 22].

General Electric acquired Converteam in 2011. Converteam has participated in man-

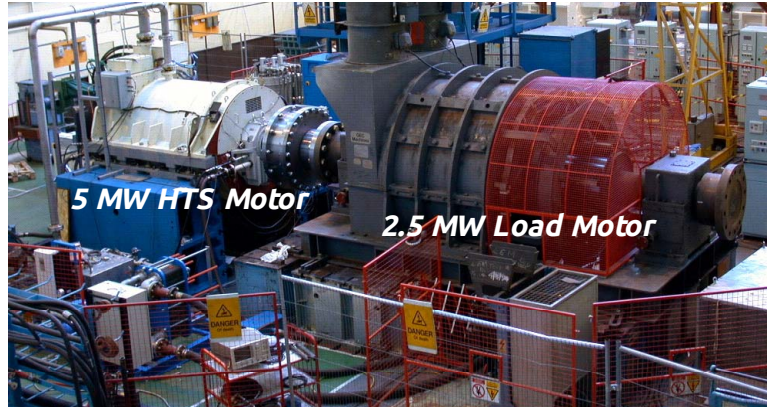


**Figure 3.19:** Converteam 5 MW HTS ship propulsion motor coupled to test machine [76].

ufacturing of HTS ship-propulsion systems. In figure 3.19, a 5 MW HTS machine manufactured by Converteam and AMSC is shown at the test facility in Rugby, U.K. Although, the HTS motor is twice as powerful as the load motor, it is much smaller.

A major project was the Hydrogenie project. Hydrogenie is a 1.7 MW, 214 rpm HTS generator designed for a hydro station in Germany. The operating temperature of the generator is 30 K and uses Bi-2223 superconducting tapes [52]. The superconducting rotor of the machine, which is presented in figure 3.20, will be retro-fitted to a conventional synchronous generator. The thermal loss of the system is about 200 W. The cooling system requires 25 kW electrical power, which is around 1.5 % of the rated power [176].

### 3.7.3 Super-GM Japan

The superconducting generator and materials program (Super-GM), is a 12-year national project of Japan, which was initiated in 1988 [125]. Three different types of rotors and one model stator were manufactured and tested to confirm the basic characteristics of a 70 MW two-pole, 60 Hz machine. The first prototype was tested in 1997 and achieved a world record of power with 79 MW. The measured full-load generator efficiency was 98.3 %. The GM team is seeking to build a full-size 200 MVA and 600 MVA machines in the future.



**Figure 3.20:** The superconducting rotor of the 1.7 MW, 214 rpm Hydrogen machine (Courtesy of GE).

#### 3.7.4 Siemens

Siemens designed and manufactured a 400 kW, 1500 rpm HTS synchronous machine (see figure 3.21) in 2001. Thermosyphon cooling concept is proposed for increased reliability. The machine employs liquid neon cryocooler with an operating temperature of 25 K. The efficiency of the machine including the cooling power is 96.8 % [90]. Siemens has continuously operated the motor for more than 2.5 years without any failure.

Siemens also built a 4 MVA, 3600 rpm HTS synchronous machine (see figure 3.22), which employs pancake coils manufactured from Bi-2223 tapes. Three cold heads are installed for redundancy and decreased cooling time. Each of these cold heads has a cooling power of 45 W at 25 K. The time for cool-down from 300 K to operating temperature is approximately 75 hours [90]. Siemens recently published some test results, including the short-circuit test, for the 4 MW HTS machine in [120].

#### 3.7.5 University of Southampton

The University of Southampton aims to develop a 100 kW HTS synchronous generator (see figure 3.23) [19, 20, 171]. The team uses a conventional synchronous stator and optimises the electromagnetic, thermal and structural design of the HTS rotor. They have developed various coreless HTS rotors with flux diverters suitable to work in liquid nitrogen temperatures.

The cryocooler used in the generator is capable of providing 120 W of cooling power at 70 K. Cooling is performed in two stages; first pressurized liquid nitrogen is used in an



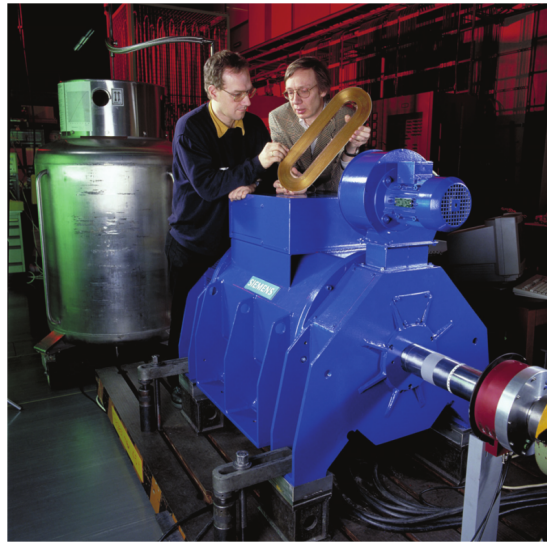


**Figure 3.21:** Siemens 400 kW, 1500 rpm HTS machine [90].

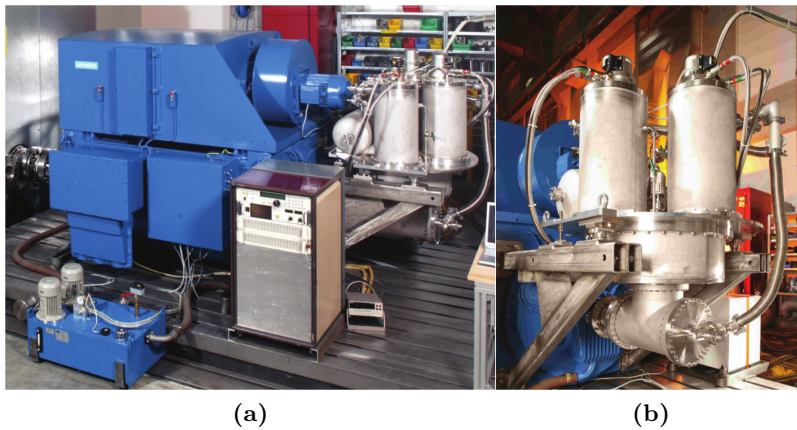


**Figure 3.22:** Siemens 4 MVA, 3600 rpm machine and cryogenic cooling system [80].

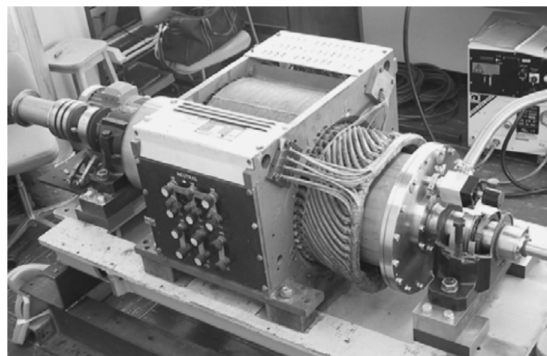


**Figure 3.23:** University of Southampton 100 kVA HTS demonstrator generator [20].

open cycle process to decrease the cooling time. By this technique, the machine cools from room temperature to 70 K in about 10 hours. In the second stage a closed-cycle cooling system is used which takes further a 8 hours to cool down to 67 K. The average cooling rate is estimated to be 2 K/hour [171]. It is also proposed to use liquid air, which has a boiling temperature of 57 K, instead of liquid nitrogen to increase the critical current.

## 3.8 Superconducting Wind Turbine Generators

In this section, some superconducting wind turbine projects and prototypes will be reviewed. The reasons why superconducting generators may be advantageous for large wind turbines have already been reviewed in section 1.2.2 and the mass of superconducting generators has been compared with conventional direct-drive generators in figure 1.7.

Although, there are not any installed superconducting wind turbines yet, there are a few direct-drive superconducting machines that operate at relatively low rotational speeds, almost all of which are ship propulsion motors. Some of the projects that aim to build large direct-drive superconducting generators for offshore wind turbines are:

### 3.8.1 AMSC-SeaTitan

AMSC, with the experience of building a 36 MW superconducting motor, will manufacture a 10 MW, 10 rpm offshore wind turbine generator, which is called SeaTitan. SeaTitan will be installed on a 190 m diameter turbine and will be introduced to the market by 2015 [54]. The generator will have 96 % efficiency and is estimated to be 150–180 tonnes with a 4.5–5 m diameter [151].

SeaTitan employs YBCO wires, and the operating temperature of the generator is about 30–40 K [24]. A slotless stator configuration is used to eliminate saturation in the stator teeth, and the stator windings are water cooled. The mechanical air-gap is 20 mm and the magnetic air-gap is significantly larger due to the air-cored structure, which increases the superconducting wire requirements [24].

The rotor structure and the cooling system are presented in figure 3.24. In order to increase the reliability of the turbine redundant cryogenic cooling systems will be installed. Most of the subcomponents (such as cryogenic cooler compressors, power converters) are placed at the bottom of the tower for easy access and replacement [55]. The cold-heads (eight in total) are being placed in the rotor and rotates with the rotor structure. However, the design still requires rotating transfer couplings, which require regular maintenance.

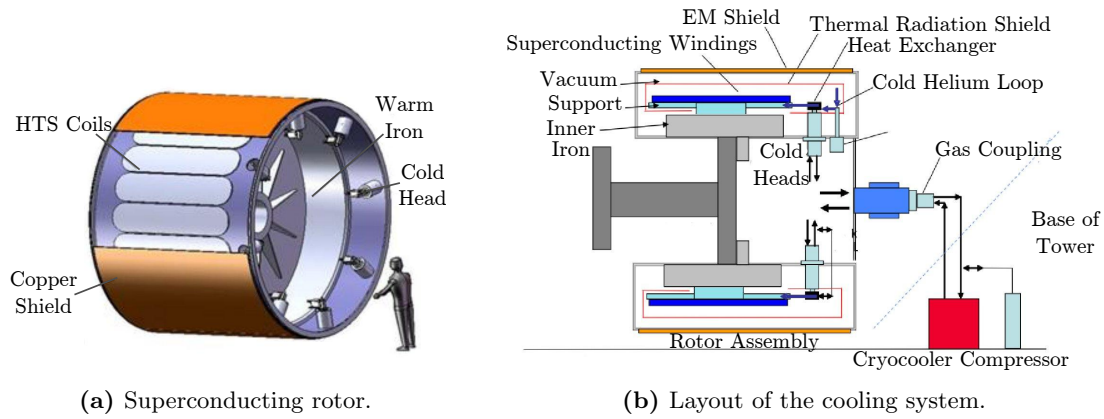


**Figure 3.24:** AMSC's 10 MW, 10 rpm SeaTitan superconducting generator structure [24].

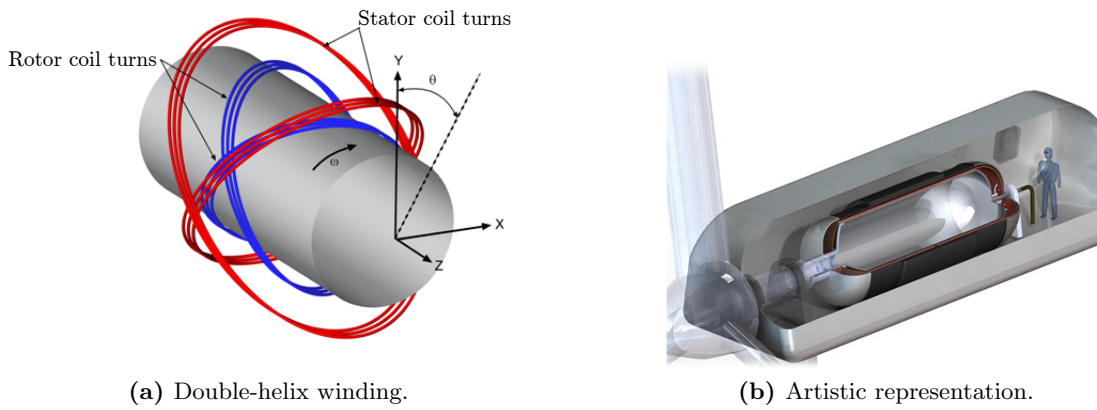


**Figure 3.25:** AML's 10 MW 10 rpm fully superconducting generator [5].

### 3.8.2 Advanced Magnet Lab

Advanced Magnet Lab (AML) is one of six companies which was awarded \$ 7.5 million in total to develop next generation wind turbines. AML is now investigating a 10 MW, 10 rpm fully superconducting generator. A double-helix superconducting winding configuration (see figure 3.25a) is proposed to minimize the AC losses on the armature coils and to limit the flux penetrating into the coils.  $\text{MgB}_2$  wires are used in the machine and the operating temperature is 20 K, cooled with helium gas. Diameter of the machine is 2 m and the axial length is 5 m [5]. Weight, including the cooling system, is expected to be 70 tonnes [110], although no other information is available. AML plans to build the full scale prototype by 2015 [5].

Diameter	4.9 m
Axial length	2.7 m
Generator Mass	93 t
Total Mass (with bearings, shaft, ventilation)	143 t
Superconductor Length	720 km (NbTi)
Ampere turns	928 kAt
Superconductor mass	3840 kg
Critical temp	6 K
Efficiency	95 %
Cooling System Power	22.5 kW

**Table 3.4:** Specifications of the GE 10 MW, 10 rpm superconducting generator [51].

### 3.8.3 GE - Ecomagination

General Electric (GE) continues research on superconducting generators with their clean-technology brand “Ecomagination”. Similar to AML, GE was also awarded a grant by the US Department of Energy for next generation wind turbines. They are designing a 10–15 MW low temperature superconducting (LTS) generator. The operating temperature will be 4 K, the lowest of all the other designs [72]. The generator uses NbTi wires which are commonly used in MRI devices. The main specifications of the GE’s 10 MW 10 rpm wind turbine generator is presented in table 3.4. The generator efficiency is 95 %, where the cooling power is 4.5 % of the total losses and 0.225 % of the power rating [51].

The novelty of the generator is in the utilization of a stationary superconducting field winding and rotating armature [154]. The sectional view of the generator is presented in figure 3.26. The proposed topology eliminates the cryogenic coupler and simplifies the superconducting coil design. However, a rotating armature requires high current electrical brushes, which are originally designed for hydro generators.

GE prefers NbTi wires because of the low cost and mature technology. However, this increases the cooling burden of the machine. GE proposes a thermosyphon type cooling for increased reliability (with a maintenance period of 5 years) [154].

The generator uses 2 dual-stage cryocoolers, one of which is for backup. The main heat losses in the first stage of coolers for different power ratings are presented in table 3.5. Radiation losses and conduction heat losses from the torque tube are the two most important losses. The total heat loss versus power rating is plotted in figure 3.27. From the figure it can be seen that, the ratio of the heat loss to the power rating decreases for larger machines, which makes superconducting machines more feasible at larger power ratings.

The diameter of the field coil diameter is larger than 4 m and the total cold mass is 21 t.



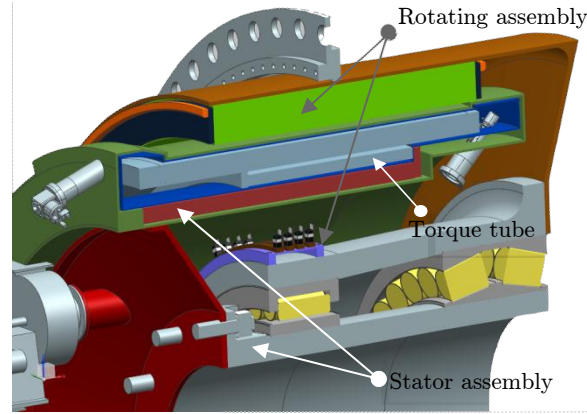


**Figure 3.26:** Sectional view of the GE 10 MW, 10 rpm superconducting wind turbine generator [154].

Thermal Load(W)	2.9 MW	6 MW	10 MW	15 MW
Radiation	20.0	29.0	54.0	69.7
Torque tube	18.0	30.0	36.0	45.0
Sleeves	8.3	12.6	16.5	20.4
Current leads	13.9	13.9	13.9	13.9
Other	5.5	5.5	5.5	5.5
Total	65.6	91.0	125.9	154.4

**Table 3.5:** Thermal load estimation for 2.9, 6, 10, 15 MW superconducting generator designs [154].

Thus, the cooling time of the generator is quite long:  $7\frac{1}{2}$  days. However, the cool-down time after a quench is much shorter, which is around 21 hours [154].

Converteam, now General Electric Power Conversion, completed a feasibility study with Zenergy in 2006 on direct-drive HTS generator for wind turbines. The project also investigated the development of maintenance-free cryocoolers [99].

The conceptual design is rated at 8 MW, 12 rpm, for a 160 m diameter turbine [99]. The design has a diameter of 5 m, axial length of 2.2 m and weight is approximately 100 tonnes. An artistic impression of the Hydrogenie machine and superconducting wind turbine generator are presented in figure 3.28.

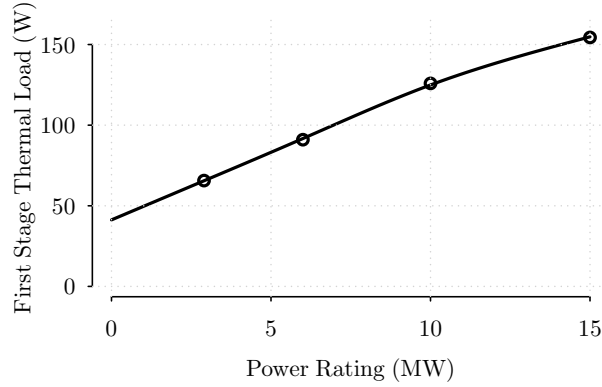


**Figure 3.27:** Thermal load variation of the first stage cooling system with power rating (Reproduced with data from [154]).

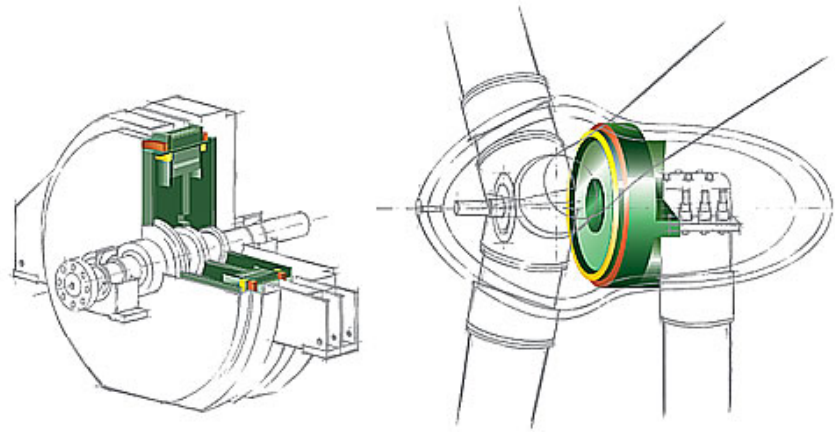


**Figure 3.28:** Converteam 1.7 MW 214 rpm HTS hydro generator and 8 MW 12 rpm direct drive HTS wind turbine generator (Courtesy of GE).

### 3.8.4 Other Projects

There are also other research projects for large superconducting wind turbines, most of which are still in the design stage. The most common rating is 10 MW, 10 rpm.

A new EU FP7 project has been initiated in 2012, which is called SupraPower [12]. The project aims to build a reliable, lightweight synchronous generator, which was patented by Tecnalia [142]. The generator design (see figure 3.29) has independent modular superconducting coils, which can be easily replaced, but the design still needs rotary feed-through.

In [158], a 10 MW, 10 rpm fully superconducting machine is proposed (see figure 3.30a). HTS tapes are used in the rotor for the DC field winding and  $\text{MgB}_2$  wires for the armature winding. The operating temperature of the generator is 20 K, the diameter of the generator is 3.7 m and weighs around 35 tonnes (excluding structural mass). The AC loss in the  $\text{MgB}_2$  wires is estimated to be 1 kW. The biggest drawback of the

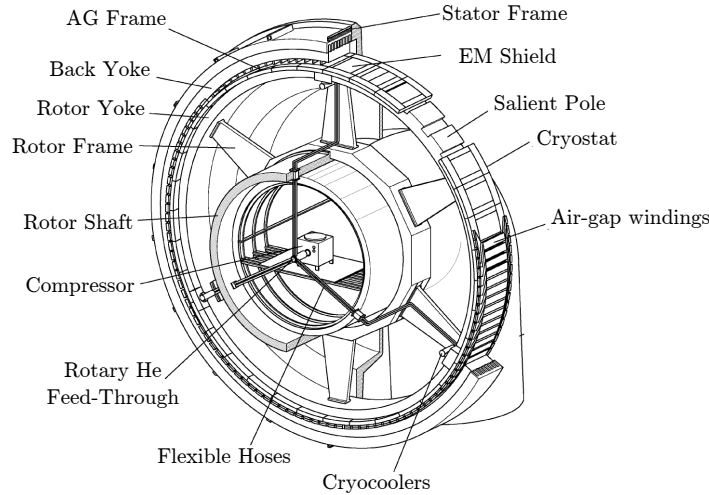


**Figure 3.29:** The 10 MW superconducting generator design for SupraPower project [142].

generator is the excess amount of superconducting wire. It requires 250–300 km of HTS tape and  $\text{MgB}_2$  wire each, which makes the design economically infeasible.

In [134], another 10 MW, 10 rpm superconducting machine is presented (see figure 3.30b), in which the machine uses a novel transverse flux configuration. The maximum flux density in the air-gap is more than 4 T. The superconducting coils are circular and hence easy to manufacture. However, the mechanical stress on the coils is very large and the support structure has to be stiff enough to cope with these forces.

A 10 MW, 10 rpm superconducting machine is also presented in [88]. It is an air-cored machine and requires extensive superconducting coil length (919 km).

A conceptual design of a 8 MW, 12 rpm machine is presented in [105]. The mass of the generator is estimated as 154 tonnes.

In [123, 124], a 10 MW, 10 rpm generator topology is presented. The generator uses bulk superconductors to divert the magnetic flux. An air-gap flux density around 3–4 T is achieved in simulations.

In [134, 135], an air-cored superconducting generator is presented. The generator uses two sets of armature windings and superconducting coils. A 8.3 MW design with a diameter of 5 m and a 12.8 MW design with a diameter of 6 m are presented. The designs require excessive amount of HTS tape (1000 km) because of the air cored topology.

In [16], a conceptual machine is designed for a 10 kW wind turbine. It is an 8-pole synchronous motor with 7.5 km of BSCCO wire requirement.

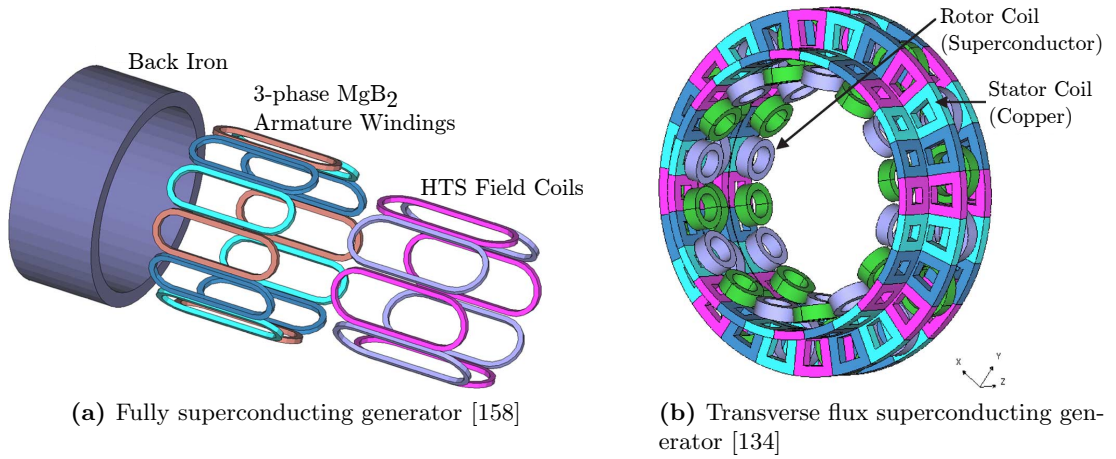


**Figure 3.30:** Schematics of 10 MW, 10 rpm superconducting generators for wind turbines.

### 3.8.5 Economics and Market Readiness

Although, there is growing interest in direct-drive superconducting generators, it may take a long time to prove the concepts and penetrate into the market. It is stated in [3] that the first commercial prototypes will enter the wind turbine market in 2014 and they will penetrate to wind turbines market by 2017.

The current price of the superconducting wires is one of the biggest obstacles in the commercialization of superconducting electrical machines. The price of YBCO wires is coming down, but it is still in the range of €30–60/kAm depending on the operating temperature [169]. The cheapest alternative is NbTi, which is around €0.7/kAm, but needs to operate below 9 K. MgB<sub>2</sub> is becoming popular with its €10/kAm price and operation range around 20–30 K [1]. It is expected that the prices will go down as the superconducting machines become popular.

In [106], the cost of an HTS machine is estimated to be lower than the cost of geared solutions for power ratings greater than 6.5 MW, and 8 MW for direct-drive PM generators. This estimation is based on current HTS wire prices, but in [99], it is proposed that the price of 2G HTS wires will beat current copper prices as the demand for superconducting wire increases. The cost of 1G HTS wire decreased significantly in the mid 1990s [162]. 2G wires first became commercially available after 2006 and just in a few years their price has become comparable to the price of 1G wire. Although, the current price of 2G HTS wire is not satisfactory for a successful entry to market, it is expected that at least the performance will continue to increase with no significant increase in cost [162]. These factors are taken into account in [97] and it is estimated that HTS machines will have a lower cost than direct-drive PM generators for applications larger than 5 MW. In [51], it is proposed that 10 MW superconducting machine will

reduce the cost of energy by 18 % compared to a geared power take-off system and by 13 % compared to a direct-drive permanent magnet generator.

In order to get a more accurate cost of superconducting generators, the decrease in installation costs, increased availability and efficiency should also be considered. In [36], the effect of superconducting generators on the overall cost of the project is estimated and it is stated that superconducting generators may reduce turbine nacelle capital expenditure by two percent. Also, the high efficiency of superconducting generators will result in a two percent increase in annual energy production [36].

### 3.9 Discussion

In this chapter, various applications of superconductors are reviewed. Superconducting electrical machines have great potential in terms of power density, efficiency and transient stability. It is possible to reduce the mass and volume by half with superconducting machines, and the mass reduction becomes more dominant at high power ratings. Thus, most of the superconducting wind turbine concepts are in the range of 10 MW.

The reliability of the cooling systems is the biggest challenge. Different types of cryocoolers are used in many industries and the reliability has increased with time. The performance of cryocoolers has been proved in controlled environments, such as a hospital for a MRI device. However, the reliability of the cooling system in the harsh conditions of an offshore wind turbine still remains unknown.

Some novel methods are being developed that aim to increase the system reliability under these conditions. AMSC's 10 MW, 10 rpm SeaTitan uses a redundant cooling system with long-life seals. Furthermore, most of the components are placed at the bottom of the tower for easy access and replacement [24, 55]. General Electric preferred a stationary superconducting winding in order to eliminate couplers and brushes. However, it uses brushes for the armature winding, which need regular maintenance. SupraPower project aims to simplify the cryostat design with modular superconducting coils. However, it and many others require rotational transfer couplers, which still remains as the single point of failure in the machine.

The rotational couplers can be eliminated by using a stationary superconducting winding, which also simplifies design of the cryostat and the mechanical structure. Therefore, the stationary superconducting field winding concept is chosen as the main feature of the designs that will be presented in the following chapters.

# Design I: Axial Homopolar Superconducting Machine

---

## 4.1 Introduction

In the previous chapters different generator topologies were reviewed for wind turbines. One of the most reliable topology is the homopolar superconducting machine. The layout of a homopolar superconducting machine is presented in figure 3.13. Homopolar superconducting machines have a stationary superconducting coil, which eliminates the cryogenic coupler and transient forces in the superconducting coil (see section 3.6.2 for details). Different homopolar machines are presented in [178, 149, 96, 58]. However, none of these machines are optimised for large-diameter structures and low rotational speed. This chapter presents a novel homopolar superconducting generator concept that has been specifically developed for direct-drive wind turbines.

## 4.2 Machine Topology

The proposed machine topology consists of a stationary field winding and air cored armature windings. The rotor consists entirely of modular ferromagnetic cores. It has a large diameter as it is specifically designed for low-speed, high-torque applications. Figure 4.1 represents the basic schematic of the machine.

### 4.2.1 Stator

The stator consists of an air-cored copper armature winding and a stationary large circular superconducting field winding as shown in figure 4.1a. The armature coils are attached to a fixed outer ring support structure, which can be mounted on the circumference of the nacelle.

Concentrated armature coils are used to minimize the end windings losses, and to have a modular stator structure. The air-cored stator coils eliminate magnetic attraction forces between rotor and stator. However, the air-cored stator has a higher

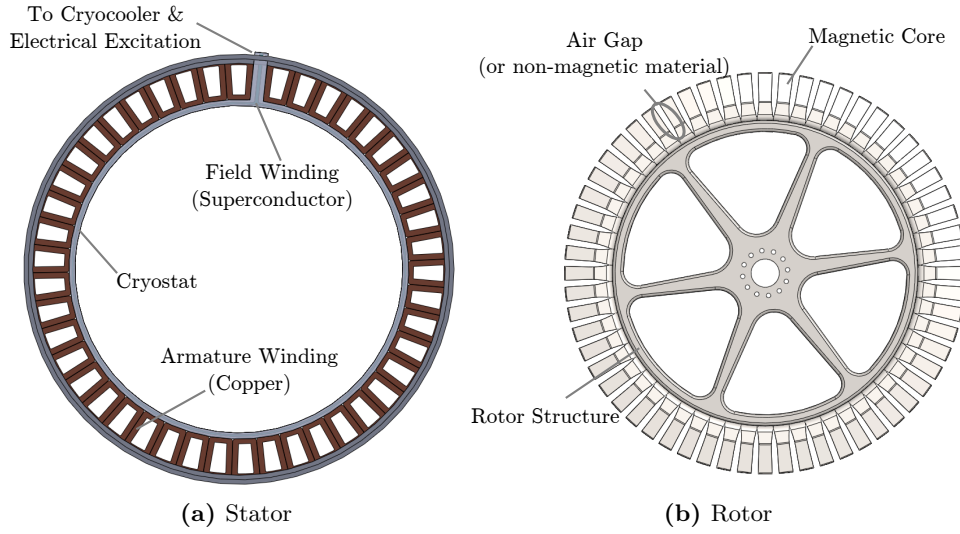


**Figure 4.1:** Axial homopolar superconducting motor.

air-gap reluctance compared to iron-cored machines, requiring higher magneto-motive-force(MMF) to achieve similar air-gap flux densities, which can be easily supplied by the superconducting field winding.

The superconducting field winding is a large circular single superconducting coil, which is mounted on the inner circumference of the stator structure as shown in figure 4.1a. The superconducting field winding is fixed and has the advantages mentioned in section 1.3:

- The rotating transfer coupler is eliminated.
- There is no need for electrical brushes or brushless excitation systems.
- There are no electromagnetic torques or centrifugal forces acting on the superconducting coil. Thus, the support system for the superconducting coil is much easier than of a conventional superconducting machine.
- The field winding is compact and the cold-mass of the machine is small.

The biggest challenge of the proposed machine is the manufacturing and assembly of the large diameter superconducting field winding in a single piece. However, the geometry of the field winding is similar to a superconducting transmission cable, which can make a technology transfer possible.

The field winding can be connected directly to the cryocooler and excitation system without any moving parts as shown in figure 4.1a. A gap between armature coils is required for cooling system connection. Depending on the diameter of the winding, any extra cryocoolers can be connected in the same manner.

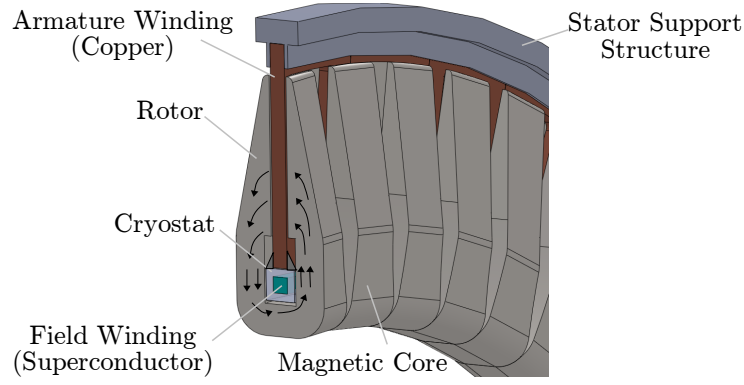


**Figure 4.2:** Cut-through section and flux lines in axial homopolar machine.

### 4.2.2 Rotor

The rotor of the proposed machine consists of modular magnetic cores as presented in figure 4.1b. The magnetic cores are C-shaped and are arranged to constitute a disc-shaped rotor. They are separated with some openings, which ensure a varying magnetic flux imposed on the armature coils.

The magnetic flux generated by the stationary superconducting coil is diverted by the magnetic core as presented in figure 4.2. The choice of the magnetic core dimensions is important to maximize the performance of the generator. For instance, the generator presented in figure 4.1 has 60 poles and 45 concentrated armature coils. The electrical frequency and hence the induced voltage magnitude can be increased by increasing the number of poles. However, this also increases leakage flux. Alternatively, the thickness of the stator coils can be increased to increase the current rating of the machine, but this increases the air-gap reluctance. In the next section, an analytical model will be presented to find the most optimum dimensions.

## 4.3 Electromagnetic Analysis of the Machine

### 4.3.1 Analytical Magnetic Model

The machine can be modelled using a magnetic network model. There are two main options for this: the magnetic permeance network based on nodal equations and magnetic reluctance network based on mesh equations. In the nodal based system Kirchhoff's Current law is applied to the magnetic circuit and nodal magnetic potentials are calculated as outputs. In a mesh based magnetic circuit, Kirchhoff's Voltage law is applied to each loop in the circuit and magnetic flux values are calculated as outputs. In [43], two models are compared and it is stated that mesh-based magnetic equivalent



circuit models are computationally more efficient in non-linear models. Thus, the mesh-based magnetic equivalent circuit model is preferred in this study. The general form of the equations are presented in 4.1.  $\mathfrak{R}$  is the reluctance matrix,  $\Phi$  is the magnetic flux vector for loops and  $F$  is the magneto-motive force (MMF) vector.

$$\mathfrak{R} \Phi = F \quad (4.1)$$

It is essential to define the geometry of the machine before proceeding into the magnetic equivalent circuit. In figure 4.3 the main dimensions in the C-core are presented. These dimensions are presented as follows:

$N_{pole}$	Number of poles
$\tau_{core}/\tau_{pole}$	Ratio of core angle to pole angle
$r_{out}$	Outer rotor radius
$L_m$	Pole Length
$h_t$	Tooth Height
$h_w$	Winding height
$a_c$	Air-gap clearance
$h_g$	Height of the gap
$w_g$	Width of the gap
$\theta_{pole}$	Pole angle(in radians)
$\theta_{core}$	Core angle(in radians)
$t_c$	Core thickness
$t_{web}$	Web thickness
$r_{tooth}$	Tooth inner radius
$r_{web}$	C-core web radius
$r_{in}$	Rotor inner radius
$k_{fill}$	Fill factor of copper
$k_{fill-SC}$	Superconductor fill factor
$J_{SC}$	Superconductor current density

### Basic Magnetic Circuit

The simplest representation of the magnetic circuit is given in figure 4.4. In this circuit, the core reluctances are represented by  $R_{web}$ ,  $R_{limb}$  and  $R_{tooth}$ . The superconducting field winding MMF is represented by  $F_{SC}$ . The air-gap reluctance is represented by  $R_{gap}$ . The air-gap reluctance is much larger than the core reluctance and the equivalent reluctance network is dominated by the air-gap reluctance.

The magnetic reluctance of a rectangular block is analogous to electrical resistance as follows:

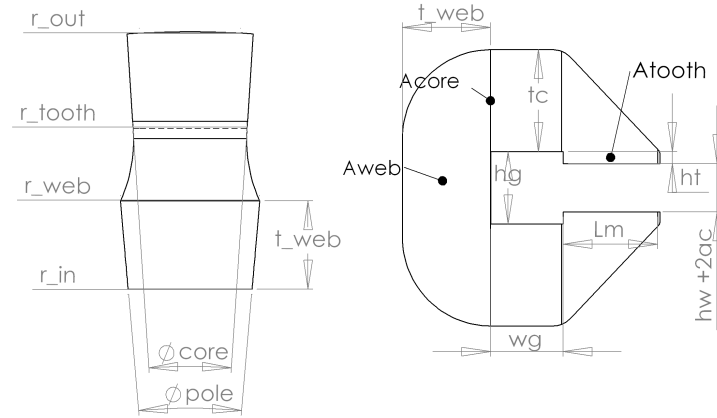


**Figure 4.3:** Axial homopolar-machine core shape and dimensions.

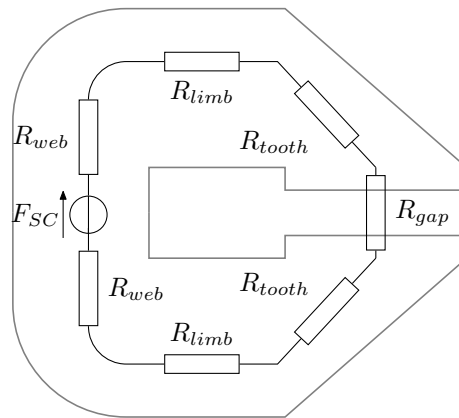


**Figure 4.4:** Simple magnetic circuit (without fringing flux).

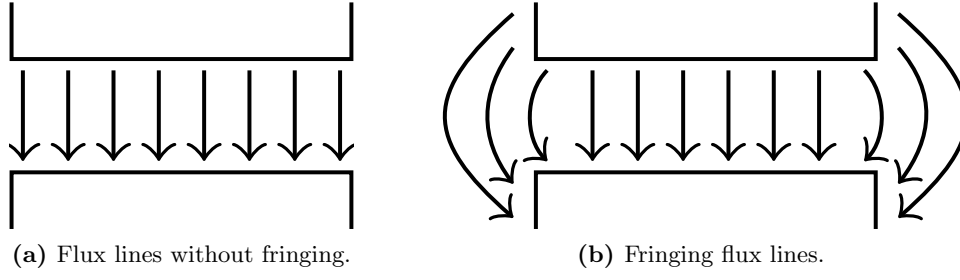


**Figure 4.5:** Comparison of basic magnetic circuit calculations with the actual case.

$$R = \frac{L}{\mu_r \mu_0 A} \quad (4.2)$$

where  $L$  is the length of the block,  $\mu_0$  is the permeability of air,  $\mu_r$  is the relative permeability of the material and  $A$  is the cross-sectional area.

The reluctance elements presented in figure 4.4 are calculated using the dimensions presented in figure 4.3. The equations to calculate equivalent circuit reluctances are presented in Appendix C.

### Extended Magnetic Circuit

The basic magnetic circuit presented in the previous section assumes that flux travels through the magnetic core tooth without any fringing between neighbouring cores as illustrated in figure 4.5a. However, fringing flux exists between the neighbouring cores as presented in figure 4.5b. Furthermore, there are also leakage flux paths, with the most dominant being the leakage flux around the superconducting coil. The basic magnetic circuit is improved by adding extra components to reflect these additional flux paths. The extended magnetic circuit is given in figure 4.6.

In the extended magnetic circuit, the air-gap flux distribution is estimated with eight branches, whereas in the simple circuit only one branch was used. The core tooth reluctance ( $R_{tooth}$ ) is divided to four branches - two side reluctances ( $R_{ts}$ ) and two centre reluctances ( $R_{tc}$ ).

$$R_{tc} = R_{ts} = 4R_{tooth} \quad (4.3)$$

The air-gap reluctance in the simple model ( $R_{gap}$ ) is divided into two centre reluctances ( $R_{gc}$ ) and two side reluctances ( $R_{gs}$ ). Furthermore, four reluctance elements ( $R_{f1}$ ,  $R_{f2}$ ) are defined to represent the fringing flux path, which are presented in appendix C.

It can be seen from figure 4.6 that the circuit has a half-symmetry along the central

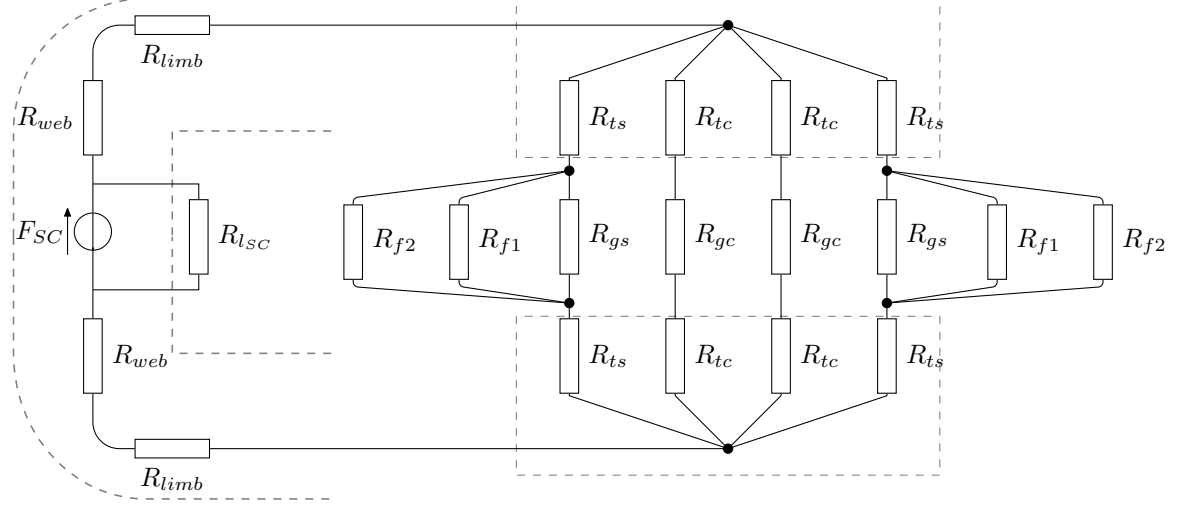


**Figure 4.6:** Expanded magnetic circuit (with fringing flux).

line of the magnetic core. The extended magnetic circuit can be simplified using that symmetry line to reduce the number of meshes from nine to five. The magnetic circuit with the symmetry is given in figure 4.7. The mesh equations of the equivalent circuit of figure 4.7 can be represented as:

$$\begin{bmatrix} R_{lsc} & 0 & 0 & 0 & 0 \\ 0 & 2(R_{limb} + R_{web}) + R_{tc} + 0.5R_{gc} & -(R_{tc} + 0.5R_{gc}) & 0 & 0 \\ 0 & -(R_{tc} + 0.5R_{gc}) & R_{tc} + R_{gc} + R_{ts} + 0.5R_{gs} & -0.5R_{gs} & 0 \\ 0 & 0 & -0.5R_{gs} & 0.5R_{gs} + 0.5R_{f1} & -0.5R_{f1} \\ 0 & 0 & 0 & -0.5R_{f1} & 0.5(R_{f1} + R_{f2}) \end{bmatrix} \begin{bmatrix} \phi_{lsc} \\ \phi_{main} \\ \phi_c \\ \phi_s \\ \phi_f \end{bmatrix} = \begin{bmatrix} -F_{SC} \\ F_{SC} \\ 0 \\ 0 \\ 0 \end{bmatrix} \quad (4.4)$$

### Non-linear Magnetic Circuit

The reluctance network presented in the previous section assumes that the reluctances of the components are constant. However, this is not the case for the magnetic core components which have non-linear magnetizing characteristics. The permeability of the core ( $\mu_c$ ) depends on the B-H characteristics of the material. The permeability of the core decreases as the magnetic field intensity (H) is increased and the core saturates. Thus, it is necessary to transform (4.4) into a non-linear equation for better accuracy in highly saturated models. The Newton-Raphson method is an efficient way to estimate non-linear equations. It is an iterative process that approximates non-linear equations using the first order Taylor series. A function can be represented using the first order Taylor series as:

$$f(x) \cong f(x_0) + f'(x_0)(x - x_0) \quad (4.5)$$

The Newton-Raphson method uses this information to approximate the solution to  $f(x) = 0$ , so equation 4.5 becomes:

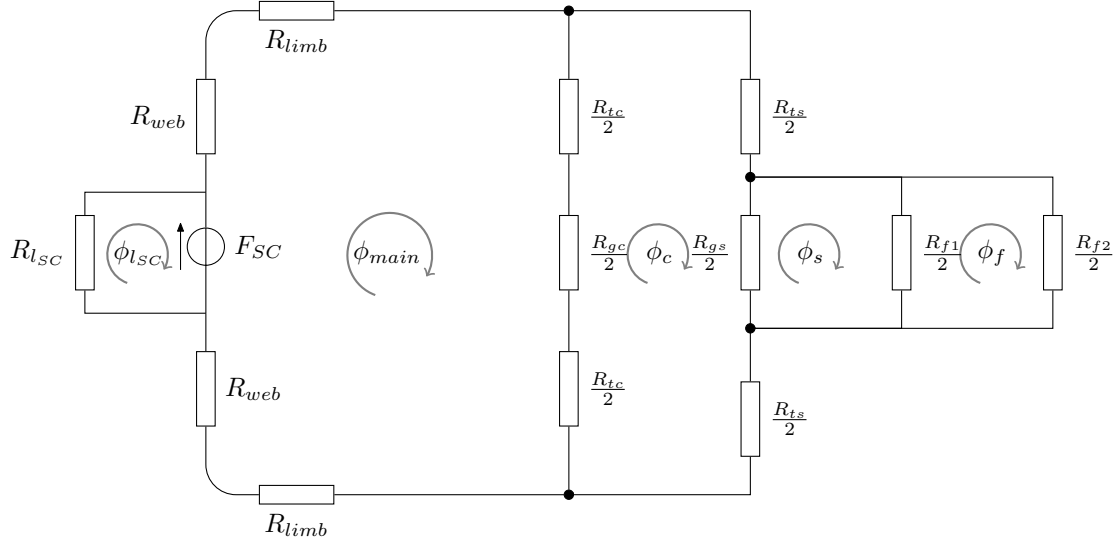


**Figure 4.7:** Expanded magnetic circuit with symmetry applied.

$$x_1 = x_0 - \frac{f(x_0)}{f'(x_0)} \quad (4.6)$$

For the given magnetic circuit problem, the Newton-Raphson method can be applied by rewriting equation 4.1 as follows:

$$\Re \Phi - F = 0 \quad (4.7)$$

After the initial input vector  $(\Phi_0)$  is assigned, the Newton-Raphson algorithm can be applied to equation 4.7 as:

$$\Phi_1 = \Phi_0 - J^{-1}[\Re_{(\Phi)} \Phi_0 - F] \quad (4.8)$$

where  $J$  is the Jacobian matrix and  $R_{(\Phi)}$  is the variable reluctance term. In the Jacobian matrix, there are only four elements, in which the permeability values are dependent on the flux density. The derivative of all the other elements is zero as the permeability of the air is constant. Thus, the Jacobian matrix becomes:

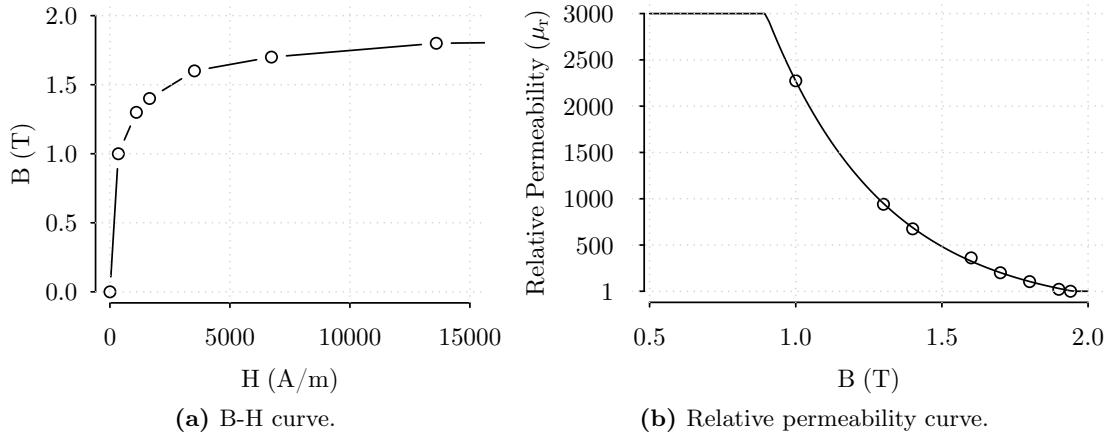


**Figure 4.8:** B-H curve and relative permeability curves used in analytical model.

$$J = \begin{bmatrix} 0 & 0 & 0 & 0 & 0 \\ 0 & \frac{\partial(2(R_{limb} + R_{web}) + R_{tc})}{\partial\phi_{main}} & \frac{-\partial R_{tc}}{\partial\phi_c} & 0 & 0 \\ 0 & \frac{-\partial R_{tc}}{\partial\phi_{main}} & \frac{\partial(R_{tc} + R_{ts})}{\partial\phi_c} & 0 & 0 \\ 0 & 0 & 0 & 0 & 0 \\ 0 & 0 & 0 & 0 & 0 \end{bmatrix} \quad (4.9)$$

A practical way to calculate the Jacobian matrix is to calculate the differential terms analytically as presented in equation 4.10.

$$J = \frac{\Re_{(\Phi+\Delta X)} - \Re_{(\Phi)}}{\Delta X} \quad (4.10)$$

For calculating the Jacobian and reluctance matrix, the B-H curve presented in figure 4.8a is used. Figure 4.8b shows the relative permeability function obtained from the B-H curve. The maximum relative permeability is assumed as 3000 and it is assumed that the relative permeability value converges to 1 for flux densities larger than 1.9 T. Then, the magnetic flux density distribution is calculated using the Newton-Raphson method and the dimensions presented in Appendix C.1.3. In figure 4.9, the magnetic flux distribution in the centre of the air-gap is presented, in which it can be seen that the maximum flux density in is estimated as 1.2 T, and the fringing flux densities ( $B_{f1}, B_{f2}$ ) are estimated as 0.5 T and 0.3 T. In the next section, these results will be verified using a finite element analysis.

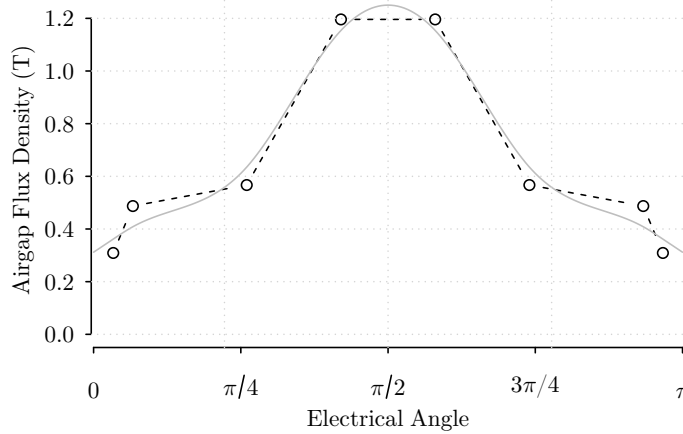


**Figure 4.9:** Air-gap flux density distribution in the air-gap using extended magnetic circuit and non-linear material properties.

### 4.3.2 Finite Element Analysis

Although, the analytical model can give quick estimation of the air-gap flux density distribution, a three dimensional (3D) finite element analysis (FEA) software has been used to get better results and to verify the analytical model.

FEA is preferred over the analytical method, for the following reasons:

- Better accuracy.
- Electromagnetic hot spots can be observed.
- Better representation of non-linear materials (magnetic core, superconductor).
- Easier to represent complex geometries.

FEA methods are more accurate than analytical reluctance networks. In fact, FEA software creates a mesh over the model which is nothing more than a reluctance network with thousands of elements. These high number of elements help to observe any electromagnetic hot spots, which would not be observed in the analytical model. Especially with complex geometries and non-linear materials, finite-element methods will give a much better insight of the flux paths in the machine.

In a superconducting machine, superconducting windings create very high magnetic fields, which result in high flux densities and heavily saturated magnetic cores. This makes the choice of machine parameters very important for a superior performance. FEA is an effective tool to analyse and identify the saturated parts in the machine core.

Furthermore, the performance of the superconducting wires are significantly effected by the magnetic flux penetrating into the wire. The effect of the flux varies according to the angle of the flux (i.e. perpendicular or parallel). It is difficult to build an analytical model that can accurately estimate the magnitude and angle of the penetrating flux. However,

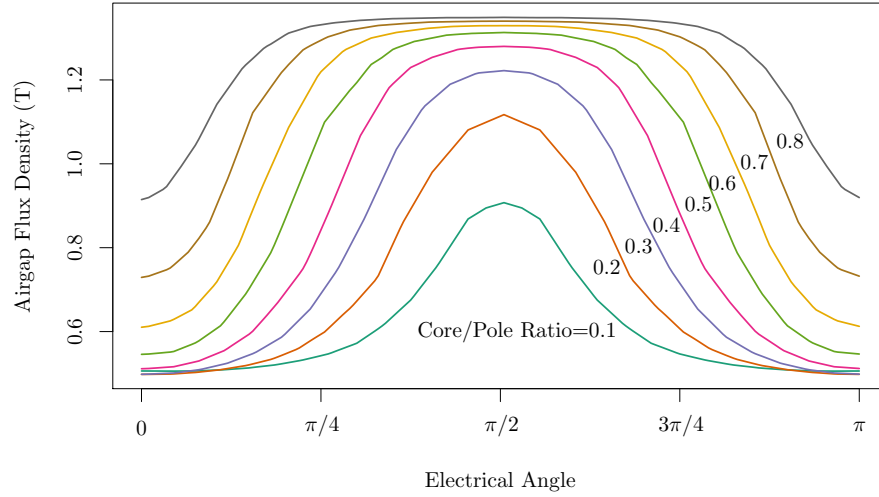


**Figure 4.10:** Air-gap flux density variation with core to pole pitch ratio.

with the FEA method it is easier to model the flux density around the superconducting wire and the accuracy can be improved by using a finer mesh.

Finally, the operating temperature has a direct effect on the performance. Although, thermal modelling of superconductors is not the focus of this study, it is believed that the FEA models built can be used as a base for thermal modelling in the future.

The software used for FEA and data analysis are described in detail in Appendix D.

## 4.4 Simulation of the Axial Homopolar Machine


In this section, FEA simulations for the axial homopolar superconducting machine are presented. FEA simulations are particularly useful for the estimation of:

- the fringing flux around the core,
- the saturation in the magnetic core,
- the penetrating flux into the superconducting coil.

Firstly, in order to see the effect of the fringing flux and to find the optimum core-to-pole angle ratio ( $\theta_{core}/\theta_{pole}$ ) various simulations are performed with varying core-to-pole ratios. The dimensions of the core are presented in Appendix C.1.3.

The air-gap flux density distribution for a single pole-pitch in the mid-plane of the stator coils is plotted in figure 4.10. Comparing the FEA simulation with a core-to-pole pitch ratio of 0.5 with the result of the analytical model presented in figure 4.9, a good agreement can be seen. However, the fringing flux in the FEA simulation is higher.



		Core Pitch to Pole Pitch Ratio ( $\theta_{core}/\theta_{pole}$ )							
		0.1	0.2	0.3	0.4	0.5	0.6	0.7	0.8
									
MMF		Air-gap Flux Density (T)							
90 kAt	Max.	0.56	0.73	0.83	0.89	0.91	0.92	0.92	0.93
	Min.	0.20	0.23	0.26	0.30	0.34	0.41	0.51	0.66
	Diff.	0.36	0.51	0.57	0.59	0.57	0.51	0.41	0.27
180 kAt	Max.	0.73	0.92	1.01	1.06	1.08	1.09	1.09	1.10
	Min.	0.33	0.34	0.35	0.37	0.42	0.49	0.60	0.77
	Diff.	0.39	0.58	0.66	0.68	0.66	0.60	0.49	0.33
270 kAt	Max.	0.83	1.03	1.14	1.19	1.21	1.22	1.23	1.23
	Min.	0.43	0.42	0.43	0.45	0.49	0.56	0.67	0.85
	Diff.	0.40	0.61	0.71	0.74	0.72	0.67	0.56	0.38
360 kAt	Max.	0.92	1.13	1.24	1.30	1.33	1.34	1.35	1.36
	Min.	0.51	0.51	0.51	0.52	0.56	0.62	0.74	0.92
	Diff.	0.41	0.62	0.73	0.78	0.77	0.72	0.61	0.43

**Table 4.1:** Maximum and minimum flux density values for varying core angle to pole angle ratio.

The simulations are repeated with four different magnetic field intensity by varying the field current from 90 kAt to 360 kAt<sup>1</sup>. Figure 4.11 shows the variation of the air-gap flux density for a single pole-pitch in the middle of the stator coil with field current and core to pole pitch ratio. Table 4.1 shows the maximum, minimum flux density and the difference between maximum and minimum values.

When the core angle to pole angle ratio ( $\theta_{core}/\theta_{pole}$ ) is small, the maximum flux density is around 1 T. As the  $\theta_{core}/\theta_{pole}$  ratio is increased, the magnitude of the air-gap flux density is limited by the saturation in the magnetic core. The maximum air-gap flux density is found to be 1.35 T. However, the minimum flux density in the air-gap is not zero due to fringing magnetic flux as mentioned in the previous section. Therefore, even if the maximum flux density is increased up to the maximum saturation limit, the difference between maximum and minimum value of the magnetic flux variation is limited, which also limits the magnitude of the induced voltage in the armature coils.

From table 4.1, it can be seen that the minimum value of the air-gap flux density is larger than 0.51 T, for a MMF of 360 kAt. The maximum value of the air-gap flux

<sup>1</sup>Although, the standard SI unit for the magneto-motive force is Amperes, Ampere-turns is used throughout this thesis to distinguish the superconducting wire current from the total field winding MMF.

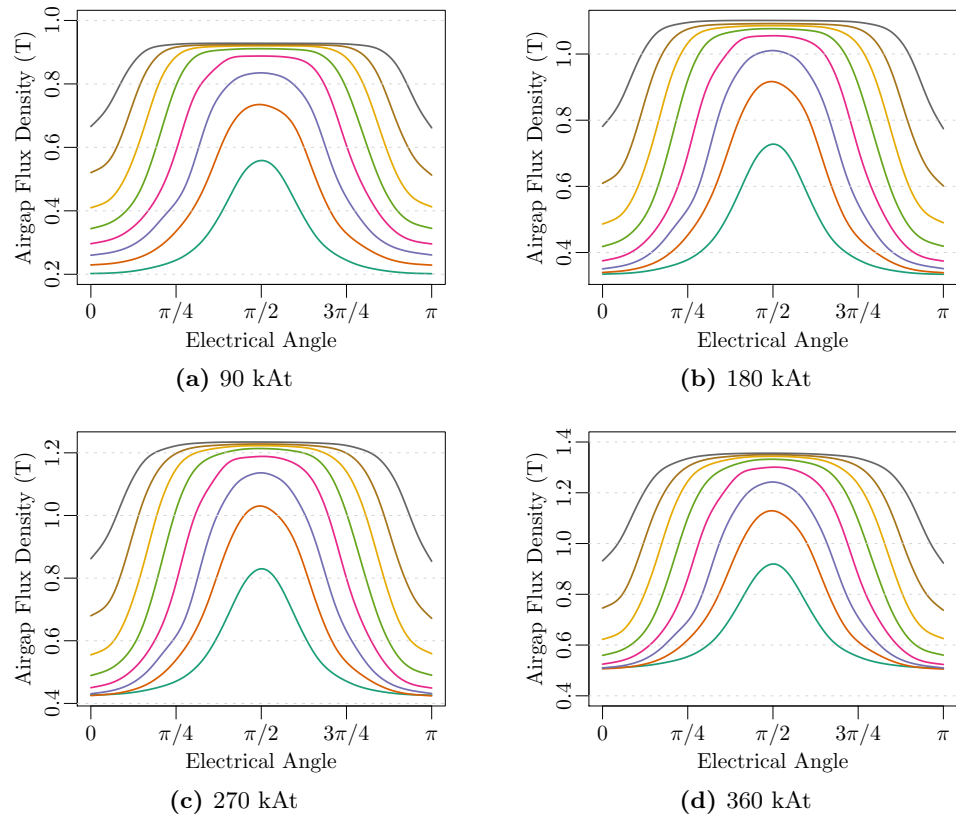


**Figure 4.11:** Air-gap flux density variation of the homopolar axial flux machine with field current and core to pole pitch ratio.

density is 1.36 T. The largest difference between the maximum and the minimum flux density values are obtained as 0.78 T for a core-to-pole angle ratio of 0.4. The flux density variation in the machine is limited and it is obvious that the power density of such a machine will be low.

## 4.5 Discussion of Results

The axial homopolar machine is proposed to simplify the cooling system by having a stationary superconducting coil. However, the electromagnetic performance of the machine is not satisfactory due to the homopolar distribution of the magnetic flux. The maximum flux density is limited by the saturation of the magnetic core, and the minimum magnetic flux is greater than zero because of fringing flux.

The topology has some mechanical challenges as well. The superconducting coil is attached to the armature coils. Armature coils, which are air-cored, should be stiff enough to support the superconducting coil and vacuum layer. Although, there is no electromagnetic torque acting on the superconducting coil, it needs to withstand the

tensile strength created by the magnetic flux around it. Furthermore, the assembly of the superconducting coil can be challenging due to the large diameter of the superconducting coil.

#### 4.5.1 Chapter Summary

In this chapter a novel superconducting machine topology is proposed. The biggest advantage of the topology is having a stationary superconducting coil. Thus, the electrical brushes and rotating transfer couplers are eliminated.

The rotor consists of modular magnetic cores. The stator has air-cored concentrated coils. A single loop shaped superconducting coil is used. Although, the main focus of this study is rotary machines, the proposed homopolar topology can be modified to build a direct-drive linear generator as shown in Appendix E.

A reluctance network model was built to model the electromagnetic circuit. The Newton-Raphson method is applied to estimate the saturation of the magnetic cores. The accuracy of the analytical model is acceptable, but it fails to model every aspect of a superconducting machine, so FEA simulations are preferred over analytical models.

FEA simulations with varying core pitch to pole pitch ratios are presented. Although, the flux density in the air-gap is quite high, the minimum flux density is larger than 0.4 T due to fringing flux. The maximum difference in the air-gap flux density is achieved when the core pitch to pole pitch ratio is between 0.4 and 0.5. The power density of this machine is quite low due to the homopolar distribution of the magnetic flux. Furthermore, there are some mechanical challenges. Therefore the homopolar machine concept is discarded. In the next chapter, a modified version of the homopolar machine will be presented.

# Design II: Axial Bipolar Superconducting Machine

## 5.1 Introduction

A homopolar superconducting machine is presented in the previous chapter. The machine has a single stationary superconducting coil. However, due to the homopolar distribution of the magnetic flux, the power density of the machine is not very high even with the high MMF created by the superconducting field winding.

In this chapter, the homopolar machine is modified to obtain a bipolar magnetic flux variation. If it is assumed that, two of the C-cores used in the homopolar machine are excited with the same current and placed facing each other as shown in figure 5.1, the core on the left has an air-gap flux direction in the -y direction, whereas the one on the right creates an air-gap flux density in the +y direction.

These two cores can be combined together as shown in figure 5.2 to produce a bipolar air-gap flux density variation. In this way, bi-directional magnetic flux is obtained along the field windings. However, this configuration should be modified slightly to make it suitable for a rotary machine. The field windings and armature winding (not shown) should be fixed to the stationary frame and the magnetic cores should be in the rotating frame. The magnetic core on the left is cut and the magnetic cores are arranged radially as presented in figure 5.3.

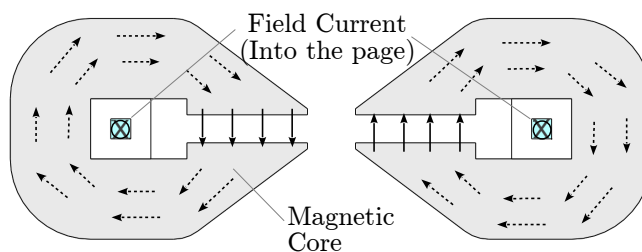


**Figure 5.1:** Two C-cores facing each other excited with the same field current.

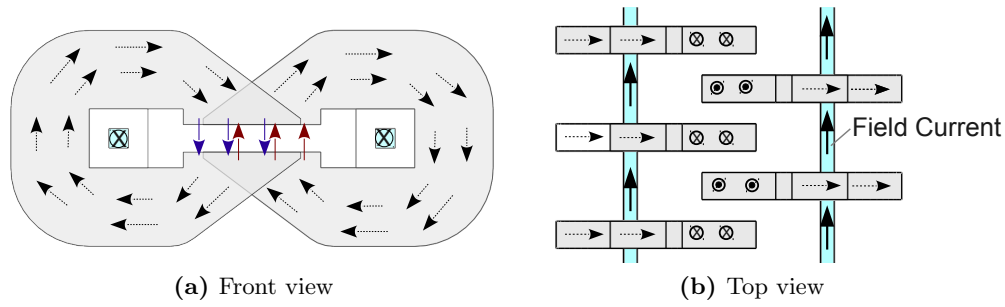


**Figure 5.2:** Two C-cores placed together to have a bipolar air-gap flux density variation.

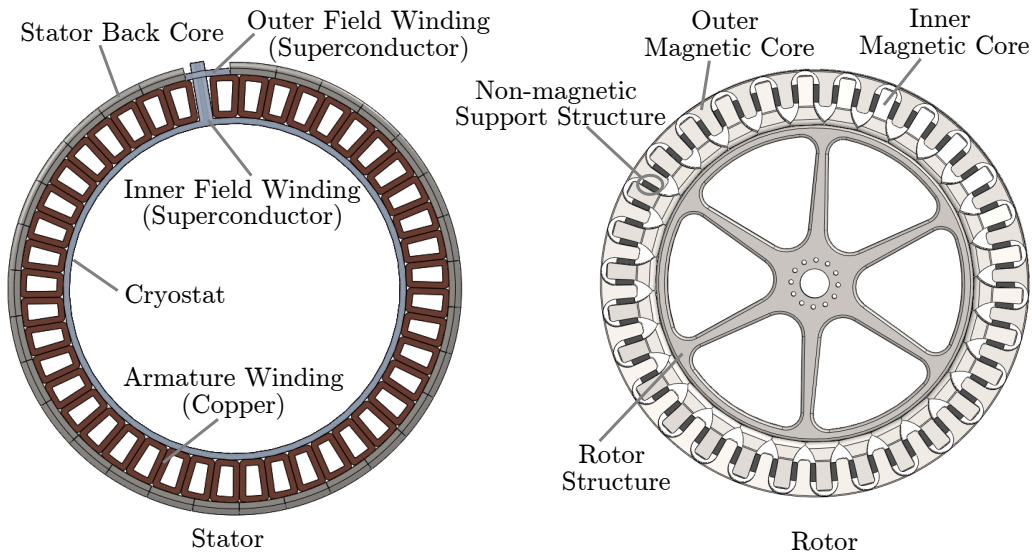


**Figure 5.3:** The stator and rotor of the axial bipolar machine.

The stator of the machine is similar to the homopolar superconducting machine. It has air-cored concentrated armature coils. Compared to the homopolar version, the bipolar axial flux superconducting machine has two separate superconducting field windings: the inner field winding and the outer field winding as shown in figure 5.3. The inner field winding is fixed to armature coils similar to the homopolar superconducting machine, and the outer field winding is mounted to the outer circumference of the armature coils. The stator back-core around the outer field winding diverts the magnetic flux. A cut-through view of the machine is presented in figure 5.4, in which, the expected direction of magnetic flux lines are shown. The inner and outer magnetic cores are magnetically separated. However, they are attached to each other with a non-magnetic support structure such as aluminium or non-magnetic steel. The air-gap clearance between the outer magnetic core and the stator back-core is exaggerated in the figure.

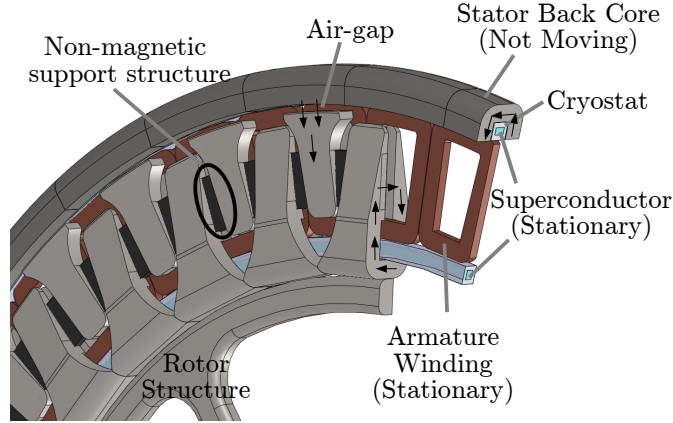


**Figure 5.4:** Cut-through view of the axial flux bipolar superconducting machine. The armature coils, superconductor windings, and the back-core (dark gray) are stationary; the rotor structure, the inner magnetic cores, and the outer magnetic cores (light gray) are rotating.

## 5.2 Reluctance Network Model

The bipolar machine is modelled using a magnetic reluctance network similar to the homopolar machine. The reluctance network of a single pole-pair is illustrated in figure 5.5. The cores are depicted side by side for easy representation. The core on the left has an extra air-gap which is represented by  $R_{gap2}$ . The core and limb reluctances are calculated similarly to ones presented in Appendix C. The fringing flux reluctances are not shown in figure 5.5 for simplicity.

The most important element in the model is the leakage flux reluctances between the neighbouring poles  $R_{leakage\ core}$ . The magnitude of this element depends on the overlapping area of the C-cores and the distance between them. In figure 5.5 only two C-cores are shown. However, in the full machine many C-cores are placed together as presented in figure 5.1. The equivalent magnetic circuit of the full machine is presented in figure 5.6. In this circuit, the blue components represent the outer field winding, stator back-core and the outer magnetic cores. The red components represent the inner field winding, and the inner magnetic cores. Leakage flux reluctances, shown as black, ( $R_{leakage\ core}$ ) are connected between adjacent cores from  $R_{limb}$  nodes of inner and outer magnetic cores.

The full magnetic circuit can be reduced by use of the cyclic symmetry. After applying the symmetry conditions, the reluctance network becomes as illustrated in figure 5.7. The reluctance network model can be improved by including the fringing flux components. However, 3D FEA models will be used to analyze the machine in the rest of this chapter.

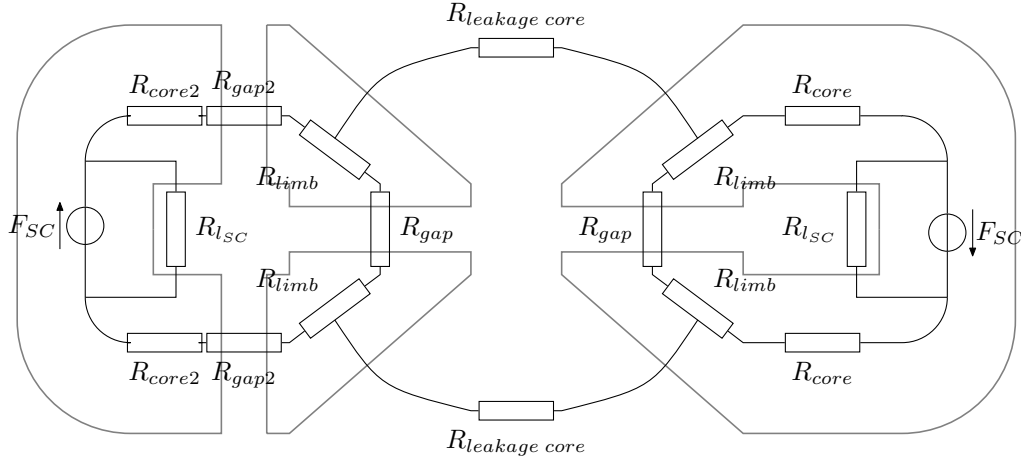


**Figure 5.5:** Basic reluctance network for the axial bipolar machine.

### 5.3 FEA Results

In this section the FEA simulation results for the axial bipolar machine are presented. The flux density vectors in the machine are simulated in figure 5.8. In the figure, the green parts represent the magnetic core, and the grey parts represent the non-magnetic support structure between cores. Figure 5.8b shows the flux distribution in the core and in the surrounding air. The current density in the field-winding area is assumed to be 100 A/mm<sup>2</sup>. The fill factor of the winding (superconducting coil to cryostat cross-section area ratio) is taken as 0.2. The magnetic core also functions as a flux diverter, reducing the amount of flux penetrating into the superconducting field winding.

#### 5.3.1 Magnetic Core Optimisation

The amount of leakage flux in the machine depends on the overlapping core area and the distance between cores. Thus, the magnetic core dimensions have a direct effect on the machine's performance. In figure 5.9, the effect of fringing flux between adjacent poles can be observed. This effect is represented in the equivalent circuit (see figure 5.6) as  $R_{leakage\ core}$ . This leakage flux reduces the amount of flux linking the armature coils and it should be minimized.

In this section, in order to find the optimum dimensions of magnetic core, various FEA simulations have been performed. The main dimensions of the magnetic core are defined in figure 5.10.

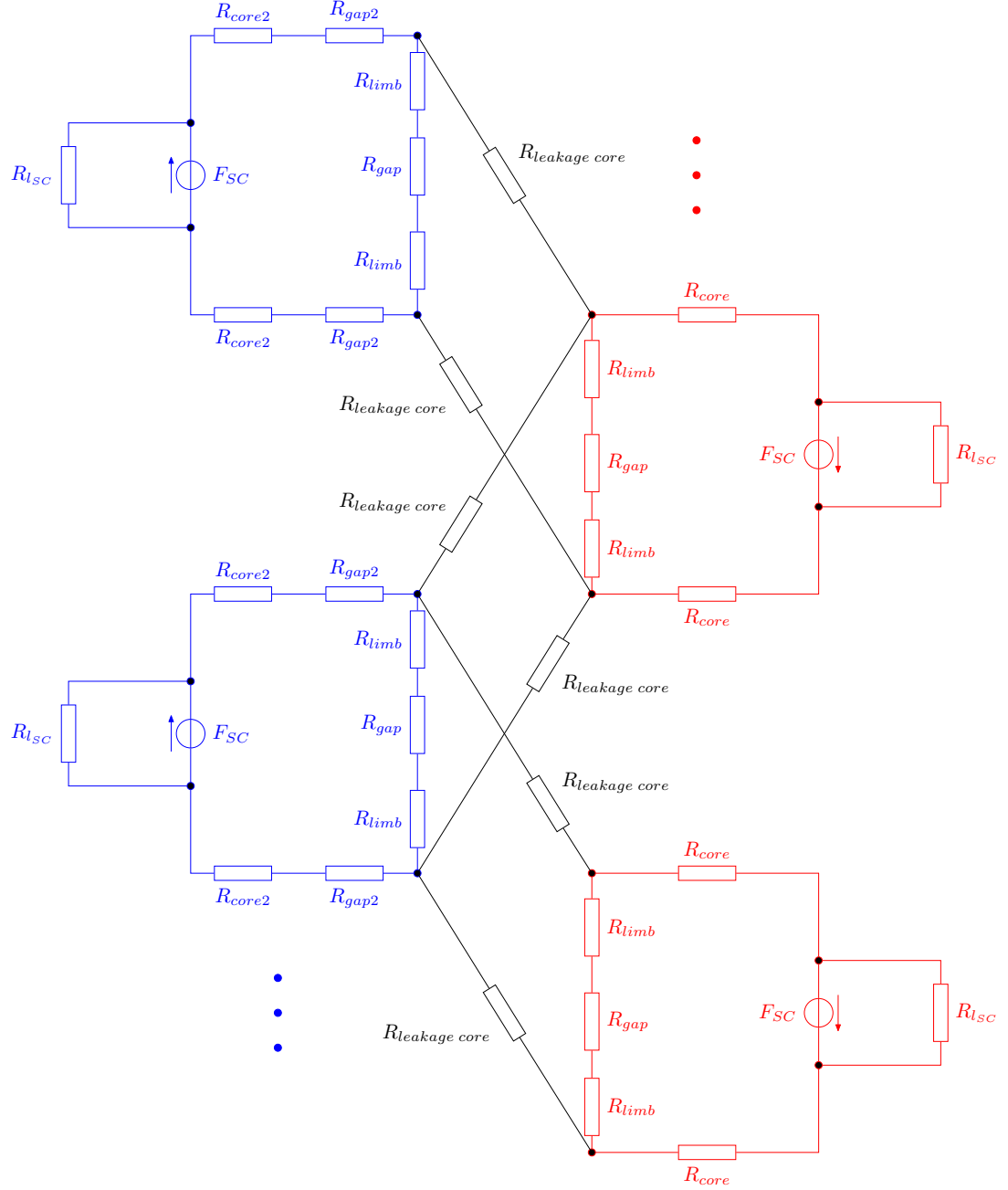


**Figure 5.6:** Expanded magnetic reluctance network for the bipolar axial flux machine.



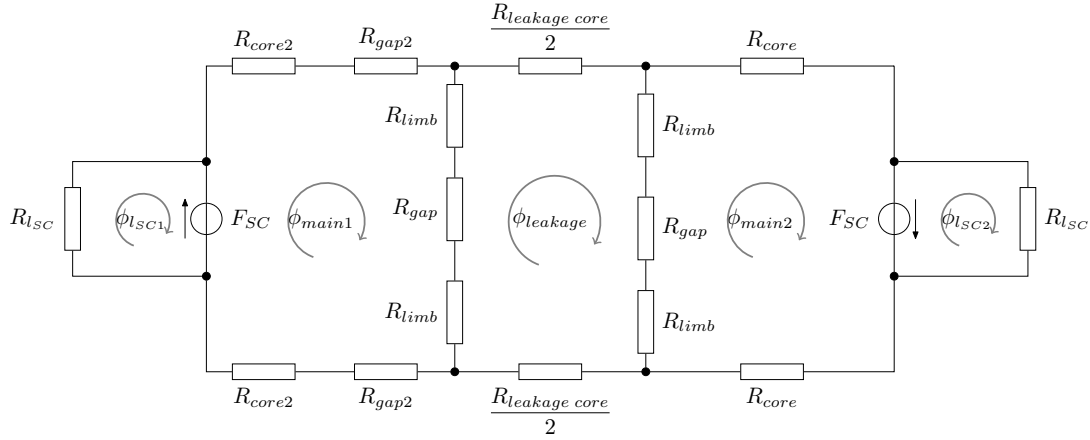


**Figure 5.7:** Magnetic circuit of the bipolar axial flux machine after symmetry conditions are applied.

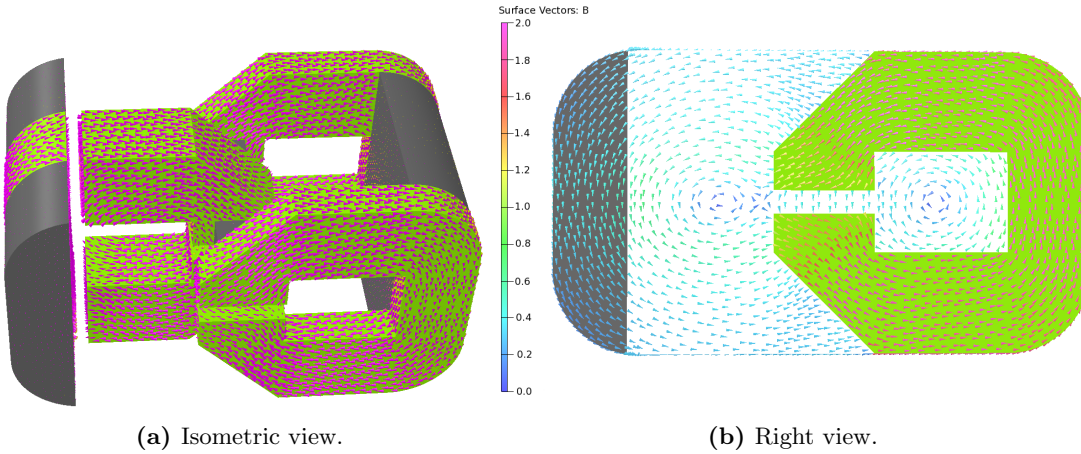


**Figure 5.8:** Flux density vectors in the axial bipolar superconducting machine with the gap. Superconducting field winding and armature coils are not shown.

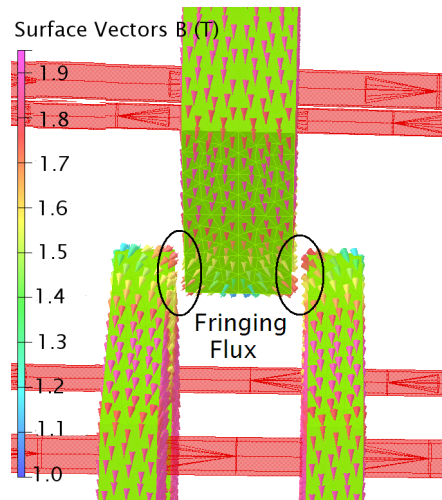


**Figure 5.9:** Fringing flux between adjacent poles.

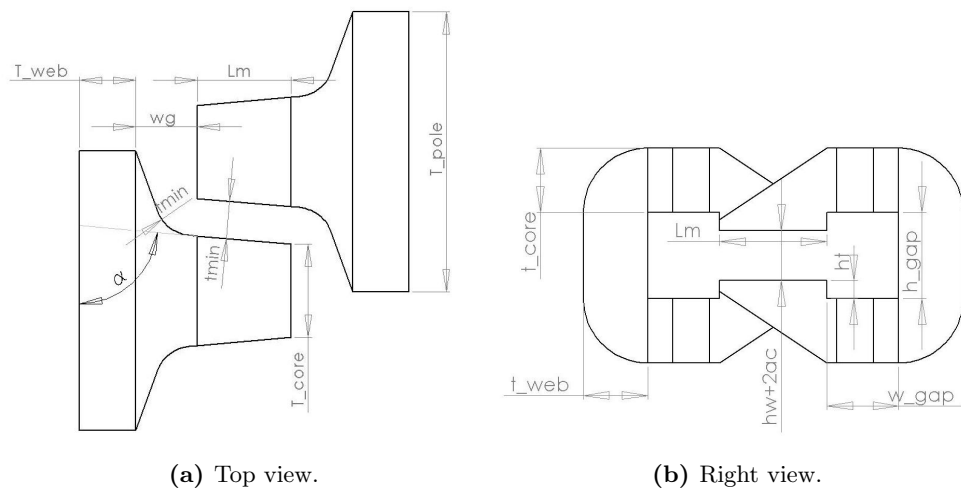


**Figure 5.10:** Main dimensions for the axial homopolar machine magnetic core.

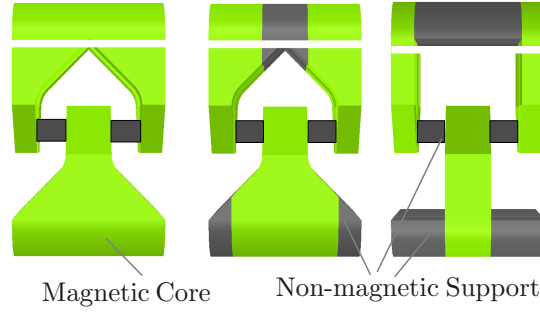


**Figure 5.11:** Different magnetic core types: Full core, half core, and simple core.

### Core Types

In order to evaluate the effect of the core shape on the machine's performance, three different core types, which are shown in figure 5.11, are analysed:

- Full core.
- Half core.
- Simple core.

In figure 5.11, magnetic cores are shown in green and non-magnetic parts are shown in grey. The first core has the largest amount of magnetic material and covers the superconducting field winding completely. This results in a small equivalent reluctance, but it also has a high leakage flux to linking flux ratio. 3D FEA has been used to calculate the flux linkage for each type in figure 5.13.

### Distance between poles

The distance between adjacent poles,  $\tau_{min}$ , has a direct effect on the amount of the leakage flux. The axial gap length between teeth ( $g = h_w + 2a_c$ ) and the core to pole pitch ratio ( $\tau_{core}/\tau_{pole}$ ) is kept constant while changing the distance between adjacent poles ( $_{min}$ ). Three cases of these simulations are presented in figure 5.12. Dimensions used in the simulations are presented in Appendix C.2.

In order to find the core type with the maximum power density, it is not enough just to compare the magnitude of the air-gap flux densities. The pole pitch for each simulation is different, which changes the electrical frequency and the induced voltage magnitude for the same rotational speed. The peak induced voltage magnitude in a coil with a single turn can be expressed as in equation 5.1, where  $\nu$  is the linear speed at the mean air-gap radius,  $\lambda_{pk}$  is the peak flux linkage in the coil,  $\tau_{pole}$  is the pole pitch.

$$e_{pk} = \frac{\pi \cdot \nu \cdot \lambda_{pk}}{\tau_{pole}} \quad (5.1)$$

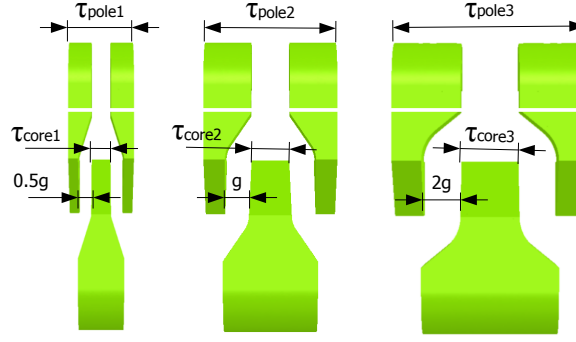


**Figure 5.12:** Varying core to gap ratio.  $\tau_{min}/g$  ratios are 0.5, 1.0, and 2.0 respectively.

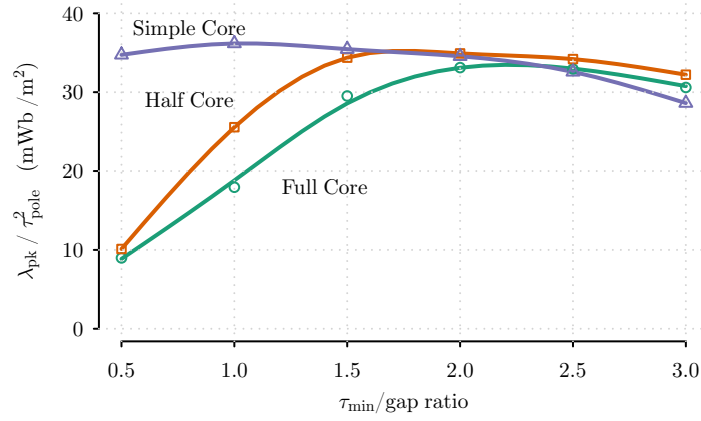


**Figure 5.13:**  $\lambda_{pk}/\tau_{pole}^2$  variation with different magnetic core types.

Concentrated coil windings are used in the simulations. The coil pitch ( $\tau_{coil}$ ) is assumed to be  $4/3$  of the pole pitch ( $\tau_{pole}$ ), and the total number of the coils in the machine can be expressed as in equation 5.2, where  $R$  is the mean air gap radius.

$$N_{coil} = \frac{3\pi R}{2\tau_{pole}} \quad (5.2)$$

The total power output of the machine can be roughly expressed as in equation 5.3, where  $N_t$  is the number of turns per coil,  $I_{coil}$  is the magnitude of the single coil current (assuming same coil width and height). Finally, if the constants are removed from equation 5.3, it can be seen that the power is directly proportional to the ratio of peak flux linkage to pole pitch squared as presented in equation 5.4.

$$P_{out} = \frac{\pi \cdot \nu \cdot \lambda_{pk}}{\tau_{pole}} \frac{N_t I_{coil}}{2} \frac{3\pi R}{2\tau_{pole}} \quad (5.3)$$

$$P_{out} \propto \frac{\lambda_{pk}}{\tau_{pole}^2} \quad (5.4)$$

The results for simple, half, and full cores are presented in figure 5.13<sup>1</sup>. The x-axis shows the  $\tau_{min}/gap$  ratio. For example, when  $\tau_{min}/gap$  equals one, the distance between adjacent magnetic poles is equal to the axial gap (air-gap clearance plus coil thickness). From figure 5.13 it can be seen that, the performance of the half core and full core is very low for a shorter distance between poles. When  $\tau_{min}/gap$  ratio is 0.5, the performance of the simple core is 3.5 times of the half and full core. However, when the distance between cores is sufficiently increased, the core shape becomes less important and all the core types have similar performance.

The best performance can be achieved with the simple-core type. The optimum point for the simple core is achieved when the distance between adjacent poles is equal to the distance between the teeth surfaces (i.e.  $\tau_{min}/gap = 1$ ). The simple-core structure holds a considerable amount of non-magnetic material as shown in figure 5.11. This part can be manufactured using light materials such as epoxy, durable plastic or aluminium profile to reduce the overall mass. However, it should be noted that in aluminium material eddy currents will be induced.

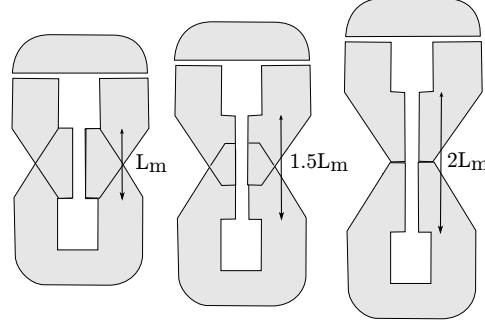
### Misalignment factor

Another way to minimize the leakage flux between magnetic cores is to reduce the overlapping tooth area. This can be achieved by placing the magnetic cores with an offset as shown in figure 5.14. In the first model, the cores are fully-overlapped. In the second model, only half of the tooth lengths ( $L_m$ ) are overlapped. In the last model, the cores are separated completely. The leakage flux reduces as the core offset is increased. However, as the cores are separated, the mean length of the armature coil increases, which increases the resistance of the coil and the copper losses in the machine.

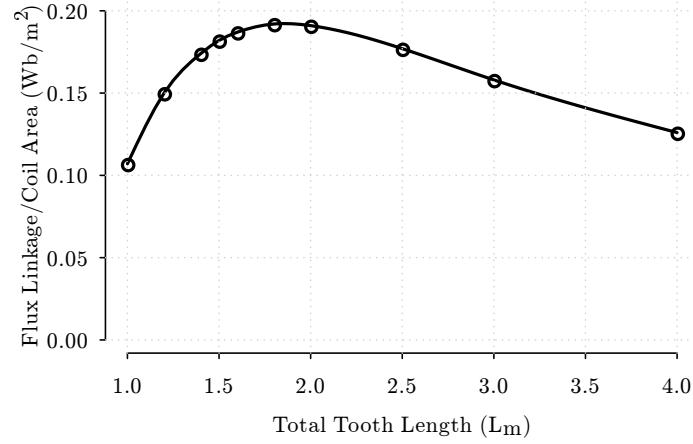
FEA simulations are performed with varying misalignment factor and results are presented as a function of the tooth length in figure 5.15. The cases are compared in terms of the ratio of flux linkage to coil area versus the tooth length. The optimum point occurs when the total tooth distance is  $1.8 L_m$ .

Figure 5.16 shows the air-gap flux density map, in which it can be seen that the maximum flux density in the air-gap is around 1.35 T, but the maximum and minimum flux densities are localized on each side of the gap. In order to maximize the flux linkage in the coil, the coil pitch ( $\tau_{coil}$ ) and the length of the coil ( $L_{coil}$ ) are varied. The coil thickness ( $t_w$ ) to coil pitch ( $\tau_{coil}$ ) ratio is assumed to be 0.3. The results are presented

<sup>1</sup>[\B:Chapter5/codes/varying\\_core\\_dimensions\\_plot.R](#)



**Figure 5.14:** Varying core misalignment ratio.



**Figure 5.15:** Simulations with varying misalignment factor.

in a contour map in figure 5.17. The maximum flux linkage is obtained with a coil pitch to pole pitch ratio of 1.32. This number is very close to  $4/3$ , in other words when the coil pitch equals to  $4\tau_{pole}/3$  the flux linkage is maximized. The flux density distribution in the armature coil is presented in figure 5.18.

### 5.3.2 Discussion of Results

In order to maximize the flux linkage in the armature coil, different core types are analysed. The simple core gives the best performance when the gap between poles is equal to the axial gap. Secondly, the misalignment factor of the cores is analysed. It is found that, the flux linkage is maximized when the total tooth length is  $1.8 L_m$  (i.e. when 20 % of the cores are overlapping). Flux densities up to 1.35 T are achieved in the air-gap (see figure 5.18). However, this value is concentrated to only a small section of the coil. Furthermore, the coil has some opposing flux, which reduces the net flux linkage in the coil.

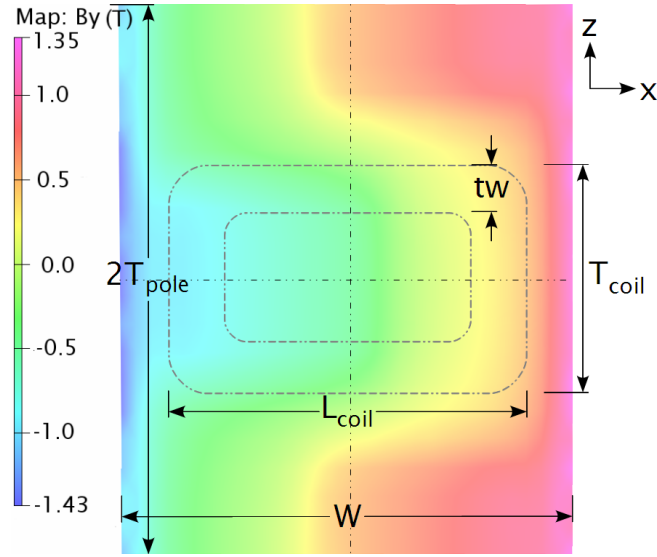


**Figure 5.16:** Flux density distribution in the air-gap and the placement of the armature coil.

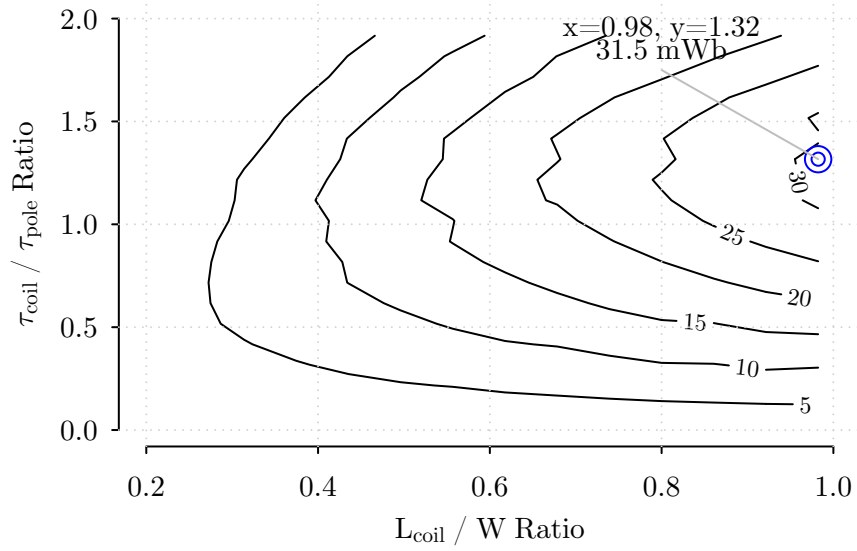


**Figure 5.17:** The contour map of the flux linkage in a single coil with varying coil pitch ( $\tau_{coil}$ ) and length ( $L_{coil}$ ).

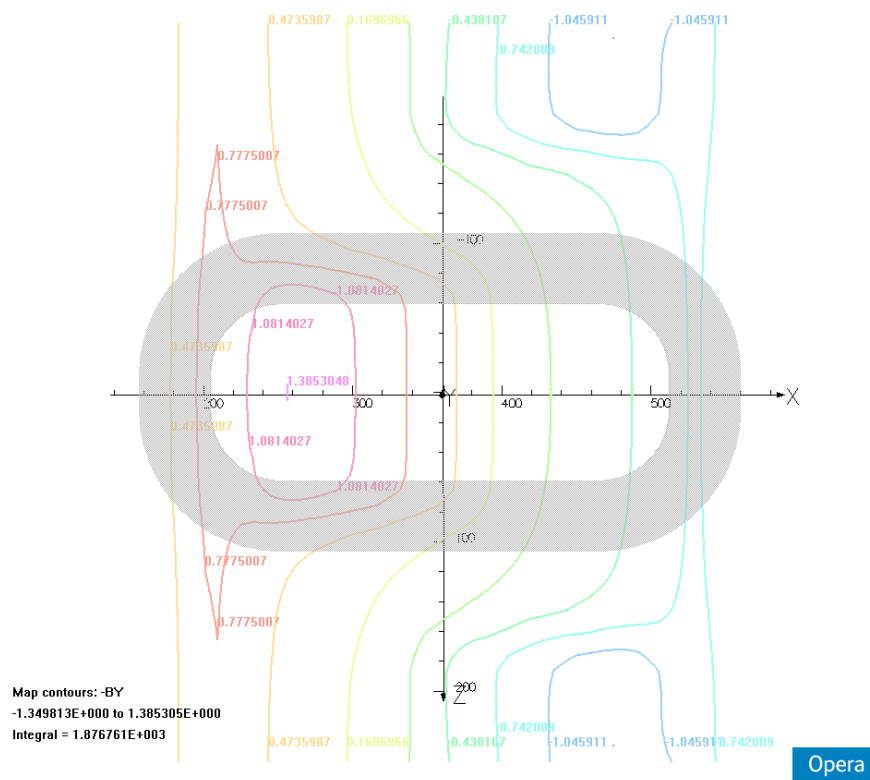


**Figure 5.18:** Flux-density distribution in the air gap. Shaded area shows the armature coil.



## 5.4 Chapter Summary

This chapter describes the bipolar superconducting machine topology, an improved version of the homopolar machine. The topology requires two separate superconducting coils to create bidirectional flux variation in the air-gap. A reluctance network model and 3D FEA simulation results are presented.

The results presented in this chapter are obtained from a few simulations without any global optimisation. Although, it is possible to improve the electromagnetic design, there are some mechanical challenges that should be addressed. First of all, it has two separate superconducting coils, which need to be connected to the armature coils. It is unclear that the air-cored armature coils are stiff enough to support this large structure. Secondly, the rotor is difficult to build. The inner magnetic cores are C-shaped and self supporting. However, the outer magnetic cores have to be attached to the inner magnetic cores with non-magnetic materials. The non magnetic material should be strong enough to cope with the magnetic attraction forces.

All these factors make this topology not suitable for high-torque, low-speed applications. Therefore, the axial-bipolar superconducting machine concept is also discarded. In the next chapter, a transverse flux claw pole superconducting machine will be presented.

# Design III: Claw Pole Transverse Flux Superconducting Machine

---

Two novel topologies have been proposed in the last two chapters. The stationary loop shaped superconducting coil, which simplifies the cooling system and can be easily manufactured, is the main feature of the concepts. Firstly, a homopolar superconducting machine topology has been presented, which has a robust structure, but the air-gap flux density varies between 1.3 T and 0.5 T, which results in low power density. The homopolar design has been modified by adding another superconducting coil, which enables bipolar magnetic flux distribution in the air-gap. However, the machine is mechanically not robust enough and requires two separate superconducting coils.

In this chapter, a novel topology is presented, which again uses a single loop-shaped superconducting coil, but achieves bipolar flux distribution due to its claw pole rotor structure.

## 6.1 Claw Pole Machines

Claw pole machines consist of a permanent magnet rotor and a single phase loop shaped armature coil. A cut-away view of such a machine is presented in figure 6.1a. The main flux path in the machine is illustrated in figure 6.1b. Claw pole machines have higher power densities than radial flux machines since the number of poles can be increased with the same MMF per pole [65]. They are primarily used as car alternators [41]. Claw poles machines can be considered as a specific type of transverse flux machine.

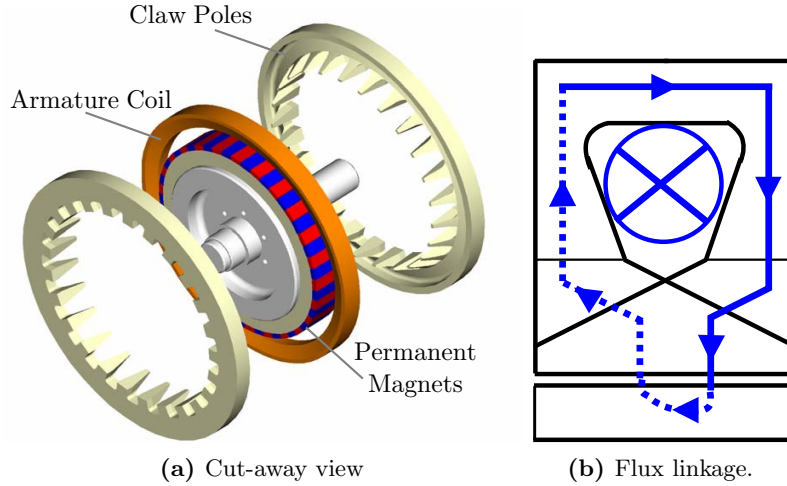


**Figure 6.1:** Single phase claw pole machine with permanent magnet rotor [70].

### 6.1.1 Transverse Flux Machines

Transverse flux (TF) machines are different from radial or axial flux machines, as the magnetic flux travels in a direction transverse to the direction of motion. A basic transverse flux permanent magnet (TFPM) machine topology is presented in figure 6.2. In [29, 104], different transverse flux topologies are reviewed; both studies give a good insight about TF machines. In [28, 131] radial and TFPM generators have been compared for direct-drive wind turbine power take-off systems. It has been stated that TFPM generators have a higher torque density than conventional machines because of their high number of poles [29], which becomes more evident at low speed applications. It should be noted that, the TFPM machines had similar torque densities with HTS machines in the comparison presented in figure 1.7, Chapter 1.

There are a few transverse flux superconducting (TFSC) machine designs. In a TFSC machine, the flux is created by the superconducting field winding instead of permanent magnets. Central Japan Railway Company and Musashi Institute of Technology have presented a novel topology in [168, 144], the cross-sectional view of which is presented in figure 6.3. The machine has a claw pole rotor, which modulates the magnetic flux created by the superconducting coil to create varying magnetic flux on armature coils. However, the machine is not suitable for low-speed applications and requires two separate superconducting coils. Another transverse flux superconducting topology is presented in [135, 134], which has been previously presented in section 3.8 and figure 3.30b. The topology requires excess amount of superconducting wire (750-1000 km) and uses rotating superconducting coils. In this chapter, a novel TFSC machine topology that eliminates the disadvantages of the existing designs will be presented.

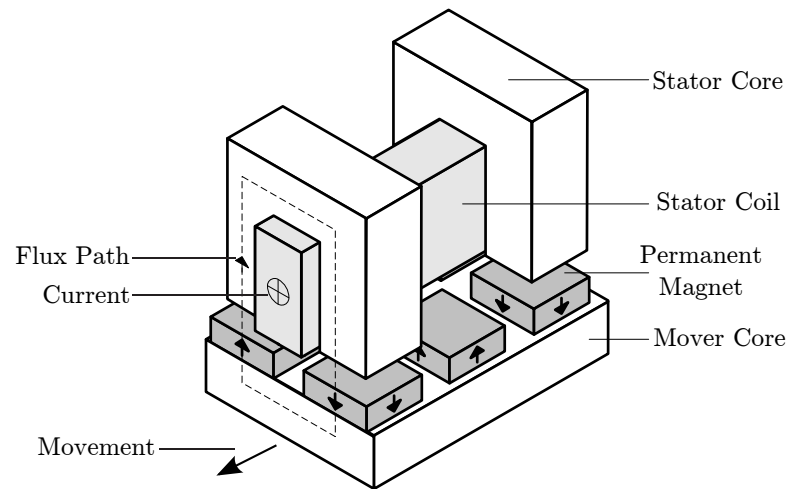


**Figure 6.2:** Basic single phase transverse flux permanent magnet topology [157].

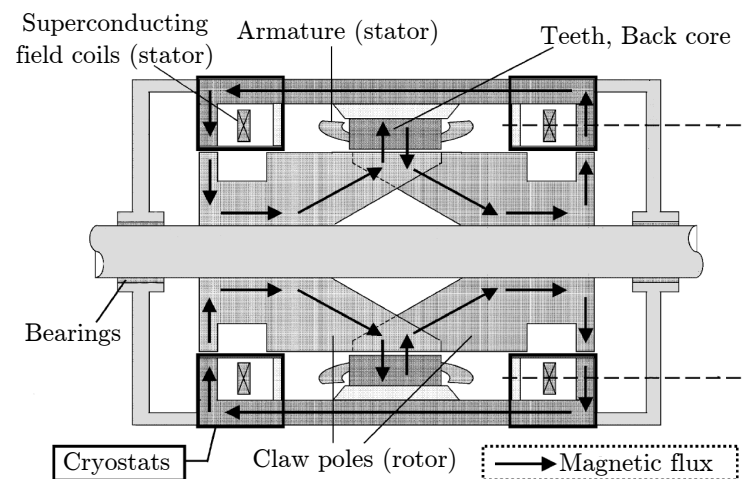


**Figure 6.3:** Cross-sectional view of the claw pole machine with double superconducting coils [168].

## 6.2 Proposed Claw Pole Topology

The proposed topology is similar to a conventional claw pole machine, but the field winding and the armature winding are swapped. The single phase armature coil in the conventional claw pole machine is replaced with a superconducting coil that functions as the field winding. The permanent magnet rotor is replaced with the armature winding. Figure 6.4 shows axial and vertical cross section views of the proposed machine with the main magnetic flux path, which takes the following route (starting from the claw pole on the left in figure 6.4a):

- Radially up to the outer stator through the claw pole,
- Tangentially through the outer stator to the adjacent claw pole,
- Radially down to the inner stator through the claw pole,
- Axially and tangentially through the inner stator to the bottom of adjacent claw pole.

Although, the machine has two radial air-gaps, which increases the equivalent reluctance of the machine, extra MMF required can be supplied by the superconducting coil. The topology consists of four main sections:

### 6.2.1 Superconducting Field Winding

Similar to the homopolar and the bipolar superconducting machines, the claw pole design also has a single stationary loop shaped superconducting field winding, which conducts direct-current. By this way, AC losses are eliminated in the coil and maximum current can be drawn from the superconducting coil. The simple design of the field winding reduces the complexity of the cooling and the electrical excitation system. As a result, brushless exciters and rotating transfer couplings are eliminated. Moreover, there are no transient torques and centrifugal forces acting on the winding which leads to a simpler winding support structure and minimized damage risk to the superconducting coil.

In figure 6.4, the insulation layers and cryocooler connections are not shown for simplicity. The cooling system will be discussed in section 6.6.2.

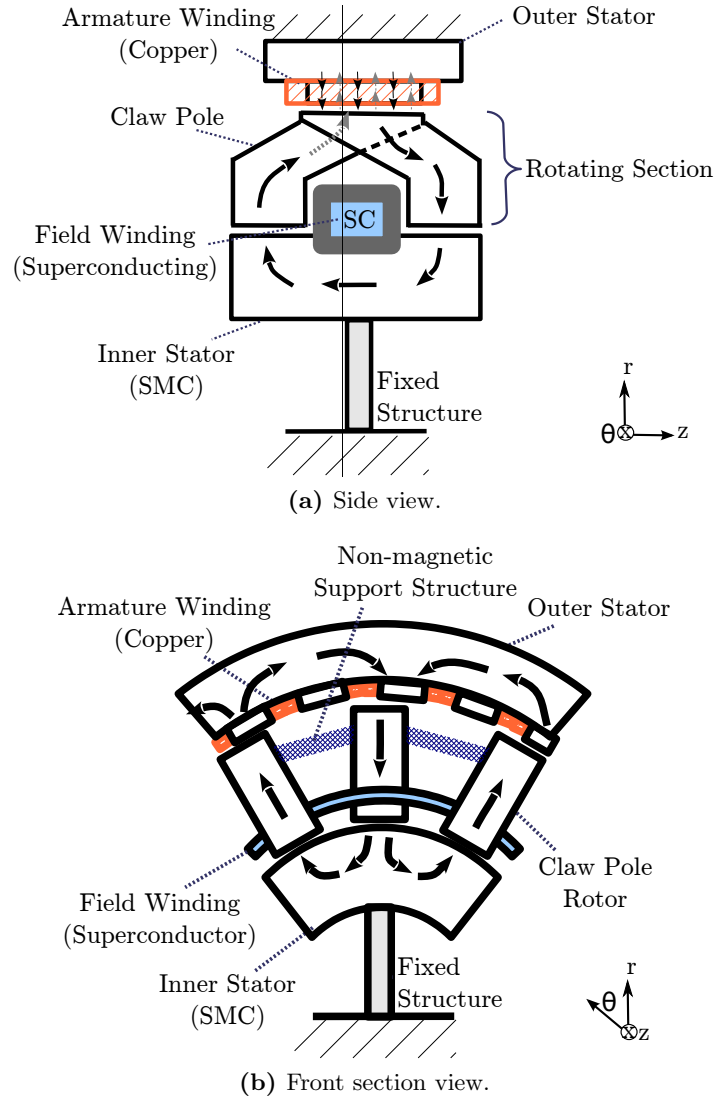


**Figure 6.4:** Basic schematic and flux lines in the claw pole superconducting machine.



**Figure 6.5:** Claw pole rotor made of soft magnetic composite material [177].

### 6.2.2 Inner Stator

The inner stator is the part that mechanically supports the superconducting field winding. It also functions as a back-iron for the magnetic flux, diverting the magnetic flux from one claw pole to the adjacent ones. The inner stator has a ring shape, but it can be divided into smaller sections.

It should be noted that, the flux in the inner stator travels in a three-dimensional way (i.e. in both axial and radial directions). Thus, it is not feasible to use electrical steel laminations. Instead, soft magnetic composite (SMC) material is preferred.

#### Soft Magnetic Composite (SMC) Materials

Soft magnetic composite materials are made of high purity iron powders. The manufacturing process includes coating and mechanical bonding of iron powders under pressure. The powder structure enables SMCs to have isotropic electromagnetic properties. As a result, SMCs are used in claw pole machines, transverse flux machines and any other type of electrical machine that exhibits true three-dimensional magnetic flux path. In figure 6.5 a claw pole rotor made of SMC material is shown.

SMC materials have high electrical resistivity owing to the insulating surface coating of iron powders. Thus, the eddy current loss is lower than electrical steel sheets, but the hysteresis loss is higher than electrical steel [64]. As a result, SMC materials are especially preferred for high frequency machines [68]. SMC materials have lower magnetic permeability than electrical steel, but this can be compensated with the extra MMF from the superconducting coil. A real challenge with the SMC materials is the reduced mechanical strength, which will be addressed in the following sections.

### 6.2.3 Rotor

The proposed machine has a variable reluctance rotor that consists of several modular claw poles. The claw poles are attached to each other with non-magnetic support structures. In figure 6.4, the mechanical support structure is not shown for simplicity, and the rotor appears to be hanging in air. Mechanical issues of the design will be discussed in detail in section 6.7. The single loop shaped superconducting coil creates uni-directional flux lines (e.g. clockwise in figure 6.4a) that travels through the claw poles. The claw poles on the left carry flux only upwards and the claw poles on the right carry flux downwards. Thus, each claw pole is magnetized in one direction and polarity does not reverse. Therefore, the eddy current losses in the claw poles are expected to be low.

The claw poles are made of laminated electrical steel. Laminations force the magnetic flux to travel in the radial direction and minimizes the leakage flux between adjacent rotor poles by increasing the reluctance in the tangential direction. It is also possible to manufacture claw poles with SMC materials to have more freedom in the claw pole shape as shown in figure 6.5. However, laminated steel is cheaper and easier to manufacture.

### 6.2.4 Outer Stator

The outer stator of the proposed topology is no different to the armature of a conventional machine. Although, in figure 6.4b a concentrated coil winding is presented, it is also possible to use an air-cored or distributed winding armature.

The outer stator is made of electrical steel laminations too, but the laminations are stacked in the axial direction. Laminations help to reduce eddy current loss and force the magnetic flux to travel in the tangential direction.

## 6.3 Analytical Model

Although, the finite element method is chosen as the primary analysis tool in this study, it is useful to model the machine analytically, which helps to quickly identify the relationship between various parameters in the machine.

A basic reluctance network representation of the claw pole machine is given in figure 6.6. In the figure the claw poles are shown in the same plane for simplicity, but in reality they are displaced as shown in figure 6.4b. The main flux path in the machine is defined in section 6.2, which has the following reluctance elements:

**$R_{is}$**  Inner stator reluctance, which represents the axial and radial path along the inner stator.



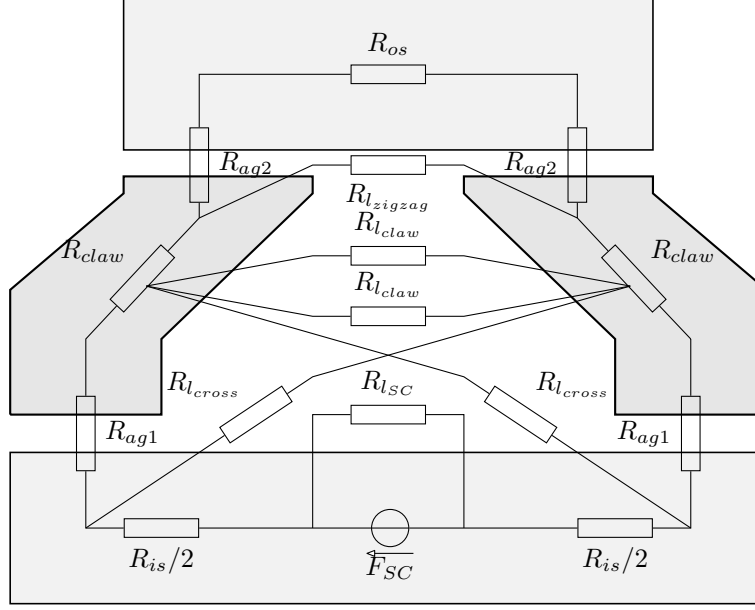


**Figure 6.6:** Basic magnetic circuit of the claw pole machine.

$R_{ag1}$	Inner air-gap reluctance.
$R_{claw}$	The claw pole reluctance. Although, this is represented as a single element in figure 6.6, it can be divided into sections as presented in Appendix C.3.
$R_{ag2}$	Outer air-gap reluctance.
$R_{os}$	Outer stator reluctance. This reluctance also includes the stator teeth reluctance.

The fact that the proposed machine has a larger equivalent air-gap than the conventional machines makes the amount of leakage flux more important. There are three main leakage flux paths in the machine, which are represented by the following reluctance elements:

$R_{lsc}$	Leakage flux reluctance around the superconducting field winding.
$R_{lclaw}$	Leakage flux reluctance between adjacent claw poles, which is the most important leakage flux term, as its value depends on the distance between claw poles and changes with number of poles. Note that, there are two $R_{lclaw}$ terms in the equivalent circuit. These represent the leakage flux on each side of the claw pole.
$R_{lzigzag}$	The zigzag leakage flux from upward face of the claw pole to the adjacent claw pole.
$R_{lcross}$	The leakage flux from the inner face of the claw pole to the opposite side of the inner stator.

The reluctances are calculated in Appendix C.3. A more detailed reluctance network model of a claw pole transverse flux machine can be found in [70].

### 6.3.1 Parameter Definition

At this stage, it is helpful to define the main parameters that will be used to model the proposed machine. In figure 6.7 the main dimensions for the claw pole, rotor section and full machine assembly are shown, which can be listed as:

$h_{gap}, w_{gap}$	Height and width of the superconducting winding (mm). These dimensions include the insulation and vacuum layers.
$h_{core}$	Height of the inner core (mm).
$w_{core}$	Width of the claw pole bottom limb (mm).
$SC_c$	The clearance between superconducting field winding and claw pole (mm).
$G$	Groove to fix the superconducting field winding (mm).
$a_c$	Air gap clearance (mm). The inner and outer air-gap clearances are the same.
$h_{claw1}$	The height of the straight section of the claw pole (mm).
$h_{claw}$	Total height of the claw pole (mm).
$d_l$	The length between corner and upper claw pole face (mm).
$w_{claw}$	Width of the upper claw pole face (mm).
$h_t$	Height of the claw pole shoe (mm).
$h_{backcore}$	Height of the armature backcore (mm).
$h_{coil}$	Height of the armature coil (mm).
$\theta_{pole}$	Pole pitch angle (radians).
$\theta_{coil}$	Coil pitch angle (radians).
$T_{core}$	Claw pole thickness (mm).
$R_{inner}$	Inner radius of inner stator (mm).
$R_{web}$	Inner web radius (mm). Radius at the outer surface of inner stator.
$R_{out}$	Outer radius (mm).
$L_{axial}$	Total axial length (mm).

## 6.4 FEA Simulations

The details of the finite element method and Opera software have been presented in Appendix D. For the first two topologies, the machine was first modelled with SolidWorks then the model file was exported to Opera Modeller, in which material properties are defined, the field excitation is applied and the mesh is constructed. Although, this work-flow is easy to implement, it is not really scalable to run many simulations in succession.

In this chapter, a parametrized model of the claw pole machine is developed using dimensions presented in figure 6.7. Script files for inner stator, claw poles, outer stator, armature coils and superconducting coils are developed. The script files import the

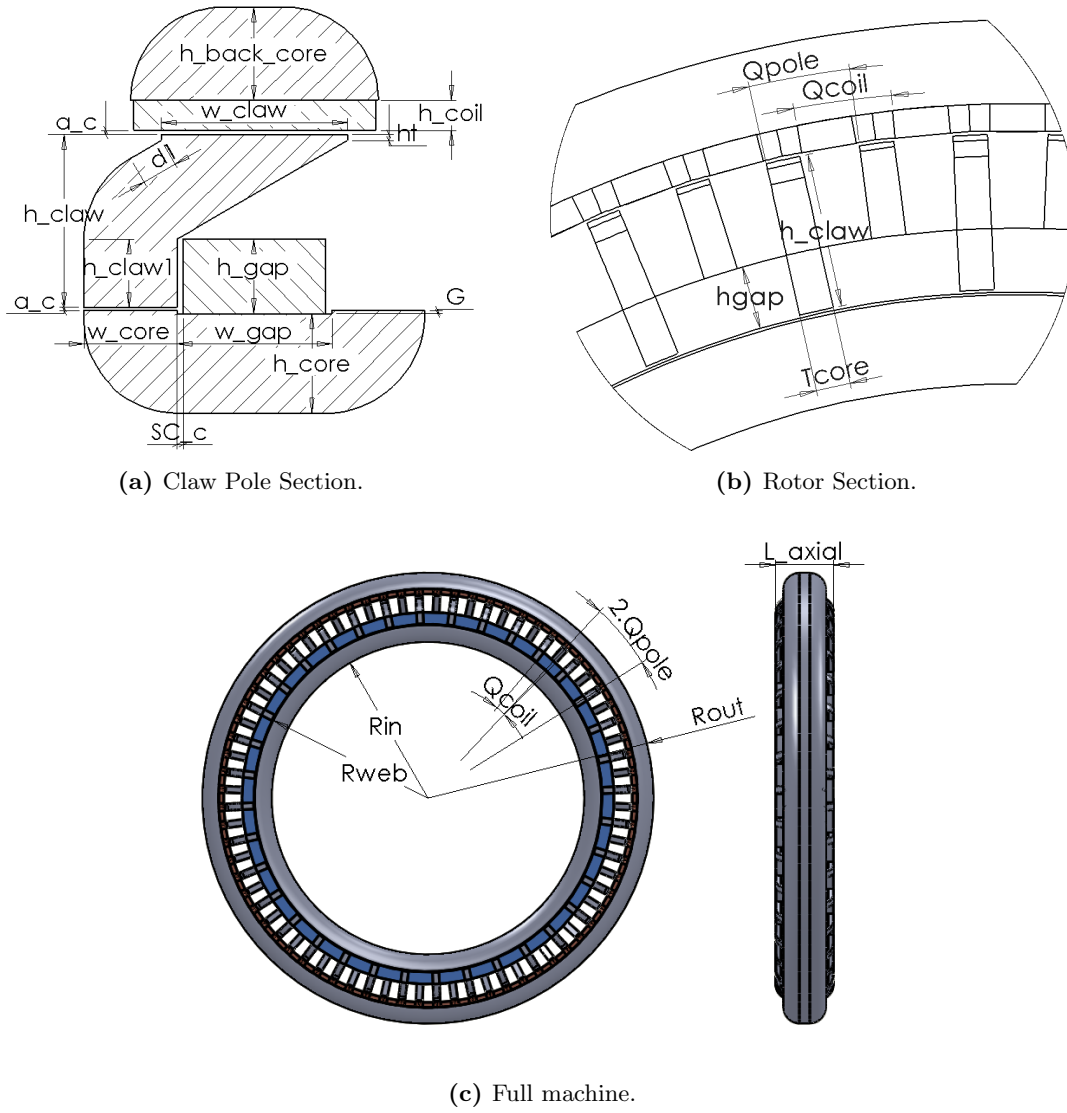


**Figure 6.7:** Main dimensions for the claw pole superconducting machine.

dimensions from an external file that defines all the dimensions. Then, all the sub-components are created separately and combined in a single model for meshing and analysis. The block diagram of the modelling method is presented in figure 6.8. The file types in the block diagram are:

- .txt: Text file
- .comi: Opera script file
- .opc: Opera 3D model file
- .bh: Material B-H data
- .op3: Opera 3D solved model
- .csv: Comma separated values (text file)

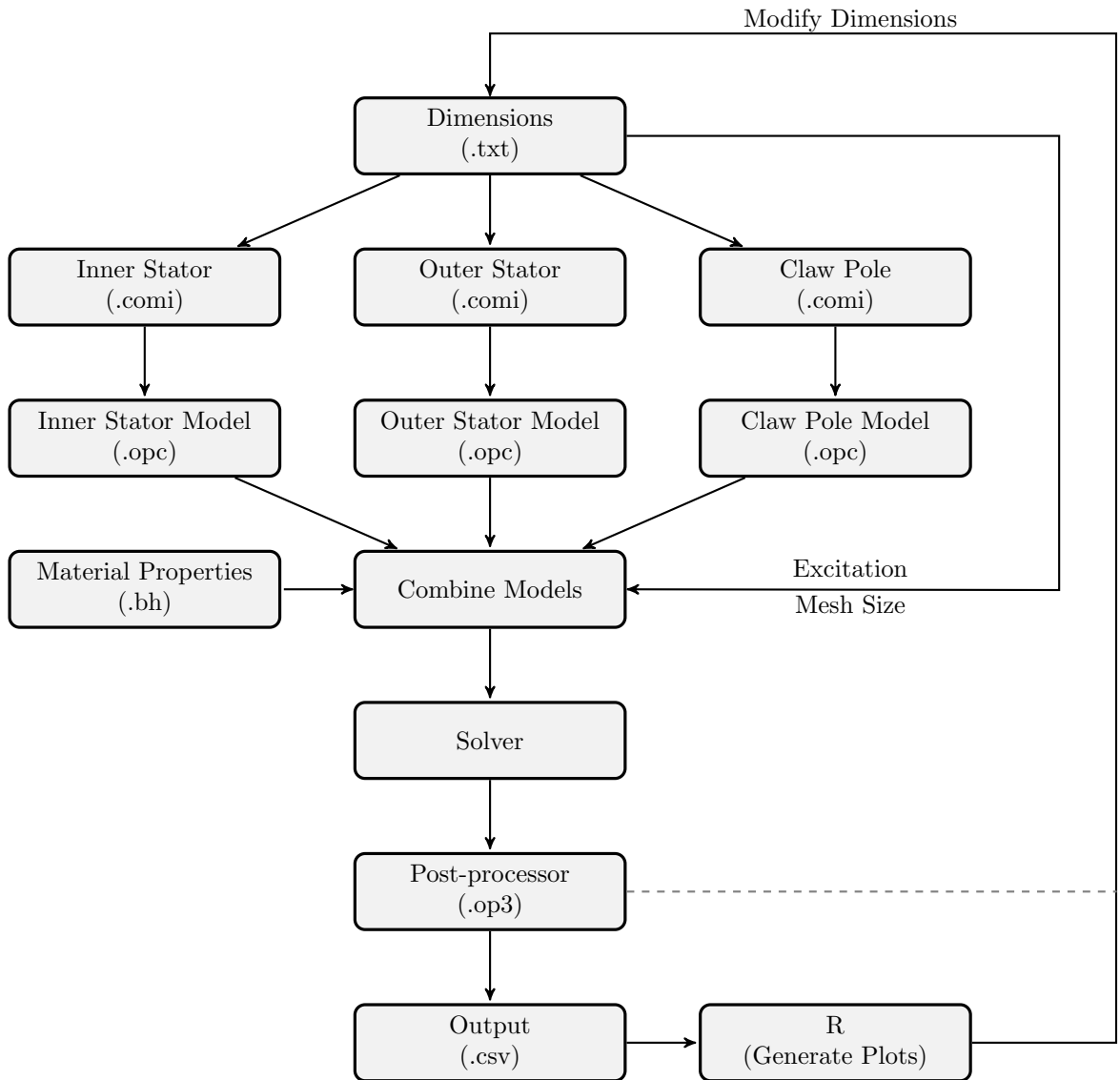


**Figure 6.8:** Block diagram for parametrized FEA analysis.

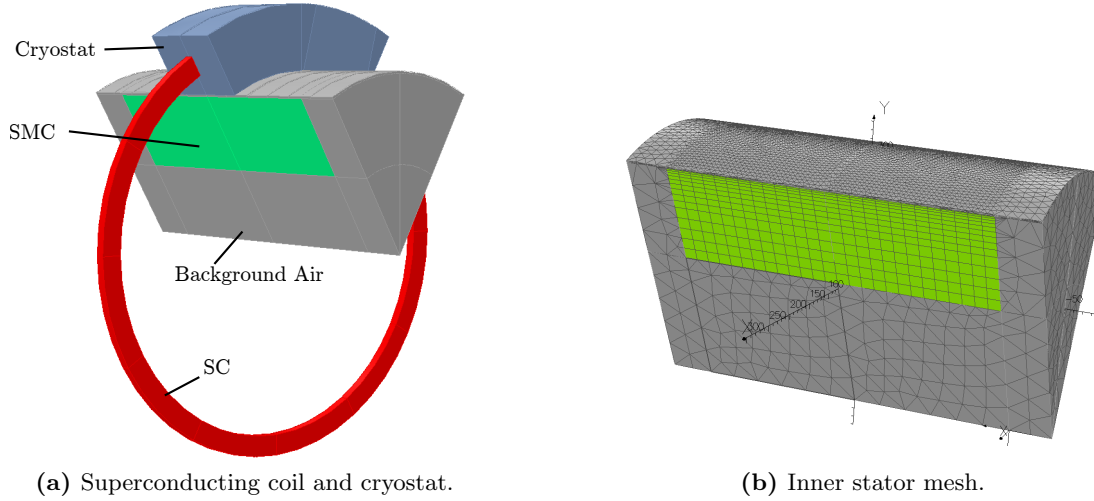


**Figure 6.9:** Modelling of the inner stator and the superconducting coil.

Although, the parametrization of each model requires a considerable amount of time to build, it minimizes the human intervention and reduces the design period in the long run. The most critical part of the modelling is to define consistent and realistic dimensions. Thus, a few algorithms have been developed to check consistency in each script.

The sub-components of the machine are modelled as follows:

#### 6.4.1 Modelling the Inner Stator

Only a section of the inner stator is modelled to benefit from the rotational symmetry. Although, modelling of the inner coil is fairly simple, the meshing is important for good accuracy. Outer surface is the most saturated part. Thus, the mesh size should be smaller at the outer surface as shown in figure 6.9, which uses hexahedra mesh in the inner stator and tetrahedra mesh in the surrounding air region.

As mentioned previously, the inner stator is made of SMC material. Höganäs manufactures three different SMC series: 1P baseline, 3P for high strength and permeability, and 5P for lowest losses [4]. 3P series are selected mostly for high mechanical strength. The 3P Somaloy series has three different products. The main properties of these materials are presented in table 6.1. Somaloy 700 series, having higher resistivity, are more suitable for high speed applications, where eddy current losses are significant. Somaloy 1000 has a low resistance, but the highest permeability. Thus, it has been selected as the most suitable option. The B-H characteristics of the Somaloy 1000 is presented in figure 6.10.

The superconducting coil is a direct-current driven solenoid shaped winding. The gap area includes the superconducting coil and surrounding insulation layers. The fill factor

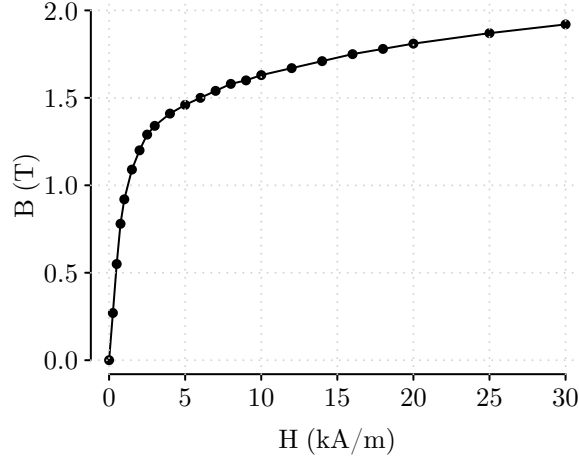


**Figure 6.10:** B-H curve for 3P Somaloy 1000 (Data from Höganäs AB).

Somaloy Material	Resistivity ( $\mu\Omega.m$ )	TRS (MPa)	B (T) @10kA/m	$\mu_{max}$	Core Loss @1 T (W/kg)		
					100 Hz	400 Hz	1000 Hz
3P 700	200	125	1.61	750	10	46	137
3P 700HR	600	120	1.57	630	11	48	137
3P 1000	70	140	1.63	850	10	46	144

**Table 6.1:** Properties of Somaloy 3P SMC materials [67].

of the superconducting winding, including the vacuum and the cryostat, is around 0.03–0.05 depending on the MMF requirements. The cryocooler connection of the superconducting winding is not included to simplify the FEA model, but it will be discussed in section 6.6.2.

The superconducting coil is modelled as a Biot-Savart conductor in FEA simulations. The Biot-Savart conductors are not part of the 3D mesh, and the field around the superconducting winding is calculated using Biot-Savart law [9]. It is also possible to mesh the superconducting coils and to make a coupled thermal electromagnetic analysis, but these types of simulations are not covered in this study.

#### 6.4.2 Modelling the Claw Pole

The claw pole transfers the magnetic flux from the inner stator to the armature coils. The claw poles are made of steel laminations stacked in tangential direction, which are shown with 3D mesh in figure 6.11. The claw poles are modelled using several dimensions, so it is possible to have claw poles with very different aspect ratios as shown in figure 6.12.

The air-gap is the most important part in the FEA model as the equivalent reluctance of the machine is dominated by the air-gap reluctance. It is therefore necessary to use

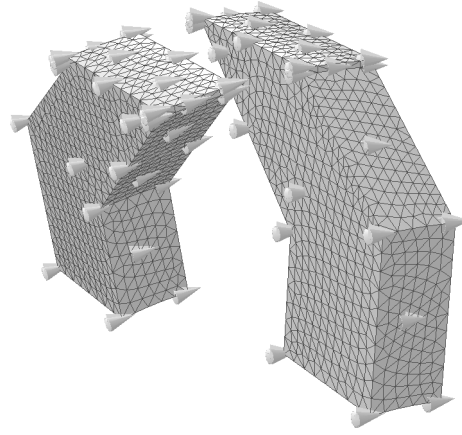


**Figure 6.11:** Claw pole mesh and lamination direction.

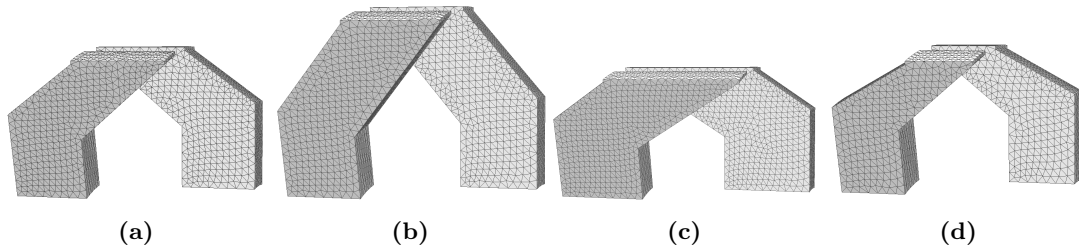


**Figure 6.12:** Claw poles with different aspect ratios.

a fine mesh in the air-gap to get accurate field estimations. A method is to use mesh layering in the air-gap (i.e. dividing the air-gap into sections in the radial direction). The air-gap is divided into three or four layers in the modelling process.

### 6.4.3 Modelling the Outer Stator

The outer stator of the proposed machine is similar to the conventional machines. A concentrated coil or distributed coil type stator can be used as shown in figure 6.13. The outer stator is also made of laminated steel, but the laminations are stacked in the axial direction.

Non-grain oriented M270–50A type electrical steel, which is specifically designed for large scale machine applications, is used in the claw poles and the outer stator. The B-H characteristics of the material is presented in figure 6.14, and other specifications can be accessed from ThyssenKrupp Steel AG catalogue [159]. Alternative lamination materials are M700–100A or M250–50A, which also have reasonable performances.

After all the subcomponents are created, they are combined in a single model which is presented in figure 6.15. It is possible to model a claw pole with varying dimensions

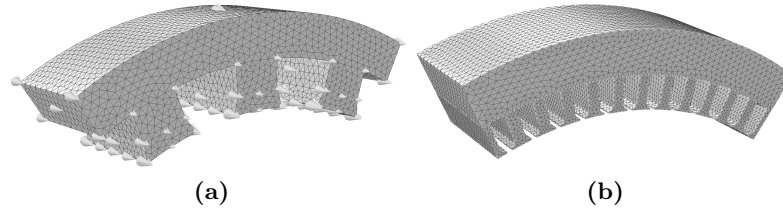


**Figure 6.13:** Meshing of the outer stator core with concentrated and distributed winding.

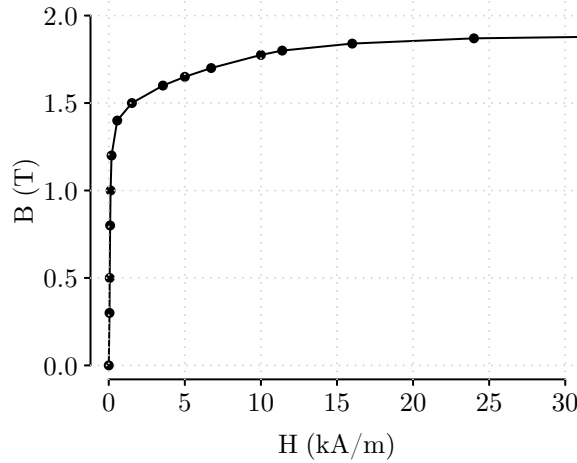


**Figure 6.14:** B-H curve for M270-50A electrical steel, which is used in claw pole and outer stator models (Data from [159]).

using the parametrized model. It is also possible to skew the stator coils if required; such a model is presented in figure 6.15c

## 6.5 Design of a Rotary Prototype

In this section, a small prototype is designed to prove the claw pole superconducting machine concept. There are several variables that can affect the machine's performance such as: number of poles, claw pole dimensions, winding configuration, MMF in the superconducting coil etc. Several FEA simulations are performed to analyse the effect of these parameters. During the analyses, the specific magnetic loading is measured. The details on specific magnetic and electric loading are presented in Appendix F.

Throughout this chapter, two different designs are used, the main dimensions of which are presented in table 6.2. Design-A is a 250 rpm machine. Design-B is the second design with improved dimensions. Design-B is slightly smaller than Design-A, and it is specifically designed for the existing induction motor driven 100 rpm, 30 kW test-rig at University of Edinburgh.



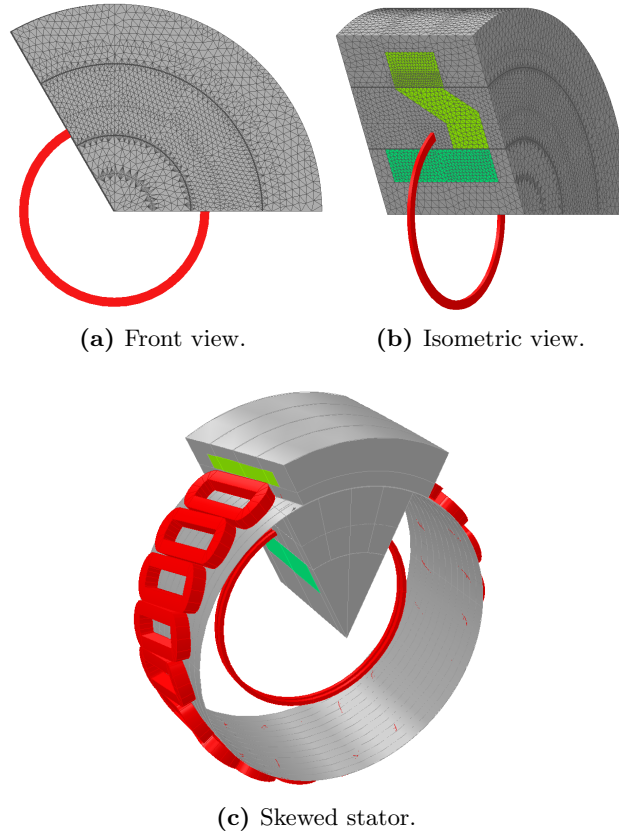


**Figure 6.15:** Full FEA model of the claw pole machine.

	Design-A Initial Design 250 rpm	Design-B Improved Design 100 rpm
$R_{out}$	640	592
$L_{axial}$	380	320
$R_{in}$	175	100
$a_c$	2.5	2.5
$w_{core}$	120	110
$h_{core}$	125	100
$w_{gap}$	140	100
$h_{claw}$	225	187
$w_{claw}$	150	150
$h_{backcore}$	60	60
$h_w$	50	40
$h_{sc}$	15	15
$w_{sc}$	12	12

**Table 6.2:** Dimensions of the two designs used in simulations.

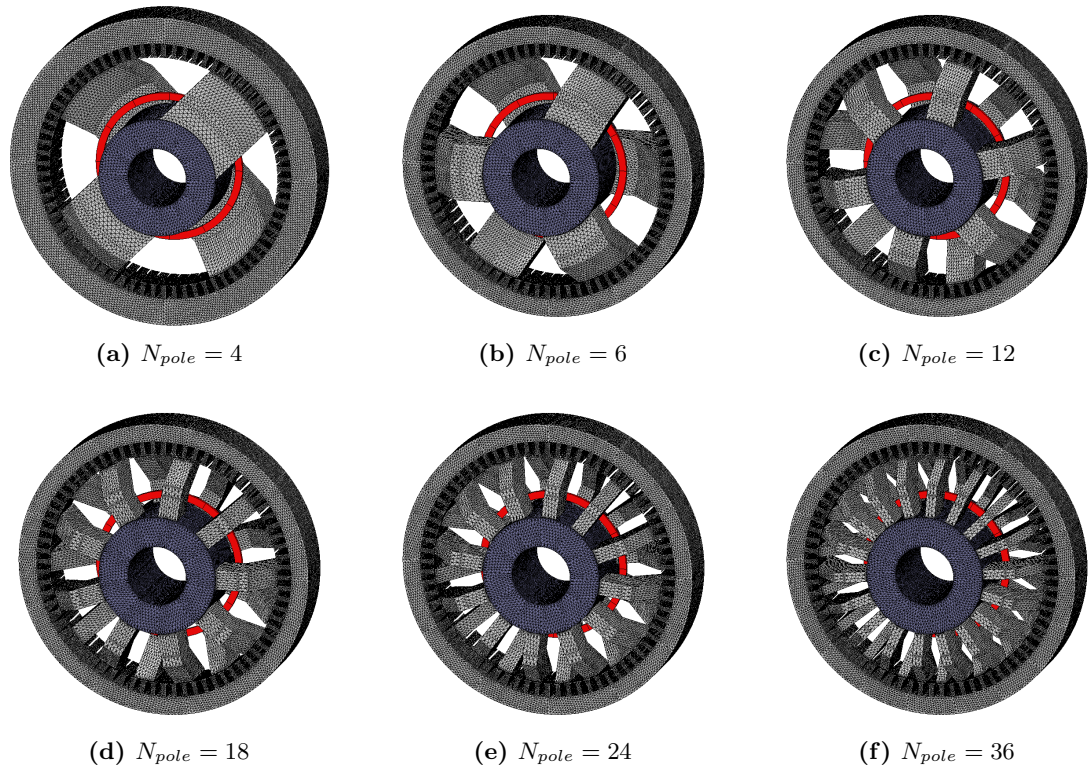


**Figure 6.16:** Models with varying number of poles.

The data and simulation files used in this study can be accessed using the methods described in Appendix A and the results can be reproduced and models can be modified. The path to model files and output logs for each simulation are listed as footnotes.

### 6.5.1 Varying Pole Number

The number of poles has a direct effect on the machine's torque capability; low speed, high torque machines usually have higher number of poles. However, the leakage flux is higher in machines with a high number of poles.

The number of poles is varied from 4 to 36 and the flux density distributions in the air-gap and stator teeth are recorded<sup>1</sup>. The models with mesh are presented in figure 6.16. The flux density magnitude and radial flux density distribution in the machine are shown in figure 6.17 and figure 6.18. The radial flux density waveform at the air-gap and mean armature winding radius are plotted in figure 6.19.

The maximum flux density in the stator teeth, magnetic loading at the air-gap, magnetic loading at mean armature winding radius are presented in table 6.3. The magnetic loading values in the table are illustrated in figure 6.20. The maximum magnetic loading

<sup>1</sup>[📁:Design-B: 0pera\\_logs\\_graphs/2013/2013\\_02\\_28\\_distributed\\_winding\\_varying\\_Npole/](#)

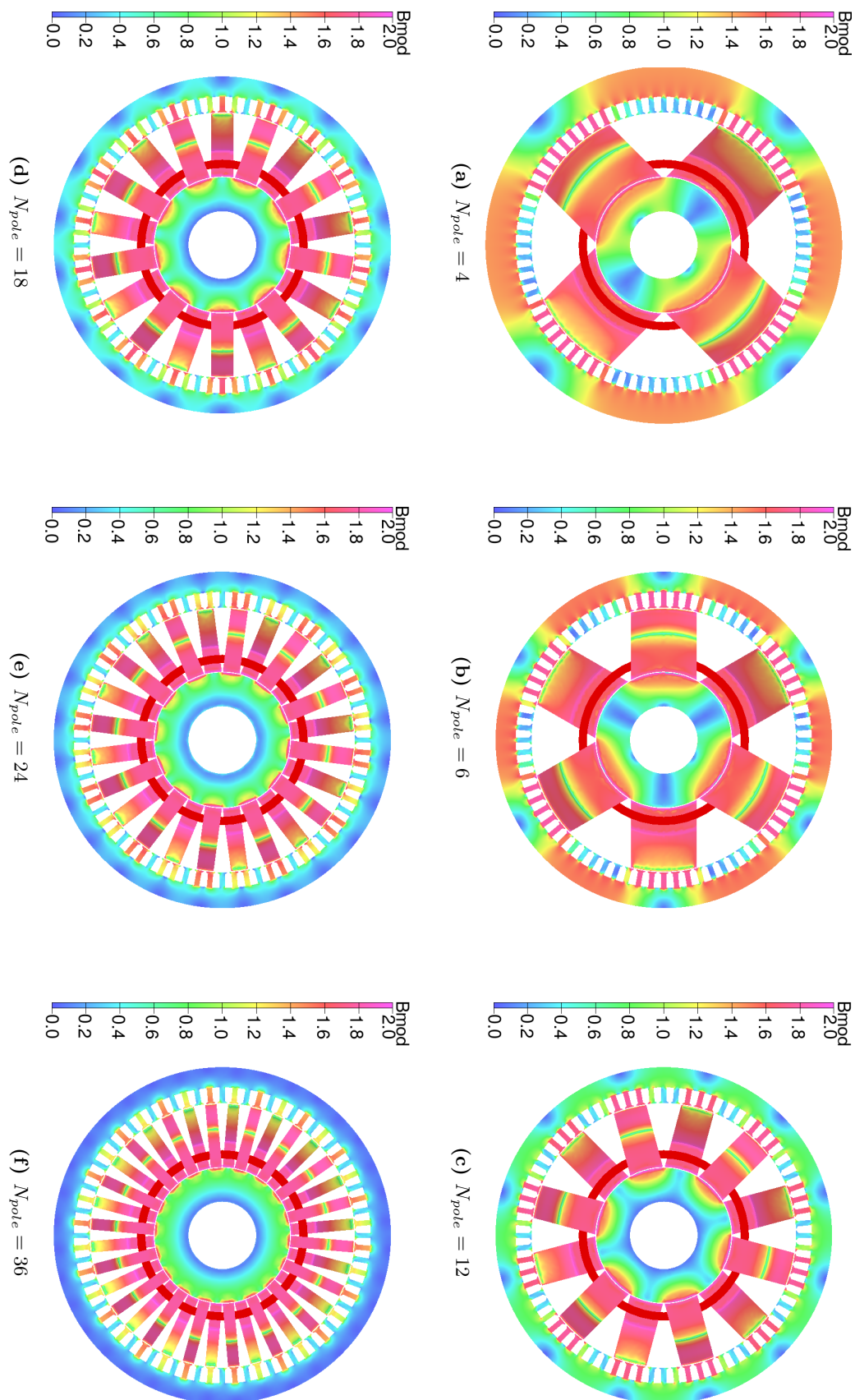


**Figure 6.17:** Magnetic flux density magnitude in the claw pole machine with varying pole number.

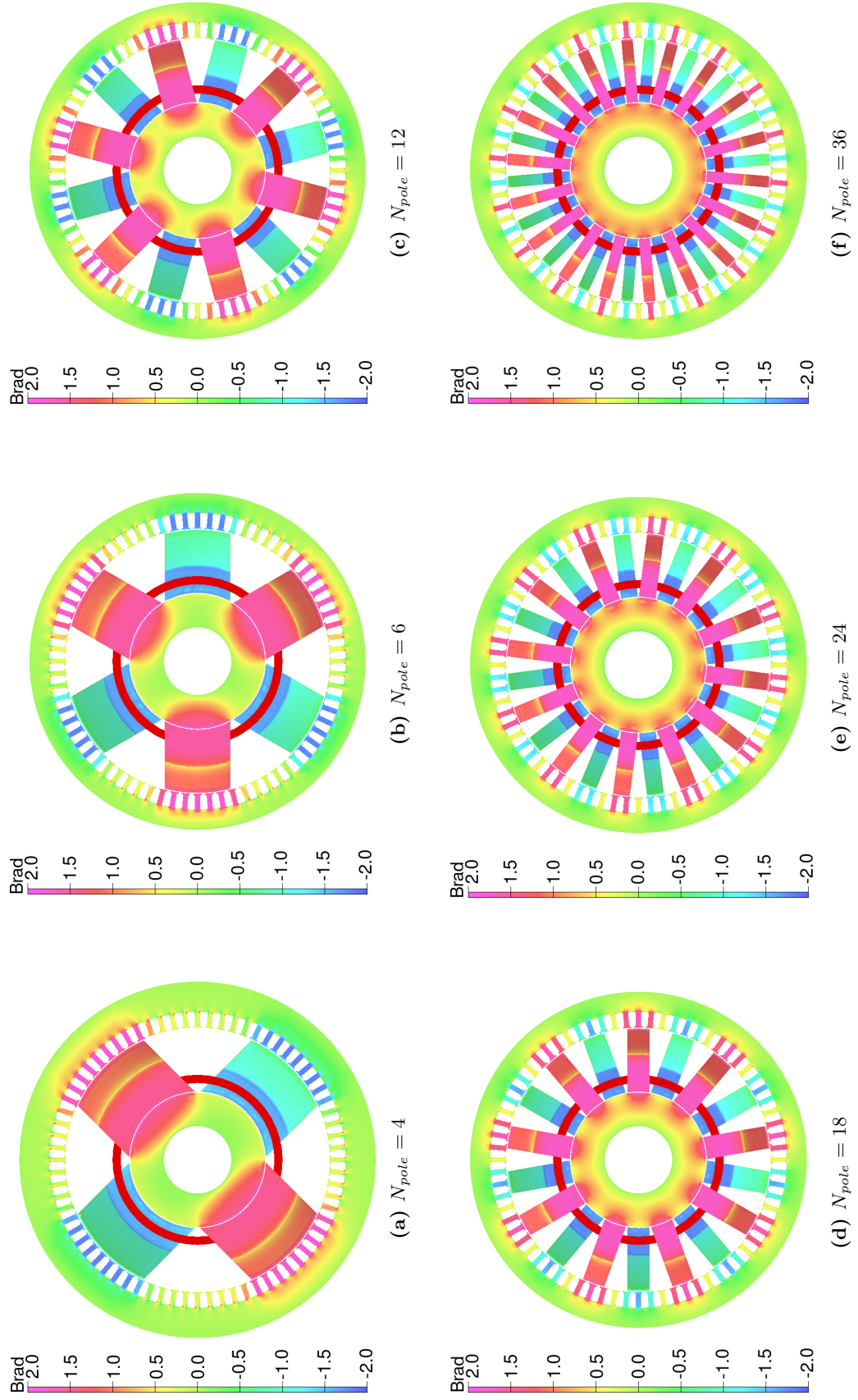


**Figure 6.18:** Radial magnetic flux density distribution in the claw pole machine with varying pole number.

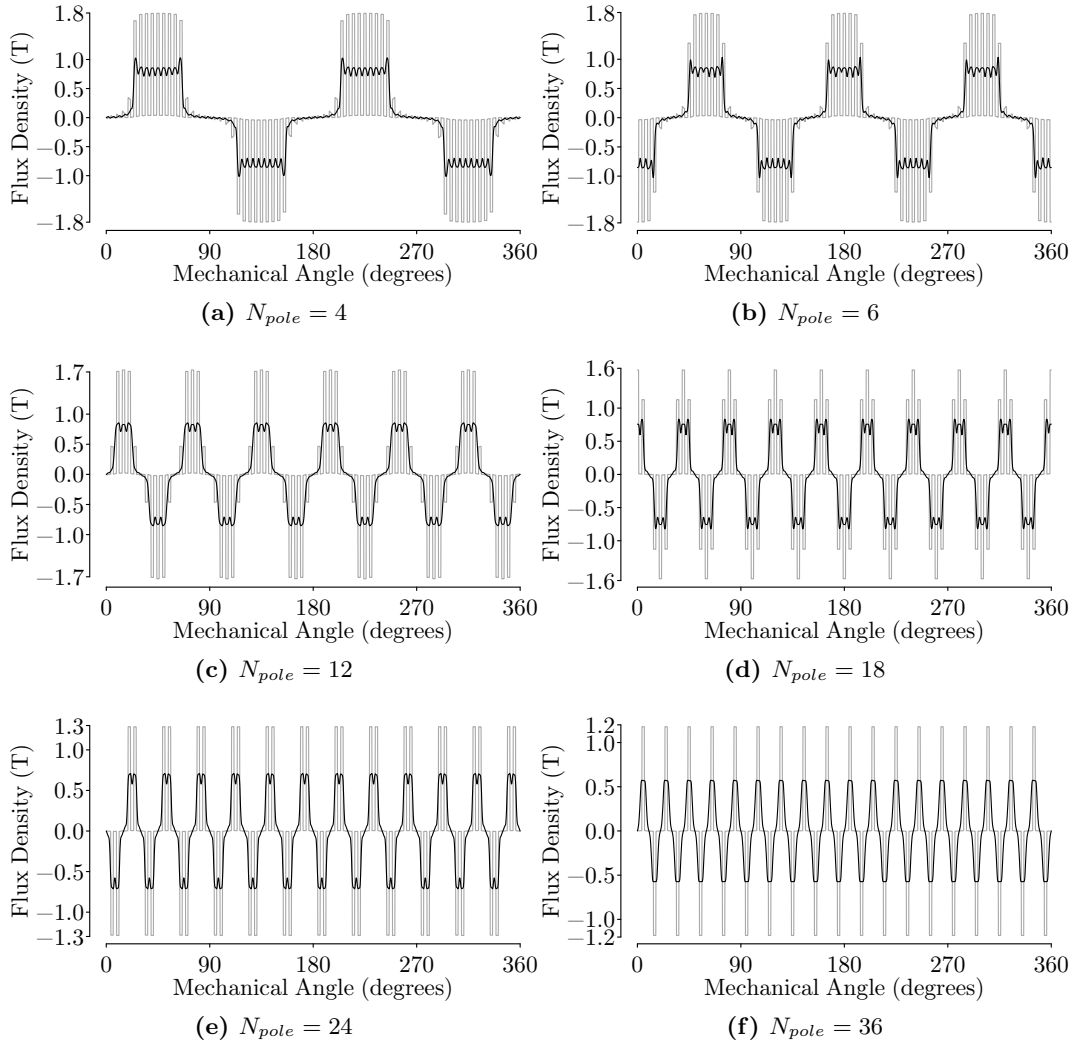


**Figure 6.19:** Radial magnetic flux density distribution in the claw pole machine with varying pole number (Black line: air-gap flux density. Grey line: tooth flux density).

is achieved with 12-pole configuration. However, this value is not a global optimum value, but varies with machine dimensions (in particular with the air-gap radius). There are two important factors that the simulations revealed. Firstly, the magnetic loading for very small pole numbers is low, even though the tooth flux density is maximum. This is due to the fact that when the pole number is small, the gap between claw poles is large which creates some electromagnetically inactive parts in the stator as can be seen from figure 6.18a. Secondly, as the number of poles is increased, the distance between claw poles decreases, which increases the leakage flux between claw poles lateral faces ( $R_{l_{claw}}$  in figure 6.6) and reduces the flux linkage in the stator teeth. Another interesting point is the difference between magnetic loading calculated at the air-gap and magnetic loading calculated at the stator teeth. For low number of poles, there is no difference

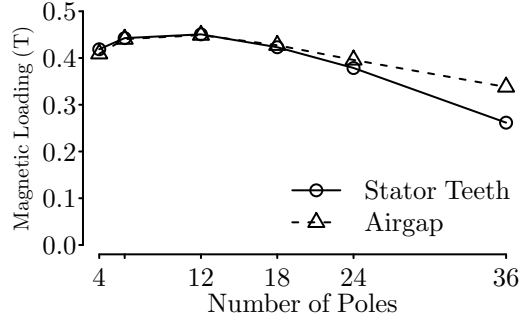


**Figure 6.20:** Specific magnetic loading variation with number of poles.

between the two values, but as the number of poles is increased the magnetic loading at the stator teeth gets smaller than the magnetic loading at the air-gap. This is because of the zigzag leakage flux ( $R_{l_{zigzag}}$  in figure 6.6).

Number of Poles ( $N_{pole}$ )	4	6	12	18	24	36
Max. Tooth Flux Density ( $\hat{B}_{tooth}$ )	1.79 T	1.79 T	1.73 T	1.57 T	1.29 T	1.18 T
Magnetic Loading at Air-gap ( $\bar{B}_{ag}$ )	0.41 T	0.44 T	0.45 T	0.43 T	0.40 T	0.34 T
Magnetic Loading at Stator ( $\bar{B}_{st}$ )	0.42 T	0.44 T	0.45 T	0.42 T	0.38 T	0.26 T

**Table 6.3:** Number of poles vs. magnetic loading and maximum tooth flux density.

### 6.5.2 Flux Density in the Inner Core

The main bottleneck for the proposed design is saturation in the magnetic core. In particular, the flux density in the inner core, where the superconducting coil's flux is diverted, should be evaluated carefully. In figure 6.21 the radial flux density distribution at the surface of the SMC material is illustrated. The maximum flux density is around 1.8 T and does not change much with the pole number.

Although, the difference between inner radius ( $R_{in}$ ) and outer radius ( $R_{out}$ ) is not significant for large diameter machines, it becomes important for smaller machines as it limits the inner stator surface area and results in higher flux density. One option to increase the flux linkage is to increase the area between claw pole and inner stator by increasing the claw pole bottom width and thickness ( $w_{core}$ ,  $t_{core}$ ).



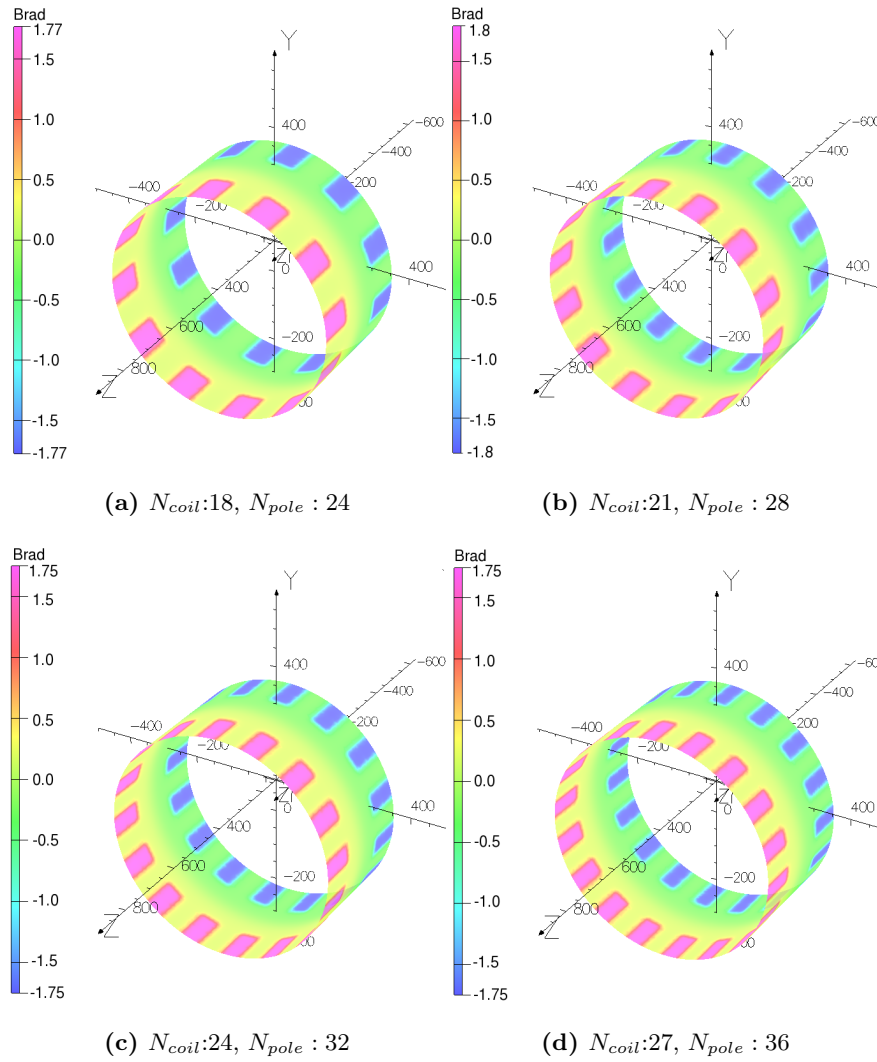


**Figure 6.21:** Radial flux density in the inner stator (surface of the SMC material) with varying pole number.

### 6.5.3 Varying Core-to-Pole Pitch Ratio

In this section, the effect of core-to-pole pitch ratio is investigated. Rotating simulations are performed using Design-A with 18 stator slots and 12 poles<sup>2</sup>. The front view and isometric mesh view of the machine is presented in figure 6.22. The core-to-pole pitch ratio is varied from 0.70 to 0.95 (see figure 6.23) and the induced voltage and rotor torque is calculated at 100 rpm with 10  $\Omega$  resistive load<sup>3</sup>. The rotational speed profile is presented in figure 6.24a.

In table 6.4 the simulation results are summarised. The current densities in the armature

<sup>2</sup>Ⓔ:Design-A: Opera\_logs\_graphs/2011/2011\_09\_02\_high\_coil\_to\_pole\_ratio

<sup>3</sup>Ⓔ:Design-A: Opera\_logs\_graphs/2011/2011\_09\_21\_100rpm\_varying\_core\_pole/

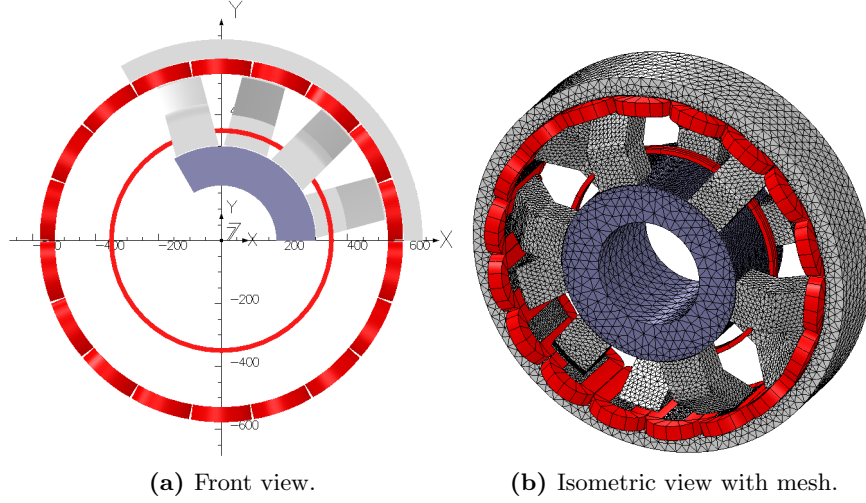


**Figure 6.22:** The small prototype model.

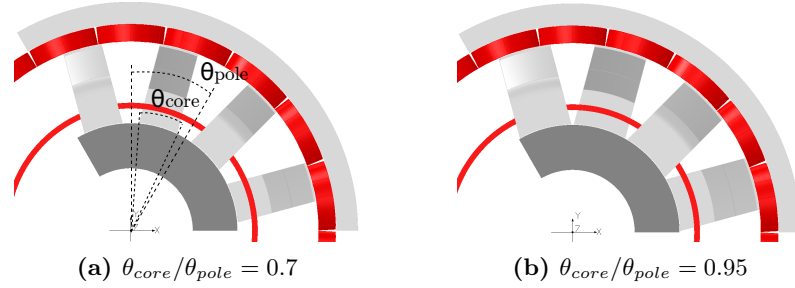


**Figure 6.23:** Varying core to pole ratio.

are calculated assuming a fill factor of 0.65 and the conductor area per coil is  $1825 \text{ mm}^2$ . The specific electrical and magnetic loading data are also presented in table 6.4.

From the table it can be seen that the power of the machine increases with core-to-pole ratio. From 0.7 to 0.95 the power increased by 56 %, but it should be noted that the simulations are performed with a constant resistive load, so the electric loading of the machine is not constant but proportional to the phase voltages. Therefore, it is better to compare the magnetic loading, which is increased by 24 %. As the core-to-pole ratio is increased the distance between claw pole reduces, which increases the leakage flux between claw poles. However, a thicker claw pole can carry more magnetic flux increasing the magnetic loading of the machine. Note that, the surface area of the claw pole is increased by 35 % from 0.7 to 0.95, but the magnetic loading is increased just by 24 % which implies an increase in the leakage flux.

The phase voltage waveform for a core-to-pole ratio of 0.95 is presented in figure 6.24. Power variation from a core-to-pole ratio of 0.7 to 0.95 is presented in figure 6.24c. The voltage waveform is not perfectly sinusoidal, which induce torque harmonics.



Core to Pole Pitch Ratio	0.70	0.75	0.80	0.85	0.90	0.95
Mean Power Output (kW)	43.9	47.9	52.9	57.9	62.7	68.7
Mean Torque (Nm)	4196	4583	5055	5531	5993	6567
Phase Voltage ( $V_{rms}$ )	382	403	424	444	462	480
Phase Current ( $A_{rms}$ )	38.2	40.3	42.4	44.4	46.2	48.0
Current Density ( $A/mm^2$ )	2.09	2.21	2.33	2.44	2.53	2.63
Electric Loading (kA/m)	41.3	43.6	45.8	48.0	49.4	51.8
Magnetic Loading (T)	0.357	0.369	0.386	0.404	0.421	0.444

**Table 6.4:** Torque, phase voltage and output power variation with core-to-pole pitch ratio.

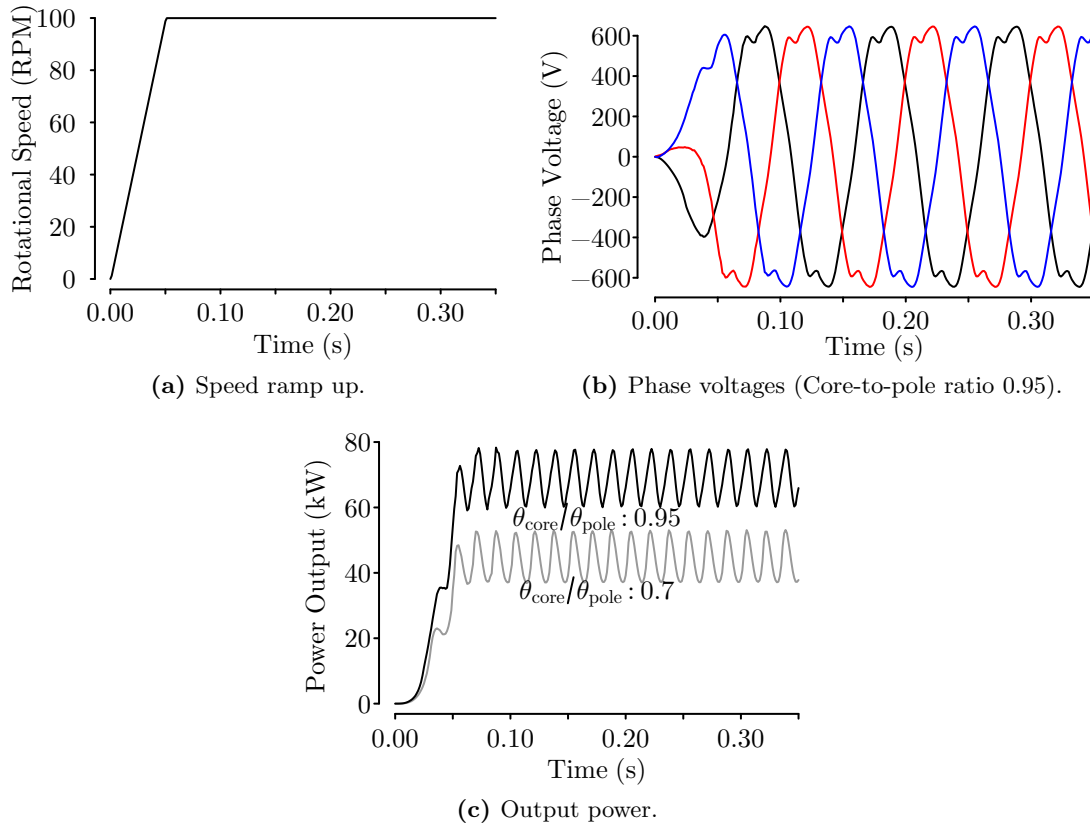


**Figure 6.24:** The rotational speed, output power and phase voltages for the small prototype.

#### 6.5.4 Varying Superconducting Coil MMF

In a superconducting machine, the required length of the superconducting tape has a significant impact on the overall cost, hence the minimum length of superconducting coil is desirable. The power output of the machine is proportional to MMF of the field winding, until the magnetic core saturates. The MMF in the field winding coil is varied from 10.8 kAt to 32.4 kAt. Design-B<sup>4</sup> is used for simulations, the main dimensions of which are presented in table 6.2.

The flux density distribution in the machine with varying MMF is presented in figure 6.26. The phase voltage versus the field winding MMF is plotted in figure 6.25 and tabulated in table 6.5. From the figure it can be seen that, the core starts saturating after 18 kAt, and increasing the MMF further to 25 kAt slightly changes the induced phase voltage. Therefore, 18 kAt is chosen as the optimum MMF for the radial prototype, which generates 25 kW at this field current.

Field Winding MMF (kAt)	10.8	14.1	18	21.6	27	32.4
Power Output(kW)	10.9	18.1	25.2	30.8	34.0	35.6
Phase Voltage ( $V_{rms}$ )	147.5	190	224.4	248.2	260.6	266.8
Ratio of Voltage to MMF	13.66	13.20	12.47	11.49	9.65	8.24

**Table 6.5:** Variation of phase voltage at no-load with field winding MMF (with 6  $\Omega$  resistive load).

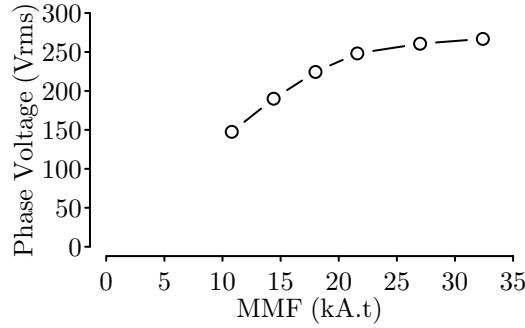


**Figure 6.25:** Variation of phase voltage at no-load with field winding MMF.

<sup>4</sup>📁:Design-B: Opera\_logs\_graphs/2011/2011\_09\_30\_varying\_mmf/

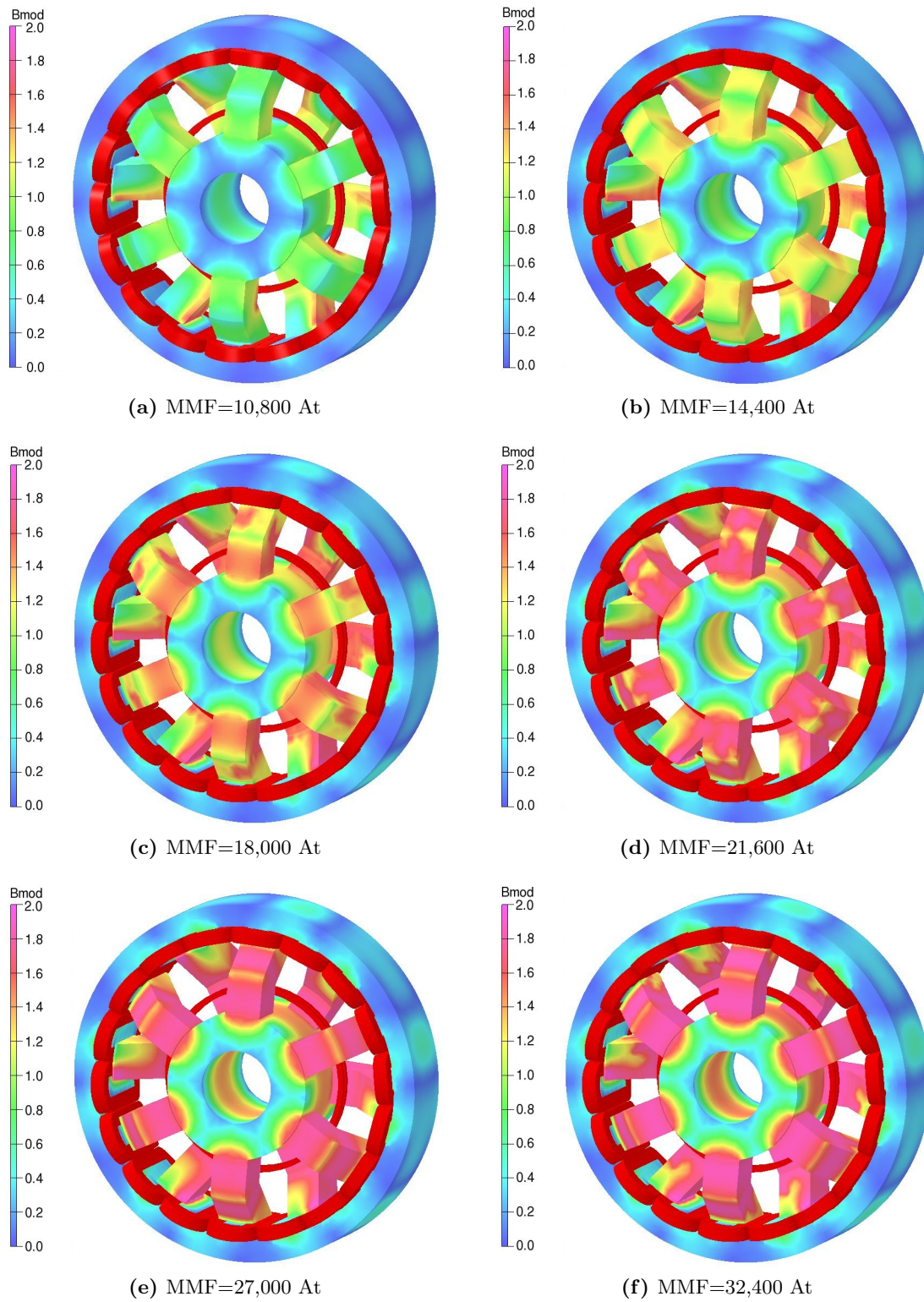


**Figure 6.26:** Magnetic flux density variation in the machine with field winding MMF

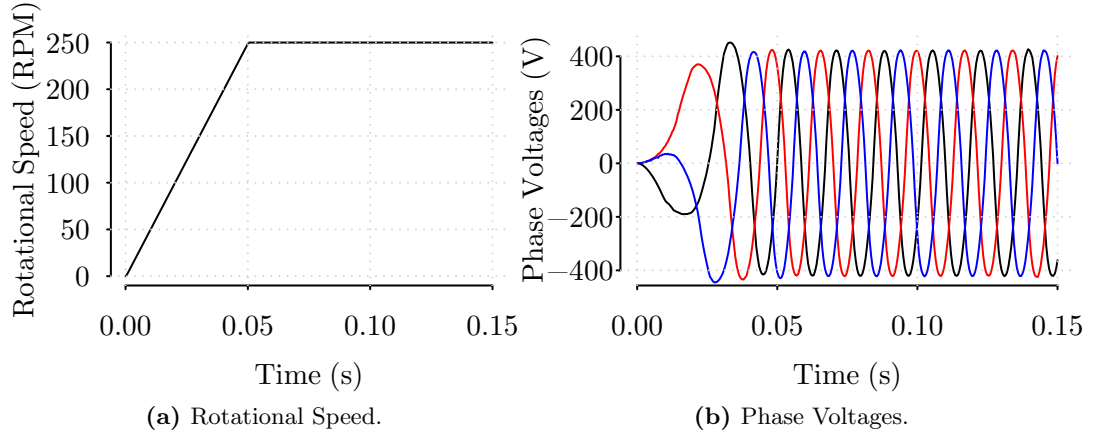


**Figure 6.27:** The rotational speed profile and the phase voltage.

### 6.5.5 Cogging Torque

From figure 6.24c it can be seen that the power fluctuation of the machine is quite large, which is also evident as cogging torque. In literature, there are studies aimed at minimizing the cogging torque [172, 179, 73]. The most common method is to choose the number of slots and poles accordingly so that any unwanted torque harmonics will cancel each other. One way of achieving that is to use a number of slots and poles that have a large least common multiple [73]. Thus, the number of slots and number of pole configurations such as 18–12, 18–24, 27–36 are not very good choices in terms of cogging torque, because these configurations have small common multiples. However, having small common multiples of slot and pole numbers creates rotational symmetries. For example, in the 18–12 configuration there is a 60 degrees symmetry, so that only  $1/6^{\text{th}}$  of the machine needs to be modelled. If the number of poles is selected as 22, then there will be no rotational symmetry and the whole machine has to be modelled. This is a big drawback for this study, since the main analysis method is 3D FEA, which is computationally demanding. Therefore, it is beneficial to use models with high rotational symmetries, but there will be significant cogging torque. This is not considered to be a serious problem, since it is possible to slightly adjust the number of stator slots and number of poles when the initial design stage is completed.

In the simulations, Design-A is rotated at 250 rpm and the phase voltage, the output torque, the rotor torque, and the stator torque are analysed. The machine is accelerated in the first 50 milliseconds, and the rotational speed is kept constant at 250 rpm for 100 milliseconds with a simulation time step of 0.5 milliseconds. Figure 6.27 shows the speed profile and phase voltage waveforms.

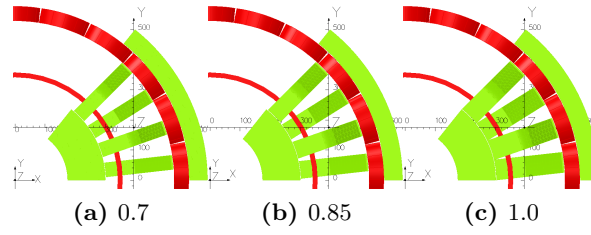


**Figure 6.28:** Varying core pitch to pole pitch simulations.  $N_{coil}:21$ ,  $N_{pole}:28$ .

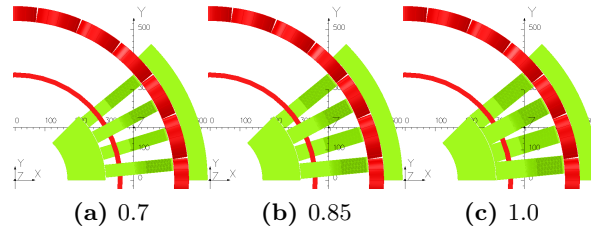


**Figure 6.29:** Varying core pitch to pole pitch simulations.  $N_{coil}:24$ ,  $N_{pole}:32$ .

### Varying Core-to-Pole Pitch Ratio

The core-to-pole pitch ratio is varied from 0.7 to 1 for two different machines ( $N_{pole}=28$  and  $N_{pole}=32$ )<sup>5</sup>. The front views of machines with rotational symmetry are shown in figure 6.28 and figure 6.29.

The torque variation for 28 pole machine with a core-to-pole ratio of 0.7 and 0.85 is plotted in figure 6.30. As well as the rotor torque, the torque at inner stator and outer stator is also shown. Cogging torque is smaller with a core-to-pole pitch ratio of 0.70. The mean rotor torque and the ratio of cogging torque amplitude to mean rotor torque is plotted in figure 6.31. From the figure it can be seen that, the mean rotor torque increases with core-to-pole pitch ratio as concluded in the previous section. There is not a clear pattern on the cogging torque, but the design with a core-to-pole pitch ratio of 0.9 has lower cogging torque and higher mean torque.

<sup>5</sup>Ⓛ:Design-A,  $J_{sc}=160$ , 0pera\_logs\_graphs/2011/2011\_06\_02\_small\_prototype\_varying\_core\_pole

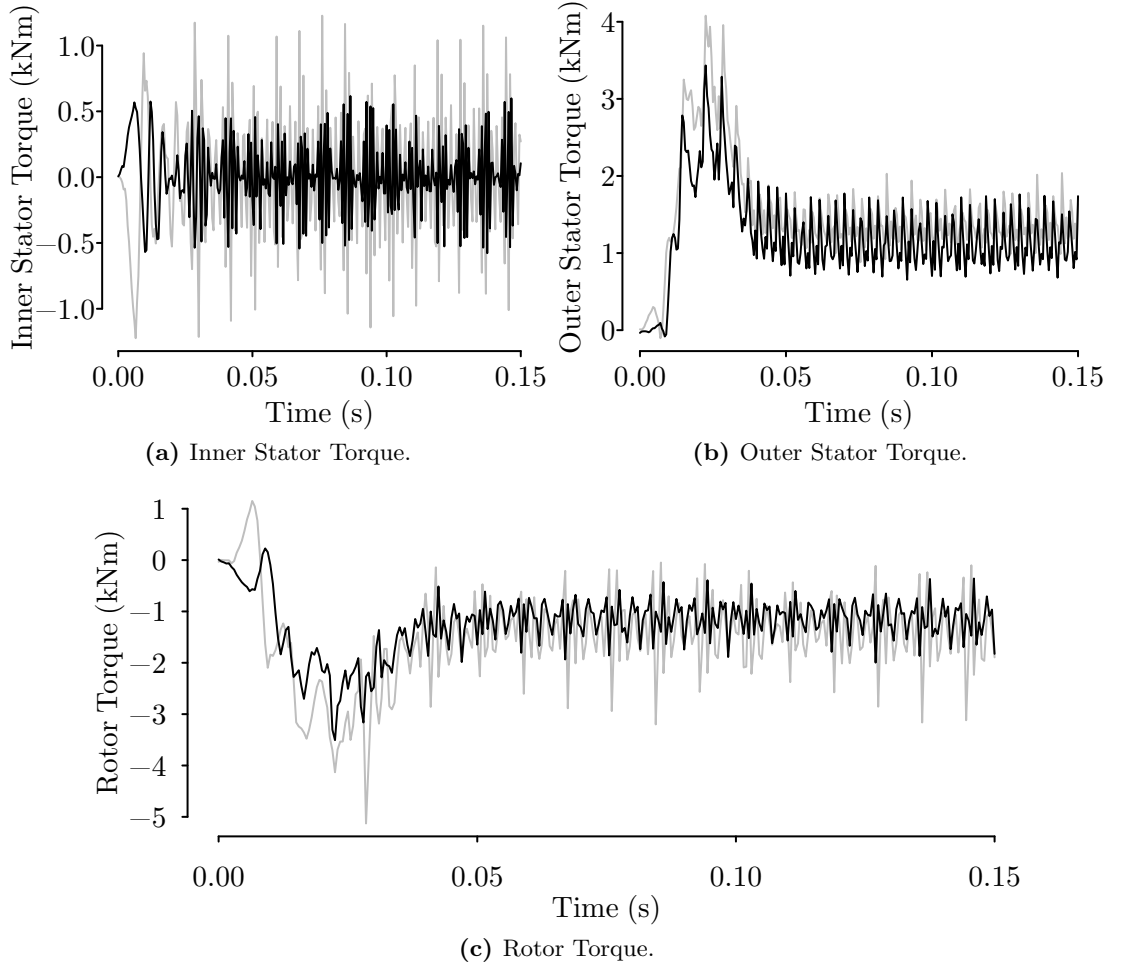


**Figure 6.30:** Torque data at 250 rpm.  $N_{pole}=28$ . Core-to-pole ratio is 0.7(black) and 0.85(grey).

### Varying Pole Number

The core-to-pole ratio is kept constant at 0.9 while varying the number of poles from 24 to 32<sup>6</sup>. The models are connected to a 3-phase 10  $\Omega$  resistive load. Rotor torques, phase voltages and phase currents for each simulation are presented in Table 6.6. The 18 pole machine has the highest induced phase voltage magnitude and rotor torque, which is consistent with the results obtained in section 6.5.1. Rotor torque variation with number of poles is plotted in figure 6.33.

<sup>6</sup> $\backslash$ Design-A,  $J_{sc}=120$ , `Opera_logs_graphs/2011/2011_06_28_small_prototype_varying_Nc_Np/`

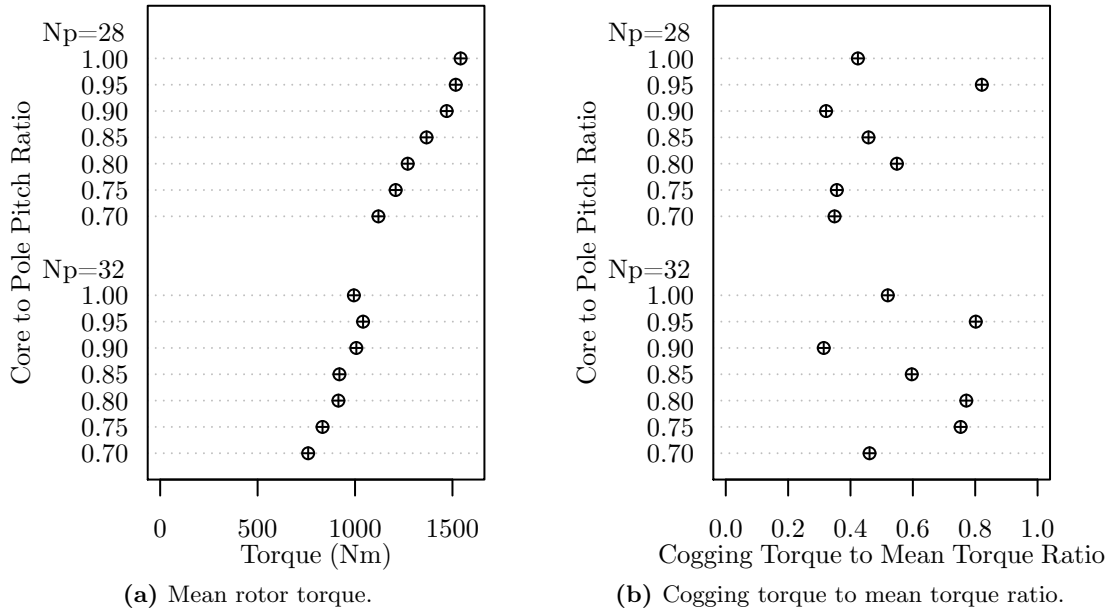


**Figure 6.31:** Mean torque and cogging torque to mean torque ratio for varying core to pole pitch ratio.

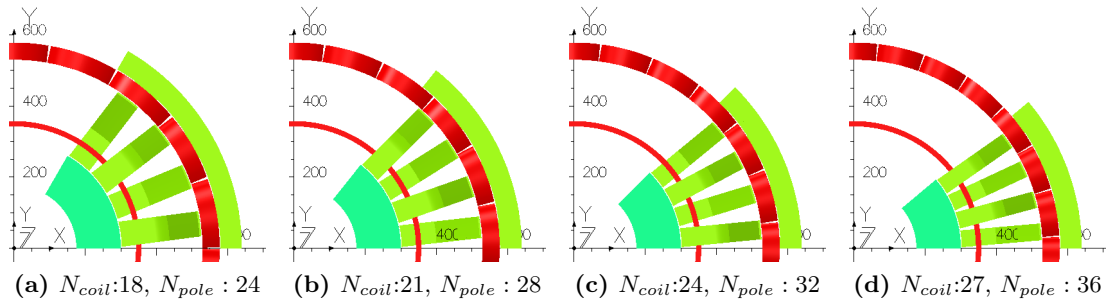


**Figure 6.32:** Varying number of poles simulations. Core to pole pitch ratio: 0.9.

$N_{coil}$	$N_{pole}$	Rotor Torque	Phase Voltage	Phase Current
18	24	2368 Nm	432 V	43.2 A
21	28	1604 Nm	364 V	36.4 A
24	32	1145 Nm	310 V	31.0 A
27	36	802 Nm	257 V	25.7 A

**Table 6.6:** Rotor torque, phase voltage and phase current with  $10 \Omega$  resistive load at 250 rpm with varying pole numbers.

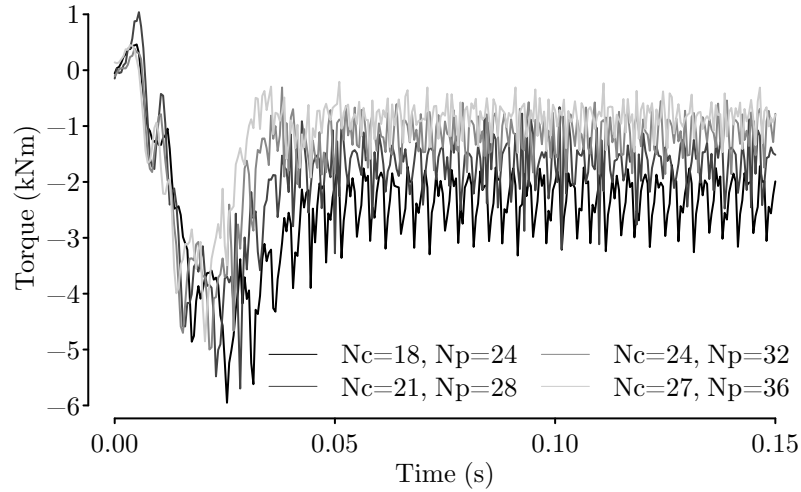


**Figure 6.33:** Rotor torque variation with number of poles.

### Stator Teeth Skew

An effective way to reduce the cogging torque is skewing the stator teeth. In figure 6.34 the torque of the machine is compared with skewed and straight stator teeth. The figures on the left presents the results of the 28 pole machine<sup>7</sup>. Rotor torque for a skew angle of 6 degree is compared with no skew condition. The figures on the right presents the results of the 24 pole machine<sup>8</sup>. Rotor torque is compared with no skew and a skew of 12 degrees. It is also possible to skew the rotor claw poles, but it will make the rotor mechanical structure and laminations more difficult to assemble, therefore it is not preferred.

### 6.5.6 Varying Stator Slot Number

In this section, the effect of number of stator slots on the flux linkage is investigated. Up to this point, the concentrated coil configuration is used, which is advantageous with minimum end-winding length and maximum flux linkage. Concentrated winding machines have more space harmonics, which results in higher iron losses [166], but this effect has not been investigated in this study. Distributed winding machines have fewer harmonics in the phase voltages, however a longer end-winding increases the copper losses. Furthermore, it is possible to manufacture the stator in a modular way with concentrated coil configuration. Thus, if a problem occurs in the armature winding, a coil can be replaced without the need to dismantle the complete armature windings. Such a concept is desirable for the offshore wind turbine application and will be discussed in detail in Chapter 8.

<sup>7</sup>[\Design-A: Opera\\_logs\\_graphs/2011/2011\\_07\\_15\\_skew\\_compare/](#)

<sup>8</sup>[\Design-A: Opera\\_logs\\_graphs/2011/2011\\_08\\_22\\_skew\\_Nysmmetry/](#)



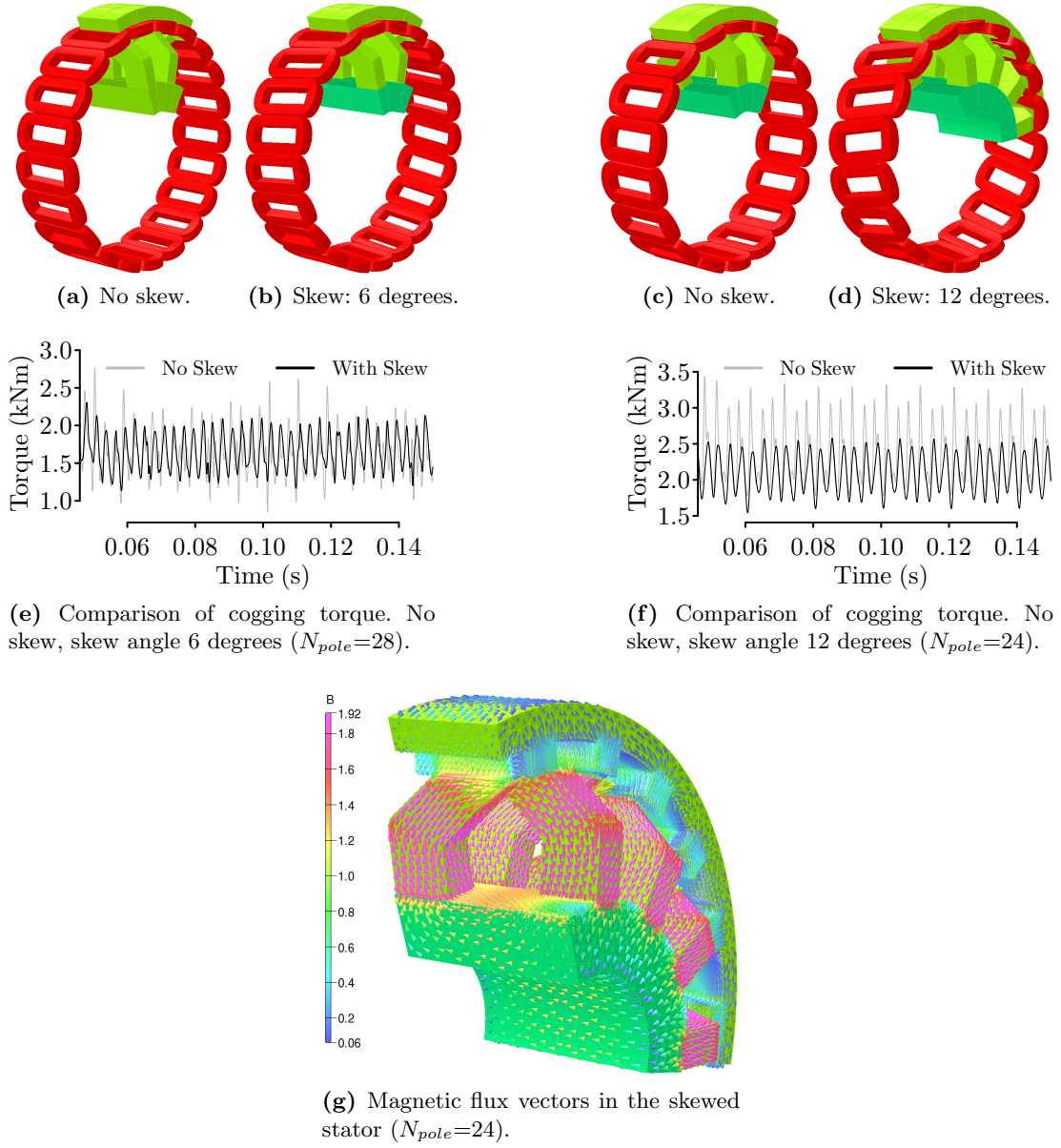


**Figure 6.34:** The effect of the skew angle to the cogging torque

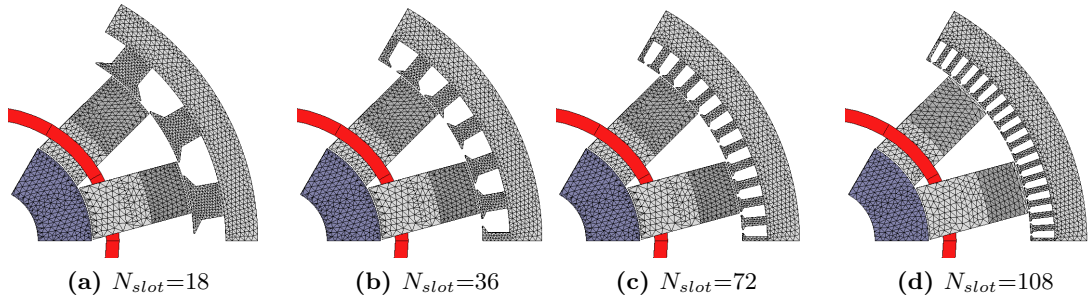


**Figure 6.35:** Models with varying stator slot number.

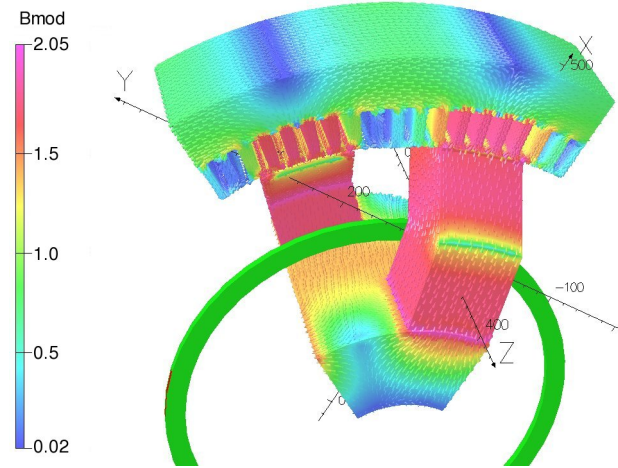


**Figure 6.36:** Magnetic flux vectors with a stator slot number of 108.

The double layer distributed winding configuration is mostly used in conventional machines. The armature winding can be full-pitched or short-pitched. The biggest advantage of the distributed winding is the improved voltage output waveform (i.e. fewer harmonic content), which also helps to reduce torque ripples. Four different stator slot configurations are compared in this section<sup>9</sup>:

- $N_{slot}=18$ , concentrated coil.
- $N_{slot}=36$ , distributed coil (full,  $2/3$  pitch).
- $N_{slot}=72$ , distributed coil (full,  $5/6$ ,  $4/6$  pitch).
- $N_{slot}=108$ , distributed coil (full,  $8/9$ ,  $7/9$ ,  $6/9$  pitch).

The number of poles is kept constant at 12. The FEA models are presented in figure 6.35. In figure 6.36 magnetic flux density vectors in the machine are presented with a stator slot number of 108.

In figure 6.37, the radial magnetic flux density magnitude is presented for a slot number of 36 and 108. In figure 6.37a a  $2/3$  pitch coil, in figure 6.37b an  $8/9$  pitch coil is

<sup>9</sup>Ⓔ:Design B:Opera\_logs\_graphs/2011/2011\_10\_10\_varying\_Nslot/

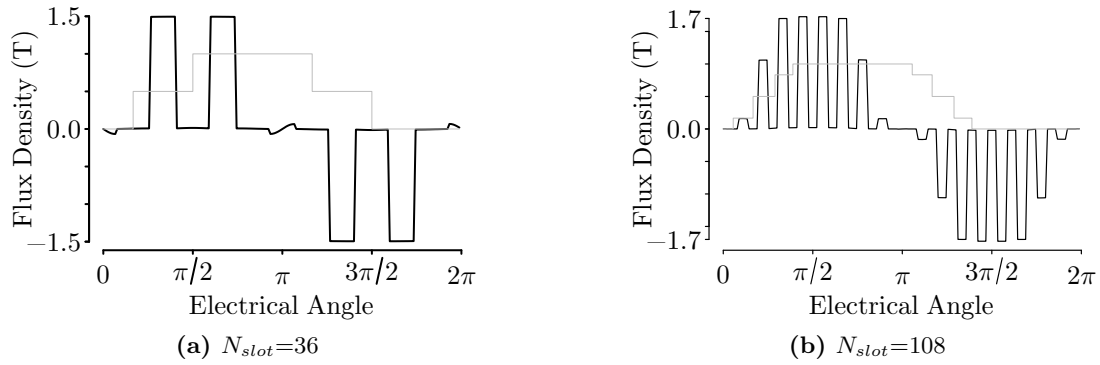


**Figure 6.37:** Flux density distribution in the stator teeth at mean armature radius (Grey line represents the position of the armature winding that is used to calculate the flux linkage).

$N_{slot}$	Armature Configuration	Peak Flux Linkage (mWb)	Magnetic Loading (T)
18	Concentrated	13.53	0.398
36	Full Pitch	16.61	0.429
	2/3 Pitch	14.46	
72	Full Pitch	15.71	0.477
	5/6 Pitch	15.51	
	4/6 Pitch	14.52	
108	Full Pitch	17.03	0.521
	8/9 Pitch	16.86	
	7/9 Pitch	16.34	
	6/9 Pitch	15.38	

**Table 6.7:** Peak flux linkage and magnetic loading for different armature configurations.

shown. Several static magnetic simulations are performed by rotating the rotor in small angles. The flux linkages in the armature coils are calculated in each step and plotted in figure 6.38. The value of the peak flux linkages are tabulated in table 6.7. It can be seen from the table that the maximum flux leakage is obtained with full-pitched winding configurations. This result is expected as the more the coil is distributed, the lower the winding factor and the equivalent flux linkage will be less.

It can also be seen from table 6.7 that the flux linkage and magnetic loading increases with number of stator slots. This is mainly because of the zigzag leakage reluctance. As the slot number is decreased, the stator tooth pitch increases. The increased stator tooth pitch creates a zigzag flux path between adjacent claw poles as shown in figure 6.39. Especially when the stator tooth is aligned between two claw poles as in figure 6.39b, the leakage flux is maximum, and hence, the flux linkage is reduced. The stator slot

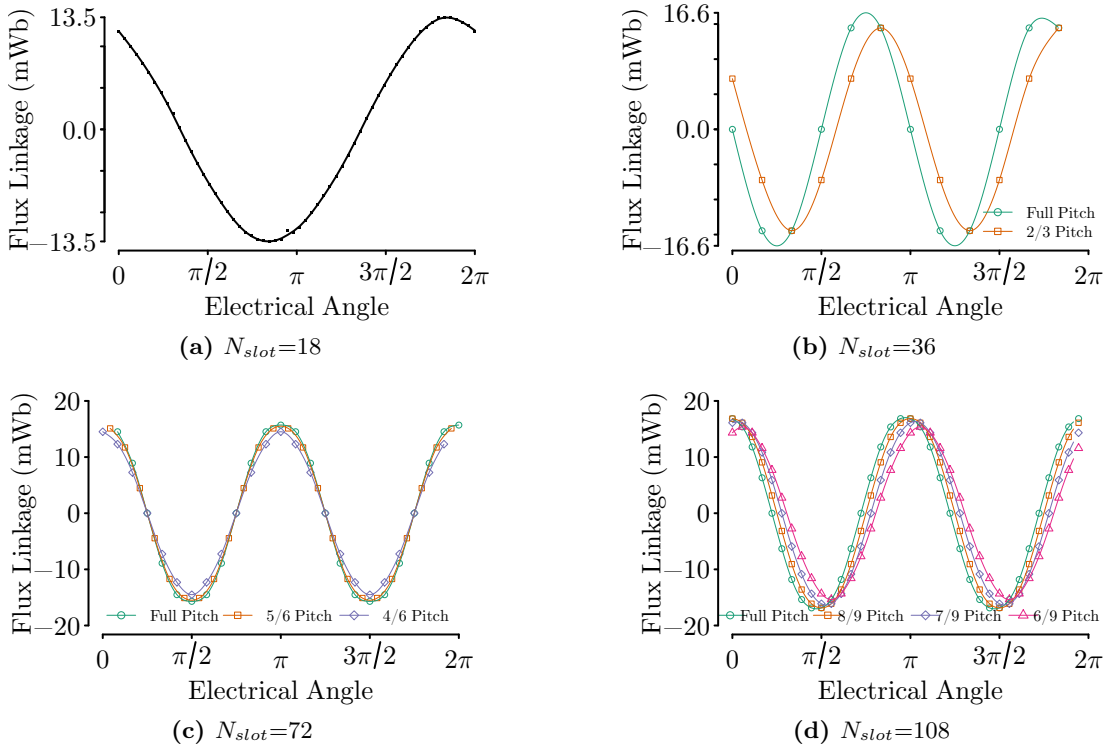


**Figure 6.38:** Flux linkage in the armature coils with different winding configurations.

shoe pitch is varied to measure the effect of this <sup>10</sup>. The flux linkage versus tooth shoe to coil pitch ratio is presented in figure 6.40, which shows the maximum flux linkage is achieved for tooth shoe to stator slot pitch values between 0.8–0.85.

## 6.6 Modelling of the Superconducting Coil

In the previous sections, the superconducting coil is modelled as a simple solenoid coil with DC excitation. The magneto-motive-force is calculated by multiplying the surface area with the current density. However, there are many factors affecting the superconducting wire's performance as mentioned in Chapter 2. The two most important design parameters are flux density penetrating into the superconducting coil and the operating temperature.

<sup>10</sup> :Design B:Opera\_logs\_graphs/2011/2011\_10\_31\_varying\_pole\_shoe/

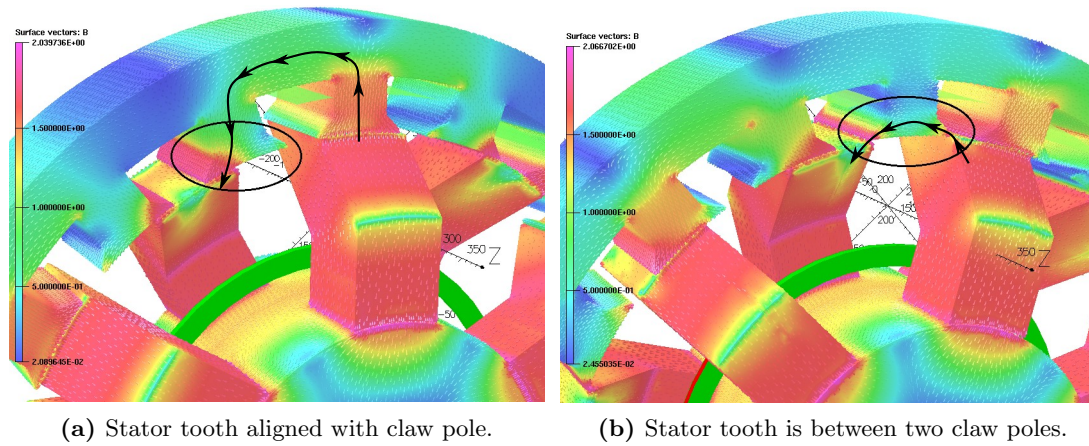


**Figure 6.39:** Zigzag flux linkage in the 18 slot machine with different rotor positions.

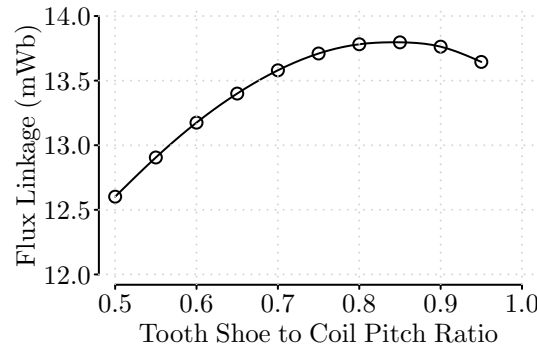


**Figure 6.40:** Maximum flux linkage variation with stator tooth shoe pitch.

### 6.6.1 Flux Penetrating into Superconducting Coil

Penetrating flux directly limits the critical current of the superconducting coil. The angle of the flux density is also important (in particular the perpendicular component is more limiting than the parallel component). The penetrating flux is a more critical issue in air-cored superconducting machine topologies, as magnetic flux tends to take the shortest path. However, in an iron-cored machine the flux travels through the magnetic core, which reduces the amount of flux penetrating into the superconducting coil.

Flux around the superconducting coil is simulated using Design B with a field winding MMF of  $18 \text{ kAt}^{11}$ . The flux density distribution around the superconducting coil is analysed in two planes: X-Y plane and Y-Z plane. Figure 6.41 shows the total flux density magnitude, perpendicular and parallel components of the flux density at X-Y plane (front-view) of the superconducting coil. The dashed line represents the position of the superconducting coil. The effect of claw poles is evident from figure 6.41b,

<sup>11</sup> :Design B:Opera\_logs\_graphs/2011/2011\_10\_21\_penetrating\_flux

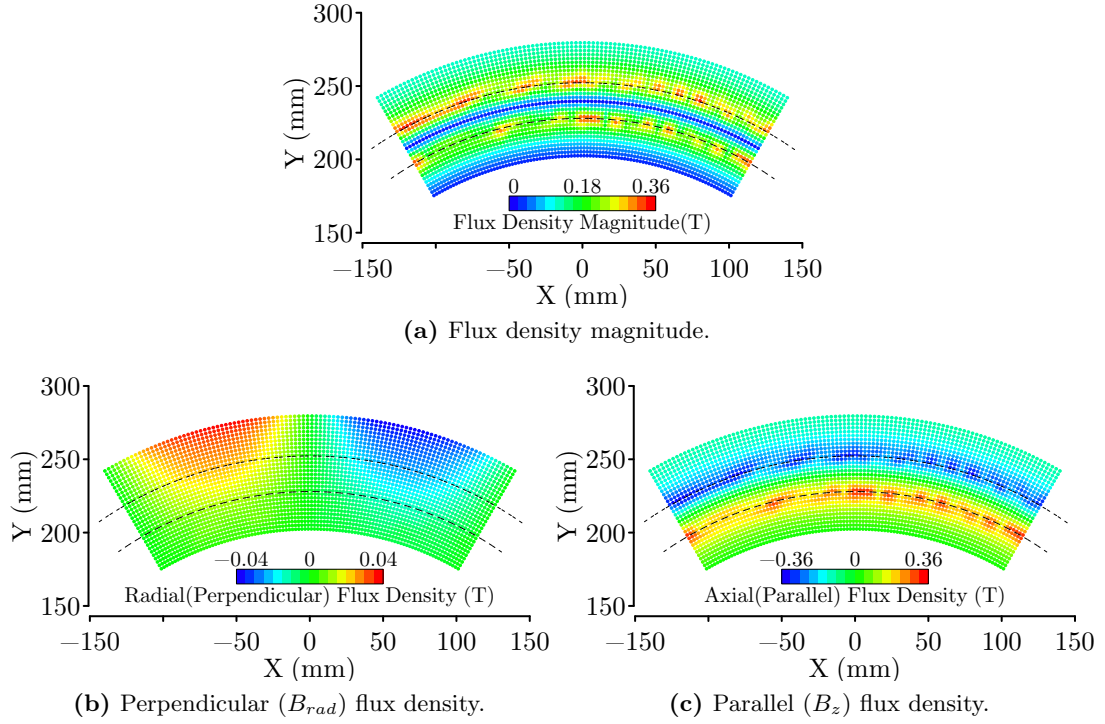


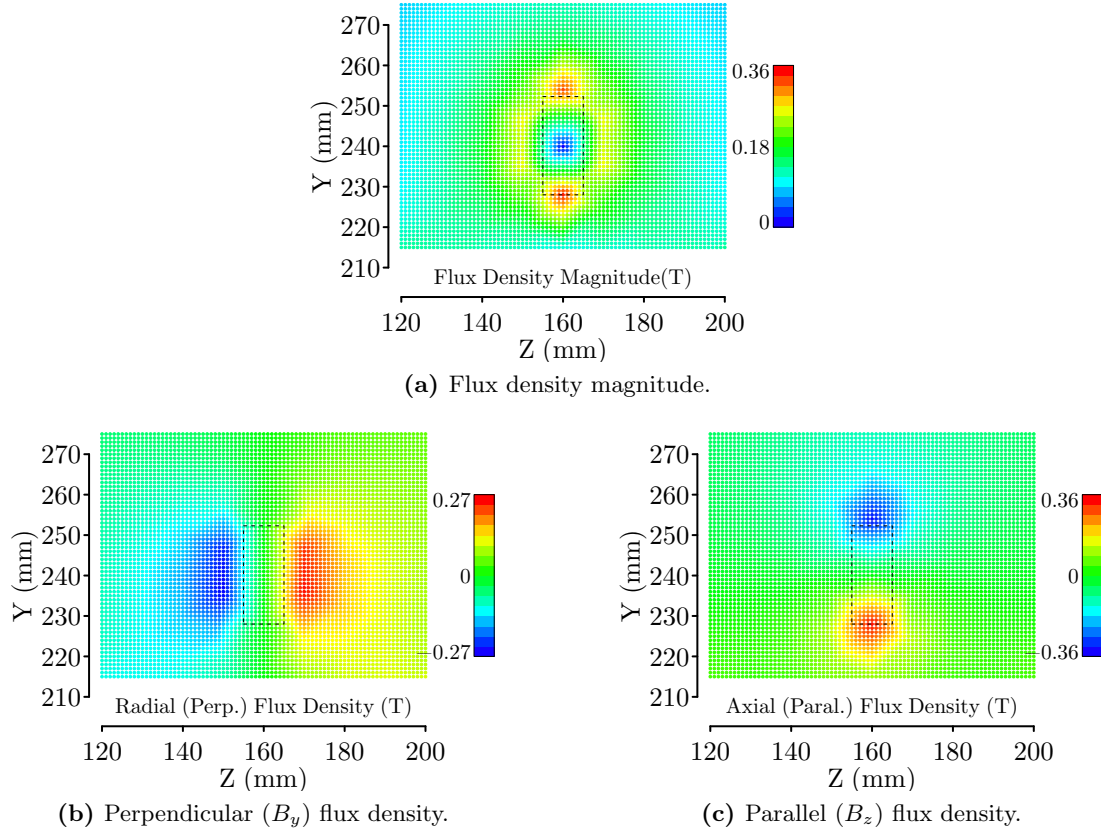
**Figure 6.41:** Flux penetrating into the superconducting coil. X-Y plane section. Dashed line represents the position of the superconducting coil.

however this effect is very limited (0.04 T) since the claw poles create a favourable path for flux around the superconducting coil. The maximum parallel flux density in the superconducting coil is around 0.36 T as shown in figure 6.41c. This value is limited on the outer and inner edges of the superconducting coil.

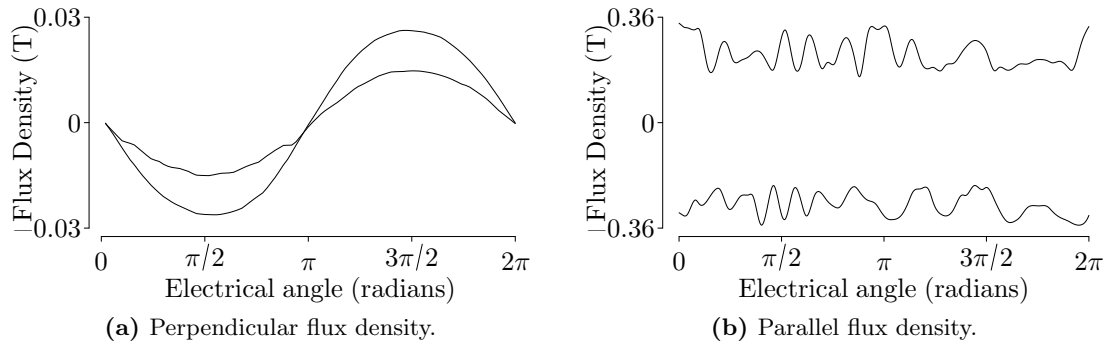
Figure 6.42 shows the flux density distribution at the Y-Z cross-section of the superconducting coil. The maximum perpendicular flux density in figure 6.42b is 0.27 T, but this value is out of the superconducting coil boundaries. The maximum perpendicular flux penetrating into the superconducting coil is around 0.11 T. The maximum parallel flux in the superconducting coil is 0.36 T with the effect of claw poles evident from figure 6.41b, however this effect is very limited (0.04 T) since the claw poles create a favourable path for flux around the superconducting coil. The maximum parallel flux density in the superconducting coil is around 0.36 T as shown in figure 6.41c. This value is limited on the outer and inner edges of the superconducting coil.

Figure 6.43 shows the perpendicular and parallel flux density variation along the inner and outer circumference of the superconducting coil. The effect of claw poles is again visible in the perpendicular flux density distribution. Although, the magnitude is very small, it may induce eddy currents on the superconducting wire. In this case, a conductive shield around the superconducting coil may be used.





**Figure 6.42:** Flux penetrating into the superconducting coil. Z-Y plane section. Dashed line represents the position of the superconducting coil.



**Figure 6.43:** Perpendicular and parallel flux densities along the inner and outer circumference of the superconducting coil.

The penetrating flux reduces the critical temperature of the superconducting wires. The critical current densities of different superconducting wires under this condition are compared to critical currents with no field in table 6.8 assuming the penetrating flux density (with a safety margin ) as 0.15 T perpendicular, 0.4 T parallel.

**Table 6.8:** Critical current variation at 0.4 T parallel, 0.15 T perpendicular field ( $I_c$  is calculated at 32 K for  $MgB_2$ , at 77 K for YBCO and BSSCO with no external field).

Temperature	$MgB_2$	BSSCO	YBCO
77 K	–	0.1 $I_c$	0.6 $I_c$
65 K	–	0.4 $I_c$	1.48 $I_c$
30 K	0.34 $I_c$	2.35 $I_c$	6 $I_c$
20 K	1.54 $I_c$	–	7.5 $I_c$

### Operating Temperature

Table 6.8 shows that the wire performance can be significantly improved by reducing the operating temperature. For an experimental prototype, the first option is to operate at 77 K, which means the coils can be flooded with liquid nitrogen to cool them down during the experiments. Although, this is not a permanent solution, the cost of the prototype can be significantly reduced by eliminating the cryocooler. However, operation at 77 K means reduced current density as shown in table 6.8. BSSCO wire performs the worst out of the three options, it can only carry 10 % of its  $I_c$  at 77 K with 0.4 T. As a result, the wire length would have to be increased to compensate this, which increases the material cost.

The second option is to operate at a much lower temperature. For example, YBCO wire at 20 K at 0.4 T can conduct more than seven times the critical current at 77 K. Although, the initial cost of the cooling system will be much higher, it gives more flexibility in the future designs.

In order to compare the wire requirements at 20 K, data-sheets of superconducting wires presented in Appendix B are used. The required magnetising field is defined as 18 kAt and the wire lengths and dimensions for each option are presented in table 6.9. The operating current is assumed as 70 % of the critical current at the operating temperature as a safety margin. Outer diameter is calculated with a fill factor of 0.75 (to include electrical insulation layer).  $MgB_2$  is wound in a twin wire configuration to limit the outer diameter. Total cryostat cross section area is 80 mm by 80 mm as presented in figure 6.42.

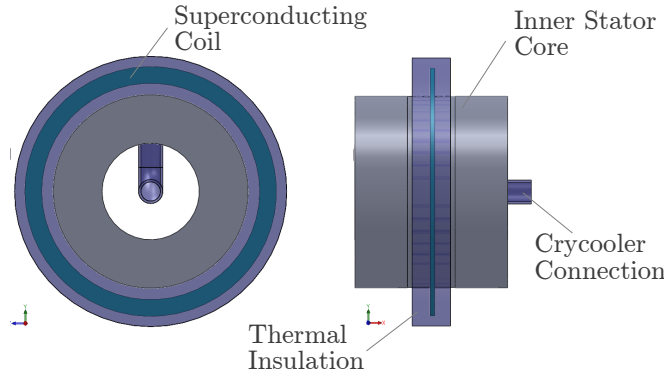
#### 6.6.2 Cooling System

The cooling system is not modelled in detail in this dissertation, but it is necessary to design the basic connections to the cooling system. Since the superconducting winding is surrounded by the claw poles, it is necessary to make the cryocooler connection through a hole in the inner stator as shown in figure 6.44. If a gas transfer cryocooler is used, the piping can be mounted along the field winding circumference. If a conduction type cold-finger is used, depending on the diameter of the coil it may be required to install



**Table 6.9:** Comparison of the superconducting wire length at 20 K ( $I_{safe} \times N_{turns}=18$  kAt).

	MgB <sub>2</sub>	BSSCO	YBCO	
Operating temp.	20	20	20	K
Wire Width	3.65	4.0	4.8	mm
Wire Thickness	0.67	0.22	0.22	mm
Critical Current	400	200	630	A
Safe Current( $0.7I_c$ )	280	140	441	A
Current Density	114	160	418	A/mm <sup>2</sup>
Number of turns	64	128	43	
Inner diameter	450	450	450	mm
Outer diameter	507	526	475	mm
Wire length	96	198	62.5	m

**Figure 6.44:** Cryocooler connection and mounting of the superconducting coil.

an extra cooler (see figure 6.45) to achieve homogeneous temperature distribution. The extra cooler can also be used to increase redundancy or to reduce the cooling time.

In some cases it may be more preferable to connect the coolers from the outer circumference of the machine, which can be achieved by turning the machine ‘inside-out’ as depicted in figure 6.46a. In this configuration, the armature winding is placed where previously the soft magnetic composite is. It is now possible to connect the cryocooler through the outer circumference of the machine similar to the one used in a homopolar machine designed by Zhang et. al. [178] (see figure 6.46b). However, it is apparent that the superconducting wire requirement is higher now as the diameter of the field winding is larger. Thus, this configuration is not preferred in the small prototype, but it may be a better option for a large diameter machine, where the difference between inner and outer diameter is negligible.

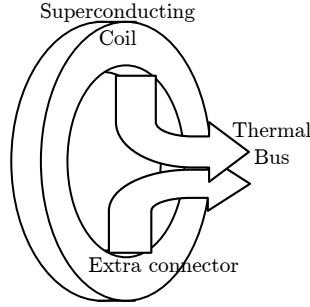


**Figure 6.45:** Extra cold-head connection for larger superconducting coil diameter.

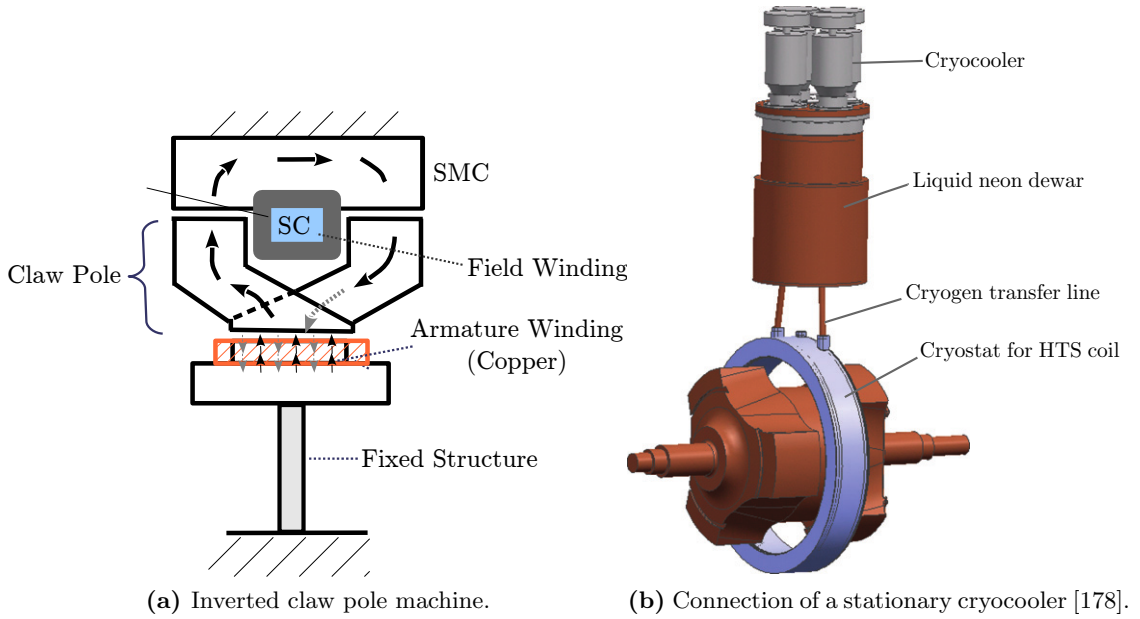


**Figure 6.46:** Inverted claw pole machine to connect the cooling system from outer circumference of the machine.

## 6.7 Structural Modelling

In electrical machines, an important force component is the normal component of the Maxwell stress, which tries to close the air-gap clearance. This component of the Maxwell stress can be expressed as:

$$P = \frac{B^2}{2\mu_0} \quad (N/m^2) \quad (6.1)$$

where  $B$  is the radial flux density magnitude in the air-gap and  $\mu_0$  is the permeability of free space. In conventional machines, the normal stress is an order of magnitude greater than the shear stress and imposes great forces on the structure of large diameter machines. This becomes more dramatic in the superconducting machines due to higher

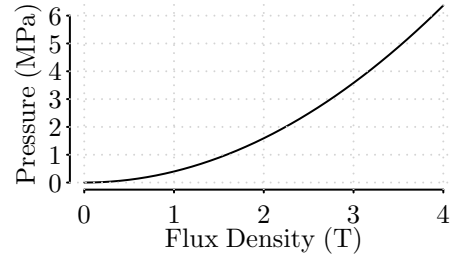


**Figure 6.47:** Flux density versus magnetic attraction stress.

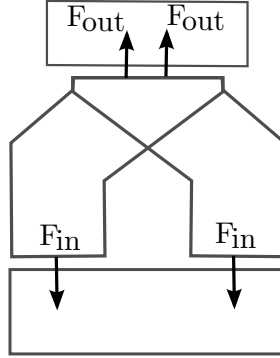


**Figure 6.48:** Main magnetic attraction forces acting on the claw poles.

magnetic flux densities in the air-gap. In figure 6.47 the variation of Maxwell stress with flux density is presented. For example, the machine structure has to withstand up to 6 MPa (60 atm) stress for an air-gap flux density of 4 T.

The proposed topology is an iron-cored topology, so the flux density is limited by magnetic saturation. However, the machine has two air-gaps, thus the forces in the claw pole and mechanical structure of the claw poles require special attention. The main magnetic attraction forces acting on the claw poles are presented in figure 6.48.  $F_{in}$  is the attraction force between the claw pole and the inner stator.  $F_{out}$  is the force between the claw pole and the outer stator.  $F_{in}$  and  $F_{out}$  are in opposite directions and partly cancel each other.

Assuming constant flux density distribution at the surfaces, the Maxwell stress and the forces ( $F_{in}$ ,  $F_{out}$ ) can be calculated as presented in table 6.10. From the table, it can be seen that even for a small claw-pole the magnetic attraction forces are quite significant.  $F_{out}$  is approximately half of  $F_{in}$ , thus there is a net force of 3100 N inwards.  $F_{in}$  and  $F_{out}$  are not perfectly aligned, so the net component also has a bending moment acting on the claw pole.

The Maxwell stress can also be expressed as in equation 6.2 assuming a homogeneous flux density distribution, where  $\Phi$  is the magnetic flux and  $A$  is the cross-sectional surface area. Thus, for the same amount of magnetic flux, the total force is inversely

	Flux Density	Maxwell Stress	Surface area	Force
Inner Surface ( $F_{in}$ )	1.75 T	1.22 MPa	5500 mm <sup>2</sup>	6710 N
Outer Surface ( $F_{out}$ )	1.1 T	0.48 MPa	7500 mm <sup>2</sup>	3610 N

**Table 6.10:** Magnetic attraction forces acting on the inner and outer claw pole cross-section.

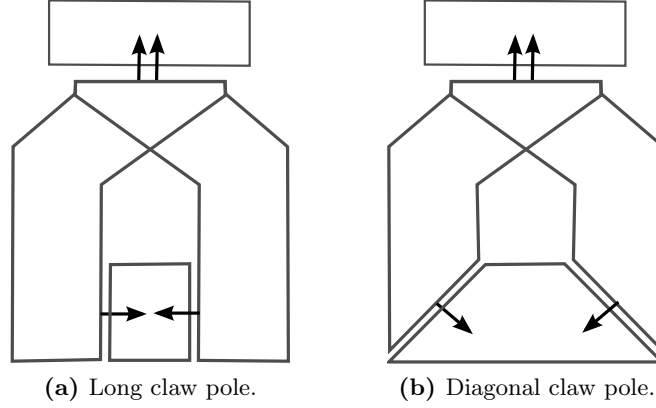


**Figure 6.49:** Alternative claw pole and inner stator shapes and resultant magnetic attraction forces.

proportional to the surface area. This is one reason for  $F_{in}$  being larger than  $F_{out}$ . One way to reduce the net inwards force in the machine is to modify inner stator and claw pole structure as shown in figure 6.49. The first option is to use a longer claw pole with a sliced inner stator core as in figure 6.49a, which will convert  $F_{in}$  into an axial force. A second alternative is to use a diagonal inner stator core as in figure 6.49b. It is possible to adjust the angle in such a way that the downward component of  $F_{in}$  cancels  $F_{out}$ , and axial components of  $F_{in}$  cancels each other. Another advantage of this configuration is that as the surface area is larger the force will be smaller as stated in equation 6.2. Increased surface area also reduces the air-gap reluctance ( $R_{ag1}$  in figure 6.6), which may help to reduce the MMF requirements. However, these modifications are not applied to the rotational prototype at this stage, and the original configuration is kept.

$$P = \frac{(\Phi/A)^2}{2\mu_0} \Rightarrow F = \frac{\Phi^2}{2A\mu_0} \quad (6.2)$$

There are two parts of the rotor structure:

- Structure that connects adjacent claw poles to each other.
- Structure that connects the claw poles to the bearings.

Straight bars are used to connect the claw poles to each other as presented in figure 6.50. These bars should be non-magnetic (e.g. aluminium or stainless steel) in order not to interfere with the magnetic circuit. The diameter of the hole is also important as it will

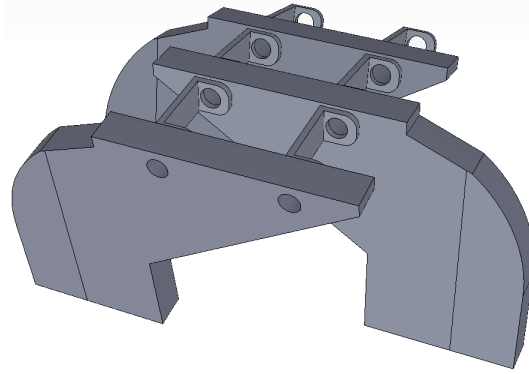


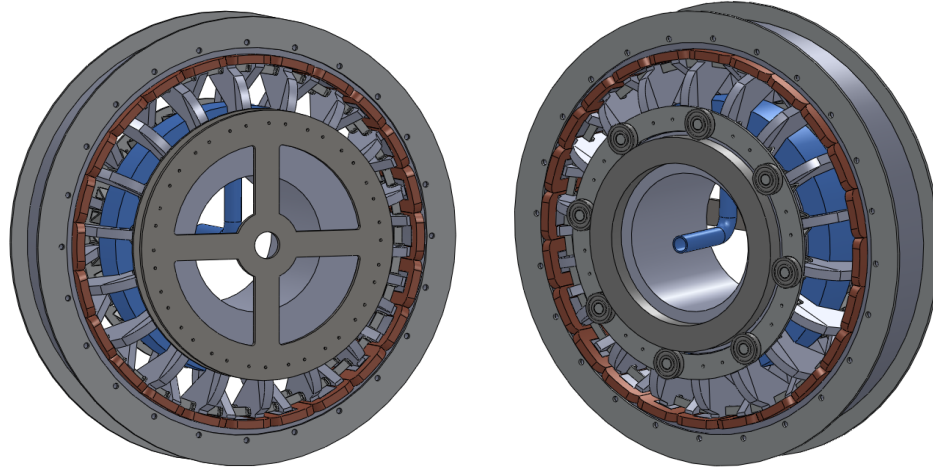
**Figure 6.50:** Structure to connect adjacent claw poles.

limit the cross-sectional area for the magnetic flux.

Another issue is the connection of the main rotor structure to the shaft. The initial design is presented in figure 6.51. The claw poles are all connected to a circular support structure, which carries all the inward force. Under ideal conditions, the inward forces cancel each other due to cyclic symmetry and no net force is transferred to the rotor torque arms. However, rotor eccentricities and manufacturing tolerances can cause unbalanced magnetic pull. A serious issue in the rotor structure is the access to the superconducting coil; in other words one side of the machine has to be clear to accommodate the cryocooler connections. In a large diameter wind turbine machine, it could be possible to install the cooling system on the inside of the inner stator, or to use a hollow shaft which is large enough to install electrical connections and piping for the cryocooler. However, in the small prototype there is not enough space for that, therefore a bearing system as shown in figure 6.51b is proposed, which is in a way similar to the NewGen concept [50]. The rotor structure is supported by eight radial ball bearings, which travel on a steel rail.

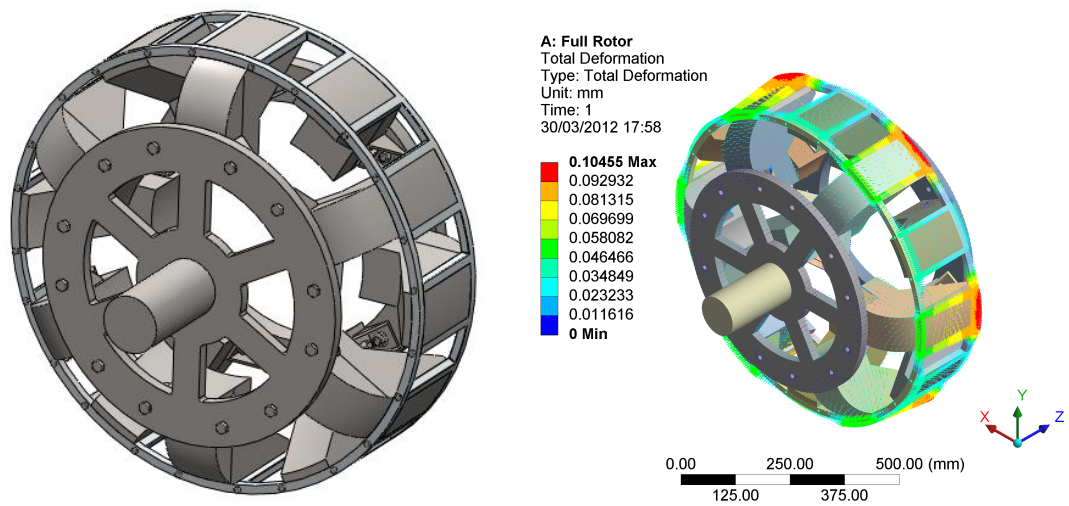
Although, the initial structure requires bearings to support the rotor, a study on the structural design of the proposed machine by Dariusz Olczak showed the rotor can be supported from just a single side [127]. Olczak proposed to use an aluminium cage structure, which is presented in figure 6.52a, instead of bars. Structural FEA simulations showed that the deflection in the claw pole is 0.1 mm without fasteners and 0.15 mm with the fasteners, which is within the acceptable range for a 2.5 mm air-gap. The total deflection in the structure is shown in figure 6.52b and more results are available in [127].

Another challenge is manufacturing the SMC inner stator in single piece, but it is possible to divide the inner stator into modular sections as presented in figure 6.53a. These sections are fixed at both ends with steel rings. The assembled radial flux prototype with the support structure is shown in figure 6.53b.



(a) Drive-end connection.

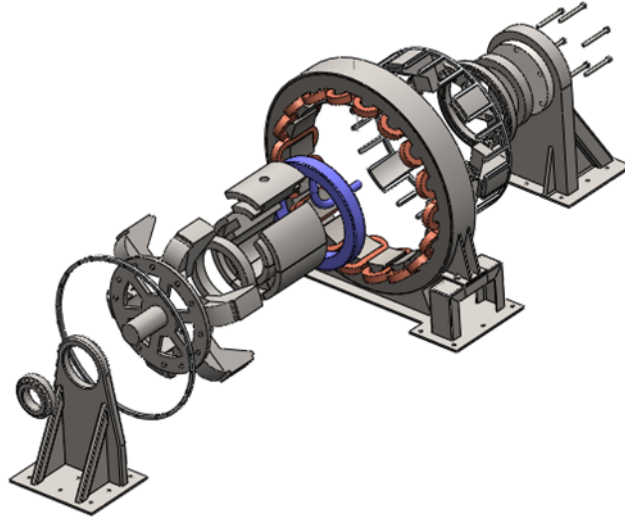
(b) Cryocooler connection.

**Figure 6.51:** Initial rotor structure for the claw pole machine.

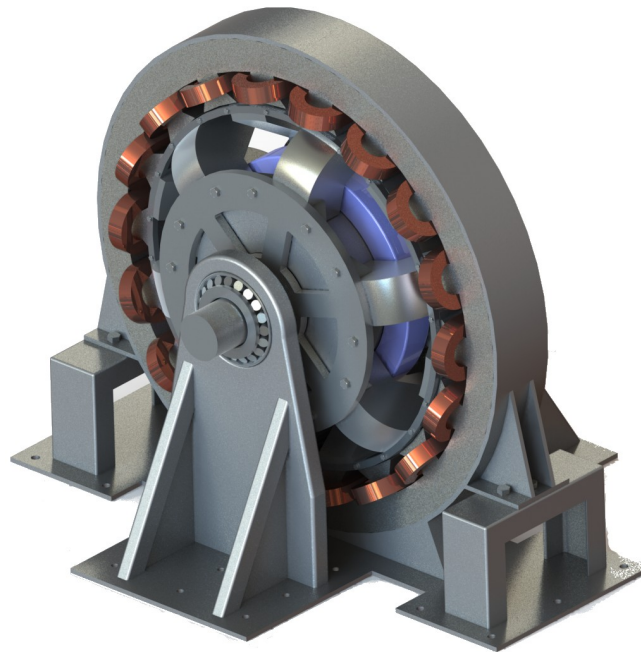
(a) Rotor structure with claw pole frame.

(b) Total deformation in the claw pole structure.

**Figure 6.52:** Rotor structure supported from single side [127].



(a) Exploded isometric view of the assembly.



(b) Assembled machine with mechanical structure.

**Figure 6.53:** Radial claw pole machine assembly [127].

## 6.8 Conclusion

In this chapter, two previous topologies presented in Chapter 4 and Chapter 5 have been improved by maintaining the single stationary superconducting field winding concept. The claw pole rotor modulates the magnetic flux created by the superconducting field winding and a varying magnetic field is created on the armature coils. The topology has two air-gaps and uses soft-magnetic composite material in the inner stator because of the three-dimensional magnetic flux.

A parametrized FEA model of the claw pole machine was built, which helps to find the optimum dimensions of the machine. Throughout the chapter, a prototype that can fit on to an existing test-rig is designed. The optimum number of poles is selected as 12, which gives the maximum magnetic loading. It is found that the torque output increases with core-to-pole ratio, although this also increases the leakage flux between claw poles. The effect of the field MMF to the output power is investigated, and 18 kAt is selected as the most optimum point considering the saturation in the magnetic core.

A concentrated coil armature is preferred because of shorter end-windings and modular armature structure, which a large diameter machine can benefit from through ease of assembly and maintenance. Cogging torque is high due to slot and rotor number configurations, but it can be reduced by skewing the stator slots. Distributed windings can also be used, in which the maximum flux linkage is achieved with the full-pitch configuration.

Flux penetrating into the superconducting coil is simulated, which is found to be not critical (0.11 T perpendicular, 0.36 T parallel). The amount of the required superconducting tape is calculated for the prototype, which is 96 m for  $\text{MgB}_2$  and 62.5 m for YBCO at 20 K.

Different claw pole configurations and the machine structure are also presented. It is possible to use an inverted claw pole design to make the installation of the cooling system easier. The shape of the claw pole can also be modified to change the direction of the magnetic attraction forces and reduce the structural loads.





# Development of a Linear Claw Pole Prototype

In Chapter 6, a radial claw pole superconducting machine topology was proposed. It was planned to build a rotational prototype to prove the concept and highlight the challenges in manufacturing. However, due to limited funding it was decided to manufacture only a section of the rotational prototype as a linear machine. The first section of this chapter explains the development of the concept, and the second section presents the experimental results. In the prototype, a copper winding is used instead of a superconducting coil to reduce the cost of the prototype.

## 7.1 Design of Linear Claw Pole Machine

The schematic of the linear claw pole machine, which is presented in figure 7.1, is very similar to the radial claw pole machine. Instead of a rotor, a translator is used, the reciprocating motion of which induces varying magnetic flux in the armature coils. The field winding is a copper coil wound around the field core.

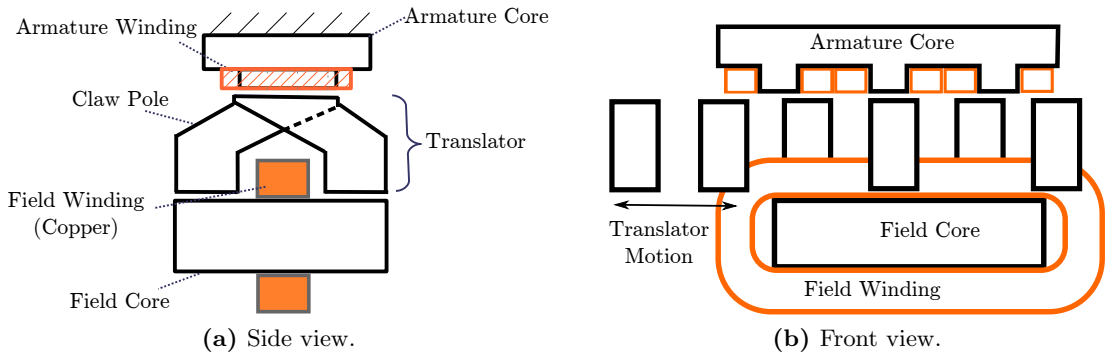


**Figure 7.1:** Basic schematic of the linear claw pole machine with copper field winding.

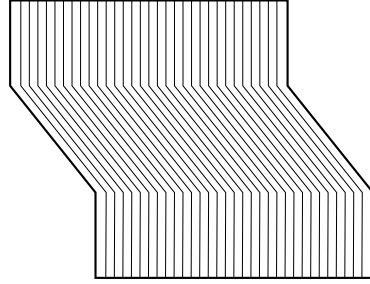


**Figure 7.2:** The field core shape and lamination pattern.

### 7.1.1 Electromagnetic Modelling

The linear machine is modelled with 3D FEA software. The model is similar to the model of radial claw pole machine, which is described in Chapter 6. One major difference is the design of the field core. In the radial claw-pole machine, soft magnetic composite material (SMC) was used to obtain three-dimensional flux path. However, in the linear machine, it is possible to use electrical steel laminations stacked as shown in figure 7.2. In this way, magnetic flux can travel from one claw pole to the next one by following the lamination direction without the need to use SMC material.

The claw poles and the armature core are also manufactured from steel laminations, and concentrated coils are used in the armature. Figure 7.3 shows the flux density distribution in the linear machine.

### Magnetic Forces

A major difference of the linear machine is the characteristics of the magnetic attraction forces. The magnetic attraction forces in the rotary claw-pole machine have a cyclic symmetry and they cancel each other [127]. However, in the linear machine, the magnetic forces act on the same plane for the field core and the armature core, which results in large net forces.

The horizontal magnetic pull in the translator due to its position with respect to the field core and stator core is another issue that should be considered. As the translator moves outside of the field core, it is pulled back to the position where the minimum reluctance position occurs. Therefore, it is important to select the field core length and the number of stator slots appropriately to minimize the unbalanced magnetic pull in the translator.

Three different sets of simulations are performed with different stator slot numbers and pole numbers at different translator positions and the magnetic attraction forces in the

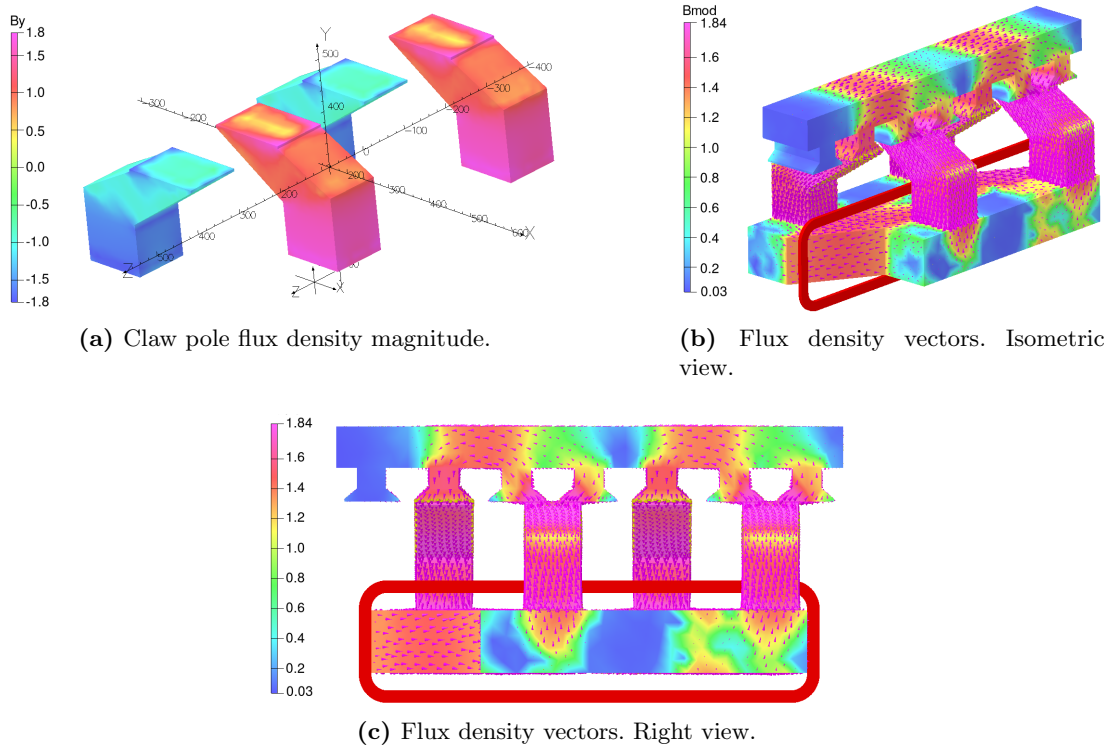


**Figure 7.3:** The flux density distribution in the linear claw pole machine (assuming a superconducting coil with a field intensity of 18 kAt).

Y and Z axes are calculated<sup>1,2</sup>. In the simulations, the field winding is excited, but the armature windings are not connected. The results are presented in figure 7.4 and in figure 7.5. From the figures, the following points can be concluded:

- Maximum attraction force acts on the field core, which can go up to 15000 N.
- The translator is pulled from both +Y and -Y directions, but the net force is in the -Y direction (towards the field core). The cancellation ratio is between 40–70 %).
- The attraction force acting on the translator in Z-direction can go up to 1500 N.
- The cogging force in the armature core (figure 7.5d) is small compared to the magnetic pull.
- The length of the field core and the number of poles can be adjusted in such a way that the force on the “entering” claw pole can be cancelled by the force on the “exiting” claw pole<sup>1</sup>.

<sup>1</sup>📁:Opera\_logs\_graphs/2012/2012\_03\_06

<sup>2</sup>📁:Opera\_logs\_graphs/2012/2012\_03\_08

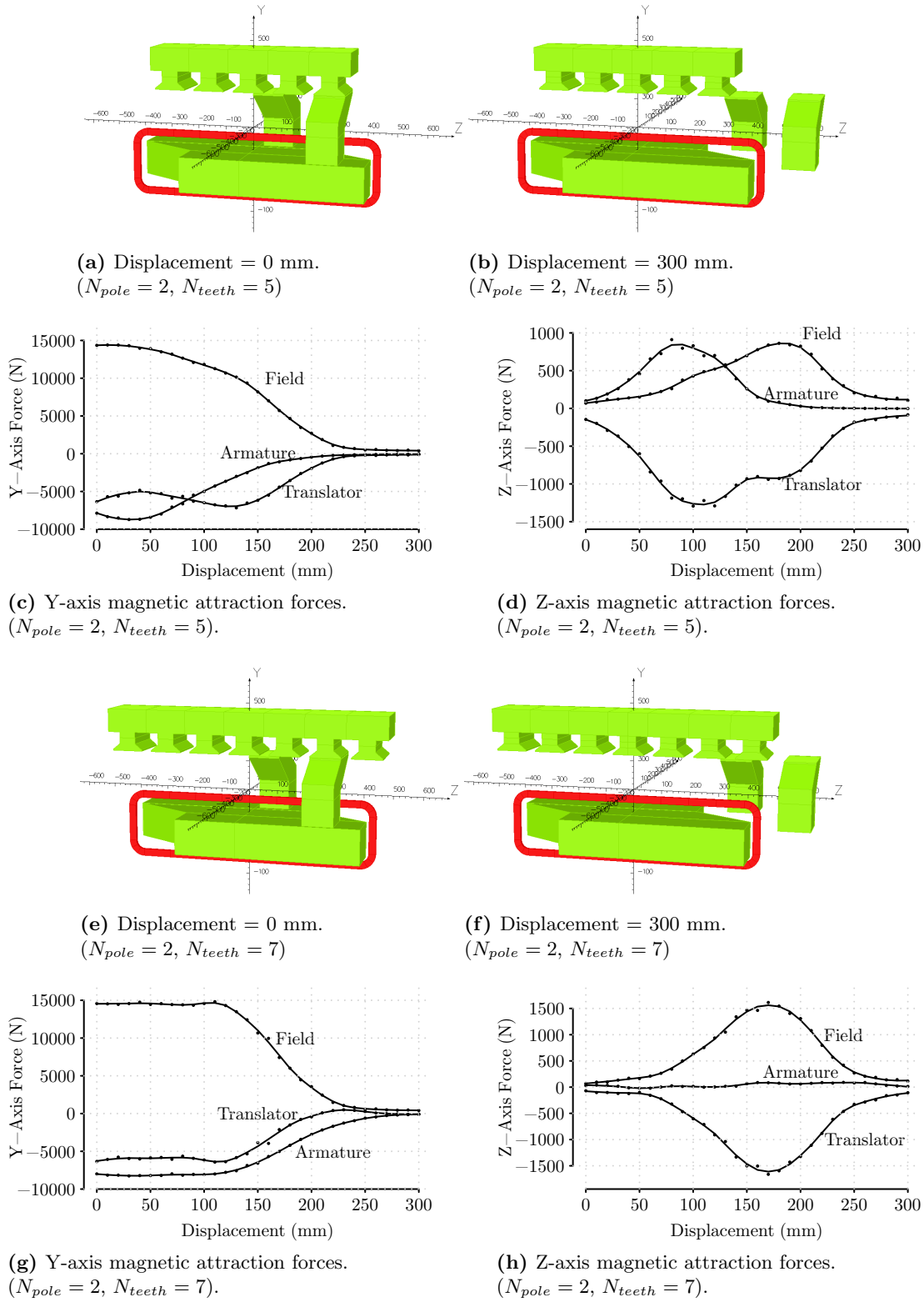


**Figure 7.4:** The magnetic attraction forces in Y and Z axes for translator, armature core and field core.

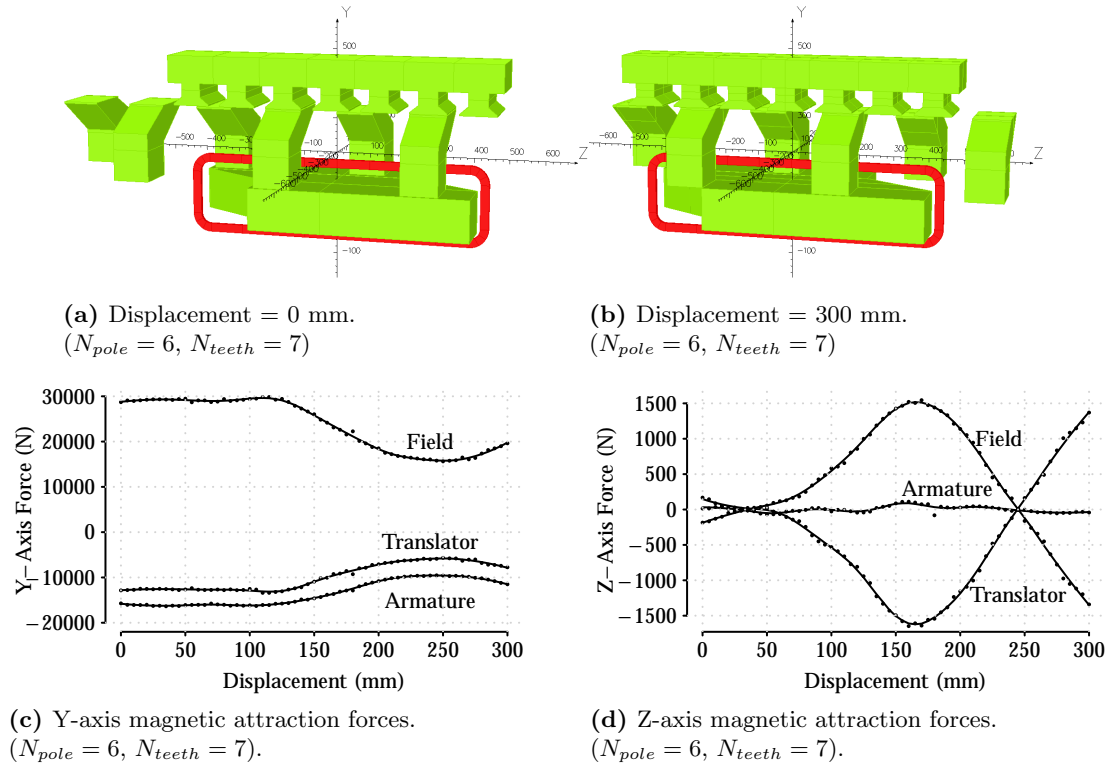


**Figure 7.5:** The magnetic attraction forces in Y and Z axes for the translator, the armature core and the field core.

### Flux Linkage

The core to pole ratio and the stator tooth to coil pitch ratio is varied and the average flux density and the flux linkage in the armature coils are recorded for each simulation<sup>3</sup>. The flux density increases as the claw pole pitch is reduced as shown in figure 7.6a and figure 7.6b. However, for the maximum power output, the value of the flux linkage multiplied by the conductor area (i.e. magnetic loading multiplied by the electrical loading) should be maximised., which is presented in Figure 7.6c. It is found that the optimum claw pitch to pole pitch ratio is around 0.75 and the optimum tooth pitch to coil pitch ratio is between 0.45 and 0.5.

<sup>3</sup>Opera\_logs\_graphs/2012/2012\_03\_11

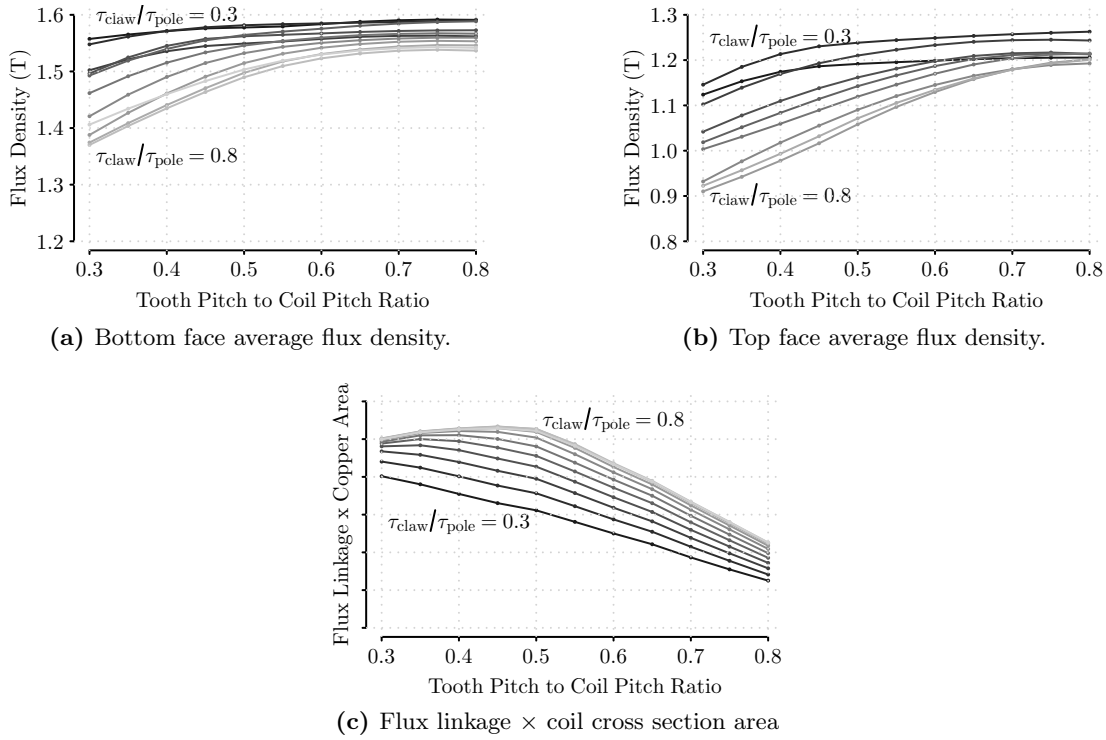


**Figure 7.6:** The flux density in the claw pole and flux linkage versus core-to-pole ratio and stator tooth to coil pitch ratio.

### Stator Teeth Skew

In Chapter 6, it was shown that the cogging torque can be reduced by skewing the stator teeth. In this section, the same technique is applied to the linear machine and the stator teeth are skewed as shown in figure 7.7b with the cogging force and flux linkage variations are presented<sup>4</sup>. Figure 7.7 shows the horizontal (Z-axis) force on the translator and the flux linkage in the middle tooth with and without the stator teeth skew. The maximum force without the skew is 120 N and it reduces to 98 N with a skew ratio of 0.9. The maximum flux linkage in the middle tooth reduces from 4.85 mWb to 4.37 mWb when the stator is skewed. Similar simulations are performed with five stator teeth<sup>5</sup> (instead of seven) and results are plotted in figure 7.8. In this configuration the maximum cogging force is 107 N without the skew and 76 N with the skew. The peak flux linkage in the middle teeth is 5 mWb for non-skewed simulation and reduces to 4.6 mWb for the skewed one. The simulations showed that the cogging force can be reduced by skewing the armature teeth, however, this also reduces the flux linkage. The skew ratio is chosen as 0.5 as a medium between maximum flux linkage and minimum cogging torque.

<sup>4</sup> :Opera\_logs\_graphs/2012/2012\_03\_15

<sup>5</sup> :Opera\_logs\_graphs/2012/2012\_03\_24

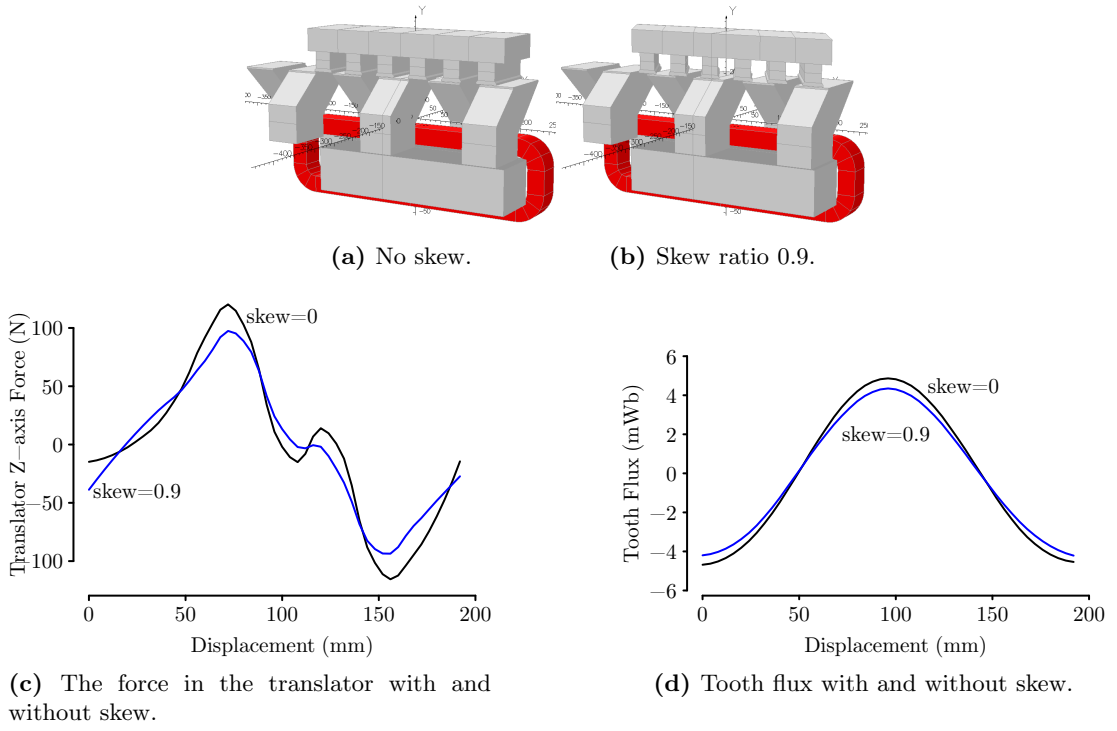


**Figure 7.7:** Effect of skewing on the cogging force and the flux linkage. ( $N_{teeth} = 7$ ).

The direction of the skew is also investigated. The armature can be skewed in the same direction or in the reverse direction with respect to the field core<sup>6</sup>. The simulations showed that the cogging force is slightly less when the armature core skew is in the same direction with the field core.

### Field Core Length and Coil Pitch

In this section, firstly the effect of the field core length to the cogging force and the flux linkage is investigated<sup>7</sup>. It is found that the flux linkage does not vary with the field core length, however the cogging force reduces with the field core length as presented in figure 7.9. The reason for that is as the difference between the field core length and total armature core length increases, the magnetic pull effect due to the minimum reluctance position becomes less dominant.

Secondly, the effect of the stator coil pitch to the cogging force and flux linkage is investigated<sup>8</sup>. The results are tabulated in table 7.1. In the simulations the pole pitch is kept constant at 96 mm. The maximum flux linkage is achieved when the coil pitch is around 64–72 mm (8/12–9/12 of the pole pitch).

<sup>6</sup> \Opera\_logs\_graphs\2012\2012\_06\_13

<sup>7</sup> \Opera\_logs\_graphs\2012\2012\_06\_05

<sup>8</sup> \Opera\_logs\_graphs\2012\2012\_06\_14



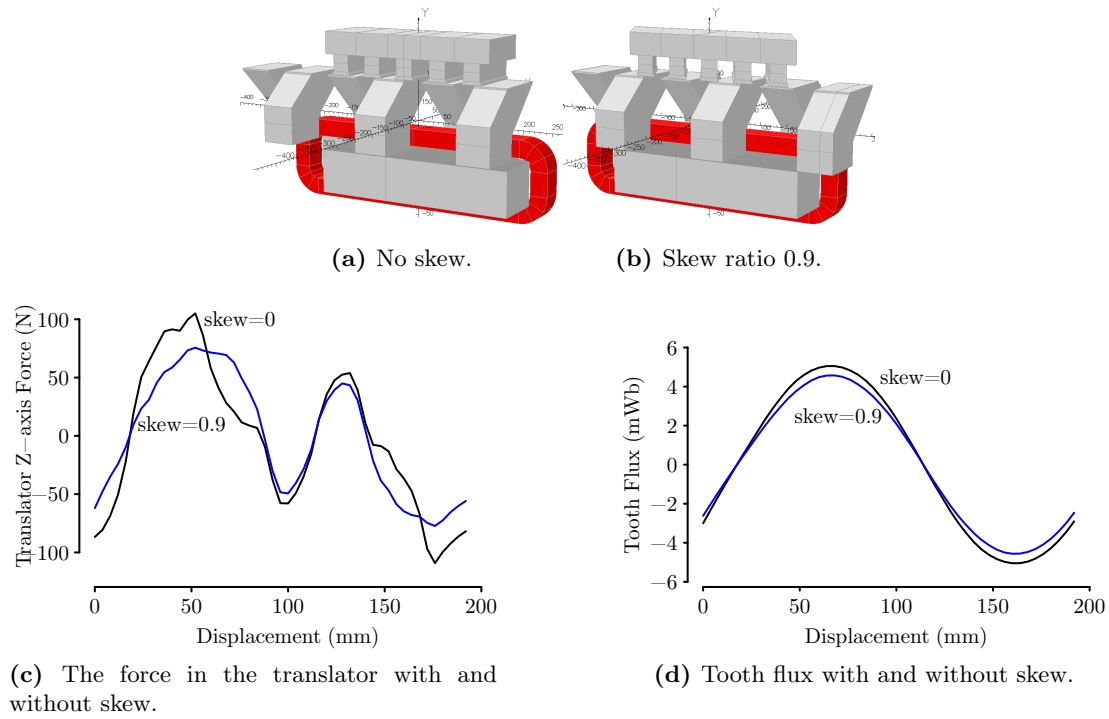


**Figure 7.8:** Effect of skewing on the cogging force and the flux linkage. ( $N_{teeth} = 5$ ).

## 7.2 Assembly of the Machine

The FEA simulations presented in the previous section are used to determine the optimum dimensions of the prototype. The technical drawings of the prototype are presented in Appendix I and the main dimensions are tabulated in table 7.2. The machine was manufactured by Fountain Design Ltd [6].

It has been showed in the simulations that the net magnetic attraction force acting on the translator is towards the field core. Thus, if the machine is turned upside down

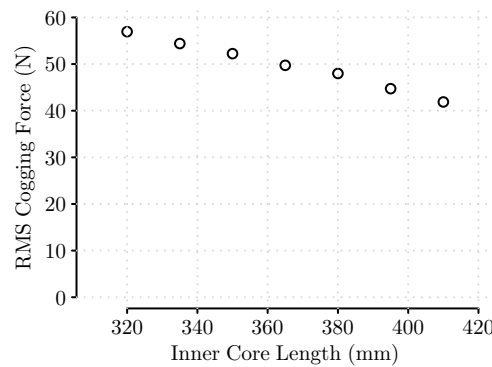


**Figure 7.9:** RMS cogging force versus the field core length.

Stator Coil Pitch (mm)	56	64	72	80	88
Maximum flux linkage (mWb)	4.13	4.52	4.59	4.43	4.29
RMS cogging force (N)	25.3	47.9	49.4	45.3	55.2

**Table 7.1:** Maximum flux linkage and cogging force variation with stator coil pitch.

$N_{pole}$	8
$N_{teeth}$	5
$\tau_{pole}$	96 mm
$\tau_{coil}$	64 mm
$a_c$	1.5 mm
$w_{claw}$	100 mm
$w_{core}$	80 mm
$\tau_{core}$	60 mm
$w_{gap}$	60 mm
$h_{gap}$	40 mm

**Table 7.2:** Main specifications of the linear prototype.

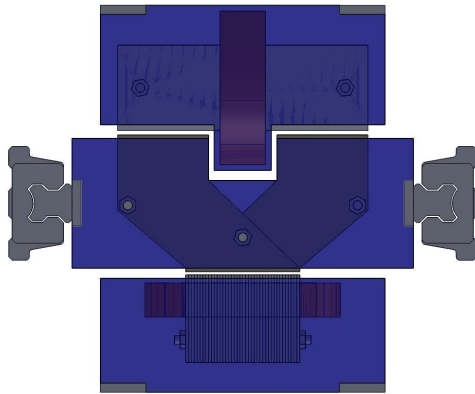
(w.r.t. to the one presented in figure 7.1), the magnetic attraction force can be balanced by the weight of the translator and there would be less force on the bearings. This configuration is presented in figure 7.10a.

Initially, it was planned to cover the cores and the coils with epoxy resin blocks to increase the structural integrity of the machine, as presented in figure 7.10a. However, initial tests showed that this was not really applicable as the large volume of resin required resulted in cracks during the curing process (see figure 7.10b), which is due to different heat transfer ratios of iron parts and epoxy resin. The large volume of epoxy and iron made it difficult to have uniform cooling in the mould. Therefore, it was decided to construct an aluminium structure around the translator.

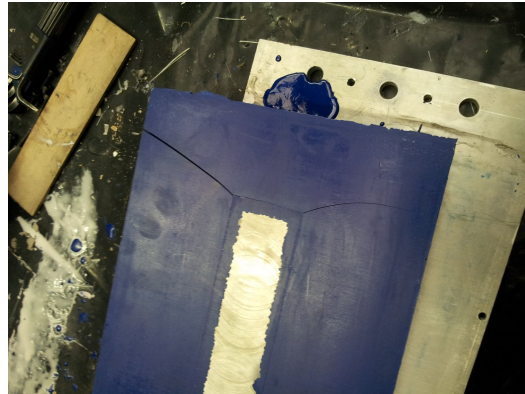
### The Field Core

The field core is placed on top of the translator. The schematic of the field core is presented in figure 7.11a. The field winding is resin impregnated, and fixed to the field core using tufnol isolation plates. The field core is attached to the main frame by using aluminium plates bolted to laminations with stainless steel screws.

In FEA simulations, it has been proposed to use bent laminations (see figure 7.2), however, these were found to be difficult to manufacture. Therefore, straight laminations are used as shown in figure 7.11b. The lamination skew is adjusted according to the pole pitch, so that the bottom claw pole surfaces are connected through lamination direction.

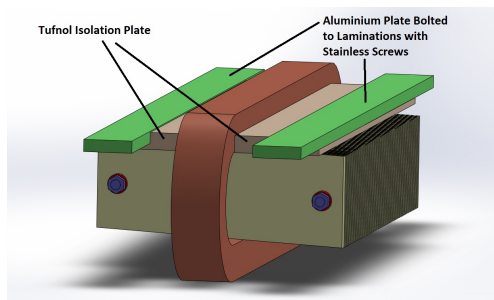


(a) Linear machine with field core on top.

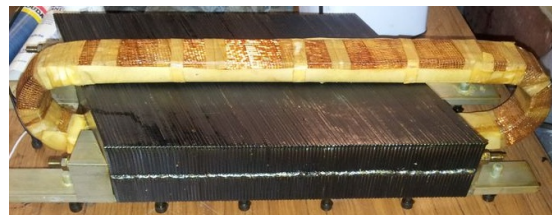


(b) Cracked epoxy resin.

**Figure 7.10:** Initial design of the prototype with epoxy supported structure.



(a) Schematic of the field core.



(b) Manufactured field core.

**Figure 7.11:** The field core and the field winding.

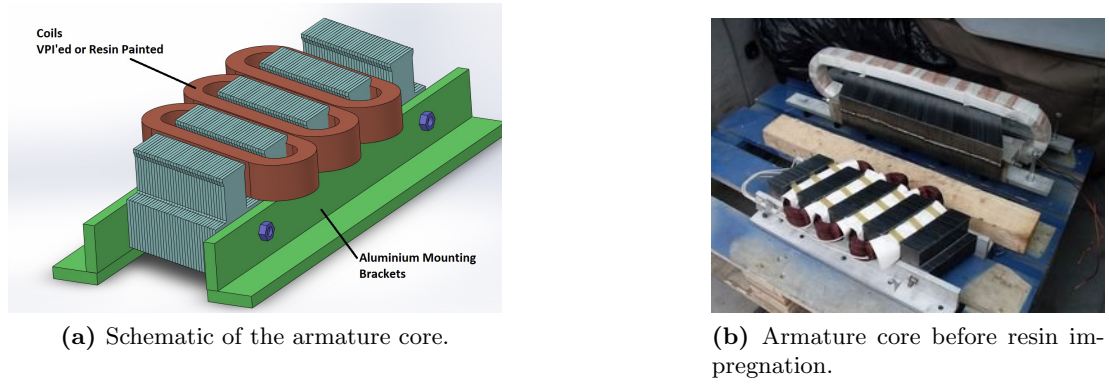


**Figure 7.12:** The armature of the linear prototype.

**Table 7.3:** The main specifications of the linear prototype.

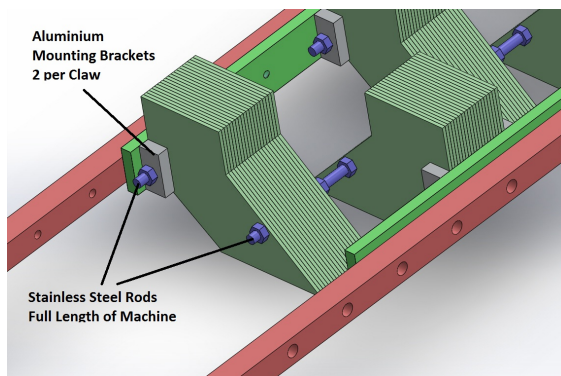
Stroke Length	500 mm
Total Mass	253 kg
Width of Laminations	3 mm
Field Coil Wire Diameter	1.6 mm
Field Coil Number of Turns	364
Field Winding Fill Factor	0.61
Armature Coil Wire Diameter	1.25 mm
Armature Coil Turns	190
Armature Winding Fill Factor	0.60

### The Armature Core

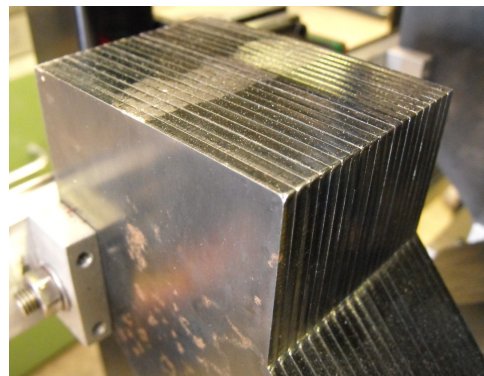
The armature has five teeth and three concentrated coils as shown in figure 7.12a. The core is mounted to the main frame by using aluminium brackets. The stator teeth have a skew ratio of 0.55. The main specifications of the armature coils are presented in table 7.3.

### The Translator

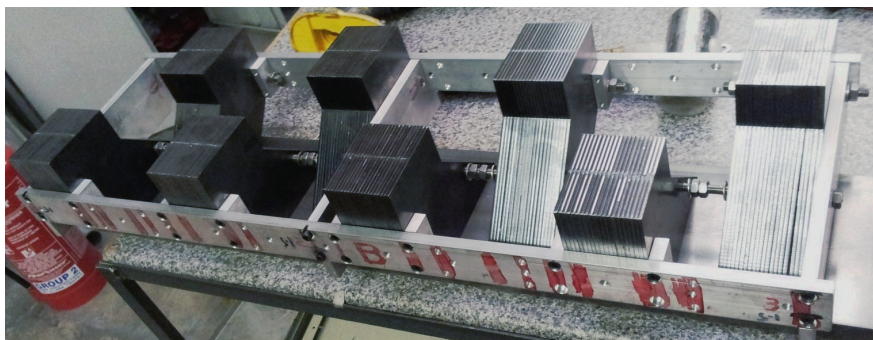
The claw poles are made of steel laminations, which are attached together by using two stainless steel rods as shown in figure 7.13a. The position of drilling holes are chosen to minimize the effect to the magnetic circuit while giving enough stiffness for mechanical integrity. Finally, the claw poles are mounted to an aluminium frame as shown in figure 7.13c. The frame and the connection bolts should be non-magnetic to prevent any magnetic short-circuit between adjacent poles.



(a) Schematic of the translator.



(b) Close-up view of claw pole laminations.



(c) Translator with the aluminium frame.

**Figure 7.13:** The translator of the linear prototype.

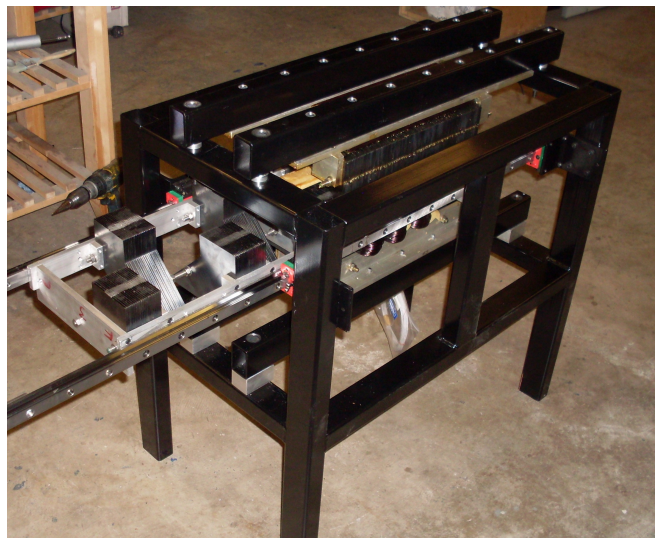
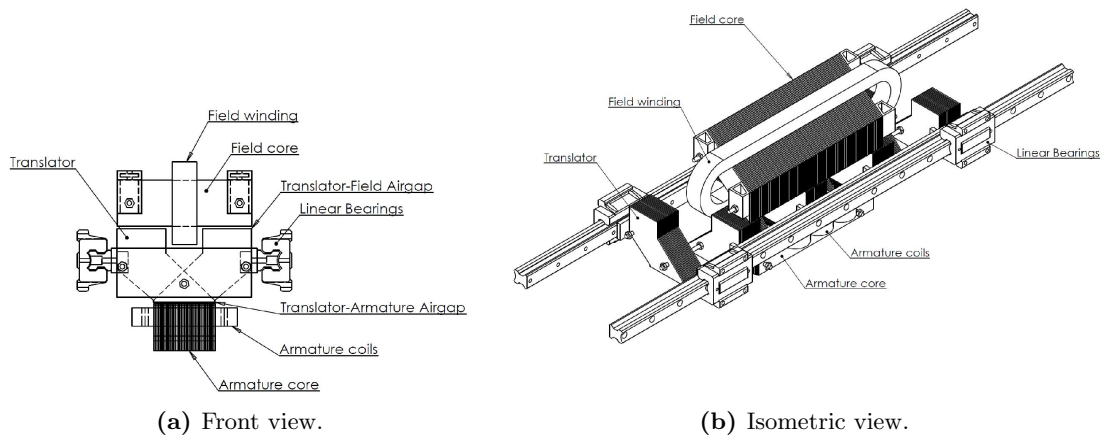


**Figure 7.14:** Mechanical structure of the linear claw pole machine and the assembled machine (Translator is suspended by four bearings).

### Assembled Machine

The assembled machine is shown in figure 7.14. The main specifications of the machine are presented in table 7.3. The air-gap clearance is 1.5 mm and the translator is attached to the frame using four linear bearings. No actuator is installed, instead the translator is moved manually by hand. The translator position is recorded by a draw-wire position sensor.

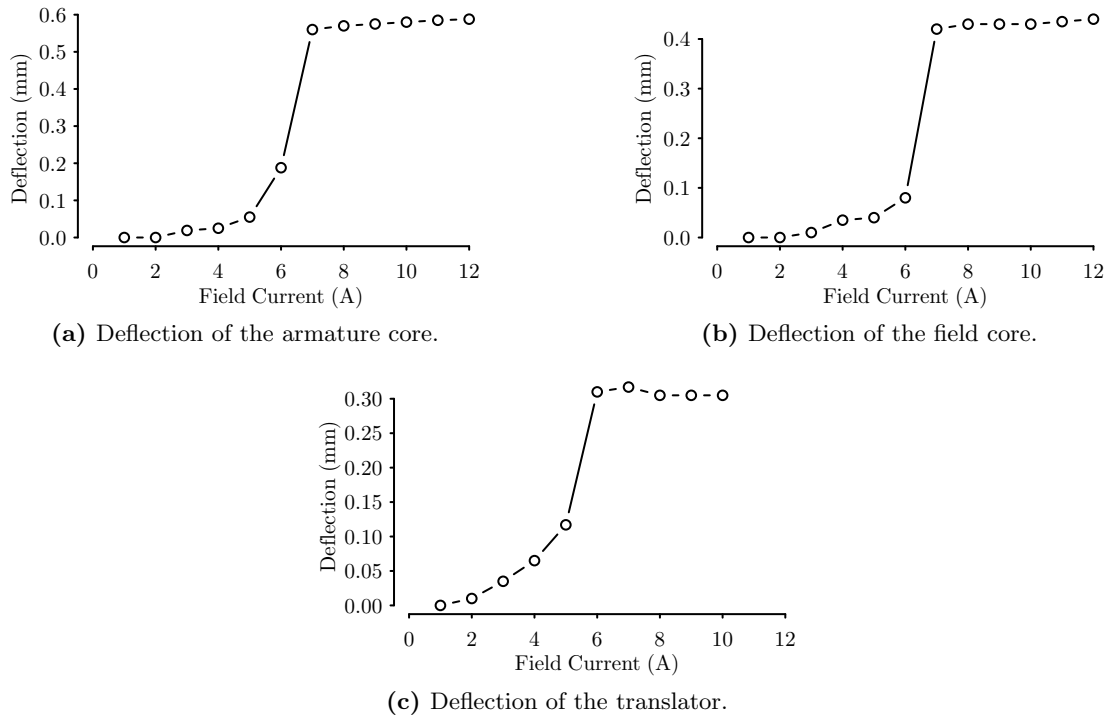


**Figure 7.15:** Deflection in the machine structure with four linear bearings as a function of the field current.

## 7.3 Experiment Results

### 7.3.1 Deflections in the Air-gap Clearance

It has already been mentioned that the magnetic attraction forces in the linear prototype do not have a cyclic symmetry. Therefore, the machine components observe a large net force. In this section, the effect of these forces to the air-gap clearance was investigated.

The main structure of the machine consists of 40x60 mm steel box section with a wall thickness of 5 mm (see figure 7.14c). The field winding is excited with direct-current and the deflection of the armature core, the field core and the translator are measured by a mechanical displacement gauge<sup>9</sup>. The gauge is placed to the middle of the structure, where the maximum deflection occurs.

The deflection amount as a function of the field current is presented in figure 7.15. From the figures, it can be seen that the deflection is proportional to the square of the field current up to 6 A. However, as the field current is further increased, it gets into a feed-forward mechanism, in which the deflection of the air-gap increases the flux density in the air-gap and this increases the magnetic attraction forces in return, which

<sup>9</sup>:LinearPrototype/Experiments/2012\_10\_09



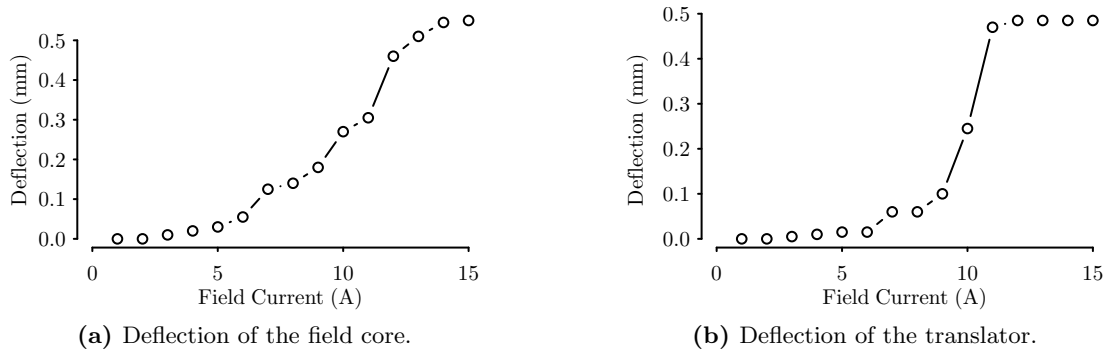


**Figure 7.16:** Deflection in the machine structure with six linear bearings as a function of the field current.

eventually results in the closure of the air-gap for currents larger than 7 A. This was the biggest challenge in the testing, as it was impossible to test the machine at the rated field current (15 A). The translator structure is initially supported by four linear bearings. The stiffness of the structure is aimed to be increased by the addition of an extra two bearings at the centre of the machine, where the maximum deflection occurs. Furthermore, extra box sections were welded to the existing ones that support the field core.

The deflection as a function of the field current is presented in figure 7.16. From the figure, it may be seen that the deflection amount is reduced with respect to the four bearings configuration. However, the air-gap still closes for currents larger than 12 A. Further investigation showed that the structure does not deflect as a whole, instead the bolts and joining parts are all contributing to it. In particular, the way that the field laminations are fixed requires further improvement.

### 7.3.2 Flux Linkage Tests

At normal operation, the field winding is excited with DC, however, in this section it is excited with AC instead. In this way, the machine basically operates as a transformer and there is no need to move the translator to observe induced voltage in the armature coils. The armature coil voltage is presented in figure 7.17 when the field winding is excited with 50 Hz AC.

In order to observe distribution of the flux linkage in the claw pole, three search coils are wound at the base of the claw pole, at the middle of the claw pole and the tip of the claw pole as shown in figure 7.18. There are 10 turns on each search coil and the armature coils have 190 turns. The induced voltage magnitudes at 2.42 A field current are presented in table 7.4. The flux linkages at each position are calculated and the ratio of the flux travelling through the claw pole are presented, which shows



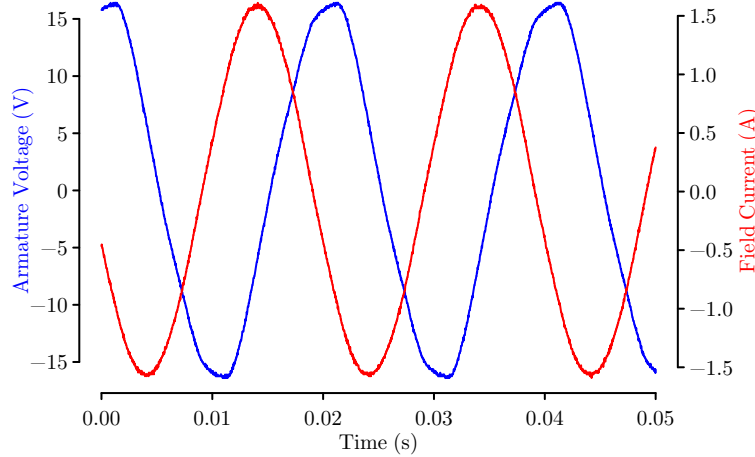


**Figure 7.17:** Induced voltage in the armature coil with AC field current.

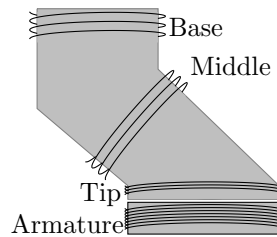


**Figure 7.18:** The position of the search coils in the claw pole field to estimate the flux linkage.

that almost 75 % of the flux entering to the claw pole links the armature coils. This is consistent with the FEA results in general where it is found to be that 70-80 % of the flux is linking the armature coils depending on the dimensions. Similar tests were performed with variable field currents<sup>10,11</sup> and the results are plotted in figure 7.19.

### 7.3.3 Flux Density Comparison

In the tests in this section, the field winding is excited with DC and the flux density in the air-gap is measured using a Gaussmeter with a transverse flux hall probe<sup>12</sup>. Two 1.5 mm aluminium L-profiles are placed at the top air-gap to protect the probes by limiting the air-gap deflection and to make a better comparison with FEA simulations. Four measurements are taken from the centre of the base and top air-gap for each field current value and the results are presented in table 7.5<sup>13</sup>. The results show good agreement between experimental results and FEA simulations; the maximum error is

<sup>10</sup>Ⓛ:LinearPrototype/Experiments/2012\_10\_12

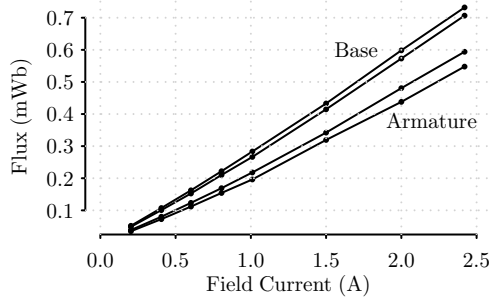
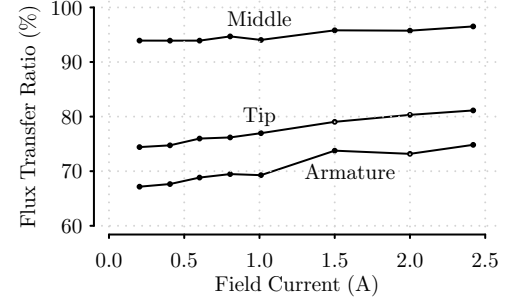
<sup>11</sup>Ⓛ:LinearPrototype/Experiments/2012\_10\_15

<sup>12</sup>Hirst Magnetic Instruments Ltd - HMIRS GM08

<sup>13</sup>Ⓛ:LinearPrototype/Experiments/2013\_05\_09

**Table 7.4:** Induced voltage and flux measurements with a 2.42 A, 50 Hz field current.

	Induced Voltage ( $V_{\text{rms}}$ )	Number of Turns	Flux ( $\text{mWb}_{\text{rms}}$ )	% of Flux Transfer
Claw Pole (Base)	2.31	10	0.732	100
Claw Pole (Middle)	2.22	10	0.707	96.6
Claw Pole (Tip)	1.87	10	0.594	81.1
Armature Coil	32.7	190	0.548	74.9

**(a)** Flux linkage in the claw pole and armature coil.**(b)** Transfer ratio of the flux.**Figure 7.19:** Flux linkage in the claw pole sections and armature coil.

12 %. The results are also plotted in figure 7.20. The slight effect of saturation is observable in the FEA results curve. However, in the experimental results there is an opposite effect (i.e. the slope of the line increases), which is due to deflection of the air-gap. At higher field currents, the air-gap clearance gets smaller which results in higher flux density measurements than in the FEA simulations.

**Table 7.5:** Comparison of FEA simulations with experimental results.

Field Current	Top Air-gap			Bottom Air-gap		
	Measurement	FEA	Error	Measurement	FEA	Error
6 A	0.38 T	0.428 T	+12.6 %	0.34 T	0.376 T	+10.6 %
8 A	0.54 T	0.571 T	+5.7 %	0.46 T	0.498 T	+8.3 %
10 A	0.68 T	0.711 T	+4.5 %	0.58 T	0.592 T	+2.1 %
12 A	0.83 T	0.840 T	+1.3 %	0.72 T	0.703 T	-2.4 %
14 A	1.02 T	0.948 T	-5.2 %	0.87 T	0.815 T	-6.3 %

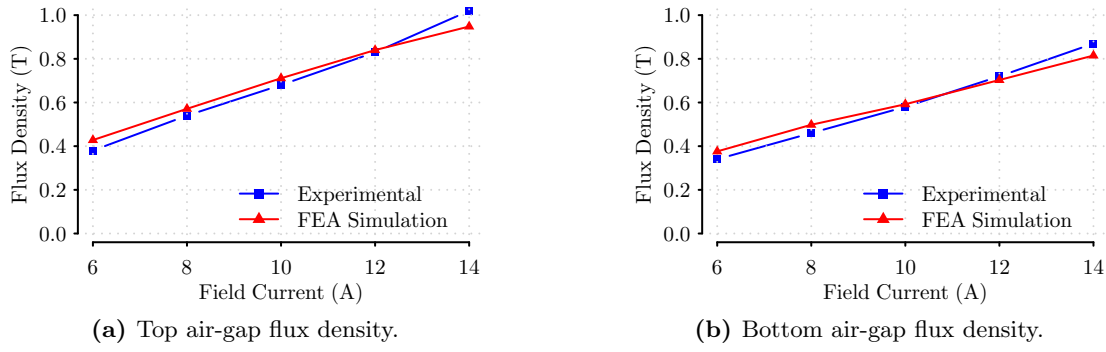


**Figure 7.20:** Comparison between FEA and experiment results.

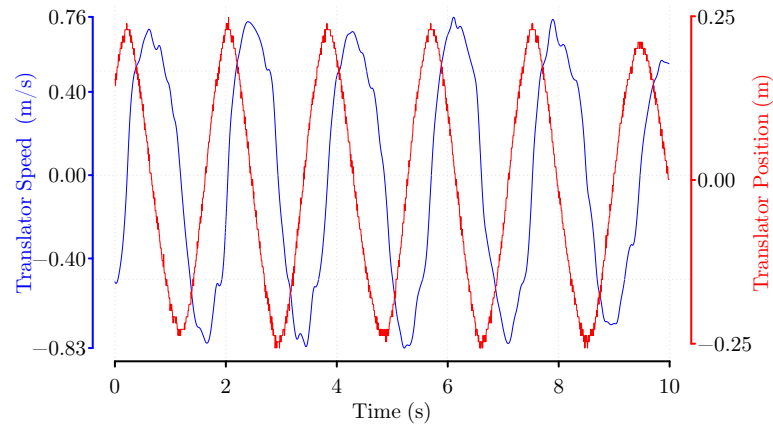
### 7.3.4 Induced Voltage Tests

In this section, the induced voltage characteristics of the linear prototype are presented. The field winding is excited with DC and the position of the translator is recorded with a displacement sensor. Figure 7.21a shows the speed and position of the translator while it is being moved manually by hand. The maximum speed is around 0.8 m/s. It is quite slow considering the linear speed of the rotor in a direct-drive generator, which is usually around 3–4 m/s. The induced phase voltages are presented in figure 7.21b. The maximum voltage magnitude is 11.6 V. The electrical frequency of the induced voltage at 0.8 m/s is 4.16 Hz.

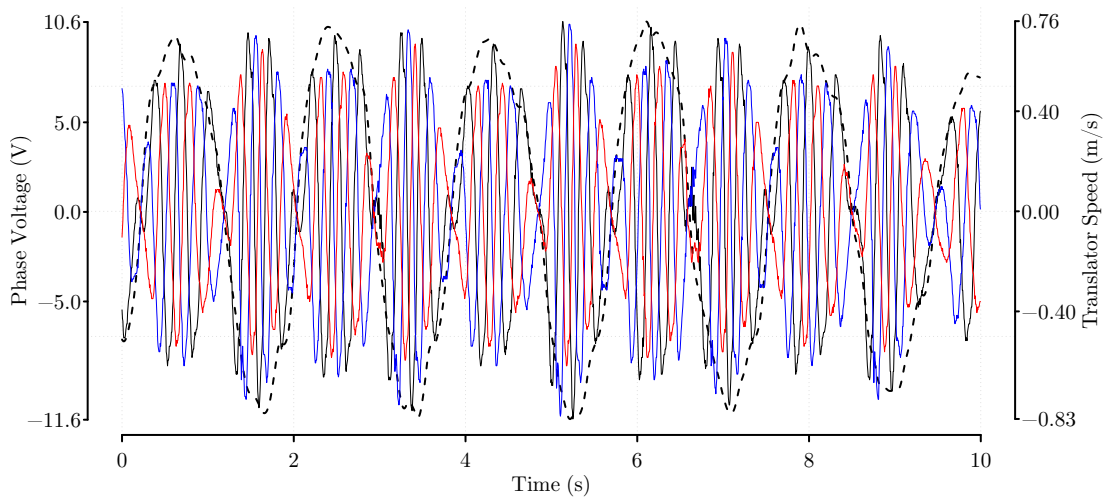
In order to compare the induced voltage waveforms with FEA simulations, the flux linkage in the stator teeth are simulated at 560 different positions with 1 mm displacement<sup>14</sup>. The flux linkage versus the position of the translator is presented in figure 7.22. The maximum flux linkage in the middle coil(phase B) is 2.24 mWb. Assuming a constant speed of 0.76 m/s, the maximum induced voltage in phase B can be calculated as 10.58 V, which is very similar to the maximum voltage induced in figure 7.21b.

Finally, the same speed profile presented in figure 7.21a is applied to the flux linkage data and the induced voltage is calculated and presented in figure 7.23. Figure 7.23b compares FEA results with experimental results (grey lines). As seen from the figures, the FEA simulations and the experimental results are consistent. The mean error of the peak phase-B voltage is 8.8 %. The experimental results are slightly larger than the FEA simulations, which is thought to be because of the deflection of the structure, similar to the one presented in figure 7.20.

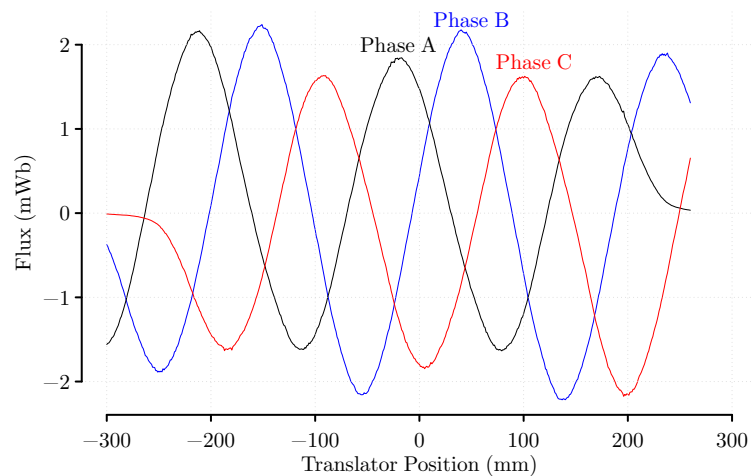
<sup>14</sup>[D:\LinearPrototype\Experiments\2012\\_10\\_12](#)

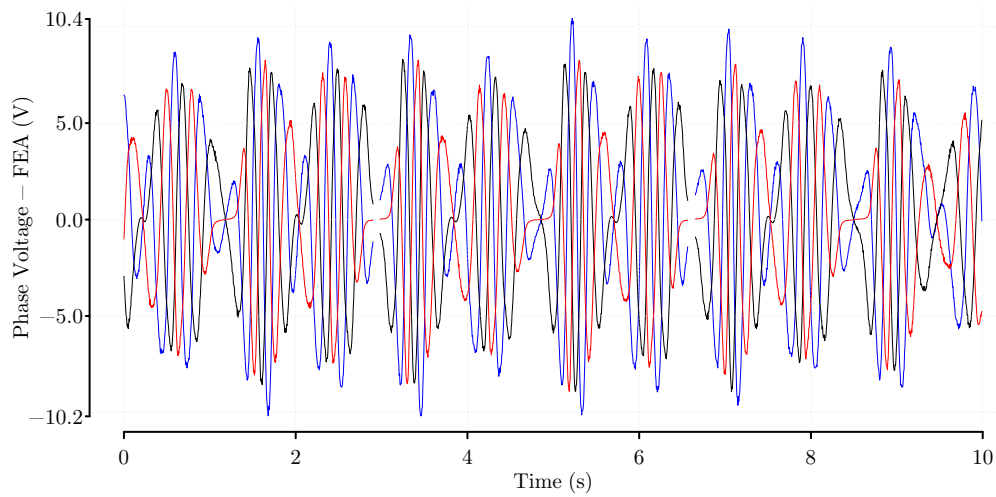


(a) Linear machine translator speed and position.

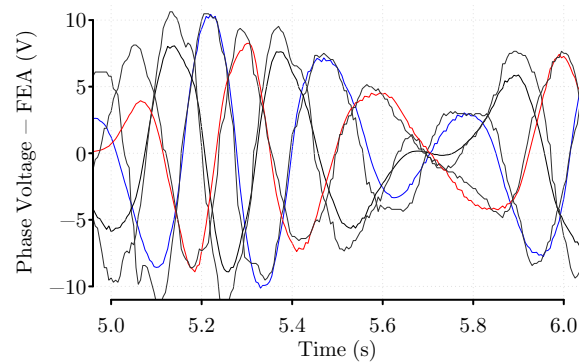


(b) Induced phase voltages with reciprocating motion of the translator.

**Figure 7.21:** Induced phase voltages and translator speed characteristic.**Figure 7.22:** FEA simulation of the flux linkage in the armature coils with translator position.



(a) Induced phase voltages.



(b) Comparison of FEA and test results.

**Figure 7.23:** FEA simulated phase voltages (Grey line: experiment result).

## 7.4 Conclusion

In this chapter, the design and manufacture of a linear prototype are presented. It was aimed to highlight the challenges in manufacturing and to verify the FEA simulations.

A linear claw pole topology has extra challenges compared to the rotational one, most of them related to unbalanced magnetic pull. To begin with, the magnetic attraction forces do not have cyclic symmetry as in the rotational machine. Thus, large net forces act on the machine components, which deflects the air-gap at high field currents. Secondly, the claw-poles are pulled horizontally when ‘entering’ or ‘leaving’, this force can be cancelled-out by varying the field core and armature core length.

The prototype was manufactured using electrical steel laminations. The support structure of the claw poles was a serious challenge as it has to be stiff enough without affecting the magnetic circuit. At first, an epoxy resin was used, but after a few unsuccessful attempts, it was replaced by an aluminium frame, which is fixed to the claw poles by steel bolts. Furthermore, two extra linear bearings are installed to reduce the translator deflection. However, it is found that the field core structure was the weakest point, which triggers the closure of the air-gap for field current higher than 10 A.

The primary aim of the linear prototype was to verify the FEA simulations. It is found that the experimental results are in good agreement with the FEA simulations, with less than 10 % error for most of the cases. In some tests, the measured phase voltage and the air-gap flux density exceeded the simulation results, which is found to be because of the deflection of the structure.

Apart from verifying the FEA simulations, the tests also showed that the structural design of the claw pole topology requires further investigation. Although, the structural design of a rotational prototype will be easier due to the cyclic symmetries, these forces will still put large stresses on the structure in a large scale machine. It is therefore, necessary to modify the radial claw pole topology to cancel out some of the magnetic attraction forces.



# Up-scaling for Large Power: Double-Claw Pole Design

---

In the previous chapters, a claw pole superconducting machine topology was proposed and the test results of a linear prototype were presented. Although, the claw pole topology is superior to the homopolar and bipolar superconducting machines, it has a few flaws, which are mostly because of the mechanical challenges, especially for large diameter machines. Firstly, the claw pole topology requires soft-magnetic composite (SMC) material, which is difficult to be manufactured in large pieces and not as strong as the electrical steel. Secondly, the unbalanced magnetic attraction forces put extra stress on the mechanical structure, which makes it difficult to build a large diameter machine without a very sturdy and heavy structure.

In this chapter, a modified version of the claw pole will be presented. The topology is especially designed for large power applications. A 10 MW, 10 rpm wind turbine generator and a 36.5 MW, 120 rpm ship propulsion motor designs are presented.

## 8.1 Double Sided Claw Pole Machine

The schematic of the radial claw pole topology, which was introduced in Chapter 6, is depicted in figure 8.1a. This design can be modified by rotating the claw poles by 90 degrees to obtain an axial claw pole topology as shown in figure 8.1b. Although, this topology has not been investigated in this study, it is stated in [127] that this version can be more beneficial in terms of the mechanical design.

Then, two axial claw pole machines can be attached together as shown in figure 8.1c, in which they operate as two independent machines with separate flux paths. Finally, these machines can be combined to form a single machine as depicted in figure 8.1d. In this configuration, there is a single superconducting field winding, and the magnetic flux travels along the claw poles and links the independent armature windings on each end.



The claw pole geometry has also been modified and now there are two different claw pole geometries as shown in figure 8.2. The larger one magnetically connects the armature cores to each other. The smaller one carries the flux through the superconducting back-core. The magnetic attraction forces acting on the large claw pole are symmetrical and cancel each other (assuming the air-gap clearance on each side is equal). The rigid structure of the large claw poles makes it easier to connect them to the main rotor structure and the smaller claw pole can be connected to the large claw pole using a similar structure to that used in the radial claw pole machine.

The double-claw machine (figure 8.1d) is expected to be lighter than the one in figure 8.1c, since the mass of the back-core is reduced. Furthermore, the soft-magnetic composite material is no longer needed as the flux through the field core travels only in the axial direction, and the field core can be manufactured from steel laminations.

The advantages of the double-sided claw pole topology can be summarised as:

- Magnetic attraction forces on the large claw poles are symmetrical and cancel each other.
- Double armature winding configuration increases the modularity.
- SMC material is no longer required. All magnetic core sections can be manufactured using laminations.
- The superconducting coil back-core mass is reduced.

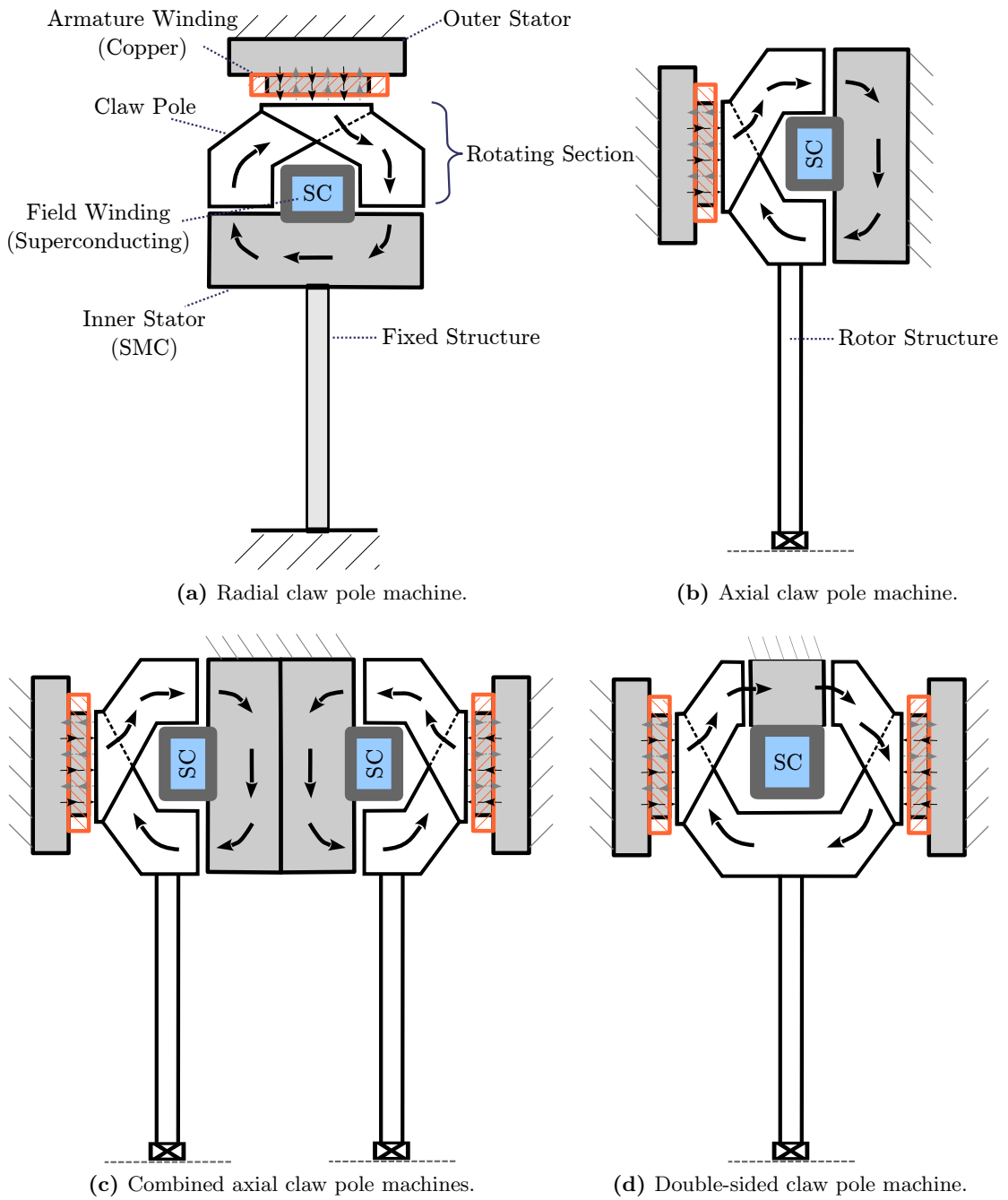
However, the flux path in the double-sided claw pole topology is longer than the initial design, in which the magnetic flux crosses the air-gap four times in a complete cycle. However, in the double-sided claw pole topology, it crosses the air-gap six times. Therefore, the machine requires more MMF in the superconducting coil for the same flux density and the leakage flux paths will be more dominant.

### 8.1.1 Analytical Model

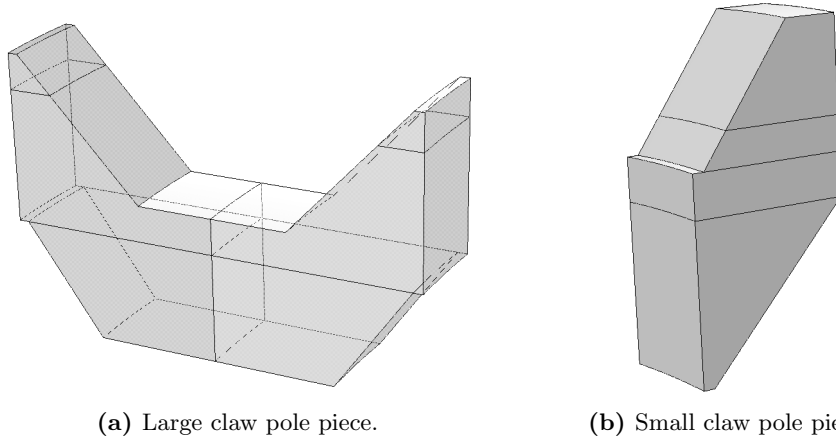
A basic reluctance network representation of the double-claw pole machine is presented in figure 8.3. Most of the parameters used in the magnetic circuit are equivalent to the ones used in the radial claw pole machine (see section 6.3). The extra reluctance elements used in this circuit are:

- $R_{claw1}$  The reluctance of the small claw pole.
- $R_{claw2a}$  The reluctance of the straight section of the large claw pole.
- $R_{claw2b}$  The reluctance of the bended section of the large claw pole.

The reluctances used in the magnetic circuit are defined in Appendix C.4.

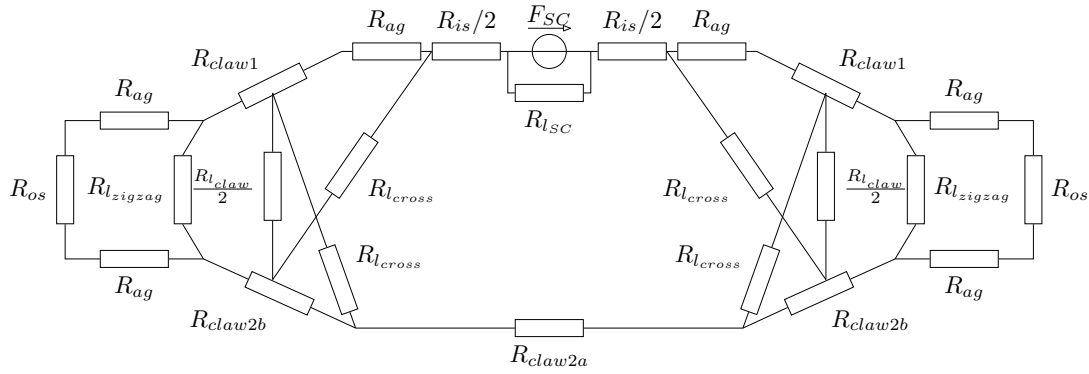


**Figure 8.1:** Evolution of the claw pole topology.



(a) Large claw pole piece.

(b) Small claw pole piece.

**Figure 8.2:** Two different claw pole shapes used in the double-claw pole topology.**Figure 8.3:** Magnetic circuit of the double-sided claw pole topology.

## 8.2 FEA Simulations

A parametrised model for the double-sided claw pole machine was developed using Opera with the same methodology that was described in section 6.4.

### 8.2.1 Material Selection: VacoFlux50

In the previous chapters, it was shown that the power output of the claw-pole machine is limited by the magnetic saturation, which uses electrical steel laminations and SMC material in the magnetic cores. The double-claw pole topology eliminates the SMC material, but still requires electrical steel laminations, which makes the choice of the lamination material critical.

Several product catalogues have been investigated and Vacuumschmelze's VacoFlux50 has been selected as the most suitable material. VacoFlux50 is a cobalt-iron alloy which can be manufactured in laminations and has an impressive magnetic saturation limit

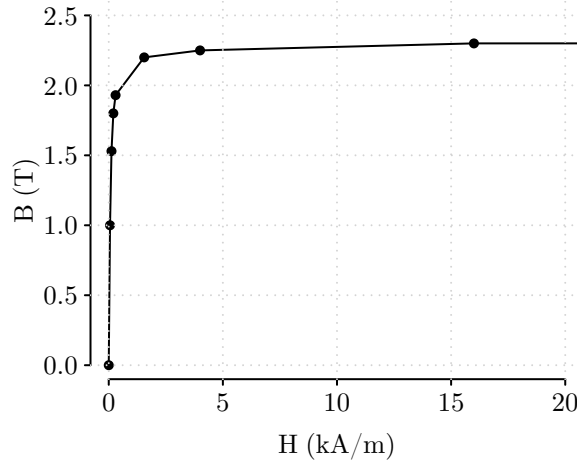


**Figure 8.4:** B-H curve for VacoFlux50 cobalt-iron alloy[163].

with 2.35 T at 16 kA/m [163]. The B-H characteristics of the VacoFlux50 is presented in figure 8.4. VacoFlux50 has a few variants, such as VacoDur with improved mechanical strength and VacoFlux17 with lower cost. In the double-claw pole machine simulations, VacoFlux50 is used. In [93] a standard non-oriented electrical steel is compared with VacoFlux50, and the core loss of VacoFlux at 50 Hz is given as 1 W/kg at 1 T and 3 W/kg at 2 T (similar compared to 2.5 W/kg at 1.5 T of a standard electric steel [159]). The core loss values at different frequencies can be found in the Vacuumschmelze's catalogues [163].

### 8.3 Electromagnetic Modelling

The 3D FEA model of the machine, which is presented in figure 8.5, has two symmetry planes:

- Rotational symmetry depending on the number of pole-pairs.
- Axial symmetry along the mid-plane passing through the superconducting coil.

The FEA model with these symmetries applied is presented in figure 8.5c. The flux density magnitude distribution in the machine is shown in figure 8.6. The machine has the following specifications<sup>1</sup>:

- Inner radius: 1 m
- Outer radius: 1.4 m
- Total axial length: 0.85 m
- Number of poles: 48
- Number of stator slots: 144

<sup>1</sup>[🔗:Double-side claw pole: Opera\\_logs\\_graphs/2013/2013\\_04\\_29\\_double\\_claw\\_varying\\_Nslot/](#)

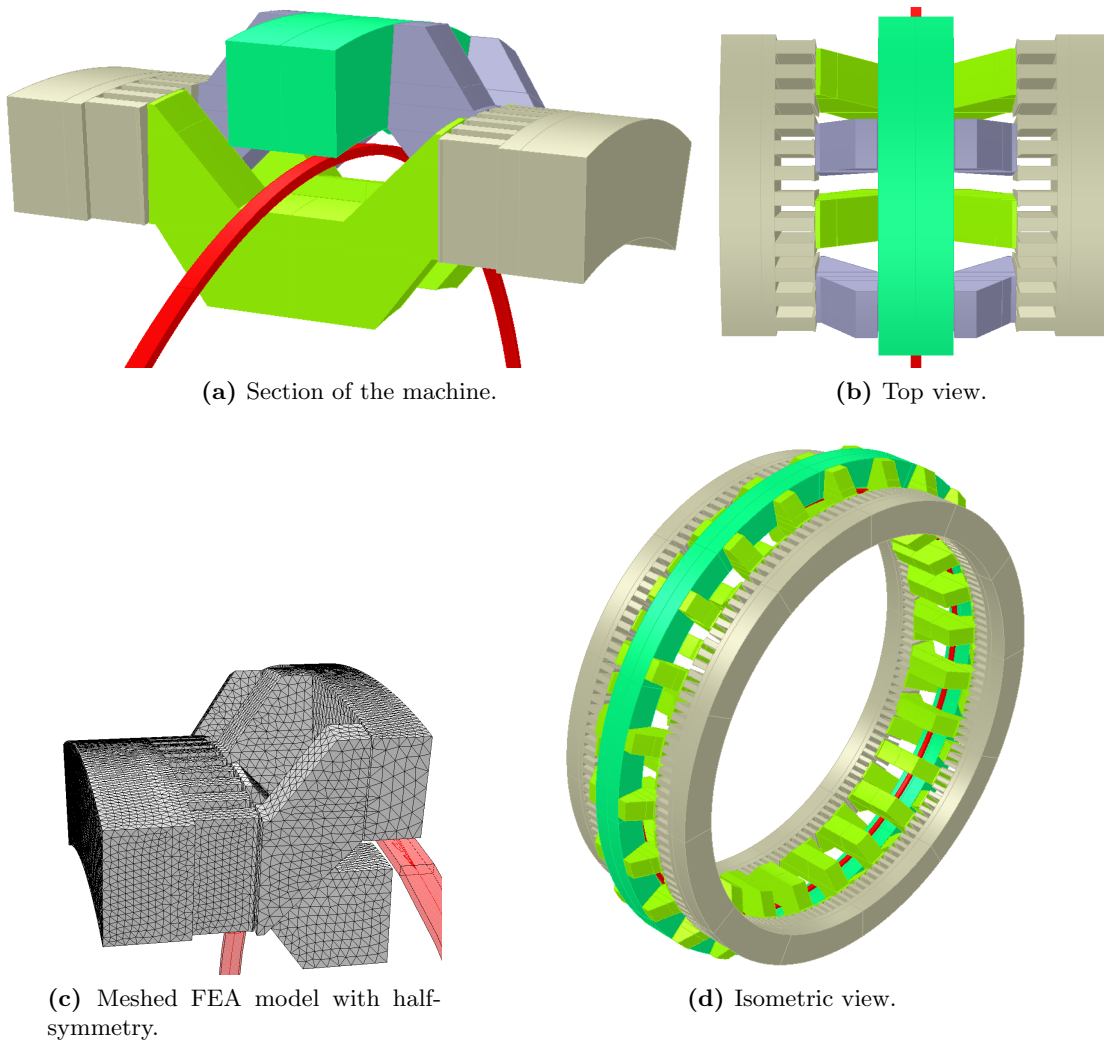


**Figure 8.5:** The double-claw pole machine model.

The flux density distribution in the core is presented in figure 8.6. From the figure, it may be seen that the magnetic core can be saturated up to 2.3 T. The stator teeth have the highest flux density (note that the dimensions are not optimised). The flux density vectors in the machine are shown in figure 8.8, which verify the operation of the double-claw pole topology as the magnetic flux created by the superconducting coil links both stator cores through the claw poles as depicted in figure 8.1d.

The flux density magnitude in the stator teeth at mid-coil radius is plotted in figure 8.7 for two different stator configurations. The graphs show that the flux density in the stator teeth can reach up to 2.1 T. Different FEA simulations are performed with the same parameters while varying the stator slot number<sup>2</sup>. The magnetic loading values

<sup>2</sup>[B:Double-side claw pole: 0pera\\_logs\\_graphs/2013/2013\\_04\\_29\\_double\\_claw\\_varying\\_Nslot/](#)

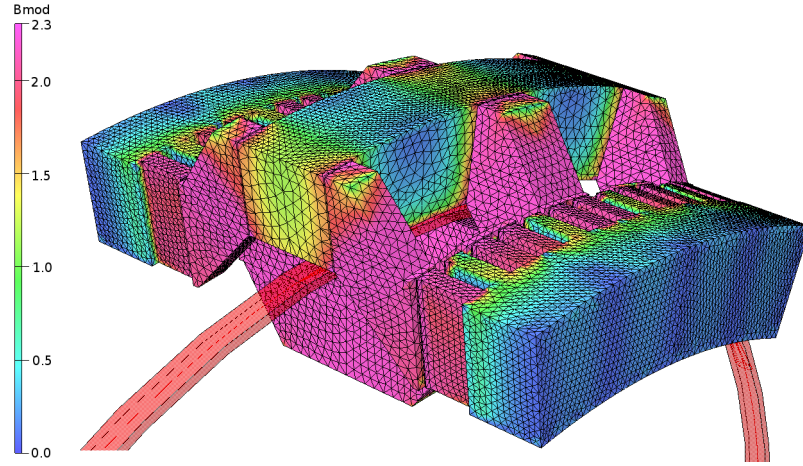


**Figure 8.6:** Flux density distribution in the double-claw pole topology.

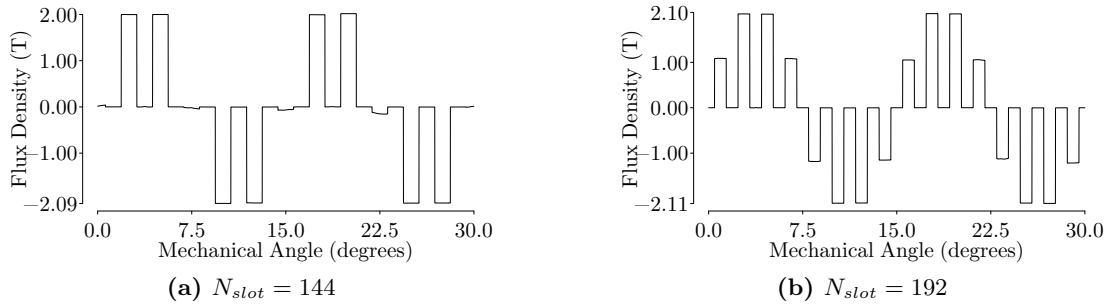
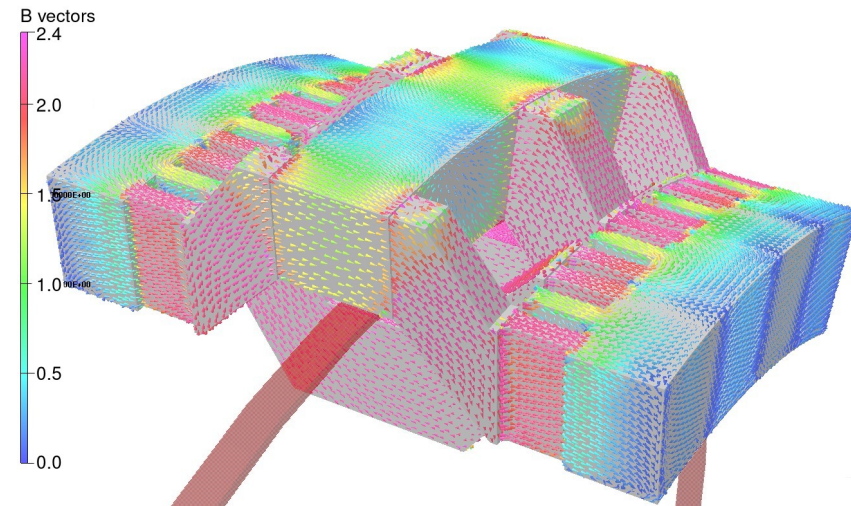


**Figure 8.7:** Flux density magnitude distribution in the stator teeth (mid-coil radius).

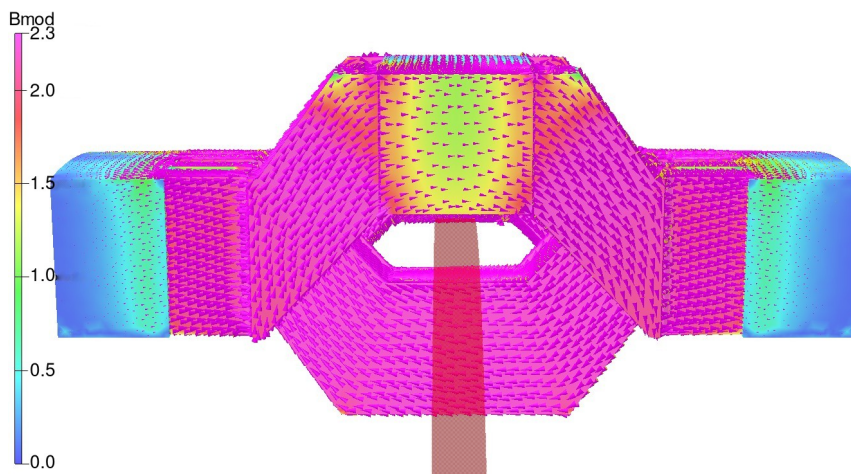
for different stator slot numbers are calculated in table 8.1. Although, the machine is not optimised, it is shown that magnetic loading up to 0.76 T can be achieved in the proposed topology. This improvement is the result of two factors: the high saturation levels of VacoFlux50 and the high magneto-motive force of the superconducting coil.

Number of Stator Slots	36	72	144	192
Magnetic Loading at Air-gap (T)	0.71	0.71	0.77	0.78
Magnetic Loading at Stator Teeth (T)	0.69	0.66	0.71	0.76

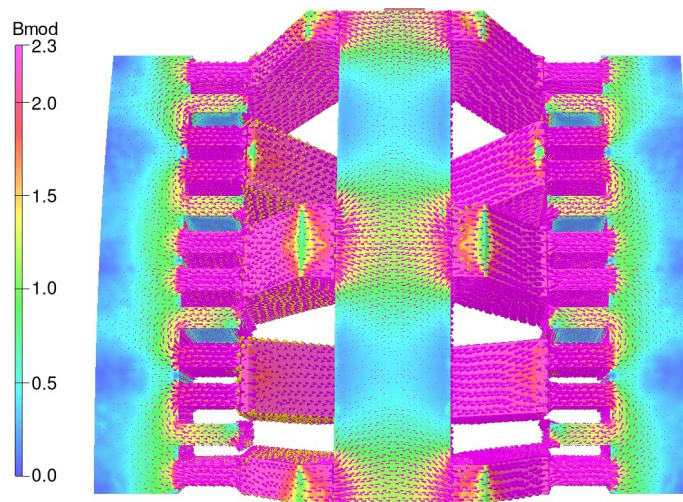
**Table 8.1:** Magnetic loading for double-claw pole topology with varying stator slot numbers.



(a) Isometric view (The vector colour is proportional to flux density magnitude).



(b) Right view (The vector size is proportional to the flux density magnitude).



(c) Top view (The vector size is proportional to the flux density magnitude).

**Figure 8.8:** Flux density vectors in the double-claw pole topology.



## 8.4 Sectioned Field Coil

The double-claw pole machine is designed for large diameter, high torque applications, but a single loop shaped superconducting coil (see figure 8.1d) can cause some problems in manufacturing and transportation. In the original design, the superconducting coil and the cryostat are fixed to the inner surface of the field core as shown in figure 8.9a. Assume that another coil is mounted on the outer surface of the field core as in figure 8.9b. These coils conduct current in the opposite directions, and the amount of the current in the coils can be halved to get the same amount of MMF in the field core. Thus, the total amount of the superconducting wire stays approximately the same (neglecting the difference between the outer and the inner circumference).

Now, assume that the cryostat and the field core are divided into two sections as shown in figure 8.9c. In this configuration, it is possible to manufacture and transport each core section separately. The field winding can be divided into smaller sections if required. The disadvantage is the total superconducting wire length is slightly increased due to the intersection areas, which becomes less important at larger diameters. There is no field core where the two cryostats are adjacent, thus the flux density in the claw pole and the armature teeth will be lower, but this effect is ignored in the simulations. It is also possible to divide the armature core into the same number of sections to coincide with the field core.

The field core can also be fixed to a T-shaped core as presented in figure 8.10. In this configuration the cryostat and the superconducting coil is mounted to the field core as in figure 8.10b. The main difference in this configuration is two armature windings are now magnetically independent i.e. there are two separate flux loops in the machine. The flux lines cross the air-gap four times, thus the MMF requirements are reduced. However, the flux has to travel in the field core in a three-dimensional way, which requires SMC to be used. Furthermore, there are radial magnetic attraction forces acting on the large claw pole. Therefore, this configuration is not very suitable for large diameter machines, and the configuration presented in figure 8.9c is used throughout this chapter.

## 8.5 Optimisation

In the previous chapters, FEA models are used, but no optimisation algorithm was applied to get the most suitable dimensions for maximum power or torque density. In this section, the double-claw pole topology is optimised by coupling the FEA model with a genetic algorithm optimisation tool.



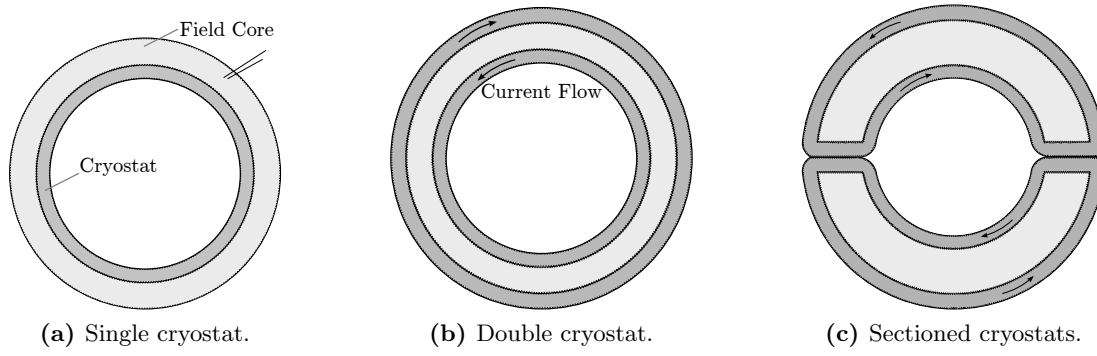


**Figure 8.9:** Different cryostat designs for the double-claw pole machine. Front view.

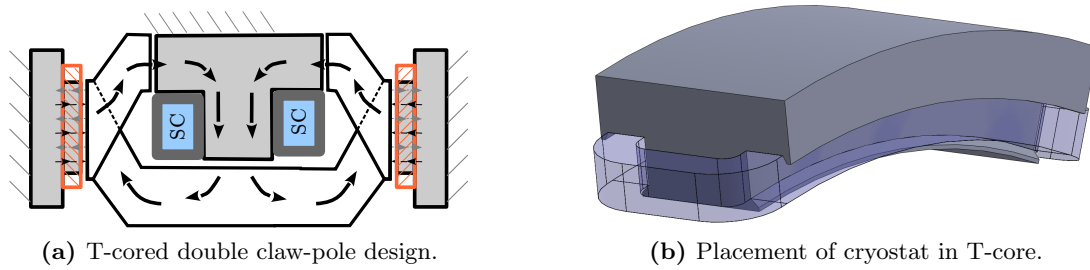


**Figure 8.10:** T-core option for the double-claw pole machine.

### 8.5.1 Genetic Algorithm Optimisation

Genetic Algorithm (GA) optimisation is a non-deterministic optimisation algorithm that mimics the biological evolution process [170]. It is stated in [170] that GA is a global search method, so it has little possibility to trap in a local minima. One advantage of GA is that it does not require derivative information, which makes it easier to implement to non-linear problems, and it is considered to be one of the most effective algorithms for optimisation of electric machines [33].

GA is an iterative process that creates a set of design candidates depending on the individuals performance. When the GA is started, an initial population, usually bigger than normal population, is created. The best individuals are selected in the initial population, which are then used to breed the next generation. After two individuals are selected, a crossover and recombination algorithm is applied to generate new individuals. Different averaging, interpolation or extrapolation techniques may be applied. For a small number of inputs, a single cross over point is usually sufficient. Higher number of crossovers and random mutations are used to encourage the GA to search on a wider space, and minimise the chance of trapping in a local minima.

After the new offspring is generated, the individuals are sorted according to their fitness value and the best individuals are selected for the next generation. In this process, the

aim is to keep the population size constant while encouraging better designs to stay in the design pool.

There are many readily available GA optimisation tools. One of the most commonly used is the Matlab's GA toolbox. In this study, the genetic optimisation tool for R "rgenoud" is used [114], which is an open-source tool with comprehensive optimisation methods and options. It can be easily modified to fit into any type of optimisation problem.

### 8.5.2 Objective Function & Penalty Factors

The objective function is the most important aspect of the optimisation process. It is used to evaluate each individual and compare their performances. The objective function is defined as the total active mass of the generator (without the structural mass). The boundaries of the problem are introduced as a penalty factor, which can be listed as follows:

- Outer Diameter: It is possible to reduce the active material mass by increasing the diameter. However, the outer diameter should be limited due to installation and manufacturing constraints.
- Power Output: The minimum power output required for the specific design.
- Phase Voltage: The minimum and the maximum phase voltage limits for connection to the power electronics and to the grid.
- Current Density: Maximum current density limit ensures that the temperature of the armature coils is within the acceptable range.

The cost function is defined as in equation 8.1, where the mass is the total active material mass (claw poles, stator and the field core).

$$F(x) = f_{mass}(x) + \sum_{i=1}^n f_{penalty_i}(x) \quad (8.1)$$

$$f_{mass}(x) = M_{claw\ poles}(x) + M_{stator}(x) + M_{field}(x) \quad (8.2)$$

Penalty function is defined as zero within the defined limits, and it is a second order parabolic function outside these limits. Each penalty function is multiplied by a constant ( $p_i$ ) to level each factor.

$$f_{penalty_i}(x) = \begin{cases} 0 & \text{if } x_{min} \leq x \leq x_{max} \\ p_i(x - x_{max})^2 & \text{if } x > x_{max} \\ p_i(x - x_{min})^2 & \text{if } x < x_{min} \end{cases} \quad (8.3)$$

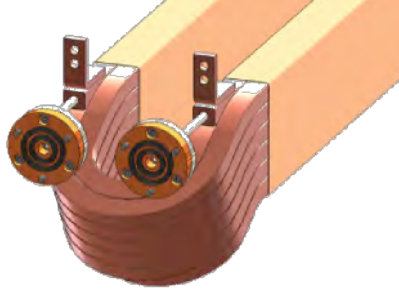


**Figure 8.11:** Direct liquid cooled concentrated stator coil for a direct-drive permanent magnet generator [21].

Apart from the penalty factors, the following assumptions are made:

- Air-gap clearance is assumed to be 0.1 % of the air-gap diameter [62].
- Number of poles is rounded to the closest multiple of four, which is required for the FEA model symmetry.
- The stator tooth pitch to coil pitch ratio is assumed as 0.5.
- The phase voltage is assumed to be 3.3 kV line-to-line. The number of coils in series is adjusted accordingly with a maximum number of turns limit of 1000.
- The fill factor in the armature coils is assumed as 0.7 assuming pre-formed coils with flat wire [164].
- Current density, or in other words electrical loading, is a factor that can directly affect the power density of a machine. It is possible to increase the power density of electrical machines by forced cooling methods such as liquid cooling. Such a machine is presented in [21] with hollow cooling channels (see figure 8.11), which has a current density around 7 A/mm<sup>2</sup>. However, this kind of electrical loading improvement is not included in this study, and the current density limit is chosen more conventionally as 5 A/mm<sup>2</sup> for the conductor (3.5 A/mm<sup>2</sup> for the stator slot considering the fill factor).

### 8.5.3 Flowchart

The flowchart of the optimisation process is presented in figure 8.12. The genetic algorithm is applied using “R”, which exports the design parameters for a specific design<sup>3</sup>. These parameters are used to build the 3D FEA model<sup>4</sup>. The FEA model exports the air-gap flux density distribution, which is then used to estimate the induced phase voltage and power output. The designs are ranked based on the cost function and the process is repeated until the solution converges or the maximum number of generation limit is reached.

<sup>3</sup>⚙️:Optimisation program: `large_wind/optimize/double_side_slotted_optimize.R`

<sup>4</sup>⚙️:FEA model: `large_wind/optimize/Create_double_sided_axial.comi`

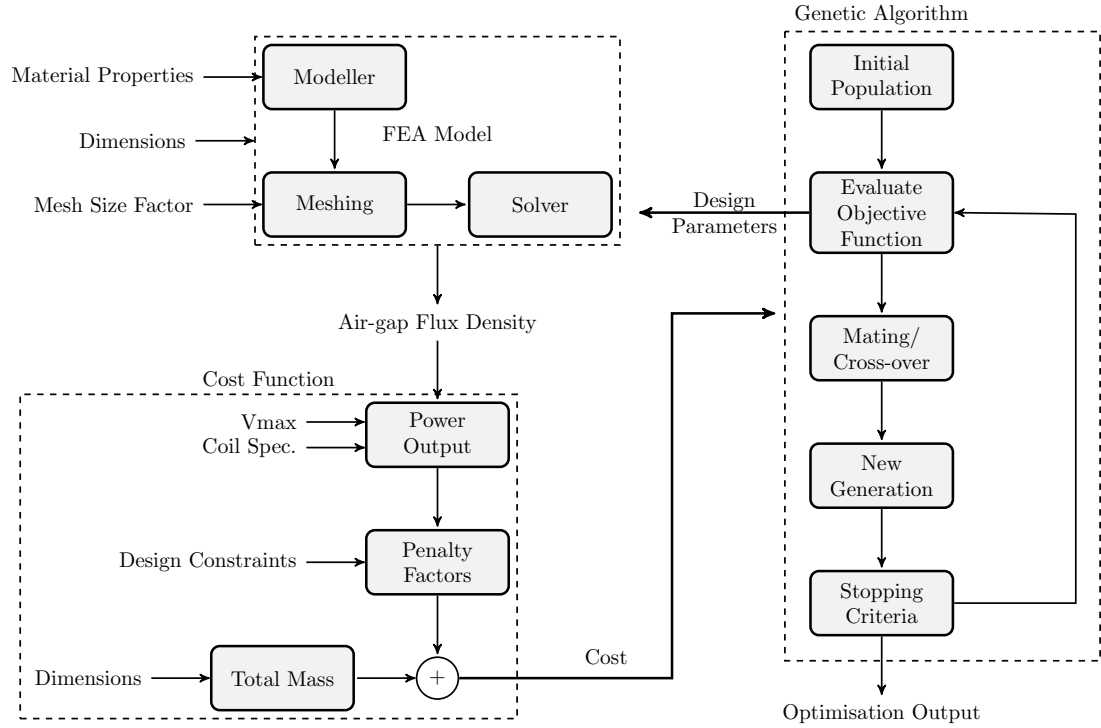


**Figure 8.12:** Schematic of the genetic algorithm optimisation.

#### 8.5.4 Computation Time

FEA based optimisations have a much higher computation burden compared to analytical methods. Thus, the FEA model should be carefully built to minimise the computation time. An excess number of mesh elements increases the computation time significantly. Although, a high number of mesh elements generally means higher accuracy, this improvement converges beyond some point.

A mesh size factor is introduced, which determines the size of all the mesh elements in the model. A large meshing factor makes the mesh rougher and a small one makes it finer. In table 8.2, the effect of the meshing factor to the computation time and accuracy is shown. With a meshing factor of 4, the total simulation time is approximately 11½ minutes and with a meshing factor of 0.75, the simulation time increases to 34 minutes. The accuracy of each simulation is calculated with respect to the finest mesh which has over a million of elements.

In order to minimise the total computation time, the following guideline is used:

- The optimization is initiated with a rough mesh to get an estimation of the search domain.
- Then, the mesh size factor is reduced gradually with each generation.
- The last few generations are simulated with a very fine mesh for the best accuracy.

Mesh Size Factor	0.75	1	2	3	4
Number of Nodes	194,266	92,442	15,111	6,336	3,615
Number of Elements	1,134,114	535,090	84,551	34,509	19,498
Accuracy(%)	100	97.8	84.1	82.2	71.7
Meshing Time (s)	339	183	80	50	46
Solving Time (s)	1684	719	148	106	47
Total (s)	2023	902	228	156	93

**Table 8.2:** Comparison of solution accuracy and computation time of a single design with various mesh size factors (Linux, 2.8 GHz, 12 GB RAM). The mesh gets finer with smaller meshing factor.

Similar tests were made before each optimisation process to minimise the computation time. Usually, the algorithm is started with a mesh factor of 2–3, and then it is gradually reduced to 0.75.

## 8.6 Design of a 10 MW Generator

In the first chapter, in figure 1.7, the mass of permanent-magnet and superconducting direct-drive wind turbine generators were compared, in which the most common power rating was 10 MW with a rotational speed of 10 rpm. In order to have a better comparison with these designs, a similar double-claw pole generator is designed.

The machine is optimised using the aforementioned constraints. The optimisation algorithm, with a population size of 100 (250 for the initial population), has converged in 20 generations (2250 designs are evaluated in total), which took 6<sup>1</sup>/<sub>2</sub> days in total using a single PC (due to software license restrictions). The average simulation time for a single model was 4 minutes. If the mesh-factor adjustment had not been applied, it would have taken 50 days to finish the same analysis. The simulation time can be further reduced by parallel computing provided that a higher number of FEA software licenses are available or by using open-source alternatives.

### 8.6.1 Optimisation Outputs

The variation of the design inputs through the optimisation process is plotted in figure 8.13, the data can also be accessed from the data repository<sup>5</sup>.

The inner radius limit is defined as 2.3 m, which the algorithm reaches in just a few generations. The diameter can be increased, but at the expense of increased structural mass. The algorithm reduced the optimum pole number from 100–140 to below 90,

<sup>5</sup>[https://github.com/10MW10rpm/optimization\\_outputs/10MW\\_10rpm](https://github.com/10MW10rpm/optimization_outputs/10MW_10rpm)

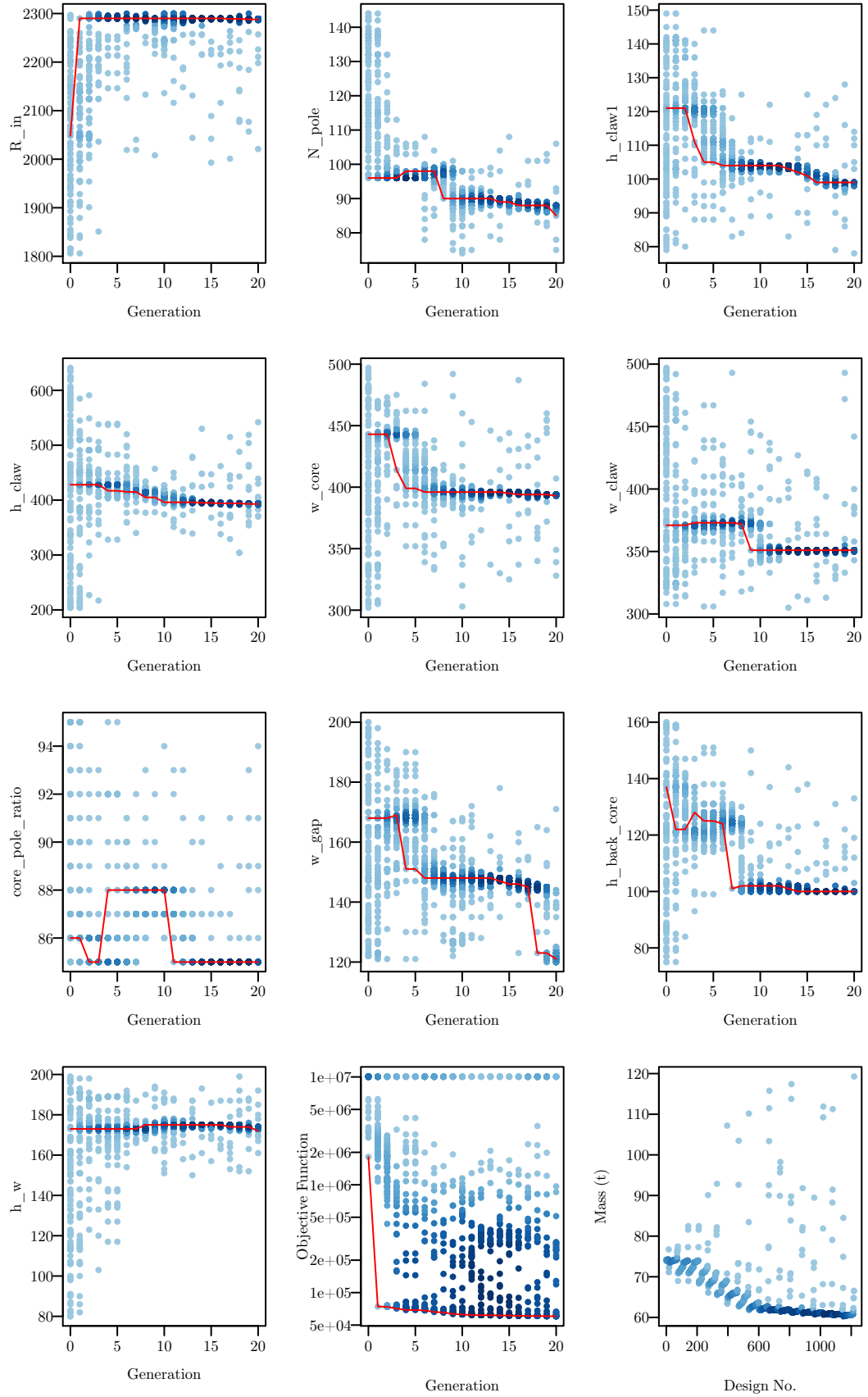


**Figure 8.13:** Genetic algorithm optimisation outputs of the 10 MW, 10 rpm wind turbine generator design. Blue dots show the design cases for each generation, red lines show the trend of the best candidates of each generation.

$R_{in}$	2288 mm
$N_{pole}$	88
$h_{claw1}$	100 mm
$h_{claw}$	393 mm
$w_{claw}$	351 mm
$w_{core}$	393 mm
$w_{gap}$	121 mm
$h_{backcore}$	100 mm
$h_w$	172 mm
$k_{core-pole\ ratio}$	0.85

**Table 8.3:** Best design parameters for the 10 MW, 10 rpm design.

which helps to increase the distance between claw poles and minimises the leakage flux. Similarly, the optimum core-to-pole ratio is selected by the algorithm as 0.85 to minimise the leakage flux between adjacent claw poles.

The objective function has a large range of values due to the effect of the penalty factors. The maximum value of the penalty factors is  $10^7$ . The active material mass of valid designs is shown in the figure, which was 75–80 tonnes in the first generations and converged to below 60 tonnes. The structural mass is estimated in the following sections. The main parameters of the optimum design are presented in table 8.3.

### 8.6.2 Optimum Design

The flux density distribution in the stator teeth of the optimum design is simulated at different rotor positions. Figure 8.14 shows the flux density distribution in the stator tooth when the large claw pole and small claw pole are aligned with the middle stator tooth. The total magnetic flux in the stator tooth versus rotor position is plotted in figure 8.15a, in which it is shown that the maximum flux in the stator tooth is 57.08 mWb when the large claw pole is aligned with the stator tooth. It should be noted that the flux waveform is not exactly symmetrical; the minimum flux is -53.66 mWb, 6 % lower than the maximum flux value. This is mainly because of the geometrical difference between the large claw pole and the small claw pole and this difference can be minimised by shape optimisation or using a different claw pole thickness. The induced voltage in a single coil at no load is plotted in figure 8.15b, which has an electrical frequency of 7.33 Hz. There are 11 coils in series and two parallel branches for each phase. The main specifications of the machine are presented in table 8.4.

The outline of the optimised generator is shown in figure 8.16. The machine has an outer diameter of 6.6 m and an axial length of 1.4 m, which is of similar size to a 5 MW direct-drive permanent magnet generator. The drawings of the claw poles and field winding are presented in Appendix H. The mass of the magnetic cores section

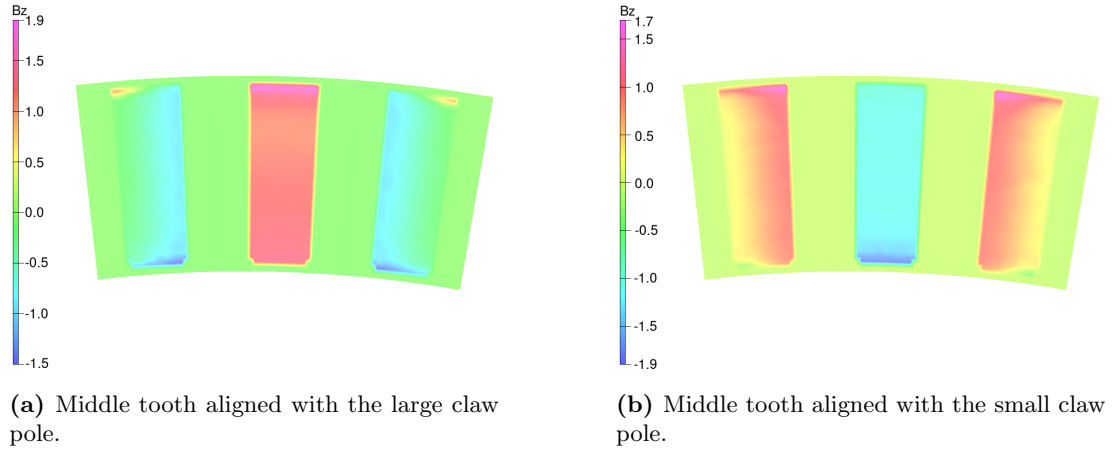


**Figure 8.14:** Flux density distribution in Z direction (into the page) in the stator teeth at mean coil radius.

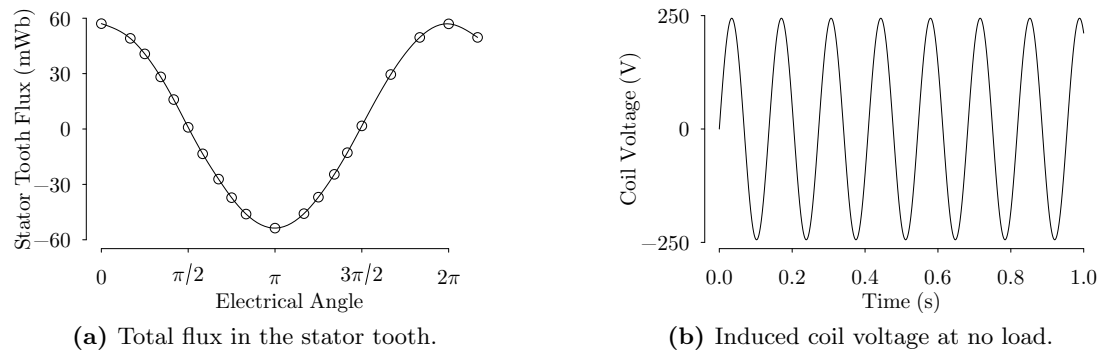


**Figure 8.15:** Total flux in the stator tooth and induced coil voltage for the optimised 10 MW, 10 rpm double-claw pole machine.



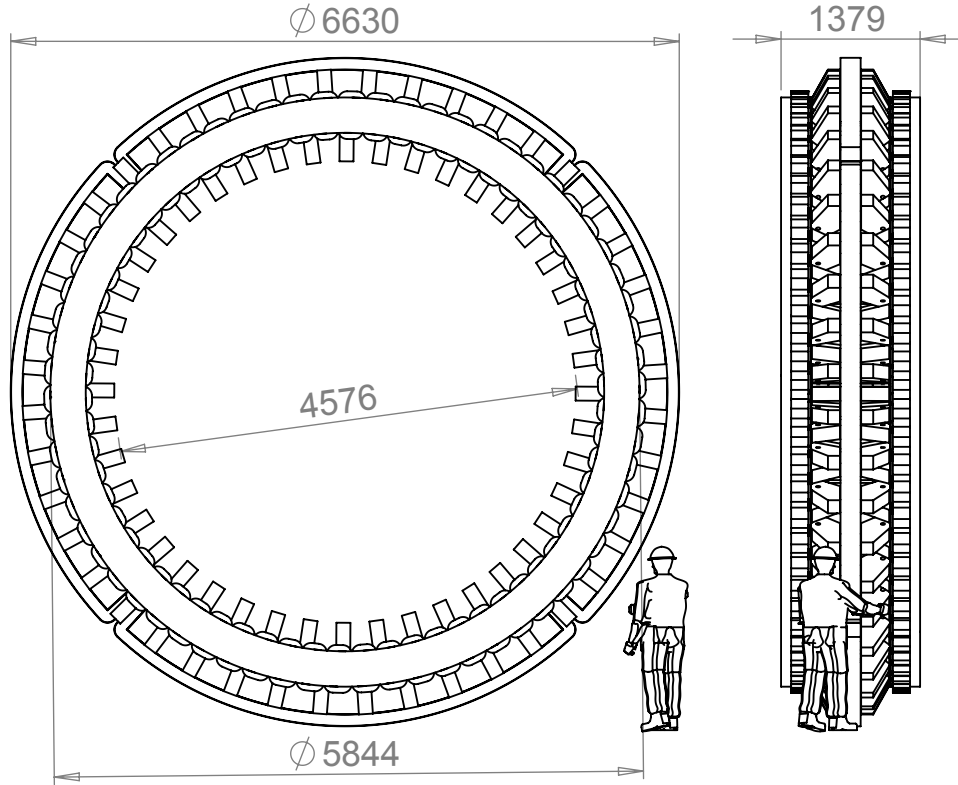


**Figure 8.16:** The outline dimensions of the 10 MW, 10 rpm generator design. Dimensions are in mm.

and the armature coils are calculated<sup>6</sup> and presented in table 8.5. The active material mass in the rotor is about 24 tonnes. The stators on each side weight around 10 tonnes. The mass of the superconducting coil and cooling system will be presented in the next section.

The main losses in the machine are presented in table 8.6, which are dominated by the copper loss<sup>7</sup>. Armature cooling is provided by 40 kW of air blowers. The electrical frequency of the machine is 7.3 Hz, which reduces the core losses in the machine. Furthermore, the core losses in the claw poles are negligible as the flux density magnitude and direction do not change. The core loss in the field core and stator core is calculated as 6.8 kW<sup>7</sup> by extrapolating the core loss values presented in [163]. The eddy current loss in the armature winding is neglected due to the low electrical frequency.

<sup>6</sup> `large_wind/optimization_outputs/10MW_10rpm/calculate_mass.R`

<sup>7</sup> `large_wind/optimization_outputs/10MW_10rpm/calculate_power.R`

Power Rating	10 MW
Rotational Speed	10 rpm
Number of Poles	88
Outer Diameter	6.63 m
Armature Diameter	5.84 m
Rotor Radius	3.20 m
Inner Radius	2.29 m
Axial Length	1.38 m
Number of Stator Slots	66
Number of Turns	96
Induced Coil Voltage	173 V <sub>rms</sub>
Phase Voltage Voltage	3.3 kV <sub>ll</sub>


**Table 8.4:** Main specifications of the 10 MW, 10 rpm design.

Small Claw Pole	114 kg
Large Claw Pole	314 kg
Single Coil	17.5 kg
Stator Core (Single Side)	8,600 kg
Single Field Core Mass	2,830 kg
Cryostat Mass	1,200 kg
Cooling System Mass	2,000 kg
Total Rotor Active Material	23,850 kg
Stator (Single Side)	9,755 kg
Total Field Core Mass	11,320 kg
Total Active Material Mass	57,9 tonnes

**Table 8.5:** Mass estimations of the 10 MW, 10 rpm machine components.

### 8.6.3 Superconducting Coil & Cooling System

Four independent cryostats are utilized in the 10 MW machine for increased modularity and ease of manufacturing. Also, the field core consists of four separate sections, the outline of which are presented in Appendix H.1. 10.4 m of superconducting coil is used for each section. The magneto-motive-force of each of the superconducting coil is selected by the optimisation algorithm as 32.4 kAt. Figure 8.17 shows the effect of varying MMF to the maximum stator tooth flux linkage<sup>8</sup>. It can be seen from the figure that, the tooth saturates for MMF values higher than 32.4 kAt, and the choice of the GA is optimum. The main specifications of the superconducting coil are presented in table 8.7.

<sup>8</sup>:Opera\_logs\_graphs/2013/2013\_05\_11\_10MW\_varying\_Jsc

Copper Loss	510 kW
Core Loss	7 kW
Cryocoolers	24 kW
Air Blowers (Armature)	40 kW
Output Power	9,987 kW
Efficiency	94.5 %

**Table 8.6:** Main losses and efficiency estimation for the 10 MW, 10 rpm design.

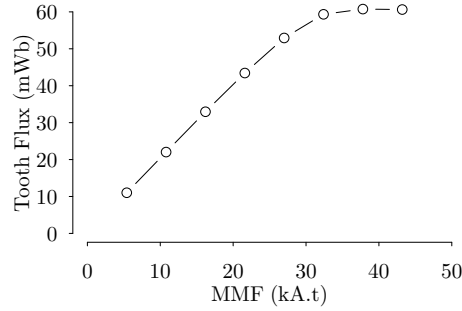


**Figure 8.17:** Stator tooth flux linkage variation with field winding MMF.

### Superconducting Wire Requirement

There is not a straightforward answer to the optimum operating temperature of a superconducting machine. Cooling power requirements increase as the operating temperature is reduced. However, the current carrying capability of the superconducting tapes increase and the amount of the superconducting wire is reduced at low temperatures. In this section, three different cases are investigated:

- $\text{MgB}_2$  tape at 30 K.
- YBCO tape at 30 K.
- YBCO tape at 65 K.

The relative critical currents of different superconducting wires were presented in table 6.8. Using this table and the superconducting wire specifications presented in Appendix B, the critical current values for superconducting wires are calculated.

At 30 K, the critical current of  $\text{MgB}_2$  is assumed to be 110 A, and 90 A is chosen as the safe operating current. The field winding requires 32.4 kAt, which gives 360 turns. Assuming a fill factor of 0.75 and eight layers, the  $\text{MgB}_2$  wire can be wound on a 30x40 mm cross-section area. YBCO at the same temperature can conduct six times of its critical current at 77 K, which gives 504 A; 400 A is chosen as the safe operation current, which gives the number of turns as 81. Assuming a fill factor of 0.75 and three layers, the winding can fit in a 15x8 mm cross-section area.

At 65 K, YBCO wire can conduct 1.48 times of its critical current at 77 K; 126 A is the critical current and 100 A is chosen as the safe operation current, which gives a

Mean turn length	10.4 m
MMF of the SC	32.4 kAt
Number of Cryostats	4
Total SC requirement	1348 kAt.m

**Table 8.7:** Superconducting winding specifications for the 10 MW, 10 rpm design.

	MgB <sub>2</sub>	YBCO	
Operating Temperature	30 K	30 K	65 K
Current ( $0.8I_c$ )	90 A	400 A	100 A
Number of turns	360	81	324
Wire thickness	0.67 mm	0.22 mm	0.22 mm
Wire width	3.65 mm	4.8 mm	4.8 mm
Space	30x40 mm	15x8 mm	15x32 mm
Wire length(per cryostat)	3744 m	842 m	3370 m
Wire length (total)	15.0 km	3.4 km	13.5 km

**Table 8.8:** Superconducting tape requirements for the 10 MW, 10 rpm design.

number of turns of 324. Assuming three layers, it can fit on a 32x15 mm cross-section area.

The superconducting wire requirements for these three cases are presented in table 8.8. Compared to conventional superconducting machines, the wire length of the proposed machine, which is 15 km, is much lower. This is mainly because of the iron-cored structure and having a single superconducting winding instead of having separate superconducting coils for each pole.

### Cooling Power

This section presents the thermal loads in the cryostat, which are used to estimate the cooling power requirements. Although, the superconducting coil length is just determined using electromagnetic optimisation, in a real design it should be linked with the cryostat design to get a more cost effective solution. However, the cooling power and operating temperature can be used to get a rough idea of the cooling system.

The main heat leakage elements in the cryostat can be listed as:

- Gas heat conduction through the vacuum.
- Radiation heat from warm walls of the cryostat.
- Conduction through superconducting coil mechanical support.
- Heat leakage through current leads.

These losses are estimated using a similar methodology presented in [15, 148].

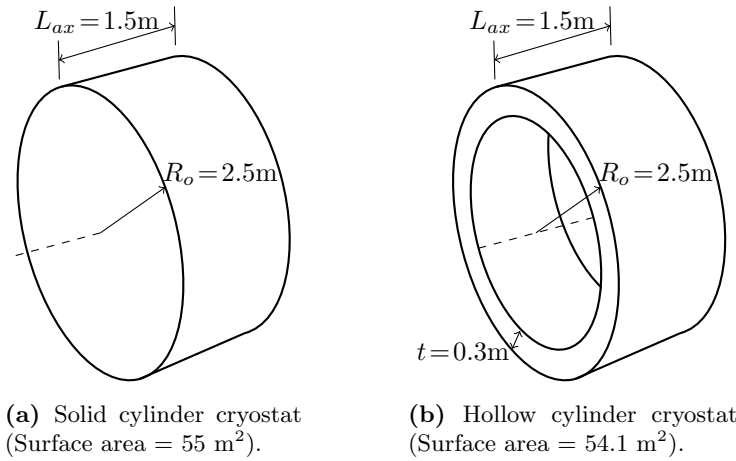


**Figure 8.18:** Common cryostat shapes for superconducting machines and estimated dimensions for a 10 MW, 10 rpm machine rotor.

*Conduction Through Vacuum:* The surface area of a single cryostat is 6.1 m<sup>2</sup>, which gives the total cryostat wall area as 24.4 m<sup>2</sup>. The cryostat shape used in the proposed design is different from usual superconducting machines, in which a cryostat-rotor is used. There are two common cryostat shapes: solid cylinder cryostat that covers all the rotor structure and hollow cylinder cryostat. Some estimated dimensions for these cryostats are presented in figure 8.18, with a rotor diameter of 5 m. The surface area for these two cryostats are 55 m<sup>2</sup> and 54.1 m<sup>2</sup> respectively. The cryostat wall area of the proposed design, with 24.4 m<sup>2</sup>, is less than half of the conventional designs, despite having a larger diameter. Thus, the heat loss through the cryostat wall is expected to be lower.

The heat conduction through low-pressure gas systems separated with two parallel surfaces can be expressed as in equation 8.4, where  $k$  is a constant for gas type (1.2 for air),  $a_0$  is related to the accommodation coefficient (0.5 is generally used in cryogenic designs),  $P$  is the pressure of the gas in Pascals (1 Pa = 0.01 mbar),  $A$  is the surface area in m<sup>2</sup>,  $\Delta T$  is the temperature difference in Kelvins [49]:

$$\dot{q}_{gas} = k a_0 P A \Delta T \quad (8.4)$$

In [15], it is stated that the pressure of a vacuum chamber can be between 10<sup>-1</sup>–10<sup>-4</sup> Pa. Thus, using equation 8.4, the heat conduction can be estimated between 0.016–16 W/m<sup>2</sup> at 30 K. The total heat conduction for all the four cryostats is between 0.4–392 W, which is a quite wide range depending on the pressure level. The operating pressure is chosen as 10<sup>-3</sup> Pa, which can be achieved using standard industrial equipments. The heat loss at this vacuum level is 3.9 W.

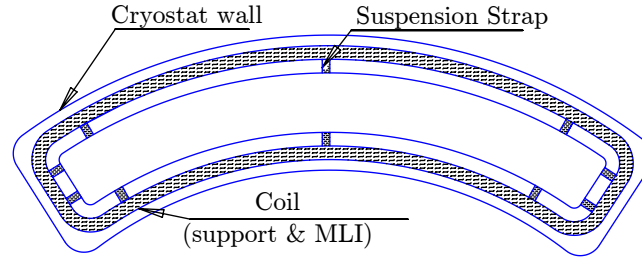


**Figure 8.19:** The suspension straps (10 in total) for the sectioned superconducting coil.

*Radiation:* An important heat leakage component is due to radiation, which is expressed in [49] as:

$$\dot{q}_{\text{radiation}} = \sigma \mathcal{E} A (T_2^4 - T_1^4) \quad (8.5)$$

where  $\sigma$  is the Stefan-Boltzmann constant ( $5.67 \times 10^{-8} \text{W/m}^2 \text{K}^4$ ),  $\mathcal{E}$  is a factor for the reflectivity and geometry of the material which is between 0 and 1, which is usually assumed to be 0.05 for polished metals used in cryogenic applications. Again, assuming  $T_2 = 298 \text{ K}$  and  $T_1 = 30 \text{ K}$ , the total radiation heat loss can be found as 545 W, which is very high. Fortunately, this value can be reduced using radiation shields with high emissivity ( $\mathcal{E} < 0.01$ ). A common practice is to use multi-layer-insulation (MLI) material, which consists of several reflective layers with insulating layers in between (thermally floating). MLI divides the large temperature gradient into several segments and the heat radiation can be reduced by  $1/(N + 1)$  by using  $N$  layers [49]. RUAG is a manufacturer of MLI materials (Mylar, Kapton, Polyimide foils), which have an average thickness of 30 layers/cm [10]. Thus, using 10 mm of MLI insulation, the radiation heat can be reduced to 3.2 % of the initial value: 17.5 W in total.

*Suspension Straps:* Another important heat input comes from the mechanical supports that fix the superconducting coils into the vacuum chamber. In the proposed machine there is no electromagnetic torque acting on the superconducting coil, which makes the design of these suspension straps relatively straightforward compared to the torque tubes of other types of superconducting machines. G10-CR fibreglass is a common material used in cryogenic applications (a torque tube built using G10 fibreglass is presented in figure 3.10). The heat conducting in a material can be expressed as in equation 8.6, where  $k$  is the thermal conductivity of the material,  $A$  is the surface area, and  $l$  is the length of the material [102]:

$$\dot{q}_{\text{cond}} = \frac{k A \Delta T}{l} \quad (8.6)$$

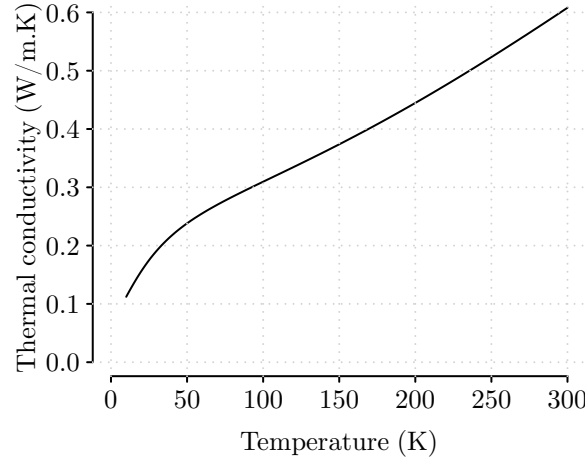


**Figure 8.20:** Variation of the thermal conductivity of G10-CR with temperature (Data points obtained from [107]).

The thermal conductivity of the G10-CR is not constant, but it changes from 0.6 W/mK at 300 K to 0.2 W/mK at 30 K as shown in figure 8.20, so it becomes a better insulator at cryogenic temperatures. A fibreglass tube shape is used for high stiffness, which has an outer diameter of 4.5 mm, an inner diameter of 3.2 mm, with a length of 60 mm, which gives 1.35 W loss per tube<sup>9</sup>. Suspension straps are placed one meter distance between each other around the superconducting coil as shown in figure 8.19, which makes 10 straps per cryostat and 40 straps in total. Thus, the total heat loss from the conduction is estimated as 54 W.

*Current Leads:* The heat loss through the current leads can be significant, which has two factors: one is due to the resistive losses and the other one is due to the heat conduction through from ambient. Thus, the heat loss in the current lead can be expressed as:

$$\dot{q}_{current\ lead} = \frac{\rho L I^2}{A} + \frac{k A \Delta T}{L} \quad (8.7)$$

where  $\rho$  is the resistivity of the current lead,  $L$  is the length,  $A$  is the cross-section area of the current lead. In order to minimise the total heat input, the resistive and the conductive elements should be balanced, which gives the ratio of length to area and the total heat loss as in equation 8.8 and equation 8.9 respectively [78].

$$\frac{L}{A} = \frac{1}{I} \sqrt{\frac{k}{\rho} \Delta T} \quad (8.8)$$

<sup>9</sup>`B:Dissertation/chapter8/codes/estimate_conduction_G10.R`

	30 K MgB <sub>2</sub> –90 A	65 K YBCO–120 A
Gas Conduction (at 10 <sup>−3</sup> Pa)	3.9 W	3.4 W
Suspension Straps	54.0 W	50.0 W
Radiation	17.5 W	17.4 W
Current leads	47.2 W	48.8 W
Cold-head sleeve	15.6 W	15.6 W
Eddy Current	4.0 W	4.0 W
Other	15.0 W	15.0 W
Total loss	157.2 W	154.2 W

**Table 8.9:** Thermal budget for the 10 MW, 10 rpm design.

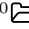
$$\dot{q}_{current\ lead} = 2 I \sqrt{\rho k \Delta T} \quad (8.9)$$

From equation 8.9, it can be concluded that the total heat loss is proportional to the product of the resistivity and the thermal conductivity. Although, this value is quite similar for a variety of materials, brass has slightly better characteristics with  $\rho = 0.04 \mu\Omega\text{m}$ ,  $k = 100 \text{ W/m/K}$  [78]. Assuming a current input of 90 A for MgB<sub>2</sub>, the heat loss in a single current lead is found as 5.9 W (11.8 W for both current leads for each superconducting coil section)<sup>10</sup>. This value is similar to the one presented in [154], which is 13.9 W for a 10 MW machine. However, the proposed design has four independent cryostats, thus the total heat loss from current leads becomes 47.2 W.

*Other Losses:* There are also other losses in the system. Conduction loss from the cold-head sleeve is given as 3.9 W per cold-head in [154], which gives 15.6 W assuming four cold-heads in total. Eddy current losses in the machine are expected to be low, due to low electrical frequency (7.3 Hz) and the iron-cored structure. It is a common practice to shield the eddy currents using copper layers on the warm-side. In [154] the eddy current for a 10 MW machine is estimated as 4 W, which is used in the calculations.

*Choosing the Cryocooler:* Total heat losses in the cryostats are tabulated in table 8.9. The heat loss at 65 K is also presented, which is estimated as 154.2 W. The total thermal budget of the machine at 30 K is 157.2 W, slightly larger than the heat loss at 65 K. Adding 25% safety margin, the machine can be cooled using 4 x 50 W cryocoolers.

A suitable cooling system for such a requirement is selected as Cryomech’s Gifford-McMahon AL230 cold-head coupled with CP950 compressor, which can supply 60 W of cooling power at 30 K [42]. The specifications can be found in table 8.10. If a lower

<sup>10</sup>:Dissertation/chapter8/codes/estimate\_current\_lead\_loss.R



Cold head mass	16.8 kg
Compressor mass	176 kg
Flexible line mass	4.2 kg
Total mass	197 kg
Input power	6 kW

**Table 8.10:** Specifications of the Cryomech’s AL230–CP950 cooling system (60 W @30 K) [42].

operating temperature is desired, the AL325 model can be used which can supply 75 W cooling power at 20 K, with 11.2 kW input power. The temperature vs. cooling power characteristics of various cryocoolers are presented in Appendix G.

Although, the total mass of the components presented in table 8.10 is 197 kg, there are many auxiliary components in the cooling system, so the total mass per cooler is assumed as 500 kg. Thus, the total cooling system in the generator becomes 2,000 kg with an electrical power input of 24 kW.

To summarize, the proposed topology has the advantage of independent cryostats, which increases the modularity and overall availability of the system. The total cryostat wall area is smaller compared to the conventional cylindrical cryostats, which helps to reduce the gas conduction and radiation losses. However, the sectioned cryostat results in higher number of current leads and suspension straps which increases the conduction losses. In general, the heat loss is within the reasonable values. For example in [152], it is stated that six to ten CTI-1020 cryogenic coolers are used for AMSC’s 10 MW superconducting generator, provides 280–450 W of cooling power. In [154], the total cooling requirement for the GE’s 10 MW LTS superconducting generator is estimated as 131 W, and in [15], 500 W is defined as the upper limit of the cooling power for a 5 MW superconducting generator.

#### 8.6.4 Structural Mass

The excess structural mass in large direct-drive generators is a serious issue. A very stiff structure is required to maintain the air-gap clearance and the structural mass increases significantly with diameter (the mass of the torque arms is proportional to  $R^3$  [113]). The proposed machine has a smaller diameter than equivalent DDPM generators, which helps to reduce the structural mass. However, the high air-gap flux density increases the stress on the mechanical structure.

There are some studies trying to estimate the structural mass for DDPM generators [113, 174]. The structural mass of different DDPM generators are compared in [27] (see table 8.11). It is stated in [30] that the structural mass is around 55 % of the total mass of a 5 MW DDPM generator. Zavvos et. al. estimated the structural mass of a 10 MW

Power	Speed	Torque	Air-gap Diameter	Structural Mass
2 MW	19.5 rpm	979 kNm	4.3 m	14.6 t
3 MW	16 rpm	1790 kNm	5.1 m	19.6 t
5 MW	12.5 rpm	3820 kNm	6.1 m	50.1 t

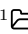
**Table 8.11:** Structural mass estimation for different DDPM generators [27].

DDPM generator with 7 m air-gap diameter as 248 tonnes [174].

There are only a few studies that take the structural mass into account for a superconducting machine design. For example, in [106] the mass of superconducting and permanent magnet machines are compared. The structural mass of a 10 MW, 10 rpm superconducting generator is estimated as 76 tonnes for a YBCO wire based generator, and 102 tonnes for a Bi-2223 wire based generator in [156]. The structural mass for these machines are around 50 % of the overall mass.

Before proceeding into the structural mass estimation, it is useful to mention the different options for installing the generator into a wind turbine nacelle. With an axial armature (see figure 8.21a), the rotor structure is directly fixed to the turbine hub. The stator structure supports both of the armature windings. Although, the forces acting on the claw poles are balanced, there is a net magnetic attraction force on each armature core, and the stator structure should be stiff enough to cope with these forces. An alternative to eliminate these axial forces is to rotate the claw poles as shown in figure 8.21b. In this configuration, the forces on the armature core act radially and cancel each other along the circular symmetry. The disadvantage of this symmetry is that the stators are no longer identical (i.e. the inner stator has a smaller diameter, which causes flux density and the induced voltage characteristics to differ). Although, the machine can be designed to minimise this effect, this configuration is not covered in this study and an axial armature configuration is assumed.

In [175], the structural mass for different types of DDPM generators are optimised. Zavvos used FEA simulations and analytical models to estimate the deflection in the structure due to tangential and normal stresses. An analytical model is presented to estimate the structural mass of machines depending on the diameter, axial length and air-gap flux density. Although, the topology is quite different, the analytical model for transverse flux permanent magnet generators presented in [175] is used to estimate the structural mass of the machine <sup>11</sup>. The number of torque arms for stator and rotor is assumed to be 5, as it is found that it is the optimum value for minimum mass [175]. The mass of the rotor structure and stator structure is presented along with the active material mass in table 8.12. Thus, the total mass of the generator is estimated as 184.2 t.

<sup>11</sup>:large\_wind/optimization\_outputs/10MW\_10rpm/structure.m

Rotor Structure	42.8 t
Stator Structure	83.5 t
Magnetic Core	52.4 t
Copper	2.3 t
HTS & Cooling	3.2 t
Total Mass	184.2 t

**Table 8.12:** The structural and active material mass estimations for the 10 MW, 10 rpm machine.

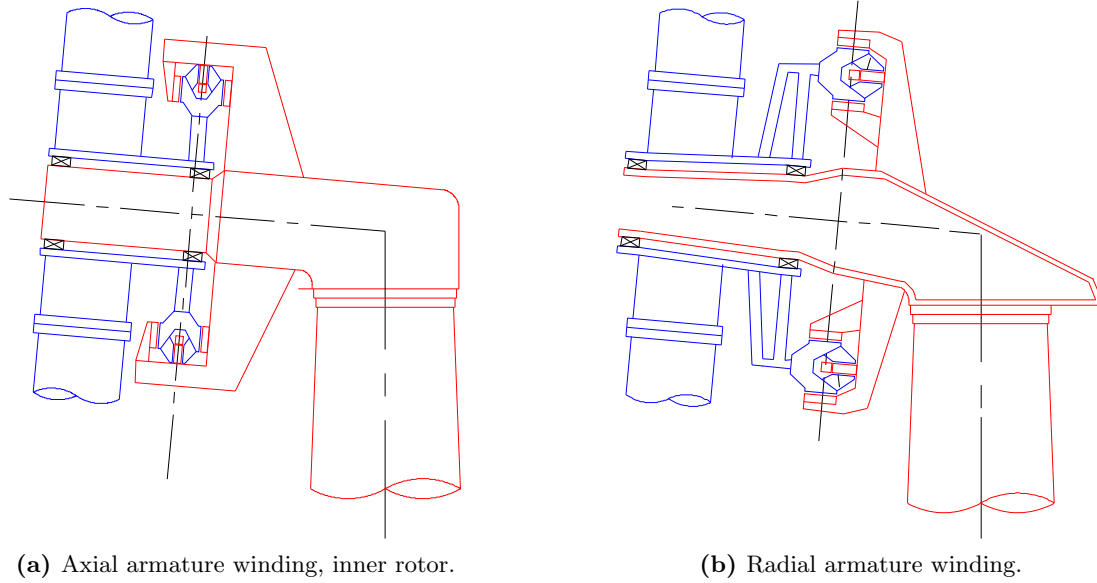


**Figure 8.21:** Two possible configurations for the installation of double-claw pole machine to a wind turbine (Drawings modified from [27]).

## 8.7 Design of a 36.5 MW Ship Propulsion Motor

Although, the main focus of this study is offshore wind, the double-claw pole topology can also be applied to other areas such as ship propulsion motor. A 36.5 MW, 120 rpm superconducting ship propulsion motor is designed in this section, which has the same power rating of AMSC's machine [80]. The optimisation outputs are presented in figure 8.22 and also can be accessed from the data repository<sup>12</sup>. The best design parameters are presented in table 8.13, and the outline of the machine is presented in figure 8.23. The machine has an outer diameter of about 4 m and axial length of 1.3 m, which is similar to the AMSC's design. The main specifications of the machine are presented in table 8.14.

Three cryostats are used in the 36.5 MW machine, with a total heat loss of 109 W

<sup>12</sup>[https://github.com/AMSC-UK/large\\_wind/optimization\\_outputs/36MW\\_ship\\_propulsion](https://github.com/AMSC-UK/large_wind/optimization_outputs/36MW_ship_propulsion)

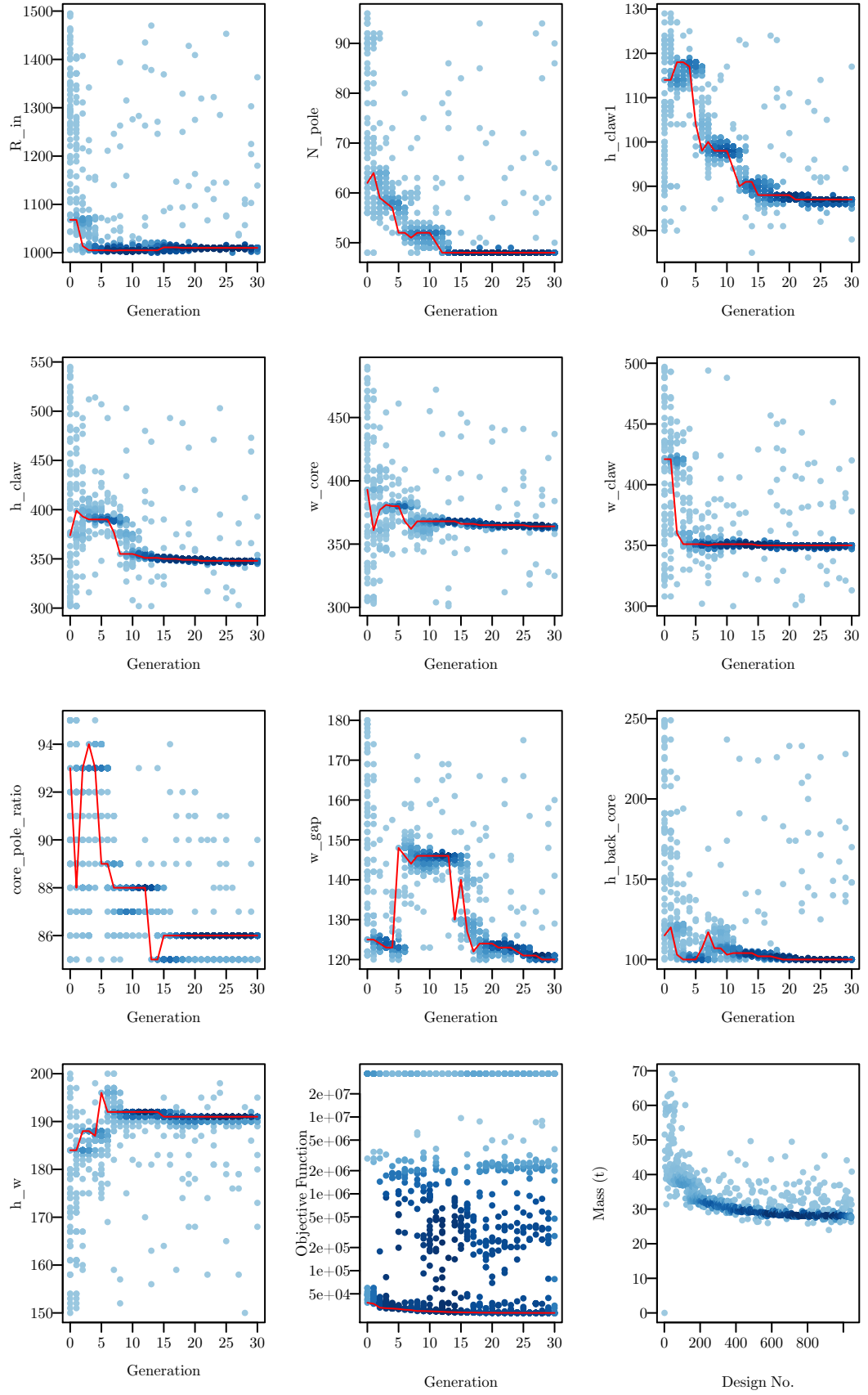


**Figure 8.22:** 36.5 MW, 120 rpm ship propulsion motor design, genetic algorithm optimisation outputs.

$R_{in}$	1010 mm
$N_{pole}$	48
$h_{claw1}$	87 mm
$h_{claw}$	348 mm
$w_{claw}$	350 mm
$w_{core}$	364 mm
$w_{gap}$	120 mm
$h_{backcore}$	100 mm
$h_w$	191 mm
$k_{core-pole\ ratio}$	0.86

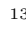
**Table 8.13:** Best design parameters for the 36.5 MW, 120 rpm ship propulsion motor.

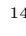
Power Rating	36.5 MW
Rotational Speed	120 rpm
Number of Poles	48
Outer Diameter	3.94 m
Armature Diameter	3.23 m
Inner Radius	1.01 m
Axial Length	1.33 m
Cryostat Heat Loss	109 W
Cooling System Power	18 kW
Superconducting Coil Requirement	660 kA-m
Superconducting Coil Length (MgB <sub>2</sub> , 30 K)	7.3 km

**Table 8.14:** Main specifications and mass estimations of the 36.5 MW, 120 rpm ship propulsion motor design.

at 30 K. In this condition, three of the 60 W cryocoolers that are used in the 10 MW machine would be enough, which gives the cooling system mass as 1,500 kg and the electrical power input as 18 kW (see table 8.14). Mean length of each superconducting coil section is 7.8 m, and the MMF of each superconducting coil is 28.2 kAt, which gives the total superconducting coil requirement as 660 kA-m. This is equivalent to 7.3 km of MgB<sub>2</sub> tape at 30 K or 6.6 km of YBCO tape at 65 K.

Total active material mass of the machine is estimated as 27 tonnes<sup>13</sup> (see table 8.15). Efficiency, including the cooling system, is 98.9 %, which is higher than the 10 MW machine<sup>14</sup>. Using the same method for the 10 MW machine, the total structural mass is estimated as 77.8 tonnes. Thus, the overall mass is calculated as 104.8 tonnes, which is 40 % higher than the AMSC's design.

<sup>13</sup>:large\_wind/optimization\_outputs/36MW\_ship\_propulsion/calculate\_mass.R

<sup>14</sup>:large\_wind/optimization\_outputs/36MW\_ship\_propulsion/calculate\_power.R

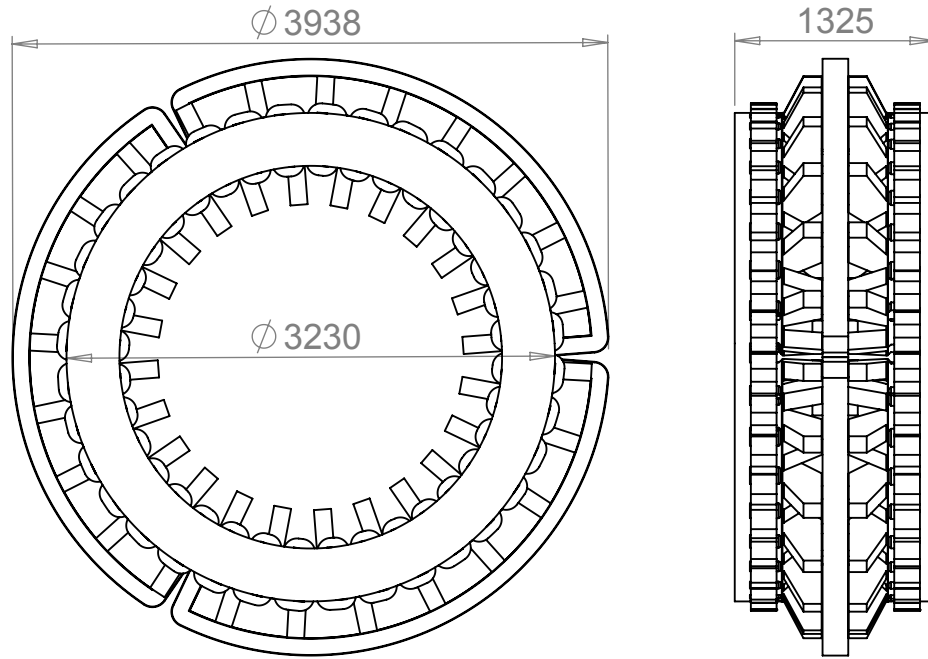


**Figure 8.23:** The outline dimensions of the 36.5 MW, 120 rpm generator design. Dimensions are in mm.

## 8.8 Mass Comparison

It is now time to revisit figure 1.7 of Chapter 1, which compares the torque densities of direct-drive permanent machines and superconducting machines. Both the 10 MW and the 36.5 MW double-claw machine designs are placed in this graph in figure 8.24. In the figure, it can be seen that the mass of two designs are above the trend-line of the superconducting machines (by 23 % for the 10 MW, by 36 % for 36.5 MW machine).

Figure 8.24 also shows the contributions of the structure, magnetic core, copper and cooling masses. It is clear that the structural mass dominates the total mass in both designs (68 % of the 10 MW design, 74 % of the 36.5 MW design). Another important component is the magnetic core, which employs 28 % of the 10 MW design and 22 % of the 36.5 MW design. The magnetic core mass could be reduced in an air-cored type superconducting generator, but the structural mass, which is usually neglected, would still be significant due to high magnetic attraction forces in the machine.

Small Claw Pole	80 kg
Large Claw Pole	217 kg
Single Coil	18.3 kg
Stator Core (Single Side)	4,716 kg
Single Field Core Mass	1,700 kg
Cryostat Mass	616 kg
Cooling System Mass	1,500 kg
Total Rotor Active Material	9,054 kg
Stator (Single Side)	5,376 kg
Total Field Core Mass	5,100 kg
Total Active Material Mass	27 t
Rotor Structure	29.8 t
Stator Structure	48.0 t
Magnetic Core	23.6 t
Copper	1.3 t
Cooling - Cryostats	2.1 t
Total Mass	104.8 t

**Table 8.15:** The structural and active material mass estimations for the 36.5 MW, 120 rpm machine.

## 8.9 Conclusions

This chapter presents a novel superconducting machine topology, which is a modified version of the radial claw-pole design. The forces acting on the rotor are balanced in this concept, so it is easier to manufacture the machine at large diameters. There is no need for SMC material as all the magnetic core sections can be manufactured from electrical steel laminations. Furthermore, the amount of the field core mass is reduced, which results in a lighter design.

A major advantage of the double-claw pole topology is its modularity; instead of using a single large circular superconducting coil, it can be divided into smaller sections. The armature winding also has similar modularity due to concentrated coils. This has the following advantages:

- Easier to manufacture and transport the machine.
- Independent operation of the cryostat sections.
- In the event of a fault in the cooling system or armature, the rest of the machine can be operated at part-load until maintenance.
- Faulty components can be replaced in situ.

All these factors are very beneficial for offshore wind turbines, where the O&M is difficult and expensive.

In order to find the optimum design, a parametrised FEA model was developed and coupled with a genetic algorithm optimisation tool. The tool was used to design a

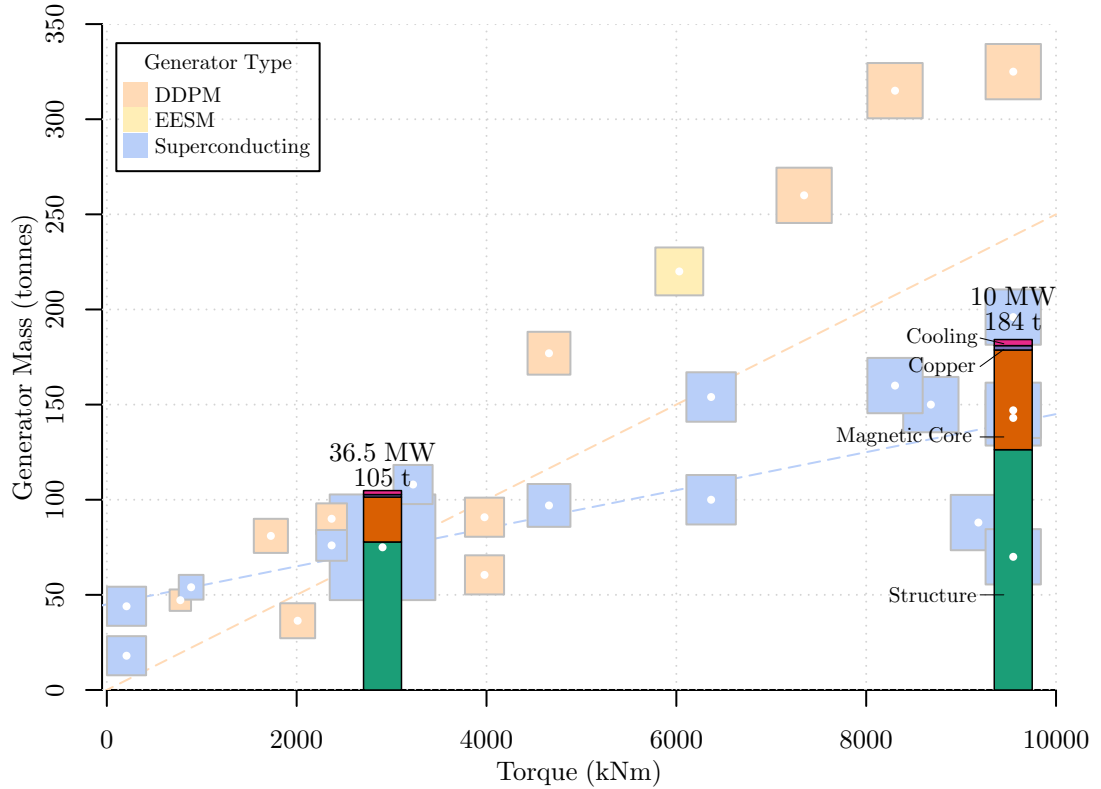


**Figure 8.24:** Mass comparison of the 10 MW and 36.5 MW double-claw machines with other direct-drive permanent magnet and superconducting machines.

10 MW, 10 rpm generator for wind turbines and a 36.5 MW, 120 rpm machine as a ship propulsion motor.

The 10 MW machine has an outer diameter of 6.6 m and an axial length of 1.4 m. The active material mass of the machine was calculated as 58 tonnes. Including the structure and the cooling system, the total mass is estimated as 184 tonnes. This is 23 % higher than the trend-line of superconducting machines, but still 40 % lighter than the similar rated direct-drive permanent magnet generators. Structural mass is a significant component of total mass (around 70 %). In fact, it is expected that it will be similar for all superconducting machines due to high air-gap flux densities, although, the structural mass is usually neglected in direct-drive superconducting machine designs. Further improvements can be made by developing novel structures, and coupling the optimisation with structural design.

One of the most important advantages of the proposed topology is the low superconducting wire requirement compared to other superconducting machine designs. For example, 10 MW air-cored superconducting generators require more than 500 km of superconducting wire (see section 3.8). Other machines require around 100 km of superconducting wire. However, the proposed 10 MW double-claw machine requires just



15 km  $\text{MgB}_2$  tape at 30 K or 13.5 km YBCO tape at 65 K. Assuming the cost of YBCO as €150/kAm [66] and the cost of  $\text{MgB}_2$  as €20/kAm [1], the total superconducting wire cost becomes €202k for YBCO and €27k for  $\text{MgB}_2$  wire. The cooling burden of the design is also very low; the electrical power required for cooling is estimated as 24 kW (just 0.24 % of the total power rating).

To conclude, it has been shown that, the claw pole topology can be applied as a direct-drive generator (and ship propulsion motor). In terms of mass, it may not be as competitive as other superconducting machine designs, but it has clear advantages in terms of modularity and increased reliability. Furthermore, it uses much less superconducting wire and is expected to be more cost-competitive than other superconducting generator designs.

# Concluding Remarks

---

This thesis presents novel superconducting direct-drive generator topologies for large wind turbines. In the first chapter, the current trends in offshore wind energy market are reviewed and the challenges for a large offshore wind turbine are highlighted as high tower-head mass and reliability. Then, the aim of the thesis is stated as:

“To propose a suitable superconducting generator topology, which can outperform existing superconducting generator topologies in terms of reliability and modularity.”

In the following sections, the steps taken to achieve this aim will be explained and the main contribution of this thesis and the future work will be presented.

### 9.1 The Approach to the Problem

Superconducting machine design is complex by the multi-physics nature of the problem and extreme operating conditions. The designers need to address the electromagnetic optimization of the machine, but the performance of the SC coils are dependent on the thermal aspects. In addition, thermal design becomes more complex due to mechanical constraints such as thermal contraction coefficients and design of the torque tube with minimum heat leakage. Furthermore, the magnetic performance of the machine is directly affected by the extended magnetic air-gap due to the cryostat walls and insulation layers.

Designing a direct-drive superconducting generator for large wind turbines introduces extra challenges to the already complex problem. The generator needs to be as reliable as possible to minimize any down-time since the maintenance of offshore wind turbines is very expensive. The modularity is also an important aspect, as it can help to increase the availability of the turbine by running the machine at partial-load in case of a fault. Furthermore, modularity makes it possible to replace faulty parts using on-site cranes without the need for specialist vessels, which increases the repair cost and time.

A common approach to this problem in the literature is to use a standard superconducting generator (i.e. copper armature, superconducting rotor) and try to increase the reli-

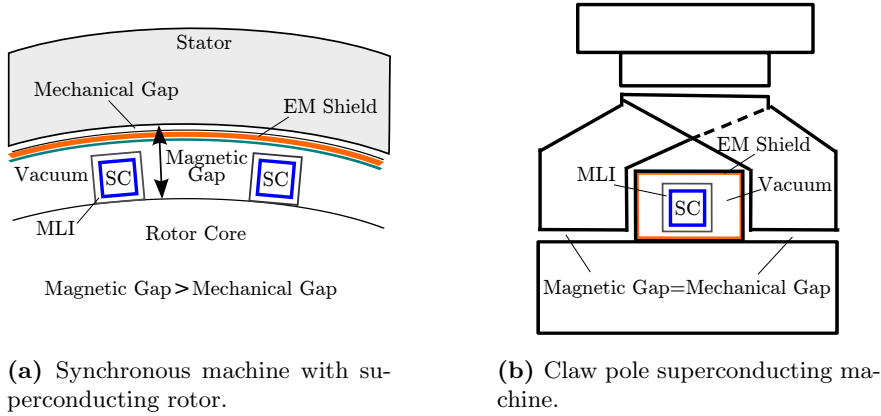


**Figure 9.1:** Magnetic and mechanical gap comparison for the typical superconducting machine and the claw pole machine.

ability by introducing some redundancy in the cooling system or using maintenance-free components (e.g. long life seals, reliable coolers). However, the cryostat, in particular the transfer couplers and brushes, still remain as the single point of failure.

This thesis presents a different approach to the problem by introducing the stationary superconducting field winding concept. The concept simplifies the cryostat design by eliminating the transfer couplers and any rotating parts, which helps to increase the reliability. Furthermore, it simplifies the multi-physics problem by de-coupling the thermal aspects from the electromagnetic and structural aspects:

- **Thermal-Electromagnetic:** Contrary to typical superconducting machine, in the claw pole machine, the main flux path does not pass through the cryostat and through the insulation layers. In other words, the magnetic air-gap is the same as the mechanical air-gap, which decouples the cryostat design from the magnetic circuit (see figure 9.1).
- **Thermal-Structural:** The electromagnetic torque does not act on the superconducting coil. Thus, the cryostat supports can be designed irrespective of the rotor torque, which de-couples the structural design from the cryostat design.

## 9.2 Contribution to Knowledge

This thesis presents four novel topologies:

- Homopolar axial flux superconducting machine
- Bi-polar flux superconducting machine
- Claw pole transverse flux superconducting machine
- Double sided claw pole machine

The main design concept of these topologies is the single stationary SC coil, which is coupled with a variable reluctance iron-core. In the evolution of these topologies various design weaknesses have been eliminated. The outcome of this evolutionary process resulted in a novel claw pole transverse flux superconducting machine that is suitable for low speed-high torque applications.

Another novelty presented in the double-sided claw pole topology is the sectioned cryostat concept, which with the double-armature configuration effectively divides the machine into eight parallel sections. This introduces modularity and redundancy to the system, which is critical for offshore wind turbines where the O&M is difficult and expensive. Also, the modularity brings operational advantages in manufacturing and maintenance as the machine will be easier to transport and faulty components can be replaced without removing the whole generator, while keeping the availability at maximum. These will translate directly into the reduced cost of energy for large offshore wind turbines.

Maybe the biggest advantage of the proposed topology is the minimal superconducting wire requirement, which is due to two main reasons. Firstly, the coil is loop shaped, which results in better utilization of the MMF per length of the coil. Secondly, as shown in figure 9.1, the magnetic gap in the claw pole topology equals to the mechanical gap. However, in a typical superconducting machine the flux has to pass through many layers (vacuum, radiation shield, EM shield, etc.) through the cryostat, which results in a much larger magnetic gap and increased MMF requirement.

A 10 MW, 10 rpm machine is designed in Chapter 8 and it was shown that the field winding requires 32.4 kAt, which is equal to 15 km of  $\text{MgB}_2$  at 30 K or 13.5 km of YBCO at 65 K. This is substantially less than other superconducting designs. In table 9.1, the superconducting wire requirements of several 10 MW designs are compared. In particular, air-cored topologies require hundreds of kilometres of superconducting wire. The closest design is the AMSC [152], which requires 36 km of YBCO at 30 K. However, the proposed design just requires 3.4 km of YBCO at that temperature, which is less than one tenth of the AMSC's design.

It may be argued that the power density of the machine is limited because of the iron-cored structure and it is heavier than its competitors. Although, it is true that the

**Table 9.1:** Comparison of superconducting wire requirements and total mass of 10 MW direct-drive superconducting generators.

	SC Wire Requirement	Total Mass
Proposed Design	15 km $\text{MgB}_2$ (30 K)	184 t
	3.4 km YBCO (30 K)	
	13.5 km YBCO (65 K)	
Abrahamsen et. al. [17]	200–300 km YBCO	88 t
General Electric [51]	720 km NbTi	143 t
AMSC/Snitchler et. al. [152]	36 km YBCO (30K)	150 t
Sung et. al. [156]	586 km YBCO	147 t
Sung et. al. [156]	222 km Bi2223	196 t
Terao et. al. [158]	270 km HTS + 275 km $\text{MgB}_2$	-
Kim et. al. [89]	919 km HTS	-
Quddes et. al. [134]	1050–1400 km HTS	-

proposed design is 23 % higher than the trend-line of superconducting machines, it is still 40 % lighter than the similar rated DDPMGs.

Thus, it is believed that the proposed claw pole topology is a very suitable design to initiate the superconducting generators for offshore wind turbines. The first prototypes can be used to prove that superconducting generators are as reliable as alternative power take-off systems. It may be the intermediate step between conventional generators and more power dense fully-superconducting generators that will be built in future, when the price of superconducting wires come down.

The work in this thesis has also contributed to a number of publications, which are listed in Appendix J.

## 9.3 Further Work

Throughout the thesis, electromagnetic modelling was at the centre of the design process, but structural and thermal aspects of the machine also requires further consideration.

Structural modelling in particular, may be the most important aspect of direct-drive superconducting machines as the high air-gap flux densities induce significant stresses on the structure. In the homopolar and bi-polar superconducting machine designs, the air-cored armature eliminates the attraction forces between the stator and rotor. However, in the claw-pole machine there are large forces acting between stator and rotor. The importance of a detailed structural analysis became apparent with the linear prototype presented in Chapter 7. The air-gap closes for large field currents, which makes it impossible to work with a superconducting coil. Although, these forces are eliminated in a double-sided claw pole machine design, the machine still requires a detailed structural modelling not only to make sure the deflections are within the acceptable range but also to minimize the structural mass, which was 70 % of the total mass in the 10 MW design.

The cryostat design can also benefit from thermal modelling. The heat loss in the system is estimated using analytical calculations, but the heat loss can be minimized by a proper design of the insulation system, suspension straps and the electromagnetic shields. Furthermore, if the cryostat cross-section area can be minimized, it will reduce the overall mass and improve the electromagnetic performance of the machine by minimizing the leakage flux.

The linear prototype is manufactured with a copper field winding to reduce the prototyping cost. In parallel, a project is planned to replace the field winding with a superconducting coil, which will prove the operation of the concept as a superconducting machine, but it requires the modification of the structural design as mentioned before. A 25 kW rotational double-claw pole machine should be built to prove the concept for wind turbine applications.

All the results presented in this thesis and FEA models are made available as a means of openness and reproducibility. The files can be accessed by the methods described in Appendix A. It is believed that the models can be a base for further research.



---

---

## Appendix A

# Accessing Data and Models

---

The data used in this thesis are made available for reproducibility purposes, which include:

- Graphs, photos and schematics,
- FEA model files and result logs,
- Scripts, and code snippets.

The path to the relevant files are presented as footnotes with a folder icon (📁) throughout the dissertation.

In order to access the files, please contact to the author or visit the University of Edinburgh's SVN repository, using the following link:

<https://svn.ecdf.ed.ac.uk/repo/user/s0977588/htsg>

The intellectual properties of the designs and topologies presented in this thesis are still belong to the author and the University of Edinburgh.





# Data Sheets for Some Superconducting Wires

---

## B.1 Bi-2223

The data-sheets for Bi-2223 tapes manufactured by Bruker HTS GmbH is presented. The wire dimensions is 4mmx0.22mm and has 121 filaments. The performance of Bi-2223 wires change with temperature and magnetic flux density as given in figure B.1. The critical current at self field with varying temperature is presented in figure B.2.

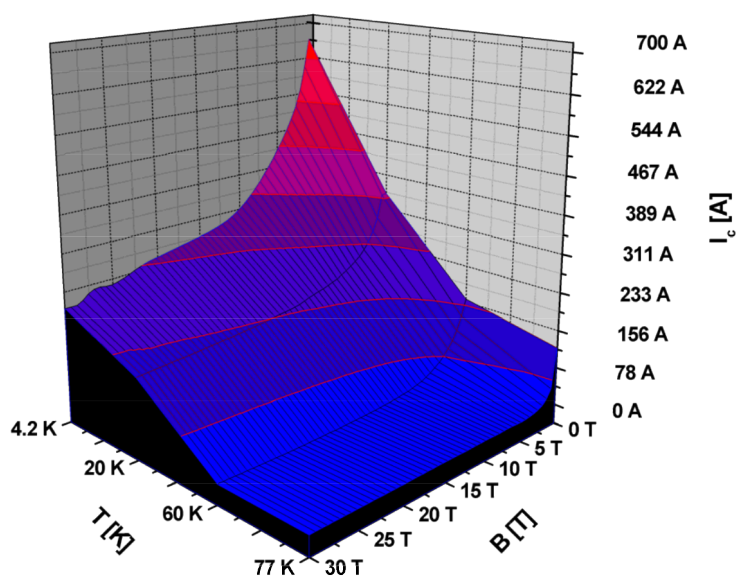


**Figure B.1:** The critical current variation of Bi-2223 wire with temperature and magnetic flux [46].

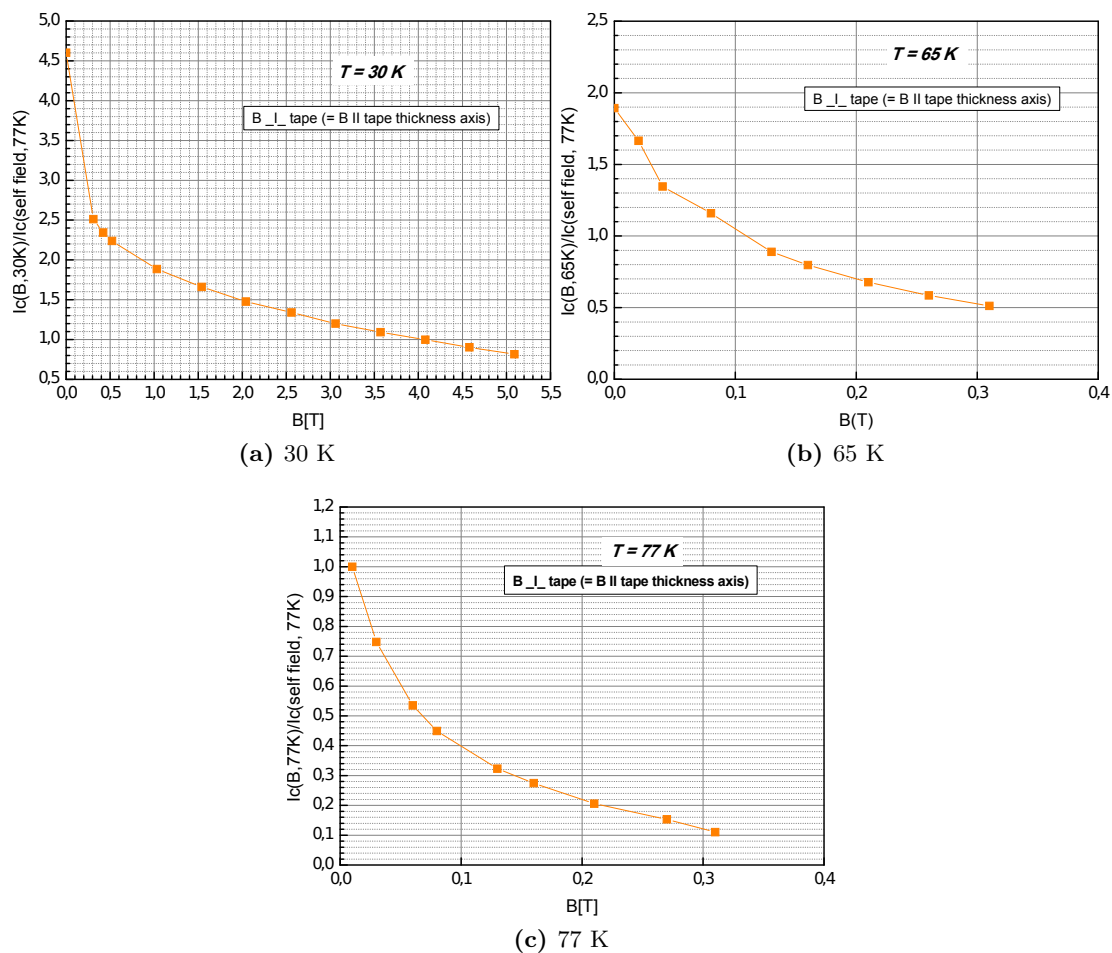


**Figure B.2:** The critical current of Bi-2223 wire at various temperatures (self-field) [46].

## B.2 YBCO

In this section, data-sheets of Amperium YBCO wires manufactured by AMSC are presented. There are two different sizes of the Amperium wires: 4.8mm x 0.2mm and 12mm x 0.22 mm. The wires has a current density around 100 A/mm<sup>2</sup> at self-field at 77 K. The performance of YBCO wires change with temperature and magnetic flux density as presented in figure B.3.

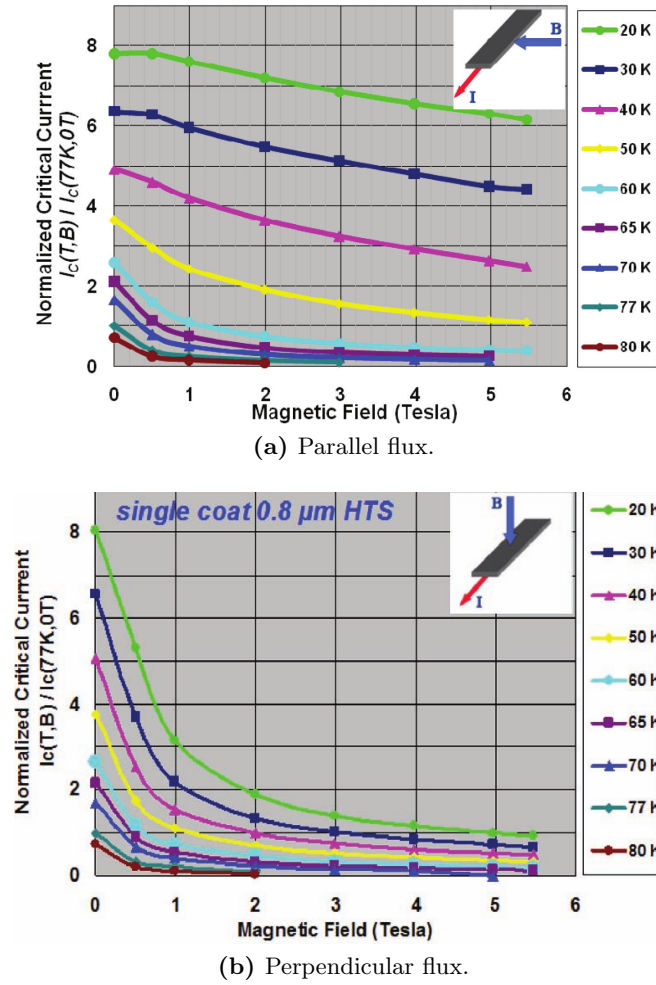


**Figure B.3:** Normalized critical current variation for Amperium YBCO wire with temperature and external magnetic field [23].

### B.3 $\text{MgB}_2$

In figure 2.19 the critical current variation of a  $\text{MgB}_2$  with external magnetic field and temperature is given. The wire is manufactured by Columbus Superconductor and has 14 superconducting filaments. The dimensions of the wire are 3.65 mm x 0.65 mm.

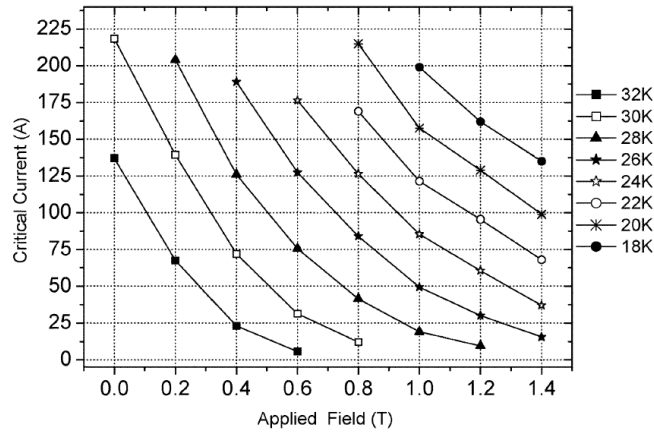


**Figure B.4:** Critical current versus magnetic field and temperature. 3.65 mm x 0.65 mm  $\text{MgB}_2$  wire with 14 superconducting filaments [116].

# Reluctance Network Parameters

---

## C.1 Homopolar Superconducting Machine

The reluctances used in the analytical model defined in section 4.3.1 is defined in this section.

### C.1.1 Basic Magnetic Circuit

*Core Web Reluctance  $R_{web}$*

$$R_{web} = \frac{\frac{h_g}{2} + \frac{\pi t_{web}}{4}}{\mu_c A_{web}} \quad (C.1)$$

*Core Limb Reluctance  $R_{limb}$*

$$R_{limb} = \frac{w_g}{\mu_c A_{core}} \quad (C.2)$$

*Core Tooth Reluctance  $R_{tooth}$*

$$R_{tooth} = \frac{\frac{\sqrt{t_c^2 + L_m^2}}{2} + h_t}{\mu_c A_{tooth}} \quad (C.3)$$

*Airgap Reluctance  $R_{gap}$*

$$R_{gap} = \frac{h_w + 2a_g}{\mu_0 A_{tooth}} \quad (C.4)$$

The cross-sectional areas of the core sections are shown in figure 4.3. The areas can be calculated as follows:

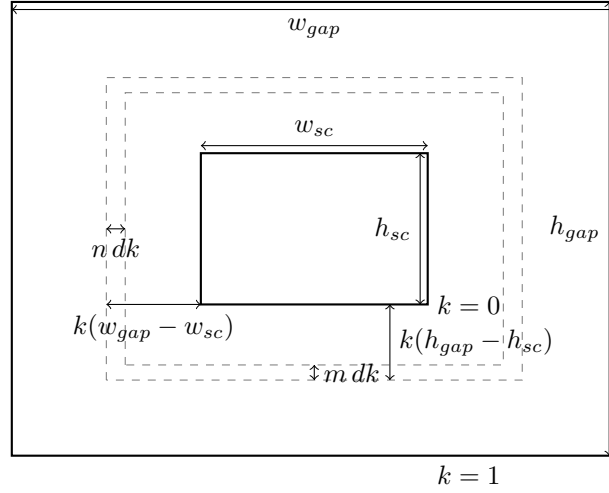


**Figure C.1:** Cut-through section and flux lines in axial homopolar machine.

Core Web Area  $A_{web}$

$$A_{web} = \frac{\theta_{pole}}{2} (r_{web}^2 - r_{in}^2) \quad (C.5)$$

Core Area  $A_{core}$

$$A_{core} = \theta_{core} r_{tooth} t_c \quad (C.6)$$

Core Tooth Area  $A_{tooth}$

$$A_{tooth} = \frac{\theta_{core}}{2} (r_{out}^2 - r_{tooth}^2) \quad (C.7)$$

*Leakage Around the Superconducting Coil* The leakage flux around the superconducting coil is estimated by combining the parallel connected reluctances of infinitely small flux paths as shown in figure C.1. In the figure the inner rectangle represents the superconducting coil cross sectional area and the outer rectangle represents the gap around the superconducting coil.

$$R_{leakage-sc} = \frac{1}{\int \frac{1}{R_{dk}}} \quad (C.8)$$

$$\int \frac{1}{R_{dk}} = \int_0^1 \frac{1}{2 \left( \frac{h_{sc} + km}{\mu_0 \tau_{sc} m dk} + \frac{w_{sc} + kn}{\mu_0 \tau_{sc} n dk} \right)} \quad (C.9)$$

$$m = h_{gap} - h_{sc} \quad (C.10)$$

$$n = w_{gap} - w_{sc} \quad (C.11)$$

$$\tau_{sc} = \frac{2\pi R_{sc}}{n_{pole}} \quad (C.12)$$

Equation C.9 can be simplified as:

$$\int \frac{1}{R_{dk}} = \frac{\mu_0 \tau_{sc}}{2} \int_0^1 \frac{dk}{C + 2k} \quad (C.13)$$

where

$$C = \frac{h_{sc}}{m} + \frac{w_{sc}}{n} \quad (C.14)$$

Thus, the equivalent reluctance of the leakage path becomes:

$$R_{leakage-sc} = \frac{4}{\mu_0 \tau_{sc} (\ln|C + 2| - \ln|C|)} \quad (C.15)$$

### C.1.2 Extended Magnetic Circuit

The air-gap reluctance is divided into four equal reluctances: two centre gap reluctances ( $R_{gc}$ ) and two side gap reluctances ( $R_{gs}$ ). These reluctances are defined as:

$$R_{gc} = R_{gs} = \frac{h_w + 2a_g}{\mu_0 \frac{\tau_{core}}{4} L_m k_{fring}} \quad (C.16)$$

$k_{fring}$  is a factor to represent fringing flux in radial extend of the core. It is assumed to be 1.1.

**Fringing Flux** In the extended magnetic circuit fringing flux around the magnetic core is represented by two reluctance terms:  $R_{f1}$  and  $R_{f2}$ .



---

$N_{pole}$	72
$R_{in}$	1520 mm
$R_{web}$	1640 mm
$L_m$	200 mm
$t_c$	180 mm
$t_{web}$	120 mm
$h_g$	170 mm
$w_g$	160 mm
$h_t$	69 mm
$t_w$	30 mm
$h_{sc}$	150 mm
$w_{sc}$	120 mm
$sc_c$	10 mm

---

**Table C.1:** Dimensions for the homopolar superconducting machine.

$$b = \frac{\tau_{pole} - \tau_{core}}{6} \quad (C.17)$$

$$R_{f1} = \frac{2\sqrt{(a_g + 0.5h_w)^2 + b^2}}{\mu_0 \left( \frac{3b}{2} L_m \right)} \quad (C.18)$$

$$R_{f2} = \frac{2\sqrt{(a_g + 0.5h_w + 0.5h_t)^2 + (2b)^2}}{\mu_0 \left( \frac{3b}{2} L_m \right)} \quad (C.19)$$

$$(C.20)$$

### C.1.3 Dimensions & Parameters

Dimensions used in the analytical model and FEA simulations are presented in table C.1.

## C.2 Bipolar Superconducting Machine

Dimensions used in the FEA simulations of section 5.3.1 are presented in table C.2. Other dimensions can be accessed from the simulation files.

$T_{min}/gap$	$t_{min}$ (mm)	$\tau_{core}$ (mm)	$\tau_{pole}(mm)$
0.5	14	21	70
1.0	28	42	140
1.5	42	63	210
2.0	56	84	288
2.5	70	105	350
3.0	84	126	420

**Table C.2:** Dimensions for magnetic core optimization of the bipolar superconducting machine.

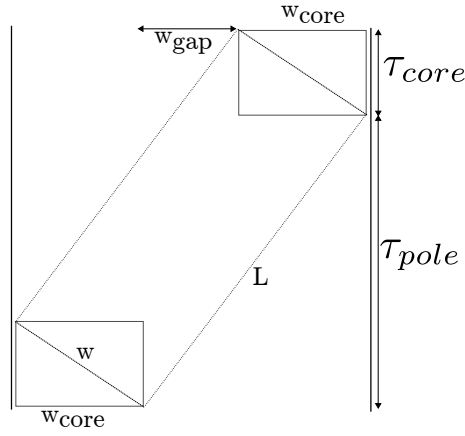


**Figure C.2:** Dimension for the inner stator reluctance term ( $R_{is}$ ).

### C.3 Claw Pole Superconducting Machine

In this section, the reluctance network parameters for the claw pole magnetic circuit (see figure 6.6) are presented.

*Inner Stator Core Reluctance  $R_{is}$*  The equivalent length and area of this reluctance component is shown in figure C.2.

$$R_{is} = \frac{\sqrt{(w_{gap} + w_{core})^2 + \tau_{pole}^2}}{\mu_{st} \sqrt{\tau_{core}^2 + w_{core}^2} h_{core}} \quad (C.21)$$

$$R_{os} = \frac{2h_w + h_{backcore}}{\mu_{st} t_{tooth} w_{claw}} + \frac{\theta_{pole} R_{os}}{\mu_{st} h_{backcore} w_{claw}} \quad (C.22)$$

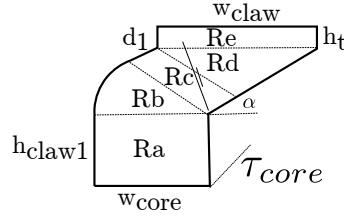


**Figure C.3:** subcomponents in the claw pole reluctance ( $R_{claw}$ ).

*Airgap Reluctance  $R_{ag1}, R_{ag2}$*

$$R_{ag1} = R_{ag2} = \frac{ac}{\mu_0 w_{core} \tau_{core} k_{fring}} \quad (C.23)$$

*Claw Pole Reluctance  $R_{claw}$*  Although, the claw pole is represented by a single component in figure 6.6, it can be divided into sections as shown in figure C.3.

$$R_{claw} = R_a + R_b + R_c + R_d + R_e \quad (C.24)$$

$$R_a + R_b + R_c = \frac{h_{claw1} + \left(\frac{\pi}{2} - \alpha\right) \frac{w_{core}}{2} + d_1}{\mu_{core} w_{core} \tau_{core}} \quad (C.25)$$

$$R_d = \frac{0.5 w_{claw} \cos(\alpha)}{\mu_{core} w_{claw} \sin(\alpha) \tau_{core}} \quad (C.26)$$

$$R_e = \frac{h_t}{\mu_{core} w_{claw} \tau_{core}} \quad (C.27)$$

*Leakage Flux Reluctances ( $R_{lSC}, R_{lclaw}, R_{lzigzag}, R_{lcross}$ )* Leakage flux between claw pole faces is represented by  $R_{lclaw}$ . The leakage reluctance can be represented as:

$$R_{lclaw} = \frac{\sqrt{k_{align} w_{pole}^2 + (\tau_{pole_{claw}} - \tau_{core_{claw}})^2}}{\mu_0 \left( w_{claw} h_t + \frac{w_{pole}^2}{4} \tan(\alpha) \right)} \quad (C.28)$$

where  $k_{align}$  is the misalignment factor similar to one in presented in 5.3.1.  $\tau_{pole_{claw}}$ ,  $\tau_{core_{claw}}$  are the pole and core pitches calculated at the centre of overlapping area.

Leakage around the superconducting coil is similar to the one calculated in equation C.15.

$R_{lzigzag}$  represents the overhang leakage reluctance from top face of the claw pole to the adjacent and it is described in detail in [133, 70]. This leakage flux depends on the type of the stator slots, dimensions of the claw pole and position of the rotor. It can be roughly approximated as:

$$R_{lzigzag} = 2 \frac{\sqrt{a_c^2 + \left(\frac{\tau_{pole}}{2}\right)^2}}{\mu_0 \tau_{core} w_{claw}} \quad (C.29)$$

$R_{lcross}$  represents the leakage flux from the inner faces of claw poles to the opposite side of the inner stator.

$$R_{lcross} = \frac{\sqrt{(0.5(w_{core} + w_{gap}))^2 + (0.75h_{claw})^2}}{\mu_0 \left( dl + \frac{w_{claw}}{2 \cos(\alpha)} + h_t \right) \tau_{pole}} \quad (C.30)$$

## C.4 Double-Claw Pole Superconducting Machine

$$\begin{aligned} R_{claw1} = R_{claw2b} &= R_b + R_c + R_d + R_e \\ &= \frac{\left(\frac{\pi}{2} - \alpha\right) \frac{w_{core}}{2} + d_1}{\mu_{core} w_{core} \tau_{core}} + \frac{0.5 w_{claw} \cos(\alpha)}{\mu_{core} w_{claw} \sin(\alpha) \tau_{core}} + \frac{h_t}{\mu_{core} w_{claw} \tau_{core}} \end{aligned} \quad (C.31)$$

$$R_{claw2a} = \frac{2h_{claw1}}{\mu_{st} w_{core} \tau_{claw}} \quad (C.32)$$



---

## Appendix D

# Software

---

In order to model the proposed machine with FEA three different software packages are used:

**SolidWorks:** Computer-Aided Design

**Opera-Vector Fields:** Finite Element Analysis

**R:** Data Analysis

### D.1 SolidWorks

SolidWorks is a popular commercial computer-aided design (CAD) software for mechanical parts and assemblies [14]. The drawings of the designs presented in this study are available as SolidWorks files. All model files have been converted to IGES files to enable access from other CAD software. IGES is a standard text-based format for exporting solid object models.

### D.2 Opera - Vector Fields

Opera is a 2D/3D electromagnetic FEA software developed by Vector Fields, which was recently acquired by Cobham [39]. Although, Opera specializes in electromagnetic design, it has extra packages for thermal and structural analysis. Opera can simulate 2D and 3D models. 2D FEA models are computationally more efficient than 3D models. However, in this study 3D FEA models have to be used due to lack of any planar or axial symmetries.

Analysing a model in Opera has three main stages: pre-processing, solving and post-processing. A block diagram for a typical Opera model analysis is presented in figure D.1.

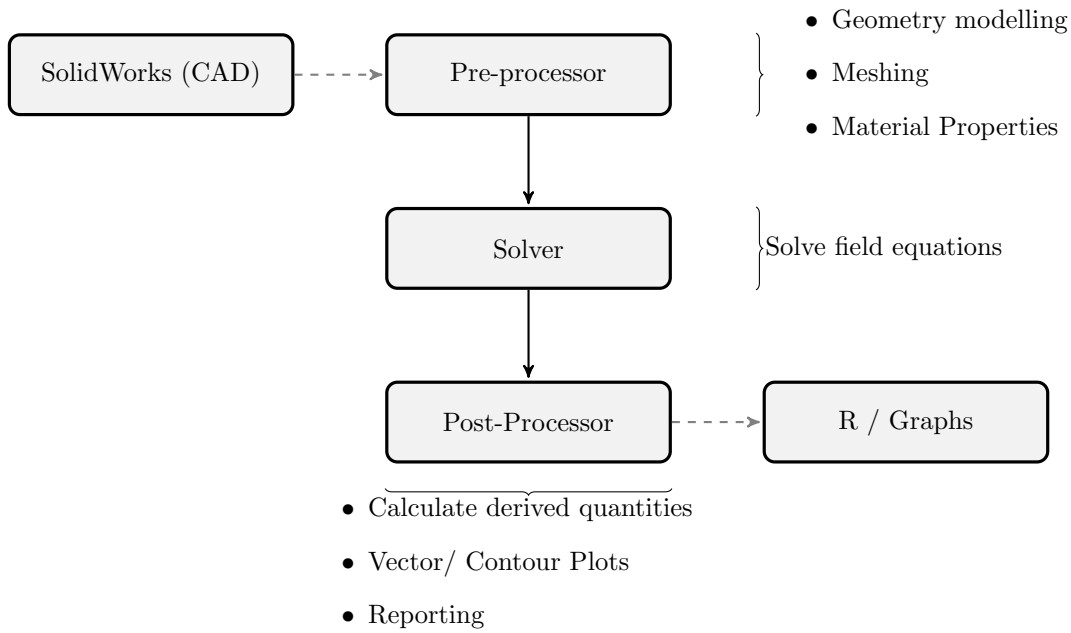


**Figure D.1:** A typical FEA block diagram using SolidWorks, Opera and R.

### D.2.1 Pre-Processor and Modeller:

The pre-processor provides an interface to draw the model geometry. Alternatively, the model geometry can be drawn using SolidWorks and imported to Opera. Although, this option is convenient for models with a few components, it can lead to errors in more complex models and it usually takes longer to mesh the imported models. A better way is to use Opera's own modeller software, which has some basic building blocks. More complex geometries can be obtained by boolean operations such as extruding or swiping. More importantly, the model can be drawn by built-in scripting tools (Fortran based) and all components can be parametrized. This method makes it possible to reproduce the same models or change some parameters to analyse the effect.

During the pre-processing stage, material properties such as conductivity and B-H characteristics are defined. The pre-processor divides the model into discrete blocks based on the mesh size definitions for each cell, which are the building blocks of a model. Any geometric element in the model should be divided into simple cell geometries for easier mesh generation. The mesh size has a direct effect on the accuracy of the simulation. In particular, the meshing of the air-gap is the most important part in an electrical machine model. A fine mesh will increase the simulation accuracy, but a model with finer mesh will take significantly longer to solve. Thus, the number of elements should be selected considering the solution tolerance and computation time. In the following sections, this selection will be described in detail. In the 3D model the mesh geometry options are tetrahedra and hexahedra.

Boundary conditions of the model are also defined in the pre-process stages. These have two functions: to limit the solution space and to apply any symmetry conditions. In the FEA process all types of symmetries should be defined to minimize the model size as much as possible. In this way, the number of elements and the computing time can be significantly reduced without sacrificing accuracy. Opera has some built-in symmetry modes such as; cyclic symmetry and planar symmetry. It is relatively easy to implement these boundary conditions. However, the model has to be understood thoroughly for a successful symmetry implementation. It is easy to get results with a FEA software, but it is much easier to get wrong results.

### D.2.2 Solver:

Opera has different solver types for different problems. Some of the solvers related to electromagnetic problems are [9]:

- Tosca: Magnetostatic or electrostatic field and current flow models.
- Carmen: Transient electromagnetic fields (rotary and linear machines).
- Demag: Demagnetization of permanent magnets.
- Elektra: Time dependant electromagnetic fields, eddy currents.
- Quench: Quench in a superconducting magnet. Transient thermal fields coupled with electromagnetic.

The main option for the solver is the type of problem, which can be linear or non-linear. In linear problems, a linear B-H characteristics is assumed and saturation is neglected. The machines proposed in this study have high flux densities and many parts of the machine are highly saturated. Thus, non-linear solution option is preferred throughout this dissertation. However, it is a good practice to simulate a new model first with linear materials to verify the boundary conditions and symmetry definitions. Once enough confidence is gained from linear simulations, the designer can focus on the accuracy and mesh size definitions.

Opera uses Newton-Raphson method in the solution of non-linear problems. The method is defined in 4.3.1. The maximum number of iterations and the solution tolerance should be defined before the solver is started. The initial number of maximum iterations is defined as 21, but for a reasonable model it doesn't usually take more than 8–10 iterations. If the simulations stop because the maximum number of iterations are reached, it is a better idea to modify the mesh size and change the tolerances than just increasing the maximum number of iterations.



### D.2.3 Post-processor:

If the solver finds a solution within the defined tolerances, it stores the model and solution in a .op3 file which can be analyzed by the post-processor. The post-processor can produce 2D and 3D plots to represent the flux density distribution. Furthermore, mathematical operations can be applied on specific volumes and surfaces, which gives a convenient way to evaluate the performance of the model. The calculated variables can also be exported as text file, which then can be analyzed later by other software.

## D.3 R/RStudio

R is an open-source programming language [136]. Although, it started as a computational tool for statistics problems, now it has packages for many computation or graphics requirements. Detailed information about the program and packages can be obtained from CRAN [136]. RStudio is an optional interface for the R. RStudio makes it easier to write R codes, plot graphs and keep track of your work with integrated version control system [141].

# Linear Versions of Homopolar and Bipolar Machine

---

## E.1 Linear Homopolar Machine

The structure of the linear version is similar to the axial machine. The stator is air-cored, and the superconducting field winding is wrapped around the armature coils. However, the translator core is not C-shaped but has a closed shape as shown in figure E.1.

The stator and the assembled linear superconducting homopolar machine is presented in figure E.2. The machine in the figure is a long stator - short translator type, but it is also possible to use a short stator - long translator configuration. In this configuration, the cost of the generator can be reduced due to the decreased superconducting wire length. However, the generator is expected to be heavier due to the increased number of magnetic cores. Furthermore, access to the superconducting coil is more difficult in a short stator configuration.

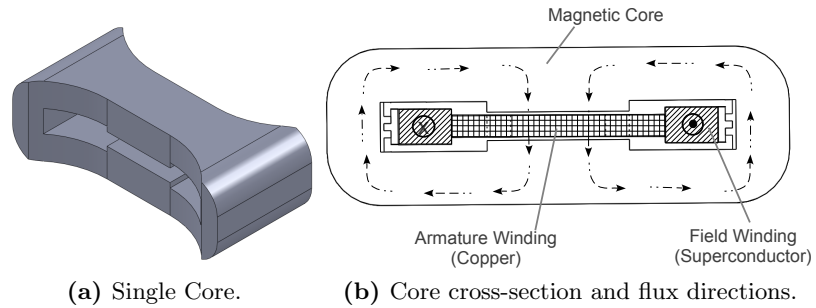


**Figure E.1:** Linear superconducting homopolar machine core.

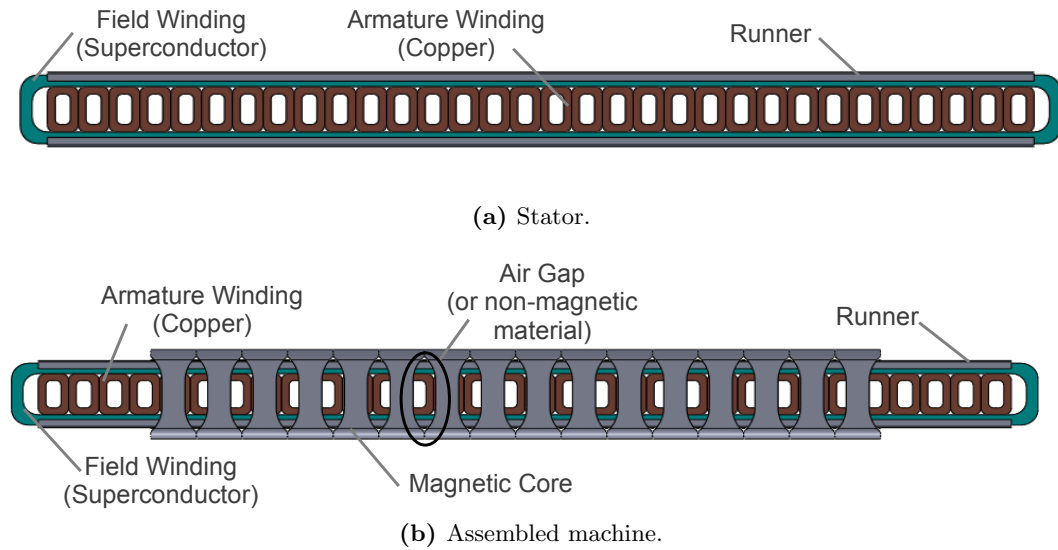


**Figure E.2:** Linear superconducting homopolar machine.

## E.2 Linear Bipolar Machine

It is also possible to modify axial bipolar machine into a linear machine as shown in figure E.3. In this configuration, two independent superconducting field windings are used. The flux is diverted using C-cores. There are two stacked machines that can operate independently.

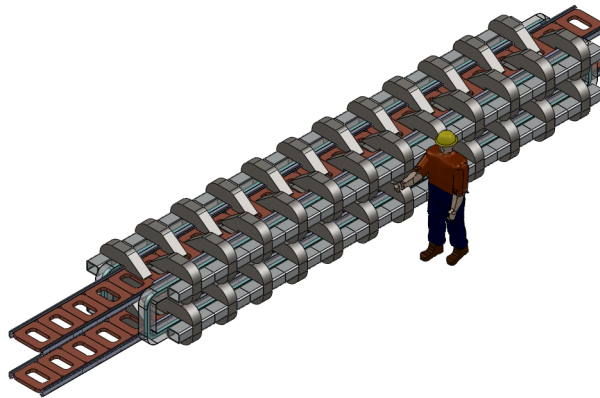


**Figure E.3:** Linear bipolar machine.

# Specific Magnetic and Electric Loading

---

There are many parameters that can be used to evaluate the performance of electrical machines. The power output, efficiency can be used for the similar size machines. Alternatively, the outer diameter, total mass and axial length of the machine can be used to compare same power rated machines. A traditional way to compare the electric and magnetic performance separately is to use specific magnetic loading and specific electric loading.

The specific magnetic loading ( $\bar{B}$ ) is defined as the mean absolute radial flux density over the entire cylindrical surface of the air-gap of a machine [69].

$$\bar{B} = \frac{1}{2\pi L} \int_0^L \int_0^{2\pi} |B_r(\theta, l)| dl d\theta \quad (\text{F.1})$$

where  $B_r$  is the radial flux density,  $L$  is the axial length of the rotor. Alternatively, the specific magnetic density can be defined in terms of magnetic flux per pole ( $\phi_{pp}$ ) as:

$$\bar{B}_{ag} = \frac{p \phi_{pp}}{\pi D_{ag} L} \quad (\text{F.2})$$

where  $p$  is the number of poles,  $D_{ag}$  is the air-gap diameter [119]. However, magnetic loading at air-gap does not consider the effect of the zigzag leakage flux or the leakage flux between stator teeth shoes. A more accurate way is to calculate the magnetic loading at the mean armature winding diameter ( $D_{st}$ ):

$$\bar{B}_{st} = \frac{p \phi_{pp}}{\pi D_{st} L} \quad (\text{F.3})$$

The magnetic loading of an electric machine is limited by the magnetic properties of the materials (i.e. saturation of the magnetic core). Although, equation F.3 does not include terms like core losses, flux harmonics, and cogging torque; it is a good way to

evaluate the magnetic performance of a machine regardless of operating speed or power rating.

The specific electric loading ( $q$ ) is defined as the total armature ampere conductors per unit length of the rotor circumference [69].

$$q = \frac{I_a}{\pi D_{ag}} \quad (\text{F.4})$$

It is also possible to define specific electric loading for AC machines in terms of the phase current ( $I_{ph}$ ):

$$q = \frac{3 \times 2N I_{ph}}{\pi D_{ag}} \quad (\text{F.5})$$

where  $N$  is the number of turns in series per phase [44]. Electrical loading in a machine is limited by the temperature rise in the armature windings, and it can be increased by forced cooling methods (e.g. water cooling). Typical specific electric loading value is around 30,000–40,000 A/m for small-medium sized machines, 40,000–50,000 A/m for large sized air cooled machines [44].

Multiplication of specific magnetic and electric loading ( $\bar{B} \times q$ ) gives the average tangential stress over the rotor surface [69]. Thus, the total torque of the machine can be calculated by multiplying the average tangential force, with air-gap surface area and radius:

$$T = (\bar{B} \times q) \times \pi D_{ag} L \times \frac{D_{ag}}{2} = \frac{\pi}{2} (\bar{B} \times q) D_{ag}^2 L \quad (\text{F.6})$$

The power can be expressed as:

$$P = T \times \omega \quad (\text{F.7})$$

Thus, equation F.6 becomes:

$$P = \frac{\pi}{2} (\bar{B} q) D_{ag}^2 L \omega \quad (\text{F.8})$$

In equation F.8, ( $D^2 L$ ) term is related to the volume –and hence mass– of the machine. Thus, the power rating of a machine is proportional with the volume multiplied by the rotational speed. This is one of the main trade-off in the wind turbine power take-off systems. The mass of the generator can be reduced if the rotational speed of the generator is increased (e.g. by using a gearbox). Direct-drive generators eliminate the

gearbox, but they are large and heavy. One way to reduce the mass of the generator is to increase magnetic or electric loading. In section 3.6 it is stated that, most of the superconducting generator designs use copper wire for armature windings and the current loading of these machines are similar to conventional machines. Thus, the magnetic loading is the only factor that can be improved for such a superconducting machine.



# Cryocooler Comparison

---

## G.1 Cooling Power vs. Temperature

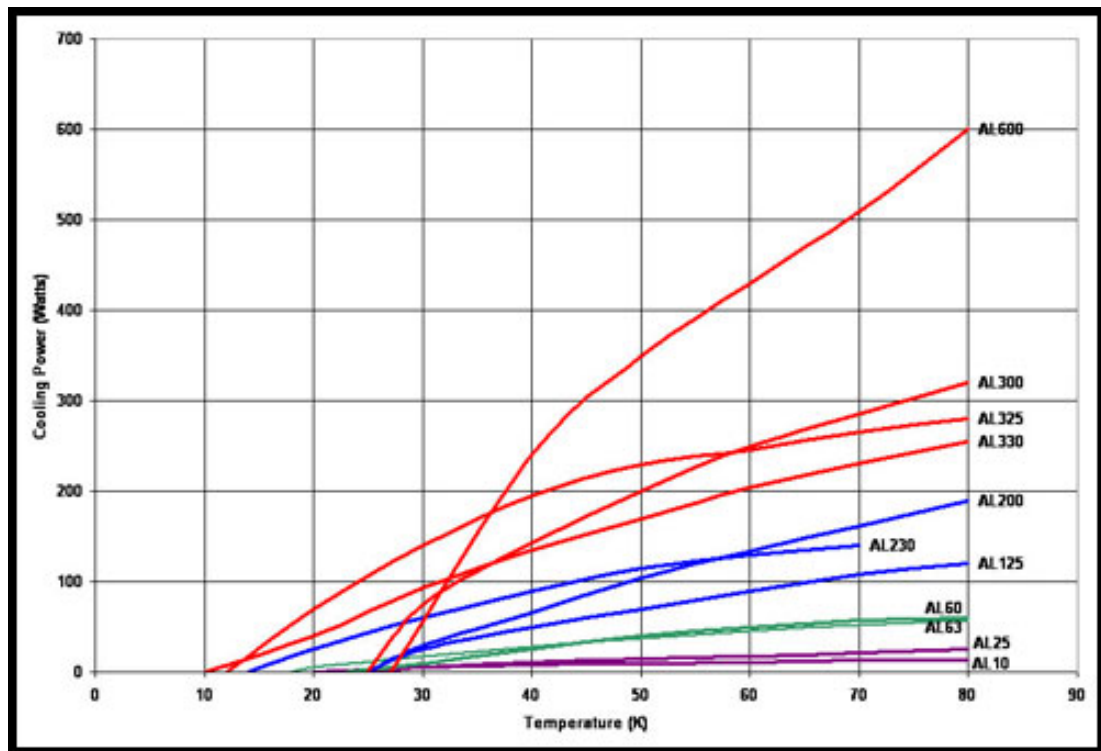


**Figure G.1:** The operating temperature vs. cooling power characteristics for Cryomech's cryocoolers (Courtesy of Cryomech) [42].





# Technical Drawings

---

## H.1 10 MW, 10 rpm Generator

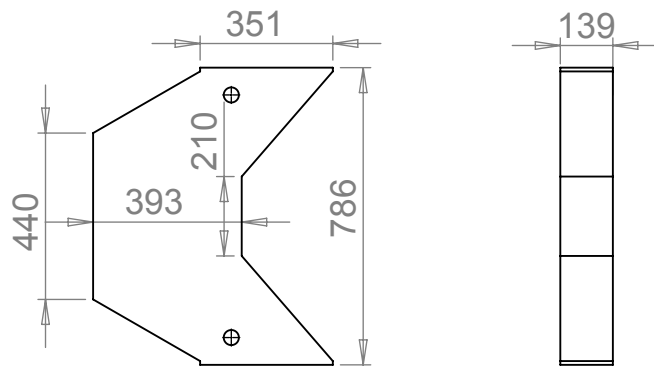


**Figure H.1:** Large claw-pole of the 10 MW, 10 rpm double-claw pole generator.

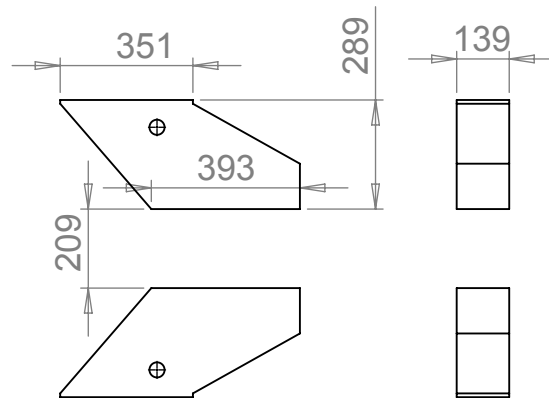


**Figure H.2:** Small claw-poles of the 10 MW, 10 rpm double-claw pole generator.

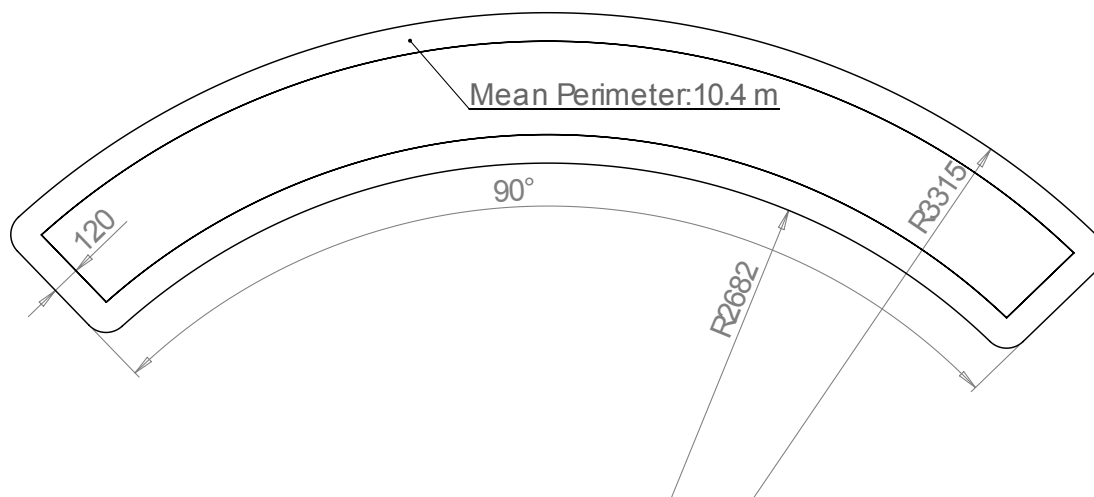


**Figure H.3:** Field winding of the 10 MW, 10 rpm double-claw pole generator.

---

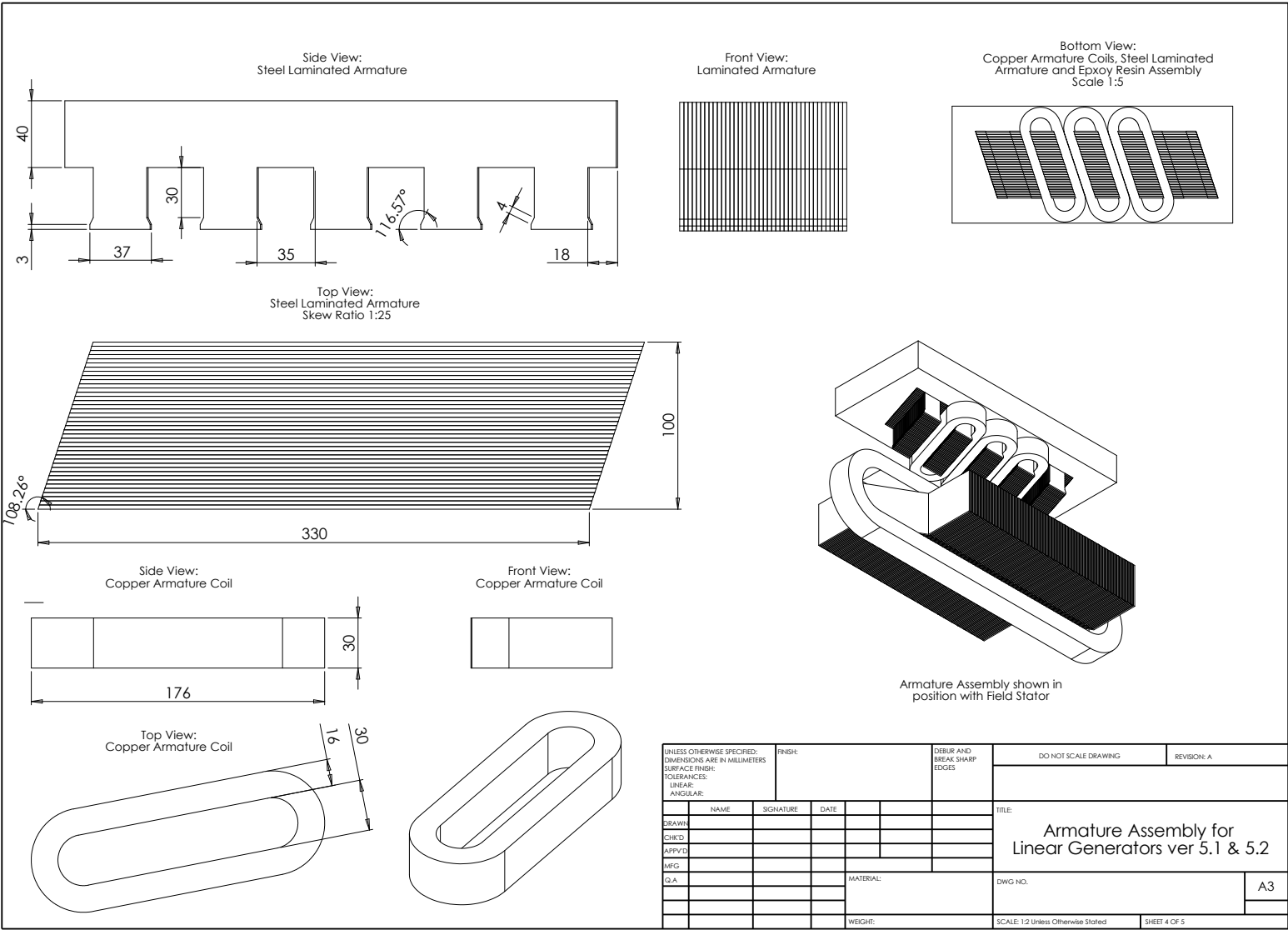
Appendix I

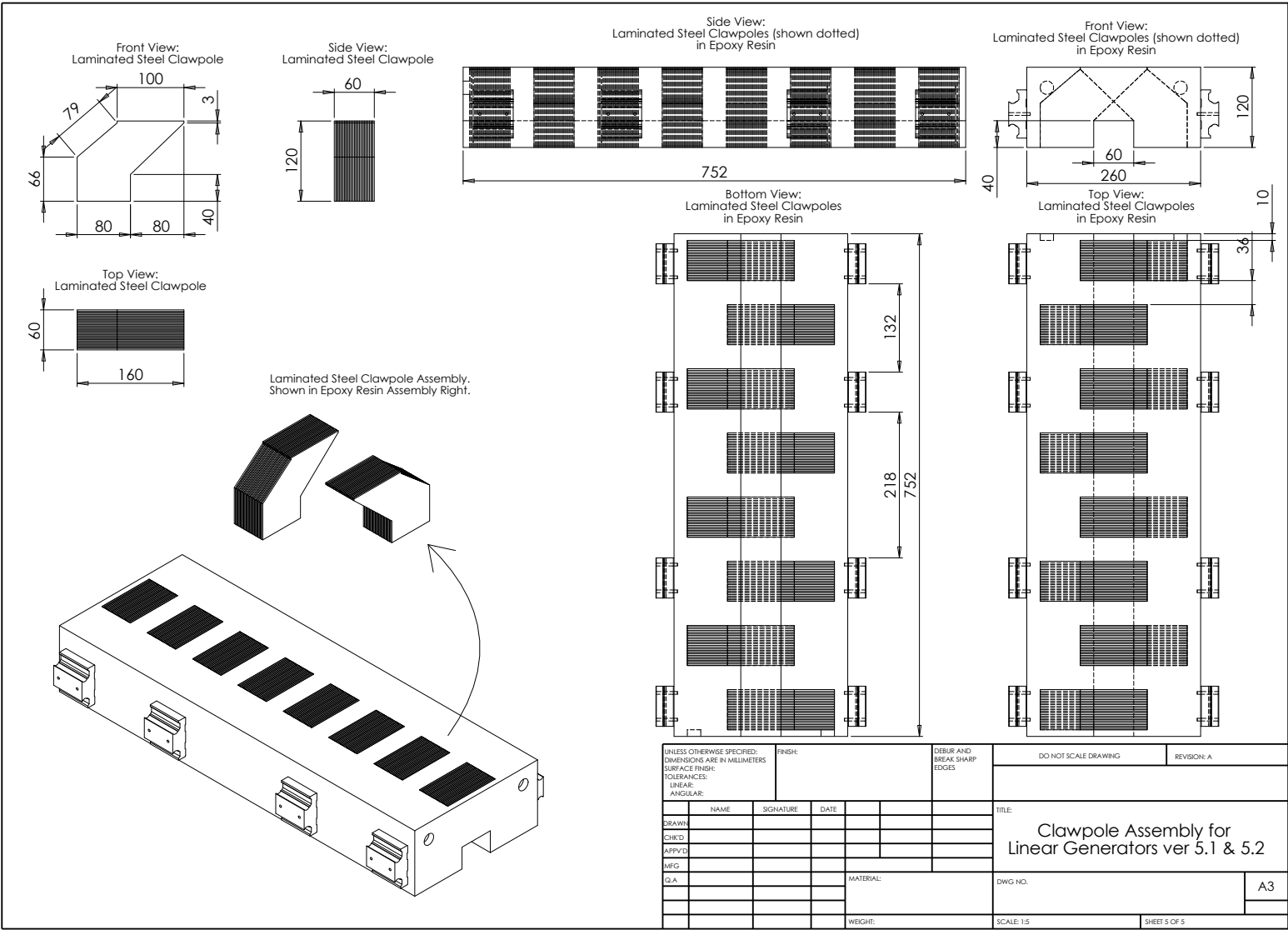
# **Linear Prototype Technical Drawings**

---



UNLESS OTHERWISE SPECIFIED: DIMENSIONS ARE IN MILLIMETERS				FINISH:		DEBUR AND BREAK SHARP EDGES		DO NOT SCALE DRAWING				REVISION: A			
SURFACE FINISH: TOLERANCES: LINEAR: ANGULAR:								TITLE:  Linear Generator ver 5.2							
NAME		SIGNATURE		DATE											
DRAWN															
CHK'D															
APP'VD															
MFG															
Q.A.				MATERIAL:				DWG NO.				A3			
								WEIGHT:				SCALE:1:10 Unless Otherwise Stated		SHEET 2 OF 5	





## List of Publications

---

- O. Keysan and M. A. Mueller. A Homopolar HTSG Topology for Large Direct-Drive Wind Turbines. *IEEE Transactions on Applied Superconductivity*, 21(5): 3523–3531, October 2011. ISSN 1051-8223. 10.1109/TASC.2011.2159005. URL <https://ieeexplore.ieee.org/xpls/icp.jsp?arnumber=5948361>
- O. Keysan and M. Mueller. Superconducting generators for renewable energy applications. In *IET Conference on Renewable Power Generation (RPG 2011)*, volume 2020, pages 12–12, Edinburgh, 2011. IET. 10.1049/cp.2011.0102. URL [http://ieeexplore.ieee.org/xpls/abs\\_all.jsp?arnumber=6136084](http://ieeexplore.ieee.org/xpls/abs_all.jsp?arnumber=6136084)
- O. Keysan and M. A. Mueller. A Transverse Flux High-Temperature Superconducting Generator Topology for Large Direct Drive Wind Turbines. In *Superconductivity Centennial Conference*, volume 01, pages 1–6, 2011. URL <http://www.sciencedirect.com/science/article/pii/S1875389212019761>
- O. Keysan and M. Mueller. A linear superconducting generator for wave energy converters. In *6th IET International Conference on Power Electronics, Machines and Drives (PEMD 2012)*, pages B134–B134, Bristol, 2012. IET. ISBN 978-1-84919-616-1. 10.1049/cp.2012.0298. URL <http://ieeexplore.ieee.org/xpl/articleDetails.jsp?arnumber=6242150>
- O. Keysan, D. Olczak, and M. A. Mueller. A Modular Superconducting Generator for Offshore Wind Turbines. *Journal of Superconductivity and Novel Magnetism*, pages 1–5, December 2012. ISSN 1557-1939. 10.1007/s10948-012-1950-1. URL <http://www.springerlink.com/index/10.1007/s10948-012-1950-1>
- O. Keysan. Application of high temperature superconducting machines to direct drive renewable energy systems. In M. Mueller and H. Polinder, editors, *Electrical Drives for Direct Drive Renewable Energy Systems*. Woodhead Publication, 2013. ISBN 84569-783-9. URL <http://www.woodheadpublishing.com/en/book.aspx?bookID=2043>
- O. Keysan, J. Burchell, and M. A. Mueller. Magnetic and Structural Analysis of a Transverse Flux Claw Pole Linear Machine (Invited Paper). In *IEEE International Conference on Industrial Technology*, pages 1–5, Cape Town, 2013. URL [http://ieeexplore.ieee.org/xpls/abs\\_all.jsp?arnumber=6505968](http://ieeexplore.ieee.org/xpls/abs_all.jsp?arnumber=6505968)





---

## Bibliography

---

- [1] Square/Round wires : different shapes and geometries for superconducting power cable application. Technical report, Columbus Superconductors, 2011. URL [http://www.columbussuperconductors.com/columbus/admin/fck\\_img/file/columbuswiresforsuperconductingpowercables\\_2011\(1\).pdf](http://www.columbussuperconductors.com/columbus/admin/fck_img/file/columbuswiresforsuperconductingpowercables_2011(1).pdf).
- [2] Design and Development of a 100 MVA HTS Generator for Commercial Entry. Technical report, General Electric Co., 2006. URL [http://www.ornl.gov/sci/htsc/documents/pdf/fy2003/HTS\\_Generator\\_Bray-Demko-Waynert.pdf](http://www.ornl.gov/sci/htsc/documents/pdf/fy2003/HTS_Generator_Bray-Demko-Waynert.pdf).
- [3] High Temperature Superconductivity Market Readiness Review - Navigant Consulting. Technical report, Department of Energy, USA, 2006. URL [http://www.suptech.com/pdf/articles/07\\_Navigant-HTS-Market-Readiness\\_Study.pdf](http://www.suptech.com/pdf/articles/07_Navigant-HTS-Market-Readiness_Study.pdf).
- [4] Hogan - Somaloy, 2009. URL <http://www.hoganas.com/en/Segments/Somaloy-Technology/Home/>.
- [5] AML Energy Home. URL <http://www.amlcleanenergy.com/>.
- [6] Fountain Design Ltd. URL <http://www.fountaindesign.co.uk>.
- [7] Global Wind Report - Global Wind Energy Council. Technical report, 2012. URL <http://www.gwec.net/publications/global-wind-report-2/global-wind-report-2012/>.
- [8] Global Offshore Wind Energy Markets and Strategies: 2009–2020, Emerging Energy Research. Technical report, 2009.
- [9] Opera 2D/3D - Reference Manual, V15R3. Technical report, Cobham Technical Services, 2012.
- [10] RUAG - Cryogenic Insulation Coolcat. URL [http://www.ruag.com/space/Products/Satellite\\_Structures2C\\_Mechanisms%\\_Mechanical\\_Equipment/Thermal\\_Systems/Cryogenic\\_Insulation\\_Coolcat](http://www.ruag.com/space/Products/Satellite_Structures2C_Mechanisms%_Mechanical_Equipment/Thermal_Systems/Cryogenic_Insulation_Coolcat).
- [11] SuperOx Web Page, . URL <http://www.superox.ru>.
- [12] Suprapower - Superconducting, reliable, lightweight and more powerful offshore wind turbine., . URL <http://www.suprapower-fp7.eu>.

- [13] UpWind - Design Limits and Solutions for Very Large Wind Turbines - EU 6th Frame Project. Technical report, 2011. URL [www.upwind.eu](http://www.upwind.eu).
- [14] 3DS. SolidWorks, 2013. URL <http://www.3ds.com/products/solidworks/>.
- [15] A. B. Abrahamsen and B. B. Jensen. Superconducting Direct Drive Wind Turbine Generators: Advantages and Challenges. In S. Mueen, editor, *Wind Energy Conversion Systems*, Green Energy and Technology, chapter 3, pages 53–80. Springer London, London, 2012. ISBN 978-1-4471-2200-5. doi: 10.1007/978-1-4471-2201-2. URL <http://www.springerlink.com/index/10.1007/978-1-4471-2201-2>.
- [16] A. B. Abrahamsen, N. Mijatovic, E. Seiler, M. P. Sorensen, M. Koch, P. B. Norgard, N. F. Pedersen, C. Traholt, N. H. Andersen, and J. Ostergard. Design Study of 10 kW Superconducting Generator for Wind Turbine Applications. *IEEE Transactions on Applied Superconductivity*, 19(3):1678–1682, June 2009. ISSN 1051-8223. doi: 10.1109/TASC.2009.2017697. URL <http://ieeexplore.ieee.org/lpdocs/epic03/wrapper.htm?arnumber=5067256>.
- [17] A. B. Abrahamsen, N. Mijatovic, E. Seiler, T. Zirngibl, C. Træholt, P. B. Norgård, N. F. Pedersen, N. H. Andersen, and J. Ostergård. Superconducting wind turbine generators. *Superconductor Science and Technology*, 23(3):034019, March 2010. ISSN 0953-2048. doi: 10.1088/0953-2048/23/3/034019. URL <http://iopscience.iop.org/0953-2048/23/3/034019/>.
- [18] D. Aized, B. Gamble, A. Sidi-Yekhlief, J. Voccio, D. Driscoll, B. Shoykhet, and B. Zhang. Status of the 1000 HP HTS motor development. *IEEE Transactions on Applied Superconductivity*, 9(2):1197–1200, June 1999. ISSN 10518223. doi: 10.1109/77.783514. URL <http://ieeexplore.ieee.org/lpdocs/epic03/wrapper.htm?arnumber=783514>.
- [19] M. K. Al-Mosawi. Design of a 100 kVA high temperature superconducting demonstration synchronous generator. *Physica C: Superconductivity*, 372-376: 1539–1542, August 2002. ISSN 09214534. doi: 10.1016/S0921-4534(02)01076-6. URL <http://linkinghub.elsevier.com/retrieve/pii/S0921453402010766>.
- [20] M. K. Al-Mosawi, C. Beduz, and Y. Yang. Construction of a 100 kVA High Temperature Superconducting Synchronous Generator. *IEEE Transactions on Applied Superconductivity*, 15(2):2182–2185, 2005. ISSN 1051-8223. doi: 10.1109/TASC.2005.849607. URL <http://ieeexplore.ieee.org/lpdocs/epic03/wrapper.htm?arnumber=1440096>.
- [21] Y. Alexandrova, S. Semken, M. Polikarpova, and J. Pyrhonen. Defining proper initial geometry of an 8 MW liquid-cooled direct-drive permanent magnet

- synchronous generator for wind turbine applications based on minimizing mass. In *2012 XXth International Conference on Electrical Machines*, pages 1250–1255. IEEE, September 2012. ISBN 978-1-4673-0142-8. doi: 10.1109/ICElMach.2012.6350036. URL [http://ieeexplore.ieee.org/xpls/abs\\_all.jsp?arnumber=6350036](http://ieeexplore.ieee.org/xpls/abs_all.jsp?arnumber=6350036).
- [22] K. Amm. 100 MVA HTS Generator Development Update. In *DOE HTS Wire Workshop*, 2005.
- [23] AMSC. AMSC, Amperium YBCO Wire Datasheet. Technical report, AMSC, 2012. URL <http://www.ams.com/library/index.html>.
- [24] AMSC. Concepts for High Power Wind Turbines - Introducing HTS Technology. In *World Green Energy Forum*, 2010. URL [www.keei.re.kr/keei/download/seminar/101117/II101118\\_a01.pdf](http://www.keei.re.kr/keei/download/seminar/101117/II101118_a01.pdf).
- [25] J. Annett. *Superconductivity, Superfluids, and Condensates*. Number May. Oxford Press, Oxford, 2004. ISBN 0198507569. URL <http://cdsweb.cern.ch/record/730995>.
- [26] S. K. Baik, Y. Kwon, E. Lee, J. Lee, J. Hong, Y.-C. Kim, T.-S. Moon, H. J. Park, and W. Kwon. Design and Analysis of 1 MW Synchronous Machine via 3D Magnetic Field Calculation. *IEEE Transactions on Applied Superconductivity*, 17(2):1549–1552, June 2007. ISSN 1051-8223. doi: 10.1109/TASC.2007.899204. URL <http://ieeexplore.ieee.org/lpdocs/epic03/wrapper.htm?arnumber=4277280>.
- [27] D. Bang. *Design of Transverse Flux Permanent Magnet Machines for Large Direct-Drive Wind Turbines*. Phd dissertation, Delft University of Technology, 2010. URL [http://repository.tudelft.nl/assets/uuid:c6867c53-fc10-468d-b6d7-082b7a052f4b/Final\\_thesis\\_DJBang\\_lowqlty.pdf](http://repository.tudelft.nl/assets/uuid:c6867c53-fc10-468d-b6d7-082b7a052f4b/Final_thesis_DJBang_lowqlty.pdf).
- [28] D. Bang, H. Polinder, G. Shrestha, and J. A. Ferreira. Review of Generator Systems for Direct-Drive Wind Turbines. In *Proceedings of the 2008 European wind energy conference, EWEC-2008*, pages 1–10, Brussels, 2008. URL <http://proceedings.ewea.org/ewec2008/>.
- [29] D. Bang, H. Polinder, G. Shrestha, and J. A. Ferreira. Ring-shaped transverse flux PM generator for large direct-drive wind turbines. In *2009 International Conference on Power Electronics and Drive Systems (PEDS)*, pages 61–66. IEEE, November 2009. ISBN 978-1-4244-4166-2. doi: 10.1109/PEDS.2009.5385933. URL <http://ieeexplore.ieee.org/lpdocs/epic03/wrapper.htm?arnumber=5385933>.

- [30] D. Bang, H. Polinder, J. A. Ferreira, and S.-s. Hong. Structural mass minimization of large direct-drive wind generators using a buoyant rotor structure. In *2010 IEEE Energy Conversion Congress and Exposition*, pages 3561–3568. IEEE, September 2010. ISBN 978-1-4244-5286-6. doi: 10.1109/ECCE.2010.5617705. URL <http://ieeexplore.ieee.org/lpdocs/epic03/wrapper.htm?arnumber=5617705>.
- [31] P. Barnes, G. Rhoads, J. Tolliver, M. Sumption, and K. Schmaeman. Compact, lightweight, superconducting power generators. *IEEE Transactions on Magnetics*, 41(1):268–273, January 2005. ISSN 0018-9464. doi: 10.1109/TMAG.2004.838984. URL <http://ieeexplore.ieee.org/lpdocs/epic03/wrapper.htm?arnumber=1381551>.
- [32] P. Barnes, M. Sumption, and G. Rhoads. Review of high power density superconducting generators: Present state and prospects for incorporating YBCO windings. *Cryogenics*, 45(10-11):670–686, 2005. ISSN 00112275. doi: 10.1016/j.cryogenics.2005.09.001. URL <http://linkinghub.elsevier.com/retrieve/pii/S0011227505001062>.
- [33] N. Bianchi and S. Bolognani. Design optimisation of electric motors by genetic algorithms. *Electric Power Applications, IEE Proceedings* -, 145(5):475 – 483, 1998.
- [34] J. W. Bray. Superconductors in Applications; Some Practical Aspects. *IEEE Transactions on Applied Superconductivity*, 19(3):2533–2539, June 2009. ISSN 1051-8223. doi: 10.1109/TASC.2009.2019287. URL <http://ieeexplore.ieee.org/lpdocs/epic03/wrapper.htm?arnumber=5067147>.
- [35] E. Bretz. Superconductors on the high seas. *Spectrum, IEEE*, 1(January):60–67, 2004. URL [http://ieeexplore.ieee.org/xpls/abs\\_all.jsp?arnumber=1317883](http://ieeexplore.ieee.org/xpls/abs_all.jsp?arnumber=1317883).
- [36] BVG. Offshore wind cost reduction pathways - Technology work stream. Technical Report May, BVG Associates, 2012. URL <http://www.thecrownestate.co.uk/media/305086/BVGOWCRPtechnologyworkstream.pdf>.
- [37] A. Chen, X. Liu, F. Xu, J. Cao, and L. Li. Design of the Cryogenic System for a 400 kW Experimental HTS Synchronous Motor. *IEEE Transactions on Applied Superconductivity*, 20(3):2062–2065, June 2010. ISSN 1051-8223. doi: 10.1109/TASC.2009.2039206. URL <http://ieeexplore.ieee.org/lpdocs/epic03/wrapper.htm?arnumber=5415677>.

- [38] B. Chen, G.-B. Gu, G.-Q. Zhang, F.-C. Song, and C.-H. Zhao. Analysis and Design of Cooling System in High Temperature Superconducting Synchronous Machines. *IEEE Transactions on Applied Superconductivity*, 17(2):1557–1560, June 2007. ISSN 1051-8223. doi: 10.1109/TASC.2007.898031. URL <http://ieeexplore.ieee.org/lpdocs/epic03/wrapper.htm?arnumber=4277325>.
- [39] Cobham. Opera, 2013. URL <http://www.cobham.com/about-cobham/aerospace-and-security/about-us/antenna-systems/specialist-technical-services-and-software/products-and-services/design-simulation-software.aspx>.
- [40] T. A. Coombs, Z. Hong, Y. Yang, and C. D. Rawlings. The Next Generation of Superconducting Permanent Magnets: The Flux Pumping Method. *IEEE Transactions on Applied Superconductivity*, 19(3):2169–2173, June 2009. ISSN 1051-8223. doi: 10.1109/TASC.2009.2018368. URL <http://ieeexplore.ieee.org/lpdocs/epic03/wrapper.htm?arnumber=5109579>.
- [41] J. Cros and P. Viarouge. New Structures of Polyphase Claw-Pole Machines. *IEEE Transactions on Industry Applications*, 40(1):113–120, January 2004. ISSN 0093-9994. doi: 10.1109/TIA.2003.821648. URL <http://ieeexplore.ieee.org/lpdocs/epic03/wrapper.htm?arnumber=1268186>.
- [42] Cryomech. AL230 with CP950 - Cryorefrigerator Specification Sheet. Technical report, 2007. URL [http://cryomech.com/specificationsheet/AL230\\_ss.pdf](http://cryomech.com/specificationsheet/AL230_ss.pdf).
- [43] H. W. Derbas, J. M. Williams, A. C. Koenig, and S. D. Pekarek. A Comparison of Nodal- and Mesh-Based Magnetic Equivalent Circuit Models. *IEEE Transactions on Energy Conversion*, 24(2):388–396, June 2009. ISSN 0885-8969. doi: 10.1109/TEC.2008.2002037. URL <http://ieeexplore.ieee.org/lpdocs/epic03/wrapper.htm?arnumber=4957571>.
- [44] M. Deshpande. *Design and Testing of Electrical Machines*. PHI Learning, New Delhi, 1st ed. edition, 2009. ISBN 8120336453.
- [45] B. Diepeveen. Seawater-Based Hydraulics for Offshore Wind Turbines. Technical report, 2004. URL <http://www.we-at-sea.org/leden/docs/reports/RL1-42004-012CDelftOffshoreTurbine.pdf>.
- [46] R. Dietrich. Bruker HTS - Bi-2223 HTS data sheet. Technical report, Bruker HTS GmbH, 2012. URL [http://www.bruker-est.com/fileadmin/be\\_user/Advanced\\_Supercon/EHTS/products/BSCCO/BSCCO\\_Data\\_Sheet.pdf](http://www.bruker-est.com/fileadmin/be_user/Advanced_Supercon/EHTS/products/BSCCO/BSCCO_Data_Sheet.pdf).
- [47] Y. Duan and R. G. Harley. Present and future trends in wind turbine generator designs. *2009 IEEE Power Electronics and Machines in Wind Applications*, pages

- 1–6, June 2009. doi: 10.1109/PEMWA.2009.5208401. URL <http://ieeexplore.ieee.org/lpdocs/epic03/wrapper.htm?arnumber=5208401>.
- [48] V. Eize de. Drive and innovation: The DeWind D8.2 with Voith WinDrive. *Renewable Energy World*, 10(2):55–65, 2007.
- [49] J. Ekin. *Experimental Techniques for Low-Temperature Measurements*. Oxford University Press, Oxford, 1 edition, 2006. ISBN 9780198570547. doi: <http://dx.doi.org/10.1093/acprof:oso/9780198570547.001.0001>.
- [50] S. Engström, B. Hernnas, C. Parkegren, and S. Waernulf. Development of NewGen - a New Type of Direct-Drive Generator. In *European Wind Energy Conference-EWEC*, volume 4, pages 22–25, 2004. URL [http://www.2004ewec.info/files/23\\_1400\\_staffanengstrom\\_01.pdf](http://www.2004ewec.info/files/23_1400_staffanengstrom_01.pdf).
- [51] F. Fair, W. Stautner, M. Douglass, R. Rajput-Ghoshal, M. Moscinski, P. Riley, D. Wagner, J. Kim, S. Hou, F. Lopez, K. Haran, J. Bray, T. Laskaris, J. Rochford, R. Duckworth, D. Wagner, J. Kim, S. Hou, F. Lopez, K. Haran, J. Bray, T. Laskaris, J. Rochford, and R. Duckworth. Next Generation Drive Train - Superconductivity for Large-Scale Wind Turbines. In *Applied Superconductivity Conference*, number 22, pages 1–29, Portland, Oregon, 2012. URL <http://www.ewh.ieee.org/tc/csc/europe/newsforum/pdf/STP307.pdf>.
- [52] R. Fair, C. Lewis, J. Eugene, and M. Ingles. Development of an HTS hydroelectric power generator for the hirschaid power station. *Journal of Physics: Conference Series*, 234(3):032008, June 2010. ISSN 1742-6596. doi: 10.1088/1742-6596/234/3/032008. URL <http://stacks.iop.org/1742-6596/234/i=3/a=032008?key=crossref.31e5bf4ab2e26dd131adb7d0fcc02f6b>.
- [53] D. Fickling. Rare Earth Elements -Beware of peak in rare-earth elements, 2011. URL <http://rareearthelementsetf.com/2011/05/05/goldman-sachs-says-beware-of-peak-in-rare-earth-elements/>.
- [54] M. Fischer. Superconductors on the high Seas. *Wind Systems*, pages 76–84, 2010. URL [http://windsystemsmag.com/media/pdfs/Articles/2011\\_May/0511\\_AMSC.pdf](http://windsystemsmag.com/media/pdfs/Articles/2011_May/0511_AMSC.pdf).
- [55] M. Fischer. High Temperature Superconductors Enable the World’s Largest and Most Powerful Wind Turbine. *Wind Power*, pages 60–62, 2011. URL [www.amsc.com/pdf/EnergeticaInternational\\_SeaTitan\\_IndiaJuly2011.pdf](http://www.amsc.com/pdf/EnergeticaInternational_SeaTitan_IndiaJuly2011.pdf).
- [56] J. Fogarty, G. Co, and N. Schenectady. Development of a 100 MVA high temperature superconducting generator. In *IEEE Power Engineering Society General Meeting*, pages 2065–2067, 2004. URL [http://ieeexplore.ieee.org/xpls/abs\\_all.jsp?arnumber=1373244](http://ieeexplore.ieee.org/xpls/abs_all.jsp?arnumber=1373244).

- [57] B. Gamble, G. Snitchler, and T. MacDonald. Full Power Test of a 36.5 MW HTS Propulsion Motor. *IEEE Transactions on Applied Superconductivity*, 21(3):1083–1088, June 2011. ISSN 1051-8223. doi: 10.1109/TASC.2010.2093854. URL <http://ieeexplore.ieee.org/lpdocs/epic03/wrapper.htm?arnumber=5676207>.
- [58] J. F. Gieras. *Advancements in Electric Machines (Power Systems)*. Springer, 2nd editio edition, 2009. ISBN 1402090064.
- [59] B. Glowacki. Hydrogen Cryomagnetics: The Way Forward For Superconductivity. In *Proceedings of 23rd International Cryogenic Engineering Conference - International Cryogenic Materials Conference*, pages 353–357, Wroclaw, 2011. URL <http://www.msm.cam.ac.uk/ascg/publications/icec23-icmc2010-glowacki.pdf>.
- [60] K. Goddard, B. Lukasik, and J. Sykulski. Alternative Designs of High-Temperature Superconducting Synchronous Generators. *IEEE transactions on applied superconductivity*, 19(6):3805–3811, 2010. URL <http://eprints.ecs.soton.ac.uk/18353/>.
- [61] P. M. Grant, C. Starr, and T. J. Overbye. A Power Grid for the Hydrogen Economy. *Scientific American*, 295(1):76–83, July 2006. ISSN 0036-8733. doi: 10.1038/scientificamerican0706-76. URL <http://dx.doi.org/10.1038/scientificamerican0706-76>.
- [62] A. Grauers. *Design of Direct-driven Permanent-magnet Generators for Wind Turbines*. Phd dissertation, Chalmers University of Technology, 1996.
- [63] S. Gruss, G. Fuchs, G. Krabbes, P. Verges, G. StoÏlver, K.-H. MuÏller, J. Fink, and L. Schultz. Superconducting bulk magnets: Very high trapped fields and cracking. *Applied Physics Letters*, 79(19):3131–3133, April 2001. ISSN 00036951. doi: 10.1063/1.1413502. URL <http://arxiv.org/abs/cond-mat/0104396>.
- [64] Y. G. Guo and J. G. Zhu. Study of Permanent Magnet Transverse Flux Motors with Soft Magnetic Composite Core. In *Australasian Universities Power Engineering Conference*, number September, pages 1–6, 2004.
- [65] Y. Guo, J. G. Zhu, P. Watterson, and W. Wu. Comparative study of 3-D flux electrical machines with soft magnetic composite cores. *Industry Applications, IEEE Transactions on*, 39(6):1696–1703, November 2003. ISSN 0093-9994. doi: 10.1109/TIA.2003.818990.
- [66] D. W. Hazelton. 2G HTS Materials for Rotating Machinery. In *Superconducting Motor Workshop*, pages 1–31, Kelnheubach, 2012. URL <http://www.superpower-inc.com/content/technical-documents>.



- [67] Hogan AB. Somaloy Technology for Electric Motors. Technical report, 2011. URL [http://www.hoganas.com/Documents/SomaloyBroschyrerochWearResist/SMC/Somaloy\\_Electrical\\_Motors\\_March\\_2011.pdf](http://www.hoganas.com/Documents/SomaloyBroschyrerochWearResist/SMC/Somaloy_Electrical_Motors_March_2011.pdf).
- [68] Y. Huang, J. Zhu, Y. Guo, and Q. Hu. Development of a High-Speed Claw Pole Motor with Soft Magnetic Composite Core. In *2007 IEEE International Electric Machines and Drives Conference*, volume 2, pages 1564–1568. IEEE, May 2007. ISBN 1-4244-0742-7. doi: 10.1109/IEMDC.2007.383661. URL <http://ieeexplore.ieee.org/lpdocs/epic03/wrapper.htm?arnumber=4270881>.
- [69] A. Hughes. *Electric Motors and Drives: Fundamentals, Types and Applications*. Newnes, Oxford, 3rd edition, 2006. ISBN 0750647183.
- [70] A. Ibala, A. Masmoudi, G. Atkinson, and A. Jack. A New Reluctance Model of a Claw Pole TFPM Using SMC for the Magnetic Circuit. In *Ecologic Vehicles - Renewable Energies*, Monaco, 2009.
- [71] M. Iwakuma, T. Ogata, S. Tomoda, T. Kisu, Y. Yoshida, A. Ishiyama, Y. Yamada, T. Izumi, and Y. Shiohara. Feasibility Study on a 400 kW - 3600 rpm REBCO Fully Superconducting Motor. *IEEE Transactions on Applied Superconductivity*, 22(3):5201204–5201204, June 2012. ISSN 1051-8223. doi: 10.1109/TASC.2011.2177229. URL <http://ieeexplore.ieee.org/lpdocs/epic03/wrapper.htm?arnumber=6086718>.
- [72] B. B. Jensen, N. Mijatovic, and A. B. Abrahamsen. Advantages and Challenges of Superconducting Wind Turbine Generators. In *International Conference E/E Systems for Wind Turbines*, number May, pages 1–29, Bremen, 2012. URL <http://orbit.dtu.dk/services/downloadRegister/9561911/AdvantagesandChallengesofSuperconductingWindTurbineGenerators.pdf>.
- [73] S. Jiang, Z. Zhu, and C. Chan. Analytical Methods for Minimizing Cogging Torque in Permanent-Magnet Machines. *IEEE Transactions on Magnetics*, 45(4):2023–2031, April 2009. ISSN 0018-9464. doi: 10.1109/TMAG.2008.2011363. URL <http://ieeexplore.ieee.org/lpdocs/epic03/wrapper.htm?arnumber=4802358>.
- [74] N. M. Jubeh and Y. S. Najjar. Power augmentation with CAES (compressed air energy storage) by air injection or supercharging makes environment greener. *Energy*, 38(1):228–235, February 2012. ISSN 03605442. doi: 10.1016/j.energy.2011.12.010. URL <http://dx.doi.org/10.1016/j.energy.2011.12.010>.
- [75] S. Kakani. *Superconductivity*. Anshan, 2009. ISBN 1848290055. URL <http://www.amazon.co.uk/Superconductivity-S-L-Kakani/dp/1848290055>.

- [76] S. Kalsi. HTS ship propulsion motors. In *IEEE Power Engineering Society General Meeting, 2004.*, volume 2, pages 2047–2048. IEEE, 2004. ISBN 0-7803-8465-2. doi: 10.1109/PES.2004.1373238. URL <http://ieeexplore.ieee.org/lpdocs/epic03/wrapper.htm?arnumber=1373238>.
- [77] S. Kalsi. *Applications of High Temperature Superconductors to Electric Power Equipment*. John Wiley & Sons, Inc., Hoboken, NJ, USA, March 2011. ISBN 9780470877890. doi: 10.1002/9780470877890. URL <http://doi.wiley.com/10.1002/9780470877890>.
- [78] S. Kalsi. Cooling and Thermal Insulation Systems. In *Applications of High Temperature Superconductors to Electric Power Equipment*, chapter 3. John Wiley & Sons, Inc., 2011. doi: 10.1002/9780470877890.ch3.
- [79] S. Kalsi, K. Weeber, H. Takesue, C. Lewis, H. Neumueller, and R. Blaugher. Development status of rotating machines employing superconducting field windings. *Proceedings of the IEEE*, 92(10):1688–1704, October 2004. ISSN 0018-9219. doi: 10.1109/JPROC.2004.833676. URL <http://ieeexplore.ieee.org/lpdocs/epic03/wrapper.htm?arnumber=1335557>.
- [80] S. Kalsi, B. Gamble, G. Snitchler, and S. Ige. The status of HTS ship propulsion motor developments. In *2006 IEEE Power Engineering Society General Meeting*, page 5 pp. IEEE, 2006. ISBN 1-4244-0493-2. doi: 10.1109/PES.2006.1709643. URL <http://ieeexplore.ieee.org/lpdocs/epic03/wrapper.htm?arnumber=1709643>.
- [81] O. Keysan and M. Mueller. A linear superconducting generator for wave energy converters. In *6th IET International Conference on Power Electronics, Machines and Drives (PEMD 2012)*, pages B134–B134, Bristol, 2012. IET. ISBN 978-1-84919-616-1. doi: 10.1049/cp.2012.0298. URL <http://ieeexplore.ieee.org/xpl/articleDetails.jsp?arnumber=6242150>.
- [82] O. Keysan. Application of high temperature superconducting machines to direct drive renewable energy systems. In M. Mueller and H. Polinder, editors, *Electrical Drives for Direct Drive Renewable Energy Systems*. Woodhead Publication, 2013. ISBN 84569-783-9. URL <http://www.woodheadpublishing.com/en/book.aspx?bookID=2043>.
- [83] O. Keysan and M. Mueller. Superconducting generators for renewable energy applications. In *IET Conference on Renewable Power Generation (RPG 2011)*, volume 2020, pages 12–12, Edinburgh, 2011. IET. doi: 10.1049/cp.2011.0102. URL [http://ieeexplore.ieee.org/xpls/abs\\_all.jsp?arnumber=6136084](http://ieeexplore.ieee.org/xpls/abs_all.jsp?arnumber=6136084).

- [84] O. Keysan and M. A. Mueller. A Homopolar HTSG Topology for Large Direct-Drive Wind Turbines. *IEEE Transactions on Applied Superconductivity*, 21(5): 3523–3531, October 2011. ISSN 1051-8223. doi: 10.1109/TASC.2011.2159005. URL <https://ieeexplore.ieee.org/xpls/icp.jsp?arnumber=5948361>.
- [85] O. Keysan and M. A. Mueller. A Transverse Flux High-Temperature Superconducting Generator Topology for Large Direct Drive Wind Turbines. In *Superconductivity Centennial Conference*, volume 01, pages 1–6, 2011. URL <http://www.sciencedirect.com/science/article/pii/S1875389212019761>.
- [86] O. Keysan, D. Olczak, and M. A. Mueller. A Modular Superconducting Generator for Offshore Wind Turbines. *Journal of Superconductivity and Novel Magnetism*, pages 1–5, December 2012. ISSN 1557-1939. doi: 10.1007/s10948-012-1950-1. URL <http://www.springerlink.com/index/10.1007/s10948-012-1950-1>.
- [87] O. Keysan, J. Burchell, and M. A. Mueller. Magnetic and Structural Analysis of a Transverse Flux Claw Pole Linear Machine (Invited Paper). In *IEEE International Conference on Industrial Technology*, pages 1–5, Cape Town, 2013. URL [http://ieeexplore.ieee.org/xpls/abs\\_all.jsp?arnumber=6505968](http://ieeexplore.ieee.org/xpls/abs_all.jsp?arnumber=6505968).
- [88] G.-H. Kim, N. Kim, K.-M. Kim, M. Park, I.-K. Yu, S. Lee, and T.-J. Park. EMTDC Based Simulation of 10 MW Class Grid-Connected Superconducting Wind Turbine Generator. *IEEE Transactions on Applied Superconductivity*, 22(3):5202105, June 2012. ISSN 1051-8223. doi: 10.1109/TASC.2011.2177797. URL <http://ieeexplore.ieee.org/lpdocs/epic03/wrapper.htm?arnumber=6093733>.
- [89] N. Kim, G. Kim, K. Kim, M. Park, I. Yu, S. Lee, E. Song, and T. Kim. Comparative Analysis of 10 MW Class Geared and Gearless Type Superconducting Synchronous Generators for a Wind Power Generation System. *IEEE Transactions on Applied Superconductivity*, 22(3):5202004–5202004, June 2012. ISSN 1051-8223. doi: 10.1109/TASC.2011.2178221. URL [http://ieeexplore.ieee.org/xpls/abs\\_all.jsp?arnumber=6095601](http://ieeexplore.ieee.org/xpls/abs_all.jsp?arnumber=6095601).
- [90] G. Klaus, W. Nick, H. Neumueller, G. Nerowski, and W. McCown. Development of High-Temperature Superconducting Electrical Machines at Siemens AG. In *International Conference on Electrical Machines, ICEM*, pages 1–6, 2006. URL [http://ieeexplore.ieee.org/xpls/abs\\_all.jsp?arnumber=1709648](http://ieeexplore.ieee.org/xpls/abs_all.jsp?arnumber=1709648).
- [91] G. Klaus, M. Wilke, J. Fraunhofer, W. Nick, and H. Neumueller. Design Challenges and Benefits of HTS Synchronous Machines. *IEEE Power Engineering Society General Meeting*, pages 1–8, June 2007. ISSN 1932-5517. doi: 10.1109/PES.2007.385756. URL <http://ieeexplore.ieee.org/lpdocs/epic03/wrapper.htm?arnumber=4275522>.

- [92] H. Kobayashi, Y. Doi, K. Miyata, and T. Minowa. Design of the axial-flux permanent magnet coreless generator for the multi-megawatts wind turbine. In *European Wind Energy Conference & Exhibition, Belgium*, pages 1–9, Belgium, 2009. URL [http://www.ewec2009proceedings.info/allfiles2/276\\_EWEC2009presentation.pdf](http://www.ewec2009proceedings.info/allfiles2/276_EWEC2009presentation.pdf).
- [93] E. Krol and R. Rossa. Modern magnetic materials in permanent magnet synchronous motors. In *The XIX International Conference on Electrical Machines - ICEM 2010*, volume 1, pages 1–3. IEEE, September 2010. ISBN 978-1-4244-4174-7. doi: 10.1109/ICELMACH.2010.5607962. URL <http://ieeexplore.ieee.org/lpdocs/epic03/wrapper.htm?arnumber=5607962>.
- [94] L. Lawrence, C. Cox, and D. Broman. High temperature superconductivity: the products and their benefits. *Oak Ridge National Laboratory, USA*, 2002. URL <http://www.ornl.gov/sci/htsc/documents/pdf/Products\&Benefits2002AdvCpy.pdf>.
- [95] J.-K. Lee, S. H. Park, Y. Kim, S. Lee, W.-S. Kim, K. Choi, and S.-Y. Hahn. Electrical Properties Analysis and Test Result of Windings for a Fully Superconducting 10 HP Homopolar Motor. *IEEE Transactions on Applied Superconductivity*, 22(3):5201405, June 2012. ISSN 1051-8223. doi: 10.1109/TASC.2011.2177052. URL <http://ieeexplore.ieee.org/lpdocs/epic03/wrapper.htm?arnumber=6086584>.
- [96] S.-H. Lee, J. Hong, Y. Kwon, Y.-S. Jo, and S. K. Baik. Study on Homopolar Superconductivity Synchronous Motors for Ship Propulsion Applications. *IEEE Transactions on Applied Superconductivity*, 18(2):717–720, June 2008. ISSN 1051-8223. doi: 10.1109/TASC.2008.921334. URL [ieeexplore.ieee.org/xpl/articleDetails.jsp?arnumber=4523015](http://ieeexplore.ieee.org/xpl/articleDetails.jsp?arnumber=4523015).
- [97] M. Lesser and J. Müller. Superconductor Technology, Generating the Future of Offshore Wind Power. *Renewable Energy World Conference, Cologne, Germany*, pages 1–10, 2009.
- [98] J. Leveque, D. Netter, B. Douine, and A. Rezzoug. Some Considerations About the Cooling of the Rotor of a Superconducting Motor. *IEEE Transactions on Applied Superconductivity*, 17(1):44–51, March 2007. ISSN 1051-8223. doi: 10.1109/TASC.2006.887542. URL <http://ieeexplore.ieee.org/lpdocs/epic03/wrapper.htm?arnumber=4120221>.
- [99] C. Lewis and J. Muller. A Direct Drive Wind Turbine HTS Generator. *2007 IEEE Power Engineering Society General Meeting*, pages 1–8, June 2007. ISSN 1932-5517. doi: 10.1109/PES.2007.386069.

- [100] H. Li and Z. Chen. Overview of different wind generator systems and their comparisons. *IET Renewable Power Generation*, 2(2):123, 2008. ISSN 17521416. doi: 10.1049/iet-rpg:20070044. URL [http://ieeexplore.ieee.org/xpls/abs\\_all.jsp?arnumber=4469298http://link.aip.org/link/ISETCN/v2/i2/p123/s1\&Agg=doi](http://ieeexplore.ieee.org/xpls/abs_all.jsp?arnumber=4469298http://link.aip.org/link/ISETCN/v2/i2/p123/s1\&Agg=doi).
- [101] L. Li, J. Cao, B. Kou, Z. Han, Q. Chen, and A. Chen. Design of the HTS Permanent Magnet Motor With Superconducting Armature Winding. *IEEE Transactions on Applied Superconductivity*, 22(3):5200704–5200704, June 2012. ISSN 1051-8223. doi: 10.1109/TASC.2011.2181293. URL <http://ieeexplore.ieee.org/lpdocs/epic03/wrapper.htm?arnumber=6111261>.
- [102] J. I. Lienhard. *A heat transfer textbook*. Phlogiston Press, Cambridge, Massachusetts, 3rd editio edition, 2006.
- [103] B. Lukasik. *Design and optimisation of a coreless superconducting synchronous generator*. Phd dissertation, University of Southampton, October 2010. URL <http://www.ncbi.nlm.nih.gov/pubmed/20561629>.
- [104] C. P. Maddison. *Transverse flux machines for high torque applications*. Phd dissertation, University of Newcastle upon Tyne, 1999.
- [105] N. Maki. Design study of high-temperature superconducting generators for wind power systems. *Journal of Physics: Conference Series*, 97:012155, February 2008. ISSN 1742-6596. doi: 10.1088/1742-6596/97/1/012155. URL <http://iopscience.iop.org/1742-6596/97/1/012155/>.
- [106] B. Maples, M. Hand, and W. Musial. Comparative Assessment of Direct Drive High Temperature Superconducting Generators in Multi-Megawatt Class Wind Turbines. Technical Report October, National Renewable Energy Laboratory (NREL), Golden, CO., 2010. URL [http://www.osti.gov/bridge/product.biblio.jsp?osti\\_id=991560](http://www.osti.gov/bridge/product.biblio.jsp?osti_id=991560).
- [107] E. Marquardt, J. Le, and R. Radebaugh. Cryogenic material properties database. In *11th International Cryocooler Conference*, pages 1–7, 2000. URL [http://link.springer.com/chapter/10.1007/0-306-47112-4\\_84](http://link.springer.com/chapter/10.1007/0-306-47112-4_84).
- [108] P. J. Masson, M. Breschi, P. Tixador, and C. A. Luongo. Design of HTS Axial Flux Motor for Aircraft Propulsion. *IEEE Transactions on Applied Superconductivity*, 17(2):1533–1536, June 2007. ISSN 1051-8223. doi: 10.1109/TASC.2007.898120. URL <http://ieeexplore.ieee.org/lpdocs/epic03/wrapper.htm?arnumber=4277591>.

- [109] P. J. Masson, J. E. Pienkos, and C. A. Luongo. Scaling Up of HTS Motor Based on Trapped Flux and Flux Concentration for Large Aircraft Propulsion. *IEEE Transactions on Applied Superconductivity*, 17(2):1579–1582, June 2007. ISSN 1051-8223. doi: 10.1109/TASC.2007.898111. URL <http://ieeexplore.ieee.org/lpdocs/epic03/wrapper.htm?arnumber=4277588>.
- [110] P. J. Masson. Wind Turbine Generators: Beyond the 10MW Frontier. In *Symposium on Superconducting Devices for Wind Energy Systems*, pages 1–8, 2011.
- [111] H. Matsuzaki, Y. Kimura, L. Ohtani, E. Marita, H. Ogata, M. Izumi, T. Ida, H. Sugimoto, M. Miki, M. Kitano, and H. Fujimoto. Mechanical and cryogenic design of a synchronous rotating machines with HTS pole-field magnets. *IEEE Power Engineering Society General Meeting*, pages 4–8, 2006. doi: 10.1109/PES.2006.1709645. URL <http://ieeexplore.ieee.org/lpdocs/epic03/wrapper.htm?arnumber=1709645>.
- [112] A. McDonald. *Structural analysis of low speed, high torque electrical generators for direct drive renewable energy converters*. Phd dissertation, University of Edinburgh, UK, 2008.
- [113] A. McDonald, M. Mueller, and H. Polinder. Structural mass in direct-drive permanent magnet electrical generators. *IET Renewable Power Generation*, 2(1):3, 2008. ISSN 17521416. doi: 10.1049/iet-rpg:20070071. URL [http://digital-library.theiet.org/content/journals/10.1049/iet-rpg\\_20070071](http://digital-library.theiet.org/content/journals/10.1049/iet-rpg_20070071).
- [114] J. W. R. Mebane and J. S. Sekhon. Genetic Optimization Using Derivatives: The "rgenoud" Package for R. *Journal of Statistical Software*, 42(11):1–26, 2011. URL <http://www.jstatsoft.org/v42/i11/>.
- [115] I. Melnik, A. Geschiere, D. Willén, and H. Lentge. Long length HTS cable with integrated FCL property. *Journal of Physics: Conference Series*, 234(3):032037, June 2010. ISSN 1742-6596. doi: 10.1088/1742-6596/234/3/032037. URL <http://iopscience.iop.org/1742-6596/234/3/032037>.
- [116] M. Modica, G. Grasso, M. Greco, R. Marabotto, R. Musenich, D. Nardelli, R. Penco, and M. Tassisto. Behavior of MgB<sub>2</sub> Reacted and Wound Coils From 14 K to 32 K in a Cryogen Free Apparatus. *IEEE Transactions on Applied Superconductivity*, 16(2):1449–1452, June 2006. ISSN 1051-8223. doi: 10.1109/TASC.2006.870780. URL <http://ieeexplore.ieee.org/lpdocs/epic03/wrapper.htm?arnumber=1643127>.

- [117] R. Moss, E. Tzimas, H. Kara, P. Willis, and J. Koorosh. Critical Metals in Strategic Energy Technologies - Assessing Rare Metals as Supply-Chain Bottlenecks in Low-Carbon Energy Technologies. Technical report, JRC-IET Scientific and Technical Reports, 2011. URL <http://publications.jrc.ec.europa.eu/repository/handle/111111111/22726>.
- [118] M. Mueller and A. McDonald. A lightweight low-speed permanent magnet electrical generator for direct-drive wind turbines. *Wind Energy*, 12(8):768–780, 2009. ISSN 10954244. doi: 10.1002/we.333.
- [119] V. K. Murthy. *Computer-aided design of electrical machines*, volume 35. BSP, Hyderabad, 1st ed. edition, 2008. ISBN 9788178001463.
- [120] W. Nick, J. Grundmann, and J. Fraunhofer. Test results from Siemens low-speed, high-torque HTS machine and description of further steps towards commercialisation of HTS machines. *Physica C: Superconductivity*, 482:105–110, November 2012. ISSN 09214534. doi: 10.1016/j.physc.2012.04.019. URL <http://linkinghub.elsevier.com/retrieve/pii/S0921453412002079>.
- [121] M. Noe. History, State-of-the-Art and Perspectives of Superconducting Power Equipment. In *Superconductivity Centennial Conference*, Den Haag, 2011.
- [122] W. J. Nuttall, R. H. Clarke, and B. A. Glowacki. Resources: Stop squandering helium. *Nature*, 485(7400):573–5, May 2012. ISSN 1476-4687. doi: 10.1038/485573a. URL <http://www.ncbi.nlm.nih.gov/pubmed/22660302>.
- [123] H. Ohsaki, M. Sekino, T. Suzuki, and Y. Terao. Design study of wind turbine generators using superconducting coils and bulks. *2009 International Conference on Clean Electrical Power*, pages 479–484, June 2009. doi: 10.1109/ICCEP.2009.5212007. URL <http://ieeexplore.ieee.org/lpdocs/epic03/wrapper.htm?arnumber=5212007>.
- [124] H. Ohsaki, Y. Terao, and M. Sekino. Wind turbine generators using superconducting coils and bulks. *Journal of Physics: Conference Series*, 234(3):032043, June 2010. ISSN 1742-6596. doi: 10.1088/1742-6596/234/3/032043. URL <http://iopscience.iop.org/1742-6596/234/3/032043/>.
- [125] I. Oishi and N. Kenichi. Summary of development of 70 MW class model superconducting generator - research and development of superconducting for electric power application. *Cryogenics*, 42(3-4):157–167, March 2002. ISSN 00112275. doi: 10.1016/S0011-2275(02)00032-2. URL <http://linkinghub.elsevier.com/retrieve/pii/S0011227502000322>.

- [126] T. Okazaki, H. Sugimoto, and T. Takeda. Liquid nitrogen cooled HTS motor for ship propulsion. In *2006 IEEE Power Engineering Society General Meeting*, pages 6–12. IEEE, 2006. ISBN 1-4244-0493-2. doi: 10.1109/PES.2006.1709647. URL <http://ieeexplore.ieee.org/lpdocs/epic03/wrapper.htm?arnumber=1709647>.
- [127] D. Olczak. *Structural Design of a High Temperature Superconducting Generator*. Meng thesis, University of Edinburgh, 2012.
- [128] I. C. on Superconductivity. Superconductivity: Present and Future Applications, 2009. URL [www.ccas-web.org/pdf/ccas\\_brochure\\_web.pdf](http://www.ccas-web.org/pdf/ccas_brochure_web.pdf).
- [129] I. Parinov. *Microstructure and Properties of High-Temperature Superconductors*. Springer Berlin Heidelberg, Berlin, Heidelberg, 2007. ISBN 978-3-540-70976-3. doi: 10.1007/978-3-540-70977-0. URL <http://www.springerlink.com/index/10.1007/978-3-540-70977-0>.
- [130] H. Polinder. Optimization of Multibrid Permanent-Magnet Wind Generator Systems. *IEEE Transactions on Energy Conversion*, 24(1):82–92, March 2009. ISSN 0885-8969. doi: 10.1109/TEC.2008.2005279. URL <http://ieeexplore.ieee.org/lpdocs/epic03/wrapper.htm?arnumber=4783055>.
- [131] H. Polinder, G. Shrestha, and J. A. Ferreira. Comparative design of radial and transverse flux PM generators for direct-drive wind turbines. *2008 18th International Conference on Electrical Machines*, pages 1–6, September 2008. doi: 10.1109/ICELMACH.2008.4800027. URL <http://ieeexplore.ieee.org/lpdocs/epic03/wrapper.htm?arnumber=4800027>.
- [132] M. Putti and G. Grasso. MgB<sub>2</sub>, a two-gap superconductor for practical applications. *MRS Bulletin*, 36(08):608–613, August 2011. ISSN 0883-7694. doi: 10.1557/mrs.2011.176. URL [http://www.journals.cambridge.org/abstract\\_S088376941100176X](http://www.journals.cambridge.org/abstract_S088376941100176X).
- [133] R. Qu and T. Lipo. Analysis and modeling of airgap & zigzag leakage fluxes in a surface-mounted-PM machine. ... *Conference, 2002. 37th IAS Annual Meeting*. ..., pages 2507–2513, 2002. URL [http://ieeexplore.ieee.org/xpls/abs\\_all.jsp?arnumber=1042798](http://ieeexplore.ieee.org/xpls/abs_all.jsp?arnumber=1042798).
- [134] M. R. Quddes, M. Sekino, H. Ohsaki, N. Kashima, and S. Nagaya. Electromagnetic Design Study of Transverse Flux Enhanced Type Superconducting Wind Turbine Generators. *IEEE Transactions on Applied Superconductivity*, 21(3):1101–1104, June 2011. ISSN 1051-8223. doi: 10.1109/TASC.2010.2099091. URL <http://ieeexplore.ieee.org/lpdocs/epic03/wrapper.htm?arnumber=5692864>.



- [135] M. R. Quddes, M. Sekino, and H. Ohsaki. Electromagnetic design study of 10 MW-class wind turbine generators using circular superconducting field coils. In *2011 International Conference on Electrical Machines and Systems*, pages 1–6. IEEE, August 2011. ISBN 978-1-4577-1044-5. doi: 10.1109/ICEMS.2011.6073420. URL <http://ieeexplore.ieee.org/lpdocs/epic03/wrapper.htm?arnumber=6073420>.
- [136] R Core Team. *R: A Language and Environment for Statistical Computing*. R Foundation for Statistical Computing, Vienna, Austria, 2012. URL <http://www.r-project.org>.
- [137] B. Raju and T. Bartram. Fault-current limiter with superconducting DC bias. *Generation, Transmission and Distribution, IEE Proceedings C*, 129(4):166–171, 1982. URL [http://ieeexplore.ieee.org/xpls/abs\\_all.jsp?arnumber=4643507](http://ieeexplore.ieee.org/xpls/abs_all.jsp?arnumber=4643507).
- [138] W. Rampen. Gearless Transmissions for Large Wind Turbines - The history and Future of Hydraulic Drive. Technical report, Bremen, 2006. URL <http://artemisip.com/news-media/papers>.
- [139] M. Razeti, S. Angius, L. Bertora, D. Damiani, R. Marabotto, M. Modica, D. Nardelli, M. Perrella, and M. Tassisto. Construction and Operation of Cryogen Free MgB<sub>2</sub> Magnets for Open MRI Systems. *IEEE Transactions on Applied Superconductivity*, 18(2):882–886, June 2008. ISSN 1051-8223. doi: 10.1109/TASC.2008.920661. URL [http://ieeexplore.ieee.org/xpls/abs\\_all.jsp?arnumber=4483762](http://ieeexplore.ieee.org/xpls/abs_all.jsp?arnumber=4483762).
- [140] H. Rogalla and H. P. Kes. *100 Years of Superconductivity*, volume 65. Taylor & Francis, 1 edition, 2011. ISBN 1439849463. URL <http://www.amazon.com/100-Years-Superconductivity-Horst-Rogalla/dp/1439849463>.
- [141] RStudio. RStudio: Integrated development environment for R, 2012. URL <http://www.rstudio.org/>.
- [142] G. Sarmiento Munoz, J. M. Merino Azcarraga, J. Garcia-Tejedor Perez, P. Ibanez Ereno, and S. Apinaniz. Direct-Action Superconducting Synchronous Generator for a Wind Turbine, 2011. URL <http://patentscope.wipo.int/search/en/W02011080357>.
- [143] R. Sato, B. Felder, M. Miki, K. Tsuzuki, H. Hayakawa, and M. Izumi. Helium-Neon Gas Mixture Thermosyphon Cooling and Stability for Large Scale HTS Synchronous Motors. *IEEE Transactions on Applied Superconductivity*, 23(3):5200704–5200704, June 2013. ISSN 1051-8223. doi: 10.1109/TASC.2013.2241592.

- URL <http://ieeexplore.ieee.org/lpdocs/epic03/wrapper.htm?arnumber=6416023>.
- [144] Y. Sato, S. Torii, E. Watanabe, K. Kikukawa, and R. Company. Evaluation of superconducting claw motor using three dimensional magnetic field analysis. *2008 18th International Conference on Electrical Machines*, pages 1–6, September 2008. doi: 10.1109/ICELMACH.2008.4800007.
- [145] R. Schiferl and C. Rey. Development of ultra efficient HTS electric motor systems. In *Advanced Cables and Conductors Program Peer Review*, Washington, 2005. URL <http://www.htspeerreview.com/2005/pdfs/presentations/schiferl1.pdf>.
- [146] R. Schiferl, A. Flory, S. Umans, and W. Livoti. High Temperature Superconducting Synchronous Motors: Economic Issues for Industrial Applications. *2006 Record of Conference Papers - IEEE Industry Applications Society 53rd Annual Petroleum and Chemical Industry Conference*, pages 1–9, September 2006. doi: 10.1109/PCICON.2006.359715. URL <http://ieeexplore.ieee.org/lpdocs/epic03/wrapper.htm?arnumber=4199075>.
- [147] W. Si, S. J. Han, X. Shi, S. N. Ehrlich, J. Jaroszynski, A. Goyal, and Q. Li. High current superconductivity in FeSeTe-coated conductors at 30 tesla. *Nature Communications*, 4:1347, January 2013. ISSN 2041-1723. doi: 10.1038/ncomms2337. URL <http://dx.doi.org/10.1038/ncomms2337>.
- [148] C. Simons. *Feasibility study of a superconducting helicopter electrical propulsion motor*. Msc thesis, Delft University of Technology, 2013.
- [149] K. Sivasubramaniam, T. Zhang, M. Lokhandwalla, E. T. Laskaris, J. W. Bray, B. Gerstler, M. R. Shah, and J. P. Alexander. Development of a High Speed HTS Generator for Airborne Applications. *IEEE Transactions on Applied Superconductivity*, 19(3):1656–1661, June 2009. ISSN 1051-8223. doi: 10.1109/TASC.2009.2017758. URL <http://ieeexplore.ieee.org/lpdocs/epic03/wrapper.htm?arnumber=5109536>.
- [150] E. B. Smith. *Design Av Nacelle fro en 10 MW VindTurbin*. Msc thesis, Norwegian University of Science and Technology, 2012.
- [151] G. Snitchler. Progress on high temperature superconductor propulsion motors and direct drive wind generators. *Power Electronics Conference (IPEC), 2010*, (c):5–10, 2010. URL [http://ieeexplore.ieee.org/xpls/abs\\_all.jsp?arnumber=5542327](http://ieeexplore.ieee.org/xpls/abs_all.jsp?arnumber=5542327).

- [152] G. Snitchler, B. Gamble, C. King, and P. Winn. 10 MW Class Superconductor Wind Turbine Generators. *IEEE Transactions on Applied Superconductivity*, 21(3):1089–1092, June 2011. ISSN 1051-8223. doi: 10.1109/TASC.2010.2100341. URL <http://ieeexplore.ieee.org/lpdocs/epic03/wrapper.htm?arnumber=5699957>.
- [153] J. N. Stander, G. Venter, and M. J. Kamper. Review of direct-drive radial flux wind turbine generator mechanical design. *Wind Energy*, 15(3):459–472, April 2012. ISSN 10954244. doi: 10.1002/we.484. URL <http://doi.wiley.com/10.1002/we.484>.
- [154] W. Stautner, R. Fair, K. Sivasubramaniam, K. Amm, J. Bray, E. T. Laskaris, K. Weeber, M. Douglass, L. Fulton, S. Hou, J. Kim, R. Longtin, M. Moscinski, J. Rochford, R. Rajput-Ghoshal, P. Riley, D. Wagner, and R. Duckworth. Large Scale Superconducting Wind Turbine Cooling. *IEEE Transactions on Applied Superconductivity*, 23(3):5200804, June 2013. ISSN 1051-8223. doi: 10.1109/TASC.2012.2231138. URL <http://ieeexplore.ieee.org/lpdocs/epic03/wrapper.htm?arnumber=6365243>.
- [155] H. Sugimoto, T. Tsuda, T. Morishita, Y. Hondou, T. Takeda, H. Togawa, T. Oota, K. Ohmatsu, and S. Yoshida. Development of an Axial Flux Type PM Synchronous Motor With the Liquid Nitrogen Cooled HTS Armature Windings. *IEEE Transactions on Applied Superconductivity*, 17(2):1637–1640, June 2007. ISSN 1051-8223. doi: 10.1109/TASC.2007.899959. URL <http://ieeexplore.ieee.org/lpdocs/epic03/wrapper.htm?arnumber=4277740>.
- [156] H. Sung, G. Kim, K. Kim, S. Jung, and M. Park. Practical Design of a 10 MW Class Superconducting Wind Power Generator Considering Weight Issue. (281):6–10, 2013. URL [http://ieeexplore.ieee.org/xpls/abs\\_all.jsp?arnumber=6449292](http://ieeexplore.ieee.org/xpls/abs_all.jsp?arnumber=6449292).
- [157] D. Svehkarenko. *On Design and Analysis of a Novel Transverse Flux Generator for Direct-driven Wind Application*. Phd dissertation, Royal Institute of Technology, Sweden, 2010.
- [158] Y. Terao, M. Sekino, and H. Ohsaki. Electromagnetic Design of 10 MW Class Fully Superconducting Wind Turbine Generators. *IEEE Transactions on Applied Superconductivity*, 22(3):5201904, June 2012. ISSN 1051-8223. doi: 10.1109/TASC.2011.2177628. URL <http://ieeexplore.ieee.org/lpdocs/epic03/wrapper.htm?arnumber=6092460>.
- [159] ThyssenKrupp-Steel. Power Core M270-50A Electrical Steel Datasheet. Technical report, Duisburgh, 2009. URL <http://www.thyssenkrupp-steel-europe.com/tiny/2f/download.pdf>.

- [160] P. Tixador. Development of superconducting power devices in Europe. *Physica C: Superconductivity*, 470(20):971–979, November 2010. ISSN 09214534. doi: 10.1016/j.physc.2010.05.014. URL <http://linkinghub.elsevier.com/retrieve/pii/S0921453410002704>.
- [161] M. Tomita and M. Murakami. High-temperature superconductor bulk magnets that can trap magnetic fields of over 17 tesla at 29 K. *Nature*, 421(6922):517–520, January 2003. ISSN 0028-0836. doi: 10.1038/nature01350. URL <http://www.ncbi.nlm.nih.gov/pubmed/12556888>.
- [162] W. Tong. *Wind Power Generation and Wind Turbine Design*. WIT Press, 2010. ISBN 1845642058. URL <http://books.google.com/books?hl=en&lr=&id=wU9bgvrl4rQC&pgis=1>.
- [163] Vacuumschmelze. VacoFlux (Soft Magnetic Cobalt-Iron-Alloys) Datasheet. Technical report, Hanau, Germany, 2012. URL <http://www.vacuumschmelze.com/>.
- [164] C. Versteegh and G. Hassan. Design of the Zephyros Z72 wind turbine with emphasis on the direct drive PM generator. In *Proc. of the Nordic workshop on power and industrial electronics (NORPIE)*, volume 31, pages 14–16, 2004. URL <http://www.elkraft.ntnu.no/norpie/10956873/FinalPapers/068-Norpiepaper.pdf>.
- [165] E. P. Volkov, V. S. Vysotsky, and V. P. Firsov. First Russian long length HTS power cable. *Physica C: Superconductivity*, 482:87–91, November 2012. ISSN 09214534. doi: 10.1016/j.physc.2012.04.024. URL <http://linkinghub.elsevier.com/retrieve/pii/S0921453412002122>.
- [166] H. Vu Xuan, D. Lahaye, H. Polinder, and J. A. Ferreira. Influence of Stator Slotting on the Performance of Permanent-Magnet Machines With Concentrated Windings. *IEEE Transactions on Magnetics*, 49(2):929–938, February 2013. ISSN 0018-9464. doi: 10.1109/TMAG.2012.2212025. URL [http://ieeexplore.ieee.org/xpls/abs\\_all.jsp?arnumber=6262480http://ieeexplore.ieee.org/lpdocs/epic03/wrapper.htm?arnumber=6262480](http://ieeexplore.ieee.org/xpls/abs_all.jsp?arnumber=6262480http://ieeexplore.ieee.org/lpdocs/epic03/wrapper.htm?arnumber=6262480).
- [167] L. Wang and S. Chen. Stability improvement of a grid-connected offshore wind farm using a superconducting magnetic energy storage. *Industry Applications Society Annual Meeting (IAS)*, 60:1–8, 2012. doi: 10.1109/IAS.2012.6374096. URL [http://ieeexplore.ieee.org/xpls/abs\\_all.jsp?arnumber=6374096](http://ieeexplore.ieee.org/xpls/abs_all.jsp?arnumber=6374096).
- [168] E. Watanabe, K. Kikukawa, Y. Satoh, and S. Torii. Development of a superconducting claw-pole motor. *Physica C: Superconductivity*, 468(15-20):2087–2090, September 2008. ISSN 09214534. doi: 10.1016/j.physc.2008.05.132.

- [169] B. Weggel. Amortization Running Cost of 1.5-T Magnets for 50-meter Chicane. Technical report, 2013.
- [170] T. Weise. *Global Optimization Algorithms - Theory and Application*. 3rd edition, 2011.
- [171] H. Wen, W. Bailey, K. Goddard, M. K. Al-Mosawi, C. Beduz, and Y. Yang. Performance Test of a 100 kW HTS Generator Operating at 67 K-77 K. *IEEE Transactions on Applied Superconductivity*, 19(3):1652–1655, June 2009. ISSN 1051-8223. doi: 10.1109/TASC.2009.2017832. URL <http://ieeexplore.ieee.org/lpdocs/epic03/wrapper.htm?arnumber=5067244>.
- [172] R. Wrobel and P. Mellor. Design Considerations of a Direct Drive Brushless Machine With Concentrated Windings. *IEEE Transactions on Energy Conversion*, 23(1):1–8, March 2008. ISSN 0885-8969. doi: 10.1109/TEC.2007.905073. URL <http://ieeexplore.ieee.org/lpdocs/epic03/wrapper.htm?arnumber=4378207>.
- [173] Y. Xin, H. Hui, W. Z. Gong, F. Ye, J. Z. Wang, B. Tian, a. L. Ren, and M. R. Zi. Superconducting cable and superconducting fault current limiter at Puji Substation. In *2009 International Conference on Applied Superconductivity and Electromagnetic Devices*, pages 392–397. IEEE, September 2009. ISBN 978-1-4244-3686-6. doi: 10.1109/ASEMD.2009.5306612. URL <http://ieeexplore.ieee.org/lpdocs/epic03/wrapper.htm?arnumber=5306612>.
- [174] A. Zavvos, D. Bang, A. McDonald, H. Polinder, and M. Mueller. Structural analysis and optimisation of transverse flux permanent magnet machines for 5 and 10 MW direct drive wind turbines. *Wind Energy*, 15(1):19–43, January 2012. ISSN 10954244. doi: 10.1002/we.543. URL <http://doi.wiley.com/10.1002/we.543>.
- [175] A. Zavvos. *Structural Optimisation of Permanent Magnet Direct Drive Generators for 5MW Wind Turbines*. Phd dissertation, University of Edinburgh, 2013.
- [176] Zenergy. Superconductors are Cool - but How to Keep them Cold? Technical report, 2010.
- [177] F. Zhang, Y. Liu, and H. Bai. Study and design of 3-D flux permanent magnet claw-pole motor with SMC stator. *2009 International Conference on Applied Superconductivity and Electromagnetic Devices*, pages 316–319, September 2009. doi: 10.1109/ASEMD.2009.5306629. URL <http://ieeexplore.ieee.org/lpdocs/epic03/wrapper.htm?arnumber=5306629>.

- 
- [178] T. Zhang, K. Haran, E. Laskaris, and J. Bray. Design and test of a simplified and reliable cryogenic system for high speed superconducting generator applications. *Cryogenics*, 51(7):380–383, July 2011. ISSN 00112275. doi: 10.1016/j.cryogenics.2011.03.004. URL <http://linkinghub.elsevier.com/retrieve/pii/S0011227511000646>.
- [179] Z. Zhu and D. Howe. Influence of design parameters on cogging torque in permanent magnet machines. *IEEE Transactions on Energy Conversion*, 15(4):407–412, 2000. ISSN 08858969. doi: 10.1109/60.900501. URL <http://ieeexplore.ieee.org/lpdocs/epic03/wrapper.htm?arnumber=900501>.